



Dipl.-Ing. Roman Zettl, BSc.

# Electrode Materials for a Hybrid Solar Cell Battery System and Ion Dynamics in Porous Materials

## Dissertation

zur Erlangung des akademischen Grades  
Doktor der Technischen Wissenschaften (Dr. techn.)

eingereicht an der  
Technischen Universität Graz

Betreuer

*Univ.-Prof. Dr. H. Martin R. Wilkening*

*Dr. Ilie Hanzu*

Institut für die Chemische Technologie von Materialien

Graz, September 2020



*”So eine Arbeit wird eigentlich nie fertig, man muß sie für fertig erklären, wenn man nach Zeit und Umständen das Möglichste getan hat.”*

- Johann Wolfgang von Goethe (1749-1832)



## **Affidavit**

I declare that I have authored this thesis independently, that I have not used other than the declared sources/resources, and that I have explicitly indicated all material which has been quoted either literally or by content from the used sources. The text document uploaded to TUGRAZonline is identical to the present doctoral thesis.

## **Eidesstaatliche Erklärung**

Ich erkläre an Eides statt, dass ich die vorliegende Arbeit selbstständig verfasst, andere als die angegebenen Quellen/Hilfsmittel nicht benutzt, und die den benutzten Quellen wörtlich und inhaltlich entnommenen Stellen als solche kenntlich gemacht habe. Das in TUGRAZonline hochgeladene Textdokument ist mit der vorliegenden Dissertation identisch.

---

Date / Datum

---

Signature / Unterschrift



# Danksagung

Zuallererst möchte ich mich bei meinen Betreuern Martin und Ilie bedanken. Danke für die Möglichkeit in dieser Arbeitsgruppe meine Dissertation durchzuführen. Man kann es nicht hoch genug einschätzen, wie ihr nicht nur fachlich, sondern vor allem auch menschlich, diese Zeit und die Erarbeitung meiner Dissertation zu einer großartigen Erfahrung gemacht habt. Ich habe die Zusammenarbeit mit euch immer sehr geschätzt. Danke auch, dass ihr mir den Forschungsaufenthalt in Utrecht ermöglicht habt. Hier möchte ich mich auch bei meinen dortigen Betreuern Peter Ngene und Petra de Jongh für eine sehr spannende Zeit in ihren Laboren bedanken. Ich durfte auch viele weitere Bekanntschaften an der *Universiteit Utrecht* machen, die mir bestimmt mein Leben lang in Erinnerung bleiben werden. Danke für die wunderbare Zeit! Natürlich gilt ein großer Dank auch meinen Kollegen in der Arbeitsgruppe in Graz. Man kann schon von großem Glück sprechen, in solch einer Gruppe arbeiten zu dürfen. Danke für eure Unterstützung und den lockeren Umgang miteinander. Ihr seid nicht nur Kollegen, sondern auch Freunde. Besonderer Dank gilt natürlich meinen Bürokollegen und längsten Wegbegleitern in der Arbeitsgruppe: Marina, Caro und Maria.

An dieser Stelle möchte ich mich besonders bei meinen Freuden in Graz, Wien und Kärnten bedanken. Es ist wie Dante Alighieri schon sagte: „*Ohne Freunde können wir kein vollkommenes Leben führen.*“ Wir haben zusammen gefeiert, Ausflüge unternommen und unterschiedlichste Sportaktivitäten gemeinsam ausgeübt. All das hat mir immer wieder Kraft und Motivation für den Alltag gegeben. Die Studienzeit war auch geprägt von besonderen Leuten, denen ich noch danken möchte: meine USW Studienkollegen. Auch wenn ich nicht in jeder Vorlesung war, war es mir doch jedes mal eine Freude mit euch auf der Uni zu sein. Danke für den Austausch von etlichen Unterlagen und Lerninhalten sowie die gemeinsamen Laborübungen und das eine oder andere Bier.

Zuletzt gilt der größte Dank meiner Familie. Meinem Vater, von dem ich das Interesse zur Technik geerbt habe. Meiner unbeschreiblichen Oma, die mich immer mit einem Essen nach der Schule versorgt hat. Ich weiß, ihr seid stolz auf mich da oben. Danke auch an meine Schwester Daniela, die mir immer in wichtigen Entscheidungen mit ihrem Rat zur Seite stand und steht. Nun weiß ich nicht, ob es Worte des Dankes gibt, die dem gerecht werden, was meine Mutter während meines gesamten Lebens für mich getan hat. Danke für einfach ALLES, Mama. Für das Warten nach der Schule oder dem Fußballtraining, für die Unterstützung in allen Bereichen, dafür dass ich mit allem, was so in meinem Leben passiert zu dir kommen kann! Nicht zuletzt auch dafür, dass du mir während einem Großteil des Verfassens dieser Arbeit, ein heimeliges Zuhause geboten hast.

Ich wäre nicht da, wo ich jetzt bin, ohne einen Einzelnen von euch.

DANKE!

## Kurzfassung

Die aktuelle Energiekrise ist eine der größten Herausforderungen unserer Zeit. Die letzten Jahrzehnte waren geprägt von der Suche nach nachhaltigen und effektiven Systemen zur Energieumwandlung und –speicherung. Das Ziel der Forschung ist es, den Anteil an fossilen Energieträgern zu minimieren und den Energiemix in Richtung erneuerbarer Ressourcen zu verschieben. Dabei sind effiziente Energiespeicher von großer Bedeutung, da sie eine durchgehende Bereitstellung der Energie gewährleisten und Fluktuationen erneuerbarer Energiequellen ausgleichen. Ein Vertreter chemischer Energiespeicher ist der Lithium-Ionen-Akkumulator (Lithium-Ionen-Akku), der vor allem in portablen Geräten Anwendung findet. Jedoch werden bei der Herstellung von Lithium-Ionen-Akkus verhältnismäßig seltene Rohstoffe verwendet und deshalb gilt ein großes Augenmerk der heutigen Batterieforschung alternativen Batteriesystemen. Auch das Sicherheitsrisiko, welches mit der Anwendung eines leicht entzündlichen sowie explosiven, flüssigen, organischen Elektrolyten einhergeht, wirft seinen Schatten auf den Lithium-Ionen-Akku. Der komplementäre Natrium-Ionen-Akku könnte das Problem, trotz seiner verminderten Energiedichte, zumindest in stationären Energiespeichern lösen. In solchen Anwendungen wäre die geringere Energiedichte kein großes Problem, da man räumlich nicht limitiert wäre und durch größere Bauweisen die Verluste an Energiedichte kompensieren könnte. Zusätzlich gibt es schon vielversprechende Fortschritte auf dem Gebiet anorganischer Festkörperelektrolyte, um die brennbaren Flüssigelektrolyte zu ersetzen.

In dieser Arbeit wird unter anderem eine Anwendung vorgestellt, die eine Solarzelle direkt mit einem Natrium-Ionen-Akkumulator verbindet; mit dem Ziel gesteigerter Effizienz. Die Ergebnisse zeigen vor allem die Leistungsfähigkeit des Konzepts und erwiesen sich als äußerst vielversprechend für zukünftige Projekte auf diesem Gebiet. Ein Kathodenmaterial aus dieser Studie wurde in weiterer Folge magnetometrisch untersucht. Mit dem Modellsystem Natriumvanadiumphosphat (NVP) wurde gezeigt, dass am Ladungsaustausch dieses Kathodenmaterials, während des Ladens und Entladens, ausschließlich die Redoxreaktion des Übergangsmetalls beteiligt ist. Diese *in-situ* Methode, die mit Hilfe der Bestimmung der magnetischen Suszeptibilität oben genannte Schlüsse zulässt, wurde bisher nur bei lithiumhaltigen Materialien angewandt.

Den zweiten großen Schwerpunkt der Arbeit bildet die Untersuchung der Ionendynamik in porösen Materialien. Dazu wurden vor allem die Techniken Impedanzspektroskopie und Kernspinresonanzspektroskopie (NMR, engl. nuclear magnetic reso-

nance) genutzt. Einerseits wird ein System untersucht, in dem die ionische Leitfähigkeit bei Raumtemperatur gesteigert wird, wenn ein Komposit aus einem anionsubstituierten Metallhydrid und einem porösen, elektrisch isolierenden Festkörper gebildet wird. Die Ergebnisse zeigen, dass unterschiedliche Kombinationen von porösen Materialien und anionsubstituierten Metallhydriden zu oben genannter Leitfähigkeitssteigerung führen. Die Ursache dieser Steigerung in der ionischen Leitfähigkeit ist nicht vollends geklärt, könnte jedoch beispielsweise auf Raumladungszonen an den Grenzflächen zwischen Elektrolyt und Isolator zurückzuführen sein. Um mehr über diesen Kompositelektrolyten herauszufinden, wurde eine detaillierte NMR-Studie durchgeführt. Hierbei konnten langreichweitige und kurzreichweitige Diffusionsprozesse sowie strukturelle Eigenschaften des Materials untersucht werden. Weiters wurden in dieser Arbeit auch poröse, metallorganische Gerüste (engl. metal-organic frameworks, MOFs) als potentielle Elektrolyte für Alkali-Ionen-Akkus untersucht. Nach der Modifizierung mit Li- und Na-haltigen Lösungen, konnten durch die Zugabe von flüssigen Elektrolyten vielversprechende Ergebnisse erzielt werden. Diese fest-flüssig Hybridelektrolyte bilden eine relativ junge Gruppe von festen Ionenleitern.

# Abstract

Today's energy crisis challenges researchers all over the world to find effective and sustainable energy conversion and storage systems. The purpose of the research is to shift the share of fossil fuels towards renewable energy resources. Hereby, large-scale energy storage is crucial, since renewable energy resources suffer from fluctuations. Lithium-ion batteries have proven to be highly suitable to store energy in mobile applications, but the abundance of the materials, required in battery production, is rather limited. Additionally, there is a severe safety concern with currently used flammable and explosive, organic-based, liquid electrolytes. These circumstances catalyse the research towards alternative battery systems like the sodium-ion battery and all solid-state batteries with solid electrolytes.

One topic of this thesis was the implementation of a sodium-ion battery in a hybrid device with an organic solar cell. The study perfectly revealed a proof-of-principle and encouraging results for future projects in this field. Following this study, we could also show that the charge compensation of a sodium cathode material, namely sodium vanadium phosphate, is only due to the redox reaction during charging and discharging. Before these investigations were realized, in-situ measurements of the magnetic susceptibility were only carried out on active materials for lithium-ion batteries.

Another main part of the thesis focusses on ion dynamics in porous materials. Impedance spectroscopy and nuclear magnetic resonance (NMR) were the main techniques applied to study both ionic conductivity and ion dynamics in these composite electrolytes. In the frame of this thesis, it will be shown that the combination of well-established techniques to boost the room temperature ionic conductivity of metal hydrides, like lithium borohydride, can be effectively combined. These approaches are (i) partial ion substitution of borohydride anions with halide anions and (ii) nanoconfinement of the metal hydride in porous supports. The composite, combining both approaches, showed significantly increased room temperature conductivity. These encouraging findings built the basis of a detailed NMR study on the model system  $\text{LiBH}_4\text{-LiI/Al}_2\text{O}_3$  to elucidate the structure of the composite and to investigate ion dynamics in detail. Beside these pure solid-state ion conductors, hybrid solid-liquid ion conductors based on porous metal-organic frameworks (MOFs) were designed, prepared and studied. We obtained promising results taken into account that this is a relatively new field of electrolytes.



# Table of Contents

|  |           |
|--|-----------|
| Eidesstaatliche Erklärung . . . . .                                      | V         |
| Danksagung . . . . .   | VII       |
| Kurzfassung . . . . .  | IX        |
| Abstract . . . . .   | XI        |
| <b>1 Introduction and Background</b>                                     | <b>1</b>  |
| <b>2 Batteries</b>   | <b>3</b>  |
| 2.1 Origin and History . . . . .   | 3         |
| 2.2 The Lithium-Ion Battery . . . . .                                    | 6         |
| 2.2.1 Working Principle . . . . .  | 6         |
| 2.2.2 Materials . . . . .  | 9         |
| 2.3 Solid-State Electrolytes . . . . .                                   | 16        |
| 2.3.1 Interest and Obstacles . . . . .                                   | 17        |
| 2.3.2 Types . . . . .  | 19        |
| 2.4 Battery Characterization . . . . .                                   | 22        |
| 2.4.1 Cyclic Voltammetry . . . . .                                       | 22        |
| 2.4.2 Galvanostatic Cycling with Potential Limitation . . . . .          | 26        |
| <b>3 Diffusion in Solids</b>   | <b>29</b> |
| 3.1 Fundamentals . . . . .   | 30        |
| 3.1.1 Fick's Laws . . . . .  | 30        |
| 3.1.2 Random Walk Theory . . . . .                                       | 31        |
| 3.1.3 Defects . . . . .  | 33        |
| 3.1.4 Diffusion Mechanisms . . . . .                                     | 37        |
| 3.2 Determination of Diffusion Parameters . . . . .                      | 39        |
| 3.2.1 Impedance Spectroscopy . . . . .                                   | 40        |
| 3.2.2 Nuclear Magnetic Resonance . . . . .                               | 45        |
| <b>4 Results</b>   | <b>53</b> |
| 4.1 Electrode Materials for a Hybrid Solar Cell Battery System . . . . . | 53        |

|          |  |            |
|----------|--|------------|
| 4.1.1    | A New Solar Cell – Battery Hybrid Energy System . . . . .                                | 54         |
| 4.1.2    | Magnetometric Observations on Sodium Vanadium Phosphate                                  | 70         |
| 4.2      | Ion Dynamics in Porous Materials . . . . .   | 77         |
| 4.2.1    | Introduction . . . . .   | 77         |
| 4.2.2    | Combining Ion Substitution and Nanoconfinement in Complex Hydrides . . . . .             | 79         |
| 4.2.3    | NMR Observations on Combined Ion Substituted and Nanoconfined Complex Hydrides . . . . . | 92         |
| 4.2.4    | Outlook on $\text{LiBH}_4$ /Oxide Composites . . . . .                                   | 108        |
| 4.2.5    | Hybrid Liquid-Solid Electrolytes Based on Metal-Organic Frameworks . . . . .             | 110        |
| <b>5</b> | <b>Summary and Conclusion</b>  | <b>133</b> |
| <b>A</b> | <b>Supplemental Material</b>   | <b>135</b> |
| <b>B</b> | <b>Experimental</b>  | <b>179</b> |
| B.1      | Standard Laboratory Procedures . . . . .   | 179        |
| B.1.1    | Electrode Preparation . . . . .  | 179        |
| B.1.2    | Electrolyte Preparation . . . . .  | 180        |
| B.2      | Measuring Procedures . . . . .   | 181        |
| B.2.1    | Electrochemical Characterization . . . . .   | 181        |
| B.2.2    | Impedance Spectroscopy . . . . .   | 182        |
| B.2.3    | Nuclear Magnetic Resonance . . . . .   | 183        |
| B.3      | Data Analysis . . . . .  | 186        |
| <b>C</b> | <b>List of Publications</b>  | <b>187</b> |
| C.1      | Journal Articles . . . . .   | 187        |
| C.2      | Oral Presentations . . . . .   | 188        |
| C.3      | Poster Presentations . . . . .   | 188        |
| <b>D</b> | <b>Bibliography</b>  | <b>191</b> |

# 1 | Introduction and Background

The energy crisis is one of the main challenges humanity has to face in the 21<sup>st</sup> century. Climate is changing all over the world and severely affects our nature. Sea levels are rising, average temperatures are increasing and glaciers are melting. The demand of energy humans need to live a "humane" life is enormous. This is particularly true in the western society. The extent, to which the current production of energy relies on fossil fuels, is far too large. The focus of a significant portion of researchers is on alternative energy conversion systems. Energy conversion systems based on renewable energy like solar cells or wind turbines, however, cannot guarantee energy on demand. The sources of energy, *i.e.* solar radiation or wind, are subject to fluctuations. Thus, when sustainable techniques for energy conversion are applied, they have to be complemented with efficient energy storage systems. If, *e.g.* solar energy is converted to electricity during sunny periods, a major part of the energy cannot be used immediately. Electrical energy has to be intermediately stored to guarantee a continuous supply of energy at night or during cloudy periods. Large-scale grid storage systems have to meet strict safety regulations and requirements in terms of performance.

Lithium-ion batteries (LIBs) proved themselves as potential candidate for this purpose. The relatively low abundance of raw materials and the toxicity of part of them hinders the application of LIBs for large-scale grid electricity storage. In this context the sodium ion battery (SIB) could be of high importance. With the same working principle and comparable components, SIBs could profit a lot from the sophisticated research on LIBs. Additionally, Na is almost indefinitely available in the earth crust. The drawbacks of SIBs like lower energy density do not affect its application in the field of large-scale grid electricity storage, since spacial requirements are a secondary issue. In mobile applications SIBs are, however, considered no realistic alternative to LIBs.

Additionally, LIBs suffer from a severe safety concern due to their highly flammable and explosive liquid, organic-based, electrolytes. This circumstance led researchers towards the field of solid-state electrolytes. The main challenges with solid-state

---

electrolytes is their limited ionic conduction and the large interfacial resistances. The issue of little ionic conduction, is, however, solved to a large extent as there are many examples in literature proposing solid-state electrolytes with room temperature conductivities above the considered benchmark of around  $1 \text{ mS cm}^{-1}$ . Two techniques have proven to be effective in shedding light on the crucial properties of potential solid-state electrolytes. Impedance spectroscopy and nuclear magnetic resonance (NMR) are the main methods carried out to observe ionic conductivity, diffusion properties and the behaviour at the interfaces. These techniques offer comprehensive information about long-range ion transport and short-range diffusion. In addition, NMR is element-specific and provides structural information of the material. This information can help understand how ions diffuse through the material and how we could manipulate or optimize the materials to achieve faster diffusion of ions. Modifications of potential solid-state electrolytes to enhance their diffusion properties include nanosizing by high-energy ball milling or nanoconfining of electrolytes into porous supports.

In the first part of the thesis the aim was to develop a sodium-ion battery which is compatible with an organic solar cell. The basic idea was to increase the total efficiency by directly combining the two devices. With focus on materials compatibility, we were able to build a solar cell–battery hybrid energy system. The implementation of a SIB has the advantages of higher safety and stability compared to the use of LIB. Furthermore, this thesis deals with the role of porous materials in solid-state electrolytes. Since huge efforts were launched already in solid-electrolytes based on different oxides [1], phosphates [2] and thiophosphates [3], with none of them entirely meeting all requirements for battery application, this work focusses on hydride-based solid electrolytes and their interaction with a porous support. In addition, another porous material was studied with respect to its diffusion behaviour. A porous metal-organic framework was modified in order to incorporate Li and Na ions into the structure. The modified MOF was additionally soaked with a liquid electrolyte. This liquid electrolyte, however, is encapsulated in the solid, which makes the solid-liquid hybrid electrolyte much less flammable than purely liquid electrolytes.

# 2 | Batteries

## Contents

---

|       |   |    |
|-------|---|----|
| 2.1   | Origin and History . . . . .                              | 3  |
| 2.2   | The Lithium-Ion Battery . . . . .                         | 6  |
| 2.2.1 | Working Principle . . . . .                               | 6  |
| 2.2.2 | Materials . . . . .                                       | 9  |
| 2.3   | Solid-State Electrolytes . . . . .                        | 16 |
| 2.3.1 | Interest and Obstacles . . . . .                          | 17 |
| 2.3.2 | Types . . . . .   | 19 |
| 2.4   | Battery Characterization . . . . .                        | 22 |
| 2.4.1 | Cyclic Voltammetry . . . . .                              | 22 |
| 2.4.2 | Galvanostatic Cycling with Potential Limitation . . . . . | 26 |

---

## 2.1. Origin and History

Currently an incredibly large amount of research resources is put into lithium-ion batteries (LIBs). When the element lithium (Li) was first discovered in the early 19<sup>th</sup> century, nobody thought that the metal would play a major role in the energy crisis of the 21<sup>st</sup> century. It was the Swede Johan August Arfwedson [4] who discovered the metal with an atomic weight of 6.95 g/mol and a density of 0.534 g/cm<sup>3</sup>. There is no metal in the periodic table with lower values of atomic weight and density than Li. A few years after its discovery, Li was first isolated from molten lithium oxide with the help of a voltaic pile.[5] Even though Li was discovered and isolated, it did not play any role in the first discoveries in battery research. In 1800, Alessandro Volta was the first who described the conversion of chemical energy to electric energy.[6] Together with his Italian compatriot Luigi Galvani and his famous experiments on frog legs, Alessandro Volta was responsible for the pioneering work in battery research.[7] In fact, Volta wanted to challenge Galvani's theory of animal electricity and showed that the body fluid of the frog simply served as electrolyte.[6] In his voltaic pile,

Volta stacked zinc and copper plates on top of each other and separated them by cloths soaked in sodium chloride.[8] In Figure 1 a schematic (a) and a prototype (b) of the voltaic pile are shown. The voltaic pile follows a simple principle similar to other electrochemical cells. Two metals A and B, with one being more noble, are in contact with an electrolyte. In the case of the voltaic pile Cu represents the more noble metal. The metals are additionally connected via an external circuit, which enables electrons to move from the negative to the positive electrode when an external load is connected. If, on the other hand, a source of current would be connected, the reactions can be inverted and the cell gets charged. The combination of a number of cells is called a battery. Thus, the voltaic pile is considered as the first electrical battery. A difference of more advanced electrochemical cells to the voltaic pile is the use of a membrane, which creates two electrolyte compartments. The free electrons are generated by redox reactions inside the cell during discharging [9, 10]:

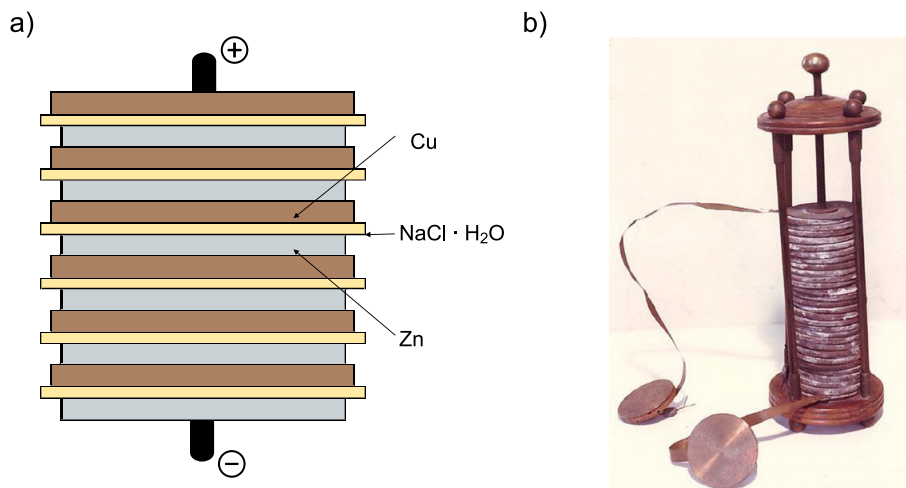
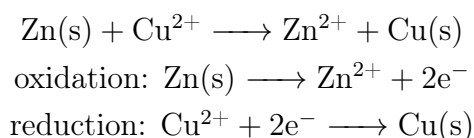


**Figure 1.** a) A schematic of the voltaic pile: Six stacks of zinc (Zn), aqueous NaCl soaked cloths and copper (Cu) are exemplarily shown on top of each other. The final zinc plate is the negative pole and the final copper plate is the positive pole. b) A prototype of the voltaic pile.[7]

The 19<sup>th</sup> century was full of new battery concepts. Two inventions, however, stand out among all of them. The alkaline battery and the lead-acid battery are

still in use nowadays, even though they were optimized.[7] In 1859, the Frenchman Gaston Planté was responsible for the development of the lead-acid battery; the first rechargeable battery.[11] Planté used lead sheets as electrodes and sulfuric acid as electrolyte.[12] Even though his concept has been improved, the lead-acid battery still helps starting our cars. The first alkaline battery goes back to Georges-Lionel Leclanché. In 1866, he used aqueous ammonium chloride as electrolyte, whereas a zinc rod and a composite of manganese oxide and carbon served as electrodes.[13] The optimization of this first primary alkaline battery included the use of zinc powder in the core of the cell surrounded by the electrolyte, which had the consistency of a paste through the addition of starch. On the cathode side still a mixture of manganese oxide and carbon is used, which is also in a paste-like state.[7]

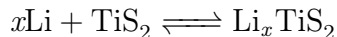
In the early 20<sup>th</sup> century, another famous type of battery was born: the nickel-cadmium battery (Ni-Cd battery). The toxicity of Cd, however, led to a ban for Ni-Cd batteries in many countries. In Austria Ni-Cd batteries are banned by law<sup>1</sup> since 2008. The increasing demand on portable electric devices and especially the demand of smaller and lighter batteries with a longer cycle life in *e.g.* medicine for pacemakers catalysed the research in new battery techniques. Due to its light weight and low electrochemical potential of  $-3.05\text{ V}$  *vs.* the standard hydrogen electrode, Li started to arouse interest of researchers. In 1986, a battery composed of Li metal (anode) and an iodine-based cathode, the lithium-iodine battery, was proposed.[14] The use of Li metal forced a change from aqueous to organic electrolytes since Li is not compatible with aqueous solutions. Together with the latter described Li-ion battery, this new concept led to a significant increase in specific capacity and triggered the huge interest in Li-based batteries.[7]

In 2019 John Bannister Goodenough, Michael Stanley Whittingham and Akira Yoshino were awarded the Nobel price in chemistry "*for the development of Li-ion batteries*".[15] The battery of Whittingham and his team was composed of Li metal at the anode side and titan(IV)-sulfid ( $\text{TiS}_2$ ) at the cathode side separated by lithium hexafluorophosphate ( $\text{LiPF}_6$ ) in propylene carbonate. Li ions, generated through oxidation of metallic Li, move to the layered cathode. At the cathode, they are intercalated between the layers of  $\text{TiS}_2$ . As  $\text{Li}^+$  does not change its charge when it is intercalated, the oxidation state of Ti changes from  $\text{IV}^+$  to  $\text{III}^+$  in order to maintain electroneutrality. This was the birth of intercalation compounds as electrodes materials for Li batteries. The electrochemical reaction could be described

---

<sup>1</sup>In 2008 the Austrian federal government, in the name of the federal minister of agriculture and forestry, environment and water management, decided on the so-called *battery enactment*. The enactment dealt with waste prevention, collection and treatment of used batteries.

as follows with  $x$  equals the degree of intercalation [16]:



The battery of Whittingham, however, suffered from safety concerns. The risk of dendrite growth followed by short circuit and explosion was too high. Therefore, Goodenough and coworkers focussed on Li metal free batteries. What they found primarily, however, was the possibility of increasing the voltage of the cathode.  $\text{TiS}_2$  only has a potential of 2.5 V *vs.*  $\text{Li}/\text{Li}^+$ , whereas the potential of  $\text{LiCoO}_2$  is 3.9 V *vs.*  $\text{Li}/\text{Li}^+$ .  $\text{LiCoO}_2$  was patented by Goodenough in the 1980s and enabled the use of anodes with higher potentials *vs.*  $\text{Li}/\text{Li}^+$  without a loss in energy density.[17] Finally, Yoshino and coworkers investigated carbonaceous structures, which were able to intercalate  $\text{Li}^+$ , just as  $\text{TiS}_2$  and  $\text{LiCoO}_2$ , but at very low potentials *vs.*  $\text{Li}/\text{Li}^+$ . These materials, with a potential as low as 150 mV *vs.*  $\text{Li}/\text{Li}^+$ , were highly promising candidates to replace Li metal as anode material. The first findings on carbonaceous  $\text{Li}^+$  intercalation materials, however, go back to Yazami *et al.* [18] They proved the reversible intercalation of Li ions into and out of carbonaceous materials. The material provides high specific capacity and in its fully charged form it appears as  $\text{C}_6\text{Li}$ . Yoshino filed a patent of a battery composed of a carbonaceous anode material and  $\text{LiCoO}_2$ , which was the first Li-ion battery (LIB).[19, 20] The commercialization of the LIB followed by Sony in 1991.[21]

Following these groundbreaking works from Volta to the Nobel laureates in chemistry of 2019 the working principle of the Li-ion battery is described in the next section. Additionally, different types of anode, cathode and electrolyte materials are presented.

## 2.2. The Lithium-Ion Battery

### 2.2.1. Working Principle

The lithium-ion battery (LIB) is a secondary battery, which means its underlying electrochemical reactions are of reversible nature, *i.e.* the battery is rechargeable. The principle is similar to that of every electrochemical cell. During discharging ions diffuse through an electrolyte from the negative to the positive electrode. In this case the metal rods or plates, like in basic electrochemical cells, are replaced by compounds which can take up and release Li ions reversibly. The positive electrode

is most commonly a transition-metal oxide whereas the negative electrode is mainly a carbonaceous material. Originally the cell is in a discharged state. Upon charging Li ions leave the cathode and diffuse through the electrolyte and are taken up by the anode. Redox reactions at the electrodes generate electrons that move from the positive to the negative electrode as well, but via current collectors and an external circuit. The flow of ions and electrons is reversed when the charger is replaced by an external load. The stored chemical energy is converted in electrochemical energy by the reversible redox reactions and supplies the external load.[10] In Figure 2 intercalation materials graphite as anode and  $\text{LiCoO}_2$  as cathode are chosen exemplarily for the representation of the working principle of a lithium-ion battery. The electrolyte in this case is  $\text{LiPF}_6$  dissolved in a mixture of ethylene carbonate and dimethyl carbonate (EC:DMC).

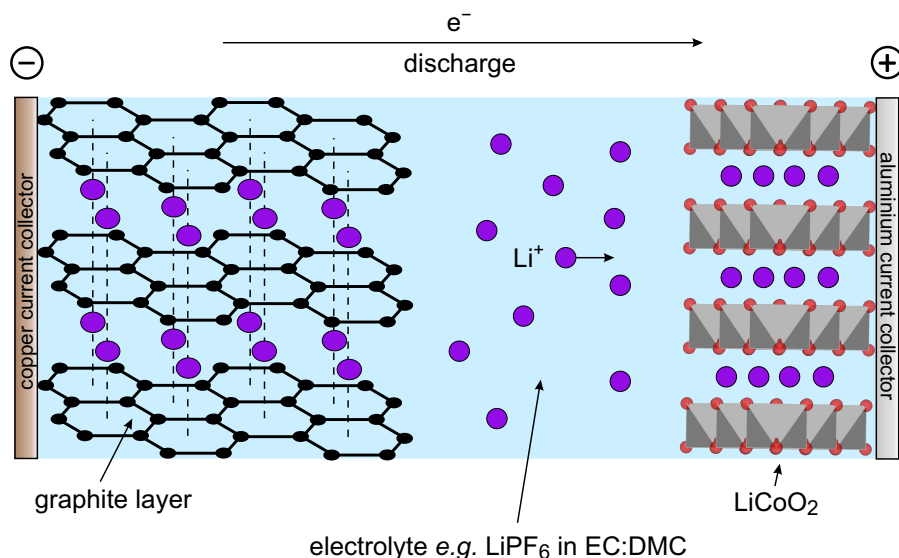


**Figure 2.** Schematic of a lithium-ion battery during discharging. Graphite as the anode and lithium cobalt oxide at the cathode side are the most common, commercially used electrode materials. Here, the electrolyte is  $\text{LiPF}_6$  in a mixture of ethylene carbonate and dimethyl carbonate (EC:DMC). Graphite is shown in a fully charged state ( $\text{C}_6\text{Li}$ ).  $\text{LiCoO}_2$  is presented in a non-stoichiometric way with  $\text{CoO}_6$  octahedra (grey), where oxygen is shown as red spheres at the corners and lithium is drawn in purple inbetween layers.

With the working principle and cell architecture of lithium-ion batteries the complementary sodium-ion battery (SIB) can be aptly described. Especially Na and Li intercalation cathode materials often share the same structural properties. The advantages of Na-ion batteries are their low cost and the higher abundance of Na

compared to Li as well as decreased toxicity of raw materials. While SIBs are suffering from lower energy densities and a lower operating voltage, their application could rather be in areas like electrical grid storage, where the weight of the battery does not play a major role. Part of the decreased energy density can also be compensated through the application of aluminium as current collector at the anode side. With Li-ion batteries the heavier copper has to be used, because Li is prone to form alloys with aluminium at low potentials. The use of graphite is, however, problematic since it can barely host Na. Alternatives like hard carbon are improvements, but still require optimization in order to reach the performance of graphite in LIBs. Advantages of SIBs compared to LIBs are the replacement of cobalt and nickel rich cathode materials. Limited lithium resources on the earth and the large abundance of sodium could be a crucial point that might make the world rely on the SIB technology in the future.[22, 23]

For practical applications individual cells are combined to a stack in order to reach higher voltages and power in different cell configurations (Figure 3). Most commonly a cylindrical shape is used, because volumetric energy density is maximized in this cell design. If the shape of the battery matters more than its energy density a prismatic or pouch cell configuration is applied. With these two alternative cell types tailored shapes are possible to meet the spacial requirements of the specific application.[24]

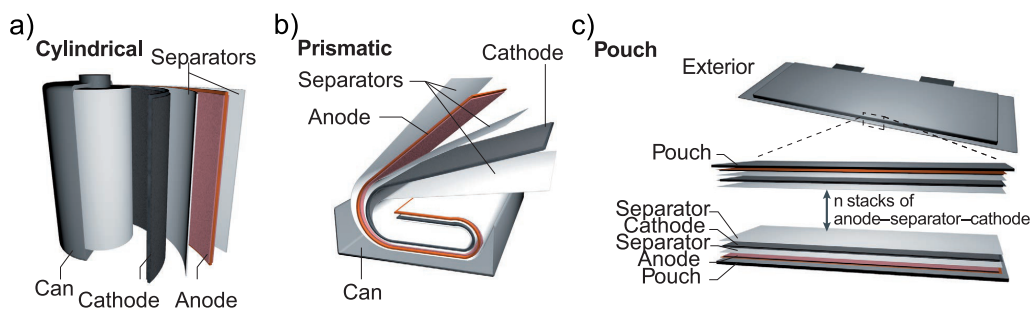


**Figure 3.** Different cell configurations of lithium-ion batteries. a) cylindrical, b) prismatic and c) pouch. [24]

A battery can be characterized via various parameters. To find out where the redox potential of a certain electrode material lies, cyclic voltammetry (CV) serves as established technique. Furthermore, the electrochemical window can be determined with CV. Information about specific capacities of individual electrode materials as well as of a full battery cell can be gained via galvanostatic cycling with potential

limitations (GCPL). Experiments about cycle life are also realized with the GCPL technique, where a real battery operation cycle with various charging and discharging steps is set prior to the measurement. A detailed description of these techniques and relevant characterization parameters can be found in section 2.4. Before focussing on battery characterization, the following subsection will deal with anodes, cathodes and electrolytes for LIBs, which were intensively researched over the last decades.

### 2.2.2. Materials

The findings of Whittingham [16] on intercalation compounds as electrode materials for lithium-ion batteries were the starting point for a tremendous research effort put on intercalation electrodes. A review by Winter *et al.* [25], from the Institute for Chemistry and Technology of Materials at TU Graz, showed that already at this time, in 1998, various research groups focussed on this topic as he cited more than 1000 references. Simultaneously, alternative electrode materials with different Li storage mechanisms were observed in order to improve the performance of lithium-ion batteries. In this subsection various types of anodes and cathodes are presented. In addition, it is described how a suitable electrolyte is chosen and examples will be given.

**Anodes.** Since the discovery of carbonaceous materials as anodes [19] various alternatives have been tested and proved their suitability. The research towards new anode materials is triggered by the fact that graphite has a relatively low specific capacity of  $372 \text{ mAh g}^{-1}$  limiting the energy density of the whole cell. Another issue is the deposition of Li on the graphite electrode surface. Even though, the major part of carbonaceous material in new anode materials is replaced by *e.g.* intercalation compounds, carbon still plays an important role in these materials. Due to limited electronic conductivity of some alternative anode materials, conductive carbon is used as an additive with up to 10 wt%. New anode materials have to meet certain requirements and to reach high energy densities the weight of the components have to be low and specific capacity has to be high. The potential of the material should be as low as possible; comparable to that of Li metal. Furthermore, electronic and ionic conductivity has to be sufficient, in order to guarantee good electron and ion transport. Moreover, electrochemical and chemical compatibility with the electrolyte as well as cheap, easy-to-produce and environmentally friendly materials are required.[26] Anodes can be classified according to their storage mech-

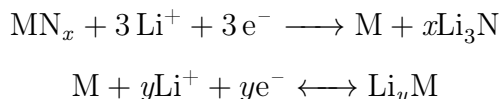
anism or according to the class of material. Different types of storage mechanisms are intercalation, conversion or alloying. In the following, anodes will be classified according to the group of material they belong to; *e.g.* alloys, metal oxides or metal nitrides.

One class of anodes which gained interest of many researchers are *alloys*. Alloy anodes have relatively low potentials of below 1 V *vs.* Li/Li<sup>+</sup>. Their potentials are, however, higher than those of carbonaceous materials, which decreases the risk of Li deposition at the surface of the electrode. Another major advantage of alloy anodes is their specific capacity, which is up to 10 times higher than that of graphite. Nevertheless, the alloy anodes have high initial capacities, it turned out they are of irreversible nature. One reason for the significant capacity fade is likely their enormous volume expansion. As Li is inserted and deinserted, the volume of the alloy anodes changes to an extent up to 300%. The changes in volume lead to a damage of the electrode as cracks are formed with the consequence that part of the material loses contact to the current collector or conductive carbon. In addition to high irreversible capacities, alloy anodes suffer from capacity fading over cycling. One main reason for this behaviour is that Li ions get irreversibly trapped in the alloy. Despite these disadvantages, there are ways to improve the performance of alloy electrodes. Approaches for optimizing alloy-based anodes are the use of (i) multiphase composites and (ii) intermetallics to buffer the volume expansion, (iii) smaller particles which can stand larger stress and strain without cracking, (iv) a limited voltage range which increases the cycle life and (v) an appropriate binder and electrolyte. Many studies on alloys have been realized and were reviewed by Zhang [27], but they still have significant hurdles to overcome like low-rate performance, temperature dependence and long-term stability. The most prominent examples of alloy anodes are based on Si, Sn and Sb.

SnO<sub>2</sub> is a representative of alloy anodes and, at the same time, it is assigned to another class of anodes; *metal oxides*. Compared to graphite, metal oxides show high capacities and good cycling stability. SnO<sub>2</sub> reaches a specific capacity of 790 mAh g<sup>-1</sup>. Furthermore, metal oxides are easily available and environmentally friendly. Transition metal oxides like iron oxide or manganese oxide are further examples belonging to this class of anodes. They are characterized by high specific capacities up to 1000 mAh g<sup>-1</sup>. The storage mechanism, however, differs from that of SnO<sub>2</sub>. Li ions reversibly react with cations of the transition metal oxide. This, so-called, conversion reaction is only sufficiently efficient when the material is applied as nanoparticles. Nanoscaling is, in general, a widely used technique

or even indispensable approach of optimization. This shall also apply for another prominent metal oxide anode material;  $\text{TiO}_2$ . The Li storage mechanism of  $\text{TiO}_2$ , differs again from the mentioned examples as  $\text{TiO}_2$  is an intercalation compound. Disadvantages of the material are low specific capacities of only  $170 \text{ mAh g}^{-1}$  and relatively high potential of  $1.7 \text{ V vs. Li/Li}^+$ . Its ability to run over a large number of cycles at high current rates is, however, overlaid by the fact of its low ionic and electronic conductivity. Again, nanostructuring is a suitable way to overcome this problem.[28] Lithium titanium phosphate (LTO) is another representative of metal oxide anodes. LTO shows almost no volume expansion while Li is inserted or deinserted as it belongs to the class of intercalation electrodes. The material is relatively cheap and easy to produce and proved excellent electronic conductivity. The practical application, however, was hindered by low specific capacity.[29, 30]

Another class of anodes is *metal nitrides* with their main advantages of high thermal and chemical stability. The storage mechanism is again based on a conversion reaction [31]:



The types of anode materials seem to be endless. Metal sulfides, selenides, fluorides, phosphides, hydrides and many more have been reported; each of them having their advantages and disadvantages. Most of them belong to the storage mechanism of conversion reaction. The research towards the perfect anode material, to fit all requirements and replace graphite is, however, still ongoing.[32] Nevertheless, silicon anodes seem to be one of the most promising candidates as alternatives to graphite, because of their extremely high specific capacity of over  $4000 \text{ mAh g}^{-1}$ . The typical problems of pulverisation and unstable formations of a solid electrolyte interface (SEI) in alloy anodes could be resolved by applying different electrode designs, as mentioned above, and choosing appropriate binders and electrolytes.[24] Very recently hierarchical porous silicon structures proved their suitability as anode material in a laboratory framework. An anode composed of carbon-nanotubes, silicon and carbon microspheres delivered high capacity with remarkable mechanical stability.[33]

**Cathodes.** In contrast to anodes, where different materials follow different storage mechanisms, the major portion of cathode materials are intercalation materials.

The class of conversion cathodes play only a minor role in cathode material's research. Cathodes are often classified according the dimension in which Li diffusion takes place in the materials. While the most applied class of cathodes is layered oxides (2D), non-layered structures include spinel(3D)- and olivine(1D)-type cathodes, which follow intercalation mechanism as well. Even though the study of Whittingham [16] on intercalation materials as effective cathodes for lithium-ion batteries and the findings of Goodenough [17] about  $\text{LiCoO}_2$  as high voltage cathode have been published about 40 years ago,  $\text{LiCoO}_2$  is still used in commercial batteries.

$\text{LiCoO}_2$  belongs to the class of *layered oxide cathodes* with the general formula  $\text{LiMO}_2$ , with M being mainly Co, Ni and Mn. Upon discharging and charging,  $\text{Li}^+$  is inserted and deinserted into and out of the layered structure of the materials in 2D. The limited energy density of around  $500 \text{ Wh kg}^{-1}$  of most commonly used cathodes,  $\text{LiCoO}_2$  and  $\text{LiNi}_{1/3}\text{Co}_{1/3}\text{Mn}_{1/3}\text{O}_2$ , hinders large-scale applications. Since different ratios of transition metals are possible in layered metal oxides, alternatives like Li- and Mn-rich compositions have been researched. Initially, this approach was applied to reduce the share of toxic and less abundant cobalt. Besides being environmentally friendly and of low cost, the Li- and Mn-rich layered oxides (LMRO) proved to be able to double the energy density of  $\text{LiCoO}_2$ . LMROs are composed of trigonal  $\text{LiMO}_2$  and the monoclinic  $\text{Li}_2\text{MnO}_3$ . Electrochemically  $\text{Li}_2\text{MnO}_3$  is inactive, but the presence of  $\text{LiMO}_2$  enables a transition to the electrochemically active  $\text{LiMnO}_2$  even in the first cycle. The exact crystal structure and detailed reaction mechanism remain, however, unclear. The main drawbacks of LMROs are irreversible capacities in the first cycles, together with poor cycle life and rate capability. [34]

*Spinel-type oxides* are another major class of cathodes for LIBs. The storage mechanism is assigned to intercalation, but differs from that of layered electrodes. Spinel-type oxides allow fast 3D  $\text{Li}^+$  diffusion, as  $\text{Li}^+$  is inserted/deinserted into/from tetrahedral sites of the spinel.[35]  $\text{LiMn}_2\text{O}_4$  is the main representative of this class, which is characterized by high voltages up to  $4.7 \text{ V vs. Li/Li}^+$ . Disadvantages are low energy density and unstable high temperature performance. Ni doping, resulting in the compound  $\text{LiNi}_{1/2}\text{Mn}_{3/2}\text{O}_4$ , helps to overcome these issues. High voltage of the materials, however, involves interfacial problems. Especially at the electrolyte/cathode interface degradation products occur due to high voltages, causing high interfacial resistances.[36]

Finally, the third major category of cathodes for LIBs is *olivine phosphates*. In these materials with the general formula  $\text{LiMPO}_4$ , phosphorous is found at octahedral sites, the transition metal ( $\text{M} = \text{Fe, Mn, Co}$ ) occupies tetrahedral sites and

lithium appears chain-like in 1D. Mixtures of different phosphates have been proposed. Here, increased capacity is the result of increasing iron content and increased operating voltage is the consequence of increasing manganese content. Thus, using this type of cathodes goes along with making compromises based on what is needed for a certain application. Some olivine cathodes suffer from safety concerns as upon charging and discharging oxygen evolves as a degradation product. Additives for olivine type cathodes include conductive phases, especially for  $\text{LiFePO}_4$ , due to limited electronic conductivity and  $\text{LiNiPO}_4$ , even though it is not used as a cathode material itself.[37]

Another phosphate cathode material is lithium vanadium phosphate (LVP). LVP appears in a monoclinic and rhombohedral structure and therefore it cannot be assigned to olivine phosphates. Since in the thermodynamically more stable monoclinic form all three  $\text{Li}^+$  ions in  $\text{Li}_3\text{V}_2(\text{PO}_4)_3$  are mobile, the intercalation mechanism is explained with this modification.  $\text{VO}_6$  octahedra and  $\text{PO}_4$  tetrahedra share oxygen atoms and  $\text{Li}^+$  is located at three different crystallographic sites. Whereas one  $\text{Li}^+$  is located at a tetrahedral site, the two others occupy 5-fold coordinated sites. Specific  $^7\text{Li}$  NMR observations on the material showed the extraordinary good mobility of all three  $\text{Li}^+$  ions. The electronic conductivity, as important as the ionic mobility in electrolytes, is, however, relatively low. To overcome this issue a carbon coating is applied by, *e.g.*, the use of citric acid in a sol-gel synthesis approach.[38]

Similarly to anodes the research in developing new cathode materials and optimizing existing promising candidates is still ongoing. *E.g.* polyanion-type intercalation cathodes and pyrophosphates such as  $\text{Li}_2\text{MSiO}_4$  and  $\text{Li}_2\text{MP}_2\text{O}_7$ , respectively, are intensively observed. Their commercial application, however, failed due to limited capacities and Jahn-Teller distortion in Mn-based compounds.[35] A recent study of nickel oxide cathodes, a member of layered metal oxides, published in *nature energy* shows the direction of research towards cathodes for automotive applications. The authors review the synthesis and optimization of high-nickel layered oxide cathodes with their advantages of avoiding cobalt and still showing comparable performances in terms of power, lifetime and safety.[39]

**Electrolytes.** In most commercial batteries non-aqueous, liquid electrolytes are used. In general, such an electrolyte is composed of a salt, a solvent and various additives. The composition of these organic electrolytes is, however, a compromise. Each component has to fulfil certain requirements. The salt is supposed to have high  $\text{Li}^+$  mobility, which means high ionic conductivity together with a high transference

number of  $\text{Li}^+$  ions. High  $\text{Li}^+$  mobility is crucial, because limited transport of the ion is one of the major sources for a large total battery impedance. Furthermore, the solubility of the salt is of vital importance, because the higher the solubility in the solvent, the more charge carriers can contribute to the total ionic conductivity of the electrolyte. A weak solubility of the salt would additionally cause precipitates. Another issue is the stability of the salt. This includes electrochemical, chemical, thermal and hydrolysis stability. Degradation upon high potential, chemical reaction products due to interactions with the electrodes and thermal runaway at high temperatures have to be prevented. In some cases it is not possible to hinder the interaction between parts of the electrolyte and electrode completely. The formation of a so-called solid-electrolyte interface (SEI) can, however, prevent further reaction and therefore stabilize the system. It is important that the SEI does not get too thick and guarantee facile ion transport to keep the total battery impedance low. The compatibility of the salt with the widely established aluminium current collector is crucial, which includes the building of a passivating layer to prevent corrosion at high potentials. Requirements for electrolyte salts also include, nowadays rather trivial, properties like low cost, environmental friendliness and the absence of toxicity.

Early representatives of salts in electrolytes for LIBs were lithium perchlorate ( $\text{LiClO}_4$ ) and lithium hexafluoroarsenate ( $\text{LiAsF}_6$ ). While  $\text{LiClO}_4$  stand out due to its high ionic conductivity, stable SEI formation and good electrochemical stability,  $\text{LiAsF}_6$  has to be characterized by its improved Li metal plating properties compared to  $\text{LiClO}_4$ .  $\text{LiClO}_4$ , however, fails in passivating the Al current collector whereas extremely toxic oxidation states of As ( $\text{As}^{\text{III}}$  and  $\text{As}^0$ ) in reduction products of  $\text{LiAsF}_6$  hinders its wide application in batteries. These disadvantageous properties lead to the nearly sole use of lithium hexafluorophosphate ( $\text{LiPF}_6$ ) in commercial LIBs, which is usually dissolved in carbonates or mixtures of them. Instability in temperature and hydrolysis forming HF is tolerated, due to the high ionic conductivity and stable layers at both the graphitic anode (SEI) and the cathode side (passivating layer at the Al current collector). The presence of HF, however, catalysed the research towards alternative salts like lithium tetrafluoroborate ( $\text{LiBF}_4$ ).  $\text{LiBF}_4$  is far less prone to hydrolysis and thermally more stable. Although its lower ionic conductivity, it is a promising salt for electrolytes since SEI layers tend to be lower in resistance compared to  $\text{LiPF}_6$ . Other alternative salts include triflate<sup>2</sup> ( $\text{LiSO}_3\text{CF}_3$ )

---

<sup>2</sup>lithium trifluoromethanesulfonate

and LiTFSI<sup>3</sup> (LiN(SO<sub>2</sub>CF<sub>3</sub>)<sub>2</sub>) which are, however, mainly used for research purposes in combination with polymer electrolytes.[40]

Nearly as important as the salt is the solvent of the electrolyte. LiPF<sub>6</sub> is commonly used with carbonate solvents. Examples of carbonate solvents include ethylene carbonate, propylene carbonate, dimethyl carbonate, ethyl methyl carbonate and diethyl carbonate. With the help of phase diagrams the perfect composition of binary or ternary carbonate mixtures are observed. Here, the determination of the eutectic point is crucial. Carbonate mixtures with compositions close to the eutectic point show decreased limits of the lower operating temperature, which is beneficial for the total battery performance.[40] A major requirement on the solvents is the lack of protons, as protons are oxidized in the range of 2 to 4 V *vs.* Li/Li<sup>+</sup>. This potential range overlaps with the typical operation voltage of LIBs, which has the consequence of an oxidation of the electrolyte in contact with the highly oxidizing cathode materials. Thus, it is vital that solvents for electrolytes used in LIBs are of aprotic nature. A reason why carbonate solvents are that well-established is their contribution to the building of a stable SEI layer. The reason in mixing the carbonate solvents lies in the large amount of requirements electrolytes have to fulfil. By combining different properties of the carbonates, where one might provide higher fluidity and the other has to be characterized by a high dielectric constant, requirements can be met more efficiently. High solubility of the salt, which is achieved through high dielectric constants and facile ion transport through high fluidity is crucial. In addition, chemical inertness to the electrodes and other battery components as well as a large temperature range in which the solvent is liquid are indispensable properties of potential solvents for LIB electrolytes. Polarity of the solvents, in order to dissolve a sufficient amount of Li-salt, is required as well. Solvents with carbonyl-, nitrile- or sulfonyl-groups are classical examples for polar aprotic solvents suitable for electrolytes.[41]

As mentioned above choosing an electrolyte is accompanied with making compromises on one or the other electrolyte requirement. Using one or more functional additives in order to optimize electrolytes is an ubiquitous method to overcome some of the drawbacks even in commercial applied electrolytes. It might be reasonable to classify types of electrolyte additives in those which are beneficial for (i) the interaction with the anode, (ii) the interaction with the cathode and (iii) in terms of safety. The use of additives has its origin in preventing undesirable thick SEI formation, *i.e.* SEI controlling. As an example, Wrodnigg *et al.* proposed ethylene sulfite as

---

<sup>3</sup>lithium bis(trifluoromethanesulfonyl)imide

anode additive [42] whereas, *e.g.*, compounds bearing unsaturated carbon–carbon bonds, carboxylic anhydrides or oxalates have been shown to improve the anode performance when added to the electrolyte as well. To prevent similar layers at the cathode side additives like diphenyl are applied to hinder decomposition of the electrolyte at high potentials.[40] It was additionally shown that aromatic compounds like biphenyl are able to built a so-called electro-conducting membrane when they are added in small amounts of around 0.1 wt%. This layer protects the cathode against further decomposition of the electrolyte and increases the battery performance due to enhanced conductivity.[43] The third major class of additives is their application due to safety reasons. Most additives for safety purposes aim to hinder overcharging. Overcharging is the uncontrolled charging of the battery when too much  $\text{Li}^+$  is extracted from the cathode and inserted into the anode. The result is an unstable cathode and Li metal plating at the anode following exothermic decomposition of the electrolyte accompanied by the production of heat and possible explosion. So-called *redox shuttle additives*, which are, *e.g.*, anisole compounds, are used to prevent overcharge as they undergo a redox process, consume current and in that way prevent voltage increase. Some other additives for this purpose (*e.g.* biphenyl or furan) undergo polymerization at certain potentials and built a protective layer at the cathode. Additional additives include additives against corrosion (*e.g.* dinitriles), for better wettability (*e.g.* long-chain aliphatics and aromatics) and supplementary Li salts to compensate for drawbacks of the main salt.[40]

Nevertheless, these optimized electrolyte formulations have their limits due to their aggregation state and organic nature. The narrow potential window and flammability of the liquid, carbonate-based electrolytes led to a strong interest in alternative electrolytes in solid state. In the following section, advantages and drawbacks of such solid-state electrolytes will be supplemented with the most prominent and promising examples.

## 2.3. Solid-State Electrolytes

In principle, solid-state electrolytes (SSE) are categorized into solid-state ceramic-type electrolytes and polymer electrolytes. In polymer electrolytes, the polymer dissolves a Li salt and  $\text{Li}^+$  ions can move along the chain network of the polymer. In some cases polymer electrolytes are composed of a polymer and a ceramic filler. In these composites the polymer acts as a host for a the ceramic, which either does or does not contribute to the total ionic transport (active or inactive filler).

The most prominent host is PEO (polyethylene oxide). While polymer electrolytes enable flexible cell design ceramic-type electrolytes are thermally more stable and usually show higher ionic conductivities compared to polymer electrolytes.[44, 45] The following section will focus only on ceramic-type electrolytes.

The first findings of ionic conduction in solids go back to Michael Faraday in 1830 who discovered remarkable conductivity in heated silver sulfide ( $\text{Ag}_2\text{S}$ ) and lead(II) fluoride ( $\text{PbF}_2$ ). The research field of solid state ionics, however, really started to emerge with the high-temperature sodium–sulfur battery in the 1960s. In the following centuries SSEs got serious attention and were considered for application in, *inter alia*, the high-temperature ZEBRA cell, polymer Li-ion batteries, Li- and Na-ion batteries with inorganic electrolytes, the Li-air battery as well as in the Li-S battery.[45]

Among these, the sodium-ion battery (SIB) and the lithium-sulfur (Li-S) battery are highly promising battery technologies as alternatives to the LIB. While the former stand out because of low cost and high abundance of the raw materials, the latter has to be characterized by extraordinary high energy density due to high specific capacities of the electrodes; Li metal anode and sulfur cathode. The Li-S battery is, however, lower in voltage (between 2.0 and 2.3 V *vs.*  $\text{Li}^+$ ) compared to the LIB. The generation of polysulfides at the cathode side requires the use of SSEs to prevent loss of active sulfur and eliminate the redox shuttle issue, respectively. Sulfide-type SSEs, which will be presented in the subsection 2.3.2, could be applied for both, all-solid-state LIBs and Li-S batteries, since they are usually stable with the sulfur cathode and guarantee fast Li-ion transport.  $\text{Na}_3\text{PS}_4$  is an example for SIBs, while its Li bearing counterpart  $\text{Li}_3\text{PS}_4$  is a potential SSE for LIBs. Thus, SIBs and Li-S batteries benefit from past and ongoing research on SSEs for LIBs, since the battery technologies are directly related.[46]

### 2.3.1. Interest and Obstacles

As previously mentioned, the most important concern related to liquid electrolytes is their flammability and the associated fire and explosion hazard. Obviously, ceramic type solid-state electrolytes (SSE) do not suffer from such a severe safety issue, because they are not flammable and stable until high temperatures. Another issue regarding safety is dendritic growth of Li, when metallic Li is used at the anode side in liquid cells. As soon as the dendrites reach the cathode, the cell undergoes short circuiting. Although Li dendrites grow through SSEs as well, effective ways to

prevent dendrite growth have been found. The implementation of protective and, at the same time conductive, layers enables the use of Li metal at the anode, which significantly increases the energy density.[47]

A problem of liquid electrolytes is also the building of a solid-electrolyte-interphase (SEI). This interphase is generated through the reaction of active electrolyte species at the anode. As the building of the SEI layer is often uncontrolled and leads to a loss of active species limiting cycle life in batteries with liquid electrolytes, batteries with SSEs are considered to deliver longer cycle life.[46] The instability upon charging and discharging, *i.e.*, building of an unstable interface, is also an issue at the cathode side. Although SSEs are considered to have longer cycle life due to potentially more stable interfaces with both, anode and cathode, still a lot of research has to be done to shed light on this possibly advantageous property of SSE compared to liquid electrolytes.[47]

Additionally, solid-state batteries can provide a large electrochemical window since many SSEs are stable at high potentials, when liquid electrolytes already tend to decompose. A large electrochemical window is important to reach high energy densities, which are required for *e.g.* large-scale electrical grid storage.[45] Further advantages of solid-state electrolytes are that there is no risk of leakage and corrosion of the current collector or other parts of the battery is hardly observed. Additionally, different cell fabrications are possible due to flexibility of polymer electrolytes or thin-films. The possibility of decreasing the space between electrodes with *e.g.* mechanically stable materials, withstanding dendritic Li growth, leads to higher energy density through miniaturization.[46]

The first main challenge SSEs had to face over the last decades is their often limited ionic conductivity. High ionic conductivity is crucial since it directly influences the power output of the battery. The obstacles of low ionic conductivity and rather limited knowledge of diffusion mechanisms of potential SSEs are the reasons why research on SSEs invariably involves techniques like conductivity spectroscopy and solid-state nuclear magnetic resonance (SSNMR). Long-range ionic transport is analysed via conductivity spectroscopy while SSNMR is able to elucidate the structures of the materials and gives insight in short-range diffusion.[47] The basic principle behind these techniques will be further explained in section 3.2. Furthermore, the determination of the transport number is important. With the Bruce-Vincent method it is possible to distinguish to which extend positive or negative ionic charge carriers contribute to the total ionic conductivity.[48]

While some SSEs are already reaching values comparable to liquid electrolytes,

the interfaces with the electrodes remain a key issue. Obviously, liquid electrolytes outperform SSE in terms of interfacial resistance, due to their often outstanding wettability. The analysis of the interfaces is rather complicated, since during cell assembling focus is laid on a close contact of the electrodes and the SSE to keep interfacial resistances small. Thus, often in-situ methods are applied. In microscopic investigations, such as transmission electron microscopy, additional sample preparation is needed to observe interfaces via a cross-sectional view of the cell. Furthermore, analysis of the chemical composition with methods based on X-radiation, like X-ray powder diffraction (XRD) or X-ray photoelectron spectroscopy (XPS), gain information about potential degradation products at the interfaces.[49] A detailed description of interface analysis is, however, beyond of the scope of this thesis.

For certain SSEs poor mechanical stability is a critical issue. It might appear that upon battery cycling cracks are forming due to brittleness of the SSE materials, which leads to enormous resistances. The cracks are additionally points of attack for possible dendrite growth. Therefore, an important feature of SSE is a small elastic modulus. High grain boundary resistance is another reason why SSE often show low conductivities, independently from the interfaces.[45]

In the following subsection various types of SSEs which are intensively investigated are presented. Each of these SSEs have its advantages and obstacles with non of them being sufficiently able to fulfil the criteria to be applied in consumer electronics or large-scale energy grid storage.

### 2.3.2. Types

Most SSEs belong to the class of oxides. Oxide-type SSE can be divided into sub-categories of garnets, perovskites and NASICON-type electrolytes. Most oxide-type SSEs show good mechanical strength and generally have to be characterized by high oxidation voltage. The latter property makes them especially interesting for large-scale grid storage.[45] Garnets, however struggle when it comes to large-scale applications, since up-scaling of the production is very expensive. This is due to required doping and special treatment of the surface to overcome significant interfacial resistances at the electrodes. Pioneering work in garnet-type SSEs was published by the group of Weppner presenting  $\text{Li}_5\text{La}_3\text{M}_2\text{O}_{12}$  with M being either Ta or Nb. These materials already showed moderate room temperature ionic conductivity.[50] Following these results,  $\text{Li}_7\text{La}_3\text{Zr}_2\text{O}_{12}$  (LLZO) gained interest of the SSE research community and was first introduced by the same group.[51] Garnets especially stand

out due to their stability against Li metal and temperatures up to 900 °C. The group of perovskite SSEs mainly consists out of  $\text{Li}_x\text{La}_y\text{AlO}_3$  with different ratios of  $x$  and  $y$ . In the general formula of perovskites  $\text{ABO}_3$ , Li and rare-earth elements like Nb and La share position A, while B is occupied by Al or Ti in perovskite-type SSEs. High grain boundary resistances in these materials can be decreased by different stoichiometry of Li, La and Nb as well as Al doping. Besides perovskites, there are also certain antiperovskites taken into consideration as SSEs. In antiperovskites cations and anions switch their positions in the crystal lattice and they usually appear as  $\text{A}_3\text{OCl}$ , with A being either Li or Na. Antiperovskites deliver high ionic conductivities up to  $10^{-2} \text{ S cm}^{-1}$ . A disadvantage of perovskite SSEs is the instability with Li metal, which makes the application of protective layers necessary when batteries with Li metal anode and high energy density are considered.[46] Another subcategory of oxide-based SSEs are NASICON materials. The term NASICON, sodium (**Na**) super ionic **con**ductor, arose in the 1970s after the observations on  $\text{Na}_{1+x}\text{Zr}_2\text{Si}_x\text{P}_{3-x}\text{O}_{12}$  as fast sodium ion conductor.[45, 46, 52] NASICON materials with the formula  $\text{AM}_2(\text{PO}_4)_3$  ( $\text{A} = \text{Li, Na or K}$ ;  $\text{M} = \text{Ge, Zr or Ti}$ ) got in the focus of scientist working in the field of SSE, because of their stability against water and air, which simplifies their production and handling. Together with the broad electrochemical window of up to 5 V, especially lithium titanium phosphate (LTP,  $\text{LiTi}_2(\text{PO}_4)_3$ ) or the Al doped form (LATP,  $\text{Li}_{1.3}\text{Al}_{0.3}\text{Ti}_{1.7}(\text{PO}_4)_3$ ) are interesting candidates for large-scale grid storage. Similar to perovskites, NASICON SSEs, are, however, not stable with Li metal, which again requires modifications leading to increased complexity of the material and rise in cost.[45, 46]

An interesting group off SSE are hydrides with its main representative  $\text{LiBH}_4$ . Common properties of hydride SSEs, such as  $\text{LiNH}_2$  or  $\text{Li}_3\text{AlH}_6$ , are good mechanical stability, compatibility with Li metal and low grain boundary resistances. They are, however, sensitive to moisture and struggle with instabilities in contact with various cathode materials.[45] Furthermore, different approaches are necessary to obtain high ionic conductivities at room temperature. Efficient methods to boost room temperature conductivity of  $\text{LiBH}_4$  are presented in subsection 4.2.2 whereas a detailed information of the structure of  $\text{LiBH}_4$ -composites and short-range diffusion is given in subsection 4.2.3. In sum, nanoconfining  $\text{LiBH}_4$  in porous supports such as silica or alumina and ion substitution of boronhydride anions with halides lead to a significant increase in ionic conductivity at room temperature. Besides other aspects of *ion dynamics in porous solids*, section 4.2 will give insight in how these strategies can be effectively combined and how mobile  $\text{Li}^+$  ions behave in these composites in

terms of long-range and short-range diffusion.

Similar to hydrides, argyrodites are sensitive to moisture and air. Argyrodites with the general formula  $\text{Li}_6\text{PS}_5\text{X}$  (X: Cl, Br, I) show, however, high ionic conductivity.[46, 53] These materials are assigned to sulfide based SSE, which in general have to be prepared under protective atmosphere due to their reactivity to moisture. Sulfide-based SSE appear in two groups: crystalline (*e.g.*  $\text{Li}_2\text{S}-\text{P}_2\text{S}_5$ ) and amorphous (*e.g.*  $\text{Li}_7\text{P}_3\text{S}_{11}$ ).[45, 47]  $\text{Li}_2\text{S}-\text{P}_2\text{S}_5$  can be identified among the very best SSEs in terms of ionic conductivity. Sulfide-based electrolytes share properties of hydride-based SSE as they show low grain boundary resistances and good mechanical strength, but have to be characterized by poor compatibility with cathode materials.[45]

For the sake of completeness, nitride based SSEs are presented. One example is LiPON which is obtained by a sputtering process of  $\text{Li}_3\text{PO}_4$  in  $\text{N}_2$  atmosphere resulting in a composition of  $\text{Li}_{2.9}\text{PO}_{3.3}\text{NO}_{0.5}$ . Although LiPON shows low ionic conductivity, the feasibility of very thin films makes it interesting in terms of energy density. The films can be as thin as hundreds of nanometers. The risk of damaging such thin layers is, however, high, especially when in contact with rough electrode surfaces. The discovery of LiPON as SSE is considered to be the first of an SSE for LIBs.[45]  $\text{Li}_3\text{N}$  is another representative of nitride-based SSEs. Its ionic conductivity is reasonably high reaching values up to  $1\text{ mS cm}^{-1}$ , but it suffers from instability due to low oxidation voltage.[46, 54]

A relatively young class of SSEs, which rather belongs to hybrid liquid-solid electrolytes, are metal-organic frameworks (MOFs) infiltrated with common liquid electrolytes. In general, MOFs are built up of an inorganic node connected by organic linkers. MOFs offer interesting features like tunability and functionality, due to different linkers and their functional groups. Because of the almost infinite possibilities of combining inorganic nodes with organic linkers, MOFs can be synthesized according to the needs of a specific application.[55] Features like high thermal stability and porosity make them interesting materials as SSE. To the best of my knowledge, the first Li ion conductor based on MOFs goes back to the group of Jeffrey R. Long in 2011.[56] They presented a porous MOF, namely  $\text{Mg}_2(\text{dobdc})$  ( $\text{dobdc}^{4-} = 2,5\text{-dioxido-1,4-benzenedicarboxylate}$ ), infiltrated with a lithium alkoxide reaching a conductivity of  $10^{-4}\text{ S cm}^{-1}$ . Further studies reported reasonable conductivity values for MOF-based ionic conductors, which demonstrates the possible suitability of MOFs as electrolytes in LIBs or SIBs.[57–60] Recent progress with this young class of MOF-based electrolytes will be presented in subsection 4.2.5. In short, modified

MIL-121, a MOF with aluminium centres linked via pyromellitic acid, is mixed with lithium and sodium perchlorate in propylene carbonate as soaking electrolyte. This liquid-solid hybrid electrolyte system is prepared via a post synthetic modification where lithium and sodium acetate react with the free carboxylic groups of pristine MIL-121 to obtain the modified (lithiated and sodiated, respectively) MIL-121. Following this introduction of mobile ion species the liquid electrolyte is added in amounts of up to 40 wt%, which makes the electrolyte system still appear dry as the liquid is soaked up by the porous solid. The purpose of the liquid electrolyte is to increase the mobility of the ions on their way through the MOF channels.

## 2.4. Battery Characterization

A suitable battery is chosen by different parameters, in order to fulfil the requirements of various applications. Depending on the application certain parameters are more or less important. For example, in mobile devices the weight of the battery and therefore the energy density is of vital importance, whereas large-scale applications require high voltages. Important criteria for the judgement of batteries are *e.g.* working voltage, specific capacity, coulombic efficiency, energy density or cycle life. In this section definitions of these parameters will be given and the focus will be laid on two characterization techniques, namely cyclic voltammetry and galvanostatic cycling with potential limitation. With the information provided by these techniques, a battery is nearly entirely characterized. Other important parameters are safety, cost, toxicity and environmental friendliness.[10, 61] The analysis of these parameters is, however, beyond the scope of this thesis. A usual approach is to choose materials which are already known as environmentally friendly as well as cheap and easy to produce.

### 2.4.1. Cyclic Voltammetry

Cyclic voltammetry (CV) is the first of two important battery characterization techniques presented in this section. Once it was called "*the spectroscopy of electrochemists*" (freely translated) by Jürgen Heinze in his publication about the basics of cyclic voltammetry.[62] In a CV experiment an electrochemical cell is connected to a potentiostat and a triangular voltage is applied to the working electrode of the cell. Starting from a lower potential limit, the potential is linearly increased until it reaches an upper potential limit. From the upper potential limit the voltage

is decreased again to the lower potential limit at the same rate. The slope of the linear voltage curve is the scan rate of the CV experiment and is given in  $\text{Vs}^{-1}$  or  $\text{mVs}^{-1}$ . [62–65] The potential of the working electrode is measured relative to a reference electrode. Usually a three-electrode configuration is used, where a counter electrode protects the reference electrode. In principle, a two-electrode configuration is sufficient, but if high currents are applied or the conductivity of the electrolyte is low, a counter electrode is necessary. In a three-electrode configuration a major part of the current is led through the working and the counter electrode. Thereby, the current that passes the reference electrode is kept almost at zero. High currents at the reference electrode or limited electrolyte conductivity lead to a change of the reference potential and therefore to falsifications of the measured voltage at the working electrode. [62]

In the resulting voltammogram the applied potential is plotted versus the measured current. If an electrochemically active material is analysed, oxidation and reduction peaks are observed in the voltammogram. The redox potential is determined by the mean of the peak positions:  $\frac{E_p^{\text{ox}} + E_p^{\text{red}}}{2}$ . Additionally, the difference of the position of the redox peaks ( $\Delta E_p = E_p^{\text{ox}} - E_p^{\text{red}}$ ), shows if the reaction is reversible or quasi-reversible, whereas the absence of either the oxidation or the reduction peak indicates a non-reversible reaction (Figure 4.a). If the oxidation and reduction peak occur at potentials very close to each other, a reversible reaction is considered. The minimum peak-to-peak separation can be calculated through  $\Delta E_p = 2.218 \frac{RT}{nF}$ . In a perfectly reversible process  $\Delta E_p$  is 57 mV, if one electron is transferred during the reaction at room temperature. Redox peaks occurring more apart from each other are of quasi-reversible nature. If more electrons are involved in the reversible redox reaction, the redox peaks appear closer than 57 mV and  $\Delta E_p$  takes values of  $\frac{57 \text{ mV}}{n}$ , with  $n$  being the number of electrons which are involved in the redox reaction. [63, 64] Depending on certain conventions positive and negative currents refer to either oxidation or reduction. In the IUPAC (**I**nternational **U**nion of **P**ure and **A**ppplied **C**hemistry) convention positive currents refer to oxidation whereas negative currents indicate reduction. [63] (Figure 4.b)

Further information can be gained from the height of the redox peaks ( $i_p$ ). First, in a reversible process the ratio of oxidation and reduction peak heights should equal to 1. Secondly, a more pronounced current peak points to better electronic conductivity of a material compared to another material. Obviously, for this comparison CV measurements of both materials have to be conducted at the same scan rate ( $\nu$ ). This is important since the scan rate is proportional to the height of the peak, which

is described through the Randles-Sevcik equation (Eq. 2.1) [63]:

$$i_p = 0.4463nFAC \left( \frac{nF\nu D}{RT} \right)^{\frac{1}{2}} \quad (2.1)$$

In 2.1  $n$  denotes again the number of electrons involved in the redox reaction,  $F$  is the Faraday constant in  $\text{C mol}^{-1}$ ,  $A$  the area of the electrode in  $\text{cm}^2$ ,  $C$  the concentration in  $\text{mol cm}^{-3}$ ,  $D$  the diffusion coefficient in  $\text{cm}^2 \text{s}^{-1}$ ,  $R$  the gas constant in  $\text{JK}^{-1} \text{mol}^{-1}$  and  $T$  is the temperature in K.

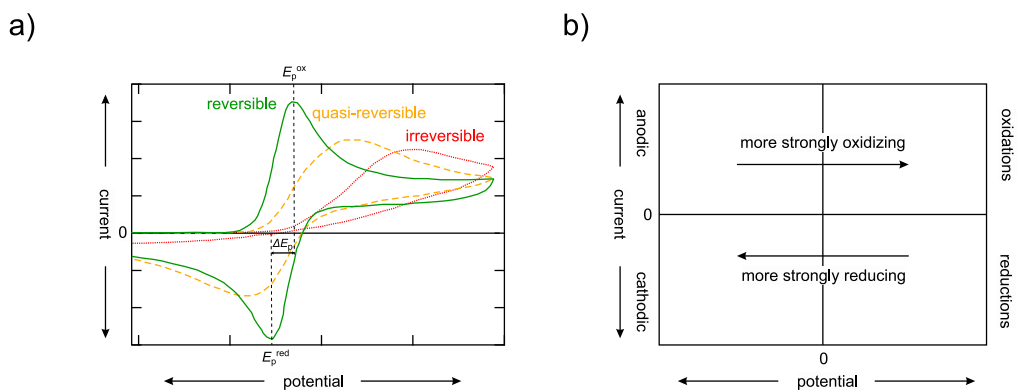


**Figure 4.** a) Different voltammograms showing reversible (green), quasi-reversible (orange) and irreversible electron transfer. b) IUPAC convention of cyclic voltammograms. (inspired by [63])

An observation of the material at different scan rates gives additional information about reversibility of the electrochemical reaction. With increasing scan rate the height of the redox peaks will increase, as expected through the Randles-Sevcik equation, but should not shift in potential in reversible redox reactions. If, with increasing scan rate, a shift in potential is observed, a quasi-reversible or non-reversible reaction takes place, whereas no shift in potentials points to fully reversible redox reactions.[63] In Figure 5.a, cyclic voltammograms of carbonized lithium titanium phosphate (LTP/C) are shown. Only a slight shift of the peak maxima is observed with increasing scan rate, which proves good reversibility of the redox reaction, *i.e.* insertion and extraction of  $\text{Li}^+$  into and out of the material. CV is also a well-established method to determine the electrochemical window of electrolytes. Signals, as seen in the blue area in Figure 5.a, point to electrolyte decomposition and indicate that the applied potential range is too high for the electrolyte solution used in the cell. In this specific case LiTFSI (lithium

bis(trifluoromethanesulfonyl)imide) dissolved in an ionic liquid (EMIM-TFSI, 1-ethyl-3-methylimidazolium bis(trifluoromethylsulfonyl)imide) was used as electrolyte, which decomposes at the higher potential limit. In Figure 5.b the voltammograms of carbonized sodium vanadium phosphate (NVP/C) are shown. Here, the peak maxima at different scan rates appear further apart than in the case of LTP/C, which indicates less reversibility. The electrolyte in this case, NaFSI in EC:DEC=4:6 (ethylene carbonate and diethyl carbonate), is, however, stable until at least 4.0 V *vs.* Na/Na<sup>+</sup> (upper potential limit of this measurement). Further evidence for a reversible process can be obtained by plotting  $i_p$  *vs.*  $\nu^{\frac{1}{2}}$ . If a reversible process is observed, the resulting curve is linear.[63]

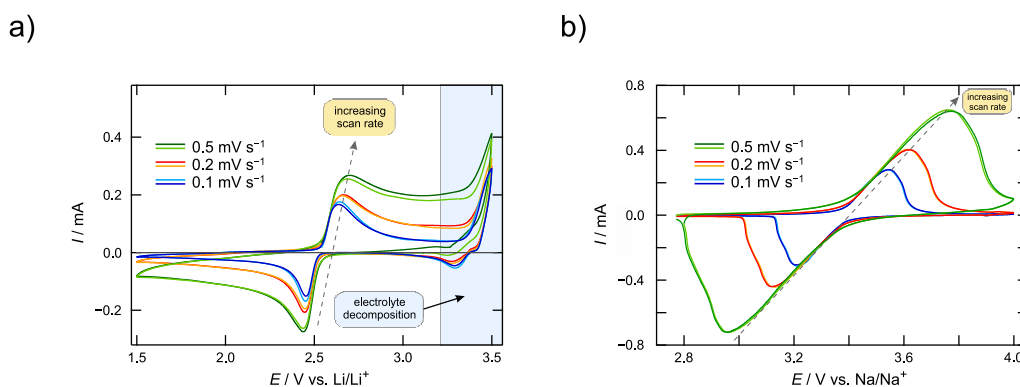


**Figure 5.** a) Cyclic voltammogram of carbonized lithium titanium phosphate (LTP/C) with different scan rates. The shift of the peak maximum from 0.1  $mV s^{-1}$  (blue) to 0.5  $mV s^{-1}$  (green) is rather small pointing to a reversible redox reaction. The blue area denotes the decomposition of the electrolyte due to the high potential. b) Cyclic voltammogram of carbonized sodium vanadium phosphate (NVP/C) with different scan rates. The shift of the peak maximum from 0.1  $mV s^{-1}$  (blue) to 0.5  $mV s^{-1}$  (green) is larger compared to LTP/C indicating lower reversibility.

Besides battery characterization, CV is additionally applied to observe biosynthetic reaction pathways, electrochemically generated free radicals, the effects of ligands on the redox potential of the central metal ion in complexes, enzymatic catalysis or intermediate oxidation states of metal complexes, to name but a few. Furthermore, information gained through CV plays an important role in energy conversion research.[64] The popularity of CV results from the simplicity of the technique together with a large number of information gained about the analysed electrochemical process. Moreover, CV is not only used for analysis of simple redox reactions in inorganic and organic chemistry, but also in processes involving multiple

electrons in biochemistry or macromolecular chemistry.[62]

### 2.4.2. Galvanostatic Cycling with Potential Limitation

Galvanostatic cycling with potential limitation, abbreviated GCPL, is an indispensable technique in battery characterization. By applying alternately a negative and a positive current in a certain potential range, battery operation with charging and discharging cycles is simulated. If charging and discharging cycles are consecutively repeated, the cycle life of a battery can be determined. Obviously, the duration, a battery is able to operate is a crucial parameter for batteries. Often a capacity as low as of 80% of the nominal capacity is defined as the end of a cycle life test. In other words, if the capacity reaches a value of only 80% of its nominal capacity, this point is called the operation limit or cycle life of the cell.[10]

Similar to CV measurements a three-electrode configuration including a working, a counter and a reference electrode is the standard assembly in GCPL measurements. The experiment is either used to characterize individual electrode materials in half cells with *e.g.* Li or Na metal as counter electrode or to characterize full cells including an anode and a cathode. The applied current ( $I$ ) is determined with the specific theoretical capacity ( $C_{th}$ ) or the specific practical capacity ( $C_p$ ) of the active material. If a full cell is characterized, the capacity of the electrode with lower capacity, *i.e.* the limiting electrode, is used for the calculation. The applied current is obtained through Eq. 2.2 with the desired discharge rate ( $r_C$ ) and the mass of active material of the electrode ( $m$ ). If  $C_{th}$  is unknown, it is determined through Eq. 2.3 where  $n$  is the number of charge carriers,  $F$  the Faraday's constant and  $M_w$  denotes the molecular weight of the active material. The factor 3.6 serves to obtain specific capacities in units of  $\text{mAh g}^{-1}$ . The use of Eq. 2.3 requires, however, knowledge about the electrochemical reaction, because some reactions include multiple steps at different potentials. Additionally, it can happen that more than one electron is involved in a certain step of the reaction. Therefore, it is important to know the number of charge carriers involved in the reaction at a certain potential and the number of steps needed to fully oxidize or reduce a material.  $C_p$  can be determined with a simple CV experiment in advance. First, the area below the CV curve is determined by integration of the current in the functional potential range of the redox process. This value is divided by the applied scan rate ( $\nu$ ) and the mass of active material. The result can be converted again through the factor 3.6 to obtain specific capacities in units of  $\text{mAh g}^{-1}$ . [66]

$$I = C_{\text{th, p}} \cdot m \cdot r_C \quad (2.2)$$

$$C_{\text{th}} = \frac{n \cdot F}{3.6 \cdot M_w} \quad (2.3)$$

$$C_p = \frac{\int_{E_1}^{E_2} i(E) dE}{3.6 \cdot m \cdot \nu} \quad (2.4)$$

GCPL experiments are performed at different *C-rates*. The C-rate is given as the capacity over time  $\frac{C}{t}$ . If a C-rate of  $\frac{C}{10}$  is set, the applied current discharges the battery in 10 hours relative to its capacity. In Figure 6 different representations of GCPL experiments are shown. In Figure 6.a the measurement time is plotted against the measured potential, which is the raw, unprocessed data of a GCPL experiment. Comparable to the redox peaks in CV, here we observe two voltage plateaus where one plateau corresponds to oxidation and the other plateau corresponds to reduction of the electrode material. Again, the value of the voltage plateaus should be as close as possible in a reversible reaction. The minimum distance of the plateaus in a reaction involving only one electron is again 57 mV. The redox potential is again the average potential of the oxidation and reduction voltage plateaus.

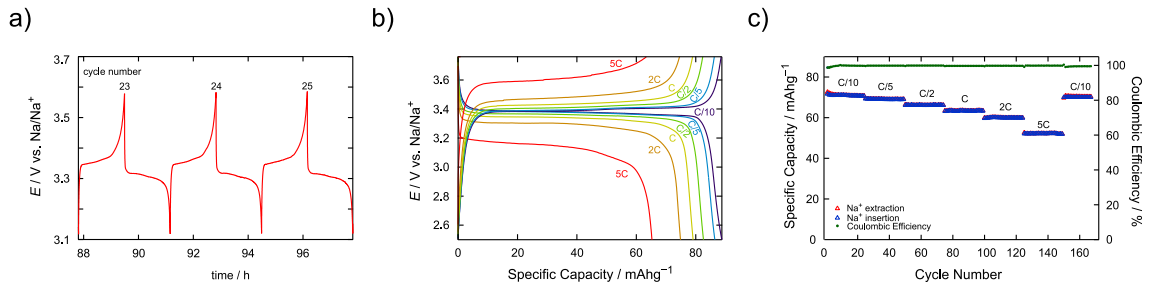


**Figure 6.** Different representations of a GCPL measurement of a NVP/C half cell: a) time vs. potential at C/2 showing cycles 23 to 25 out of 50 b) charge-discharge curves at different C-rates between C/10 and 5C and c) cycle number vs. capacity and coulombic efficiency, respectively, at different C-rates between C/10 and 5C. Here, the total number of cycles is 175.

Figure 6.b shows the typical charge-discharge curves. The practical specific capacity  $C_p$  is plotted against the potential.  $C_p$  is calculated through Eq. 2.5 and 2.6 with the charge capacity  $Q_{c/d}$  and the mass of active material of the electrode.  $Q_{c/d}$  is determined by the applied current  $I$  and the charge/discharge time  $t_{c/d}$ .

In an ideal case the voltage would drop to zero when the cell is fully discharged. Higher C-rates lead to decreased specific capacities since polarization effects occur and ohmic losses are higher due to the higher currents applied. The plot is often also presented in units of % specific capacity. This representation serves for comparison of different battery or energy storage systems. A flat charge-discharge curve is desired, since it indicates a constant voltage during battery operation.[10, 61]

$$Q_{c/d} = I \cdot t_{c/d} \quad (2.5)$$

$$C_p = \frac{Q_{c/d}}{m} \quad (2.6)$$

In Figure 6.c the specific capacity (left y-axis) and the coulombic efficiency (right y-axis) are plotted against the cycle number. In this case a comparison of different C-rates is shown. The material shows stable cycling within a certain C-rate and only little drops in specific capacity from one C-rate to the other. The latter behaviour could already be observed in the charge-discharge curves, but here a number of consecutive cycles is shown. If charge and discharge cycles are repeated at a certain C-rate, information about the cycle life is obtained. As already mentioned above, the cycle life of a battery is often defined as the number of cycles until a the specific capacity of only 80 % compared to its starting value is reached. Alternatively, the specific capacity is given as the capacity per electrode surface area rather than per weight of active electrode material. The coulombic efficiency is the ratio of discharge capacity and charge capacity. In the case of intercalation materials the value indicates how effective the intercalation process into and out of the material is.[10, 61]

In order to compare different battery types and other energy storage systems, energy density or power density are commonly used parameters. Energy density is given as the ratio of energy and weight or volume. Especially for mobile applications as electronic vehicles, maximum energy or power together with minimum weight and volume is desired. For example aqueous secondary batteries deliver an energy density of only 80 Wh kg<sup>-1</sup> compared to non-aqueous batteries with 180 Wh kg<sup>-1</sup>. A gasoline engine reaches an energy density of 3000 Wh per kg of gasoline.[10]

# 3 | Diffusion in Solids

## Contents

---

|       |   |    |
|-------|---|----|
| 3.1   | Fundamentals . . . . .                          | 30 |
| 3.1.1 | Fick's Laws . . . . .                           | 30 |
| 3.1.2 | Random Walk Theory . . . . .                    | 31 |
| 3.1.3 | Defects . . . . .                               | 33 |
| 3.1.4 | Diffusion Mechanisms . . . . .                  | 37 |
| 3.2   | Determination of Diffusion Parameters . . . . . | 39 |
| 3.2.1 | Impedance Spectroscopy . . . . .                | 40 |
| 3.2.2 | Nuclear Magnetic Resonance . . . . .            | 45 |

---

One of the most important requirements of solid-state electrolytes for lithium-ion batteries is high ionic conductivity. Therefore, detailed knowledge about the diffusion mechanisms in solids is vital. The following chapter deals with fundamentals of diffusion in solids which includes Fick's first and second law of diffusion and the random walk theory. The diffusion of ions in a solid is enabled by the presence of defects. In the following different kinds of defects will be presented and various diffusion mechanisms will be explained as well. Moreover, experimental techniques, that enable the determination of diffusion parameter like ionic conductivity, activation energies, jump rates and diffusion coefficients are described.

According to their long range order solids are separated into crystalline and amorphous solids. The structure of crystalline solids consists of a repeating unit called unit cell. Amorphous solids, however, are randomly organized. On an atomic scale crystalline solids have a high degree of symmetry and long-range order. Another difference occurs in the observation of the melting point. While crystalline solids show sharp melting points, amorphous solids have a temperature range in which the material melts. Commonly solids are characterized by X-ray powder diffraction (XRD). Sharp diffraction reflexes point to crystalline materials, while broader and diffuse patterns are observed in amorphous materials. Nanocrystalline materials, however, do not show a sharp diffraction pattern. Electron diffraction or neutron

diffraction is necessary to distinguish them from amorphous materials.[67] With the famous Scherrer equation (Eq. 3.1), it is possible to calculate the particle size of the material [68]:

$$\langle d \rangle = \frac{K \cdot \lambda}{\beta \cdot \cos\theta} \quad (3.1)$$

Here,  $\langle d \rangle$  denotes the crystallite size,  $\lambda$  is the wavelength of X-radiation,  $\beta$  is the crystallite size broadening, *i.e.* the width of the reflex, and  $\theta$  is the Bragg angle.  $K$  is constant for a certain particle geometry and it takes a value of 0.89 for spherical particles.[67] A detailed description of the method and its applications can be found in *e.g.* references [68] and [69].

## 3.1. Fundamentals

### 3.1.1. Fick's Laws

Diffusion is the process of atoms or molecules aiming to equilibrate a concentration gradient.[70] Diffusion takes place due to *e.g.* differences in concentration, pressure or temperature of ions, atoms or molecules within a material. In 1855, Adolf Fick laid the foundation of today's understanding about diffusion [71]; not only in gases and liquids but also in solids. With his experiments on a mixture of salt and water, he was able to introduce the diffusion coefficient, which is used to compare diffusion of a certain species in different materials. For comparison, diffusion in gases happens at a rate of  $\text{cm s}^{-1}$ , whereas in liquids it is usually below  $\text{mm s}^{-1}$ . In solids, however, diffusion is strongly dependent on temperature and has a rate of about  $\mu\text{m s}^{-1}$  near the melting point, whereas at temperatures near half the melting point, diffusion only occurs at a rate of  $\text{nm s}^{-1}$ . [72] The first Fick's law relates the flux of particles  $J_x$  in a direction  $x$  with the concentration  $C$  of particles, ions or molecules and the proportionality factor  $D$ :

$$J_x = -D \frac{\partial C}{\partial x} \quad (3.2)$$

$D$  is the diffusion coefficient, also referred to as diffusivity with the SI unit  $\text{m}^2 \text{s}^{-1}$ . The minus sign describes the opposite orientation of particle flux and concentration. Eq. 3.2 is, however, only valid for isotropic systems like glassy solids, polycrystalline

materials or cubic crystals, where chemical and physical properties are independent from direction. By applying the vector notation on Eq. 3.2, this yields in:

$$\mathbf{J} = -D\nabla C \quad (3.3)$$

Eq. 3.3 is Fick's first law for anisotropic media. Vector symbols are written in bold letters. The nabla operator acts on the concentration  $C$  to obtain a concentration gradient  $\nabla C$ . If anisotropic materials are considered,  $D$  is a tensor and is called tracer diffusion coefficient  $D^T$ . Like other chemical and physical properties, diffusion properties are dependent on different directions in anisotropic media. If the diffusing species is conserved during the diffusion process, the equation of continuity can be applied on Fick's first law. In homogeneous systems the diffusion coefficient is independent from concentration which yields, together with the continuity equation, to a simplified form of Fick's second law in anisotropic media like, *e.g.*, non-cubic single crystals or composite materials:

$$\frac{\partial C}{\partial t} = D^T \Delta C \quad (3.4)$$

$\Delta$  ... Laplace operator

A detailed derivation of the given Eqs. can be found in Refs. [70] and [72].

### 3.1.2. Random Walk Theory

The tracer diffusion coefficient is defined on a macroscopic scale. In this section, alternatively, a second diffusion coefficient will be introduced. The so-called self-diffusion coefficient is based on the *random walk theory* and is also known as the microscopic diffusion coefficient. In contrast to Fick's laws, here diffusion is not dependent on a concentration gradient, but happens randomly. Albert Einstein, based on findings of Robert Brown and the Brownian motion, related the diffusion coefficient with the mean square displacement of particles. The Brownian motion is the random movement of a particle in a fluid. Einstein carried out a mathematical analysis of the Brownian motion and proposed that the movement of particles is influenced by other particles, atoms or molecules as well as thermal movements due to the Boltzmann distribution. In solids, motion of particles occurs in jumps from *e.g.* an interstitial site to the other (interstitial diffusion mechanism, see 3.1.4) with a certain probability that the particle jumps back.[70, 72–75]

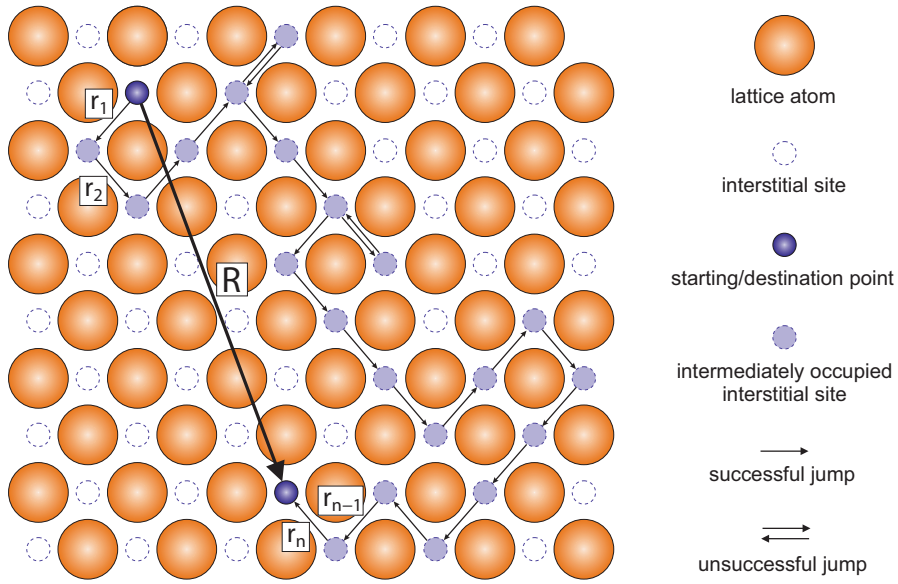


**Figure 7.** A random walk of a particle, hopping from one unoccupied interstitial site to another. The arrows show the direction of diffusion and arrows in two directions denote unsuccessful jumps. The mean square displacement  $R$  of the moving particle is shown as a large arrow from the starting point to its final destination. (inspired by [70, 73])

The relation of the self diffusion coefficient  $D^{\text{SD}}$  with the mean square displacement  $\langle R^2 \rangle$  includes also the residence time or correlation time  $\tau_c$  of a particle at an interstitial site:

$$D^{\text{SD}} = \frac{\langle R^2 \rangle}{6\tau_c} \quad (3.5)$$

$R$  is the total displacement which is the sum of all individual jump lengths  $r_i$  (see Figure 7). The double sum contains correlation effects. For totally uncorrelated motion the double sum vanished and Eq. 3.5 is simplified to:

$$D^{\text{SD}} = \frac{a^2}{6\tau_c} \quad (3.6)$$

Here,  $a$  is the distance from one lattice site to its nearest neighbour. This equation is called the Einstein-Smoluchowski relation. The macroscopic diffusion coefficient and the microscopic diffusion coefficient are related through a correlation factor  $f$  which can take values between 0 and 1. A correlation factor of  $f = 1$  means that the diffusion process is completely governed by uncorrelated motion of the observed

species.[70, 72–74] No matter if correlated or uncorrelated motion takes place in a solid,  $D$  is temperature dependent and usually follows an Arrhenius law with a pre-exponential factor  $D_0$ :

$$D = D_0 \cdot e^{-\frac{E_A}{k_B T}} \quad (3.7)$$

In Eq. 3.7  $E_A$  is the activation energy,  $k_B$  the Boltzmann constant  $1.38 \times 10^{-23} \text{ m}^2 \text{ kg s}^{-2} \text{ K}^{-1}$  and  $T$  denotes the absolute temperature in K.

### 3.1.3. Defects

The origin of ionic diffusion in solids is the presence of defects in the material. The type and number of defects, in turn, might directly or indirectly influence the ionic conductivity of a solid-state electrolyte. In crystalline solids, the material is usually more conductive when the number of defects is increased.[67] The opposite is true for amorphous materials, where the introduction of defects via, *e.g.* ball-milling, is disadvantageous in terms of conductivity.[76] In contrast to ball-milling the process of annealing, *i.e.* high temperature treatment, has the consequence of reducing defects. A number of intrinsic, native defects will remain in the material no matter how it is treated.[75]

In Figure 8.a energy is plotted *vs.* defect concentration. We see, that at the beginning, where the defect concentration is low, the gain in entropy  $\Delta S$  is higher than the energy required to introduce defects  $\Delta H$ . At a certain point, the rise in entropy gets smaller compared to  $\Delta H$  of defect formation and  $\Delta G$  (blue curve) is starting to rise.  $\Delta G$  (as given by Eq. 3.8) runs through a minimum in energy at a certain defect concentration. At this point the material is in equilibrium.[77]  $\Delta H$  is always positive, as the formation of defects is accompanied by (i) a change in volume and (ii) increase in lattice energy due to removal of atoms. A third (iii) contribution to  $\Delta H$  is rather small and leads a decrease in lattice energy due to relaxation of the surrounding.[73] Even though, the plot starts at a defect concentration of zero, a perfect crystal, *i.e.* a crystal with no defects, is, in theory, only possible at absolute zero. According to the third law of thermodynamics it is, however, not possible for a system to reach absolute zero. Hence, under realistic conditions, a material with zero defects does not exist.[77]

$$\Delta G = \Delta H - T\Delta S \quad (3.8)$$

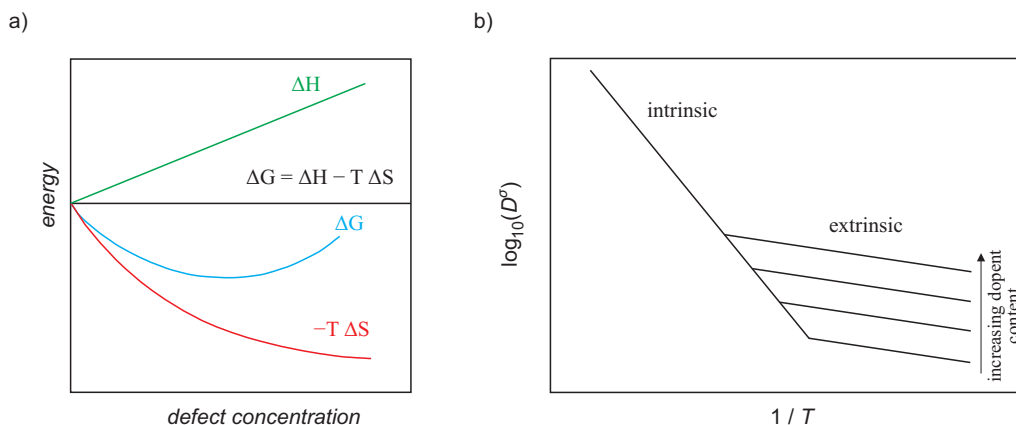


**Figure 8.** a) Energy *vs.* defect concentration. A simplified representation showing that there is a limit of disorder, where the formation of more defects prevails the gain in entropy of the system. (inspired by [73, 77]) b) Arrhenius plot of the conductivity diffusion coefficient  $D^\sigma$ . The contribution of intrinsic and extrinsic defects to  $D^\sigma$  is temperature dependent and the transition from intrinsic to extrinsic behaviour is dependent on the dopant content in *e.g.* alkali halides. (inspired by [72])

**Point defects.** Defects are usually classified according to their dimensionality. Mainly responsible for diffusion in solids are point defects, which are also called 0-dimensional defects. Point defects occur differently in ionic crystals, metals and semiconductors. While the point defects in metals are uncharged, in semiconductors point defects lead to electronic energy levels and are of either neutral or ionic nature. In ionic crystals, point defects are restricted in terms of charge, as charge neutrality has to be maintained.[72] Point defects include *e.g.* vacancies, interstitials or misplaced atoms, which are of intrinsic nature. In a binary system AB, a vacancy is an unoccupied lattice site, whereas an interstitial is an atom occupying an interstitial site on the crystal lattice. A misplaced atom is the presence of A on a lattice position, which is normally occupied by B.[78] Intrinsic point defects have to be supplemented by the so-called *Schottky* and *Frenkel* defects. In NaCl and other alkali halides, one will observe missing cations and a missing anions, *i.e.* Schottky defects are the simultaneous presence of cation and anion vacancies. In Frenkel defects, a cation is found on an interstitial site and at the same time it leaves a vacancy behind that has a negative charge in order to maintain electroneutrality. The same phenomenon can occur with anions, which is called *anti-Frenkel* defect. While Frenkel defects are predominant in *e.g.* AgCl, anti-Frenkel or anion Frenkel defects are seen in crystals appearing in fluorite structure, like CaF<sub>2</sub>. [77, 78]

Moreover, it might occur that another class of intrinsic defects is present in a material. Free electrons and holes are so-called electronic defects. At high temperatures it is likely that an electron is excited from the valence band to the conduction band and might occupy *e.g.* a vacancy position of the crystal lattice. The most famous example of an electron defect is the F-centre<sup>4</sup>. Extrinsic electron defects are also possible, which form during a process of ionization of atomic defects.[77]

Non-electronic extrinsic defects are dopants or impurities. In principle, chemically there is no difference in dopants and impurities. While dopants are intentionally added to the material to boost its properties, the term impurities is usually applied when a foreign ion species or atom is not desired. It might appear that extrinsic defects species have the same charge as the regular lattice ion or it is of aliovalent nature, meaning of different charge. An aliovalent cation substitutional has the consequence of *e.g.* an additional cation vacancy in order to maintain electroneutrality. This shows why doping is efficient in increasing the conductivity of materials. Via doping of cations with higher valence than the host cation, vacancies are produced, which are beneficial for diffusion of ions and, in this way, boost the conductivity of the material. The position in the crystal lattice of extrinsic defects can be either on a regular lattice site (substitutional) or on an interstitial site (interstitial). Usually doping is realized with cations rather than anions, as from an experimental point of few, they are easier to realize due to smaller ionic radii compared to the corresponding atomic radii.[72, 75, 77, 78]

In Figure 8.b the conductivity diffusion coefficient  $D^\sigma$  is plotted *vs.* inverse temperature. Two regimes are observed in alkali halides, which both follow an Arrhenius behaviour. At higher temperatures, *i.e.* small values of  $1/T$ , the slope of  $D^\sigma$  is dominated through the contribution of intrinsic defects. At a certain transition point the slope flattens and the contribution of extrinsic defects is predominant. The transition temperature is dependent on the concentration of extrinsic defects and occurs at higher temperatures when more extrinsic defects are present. This schematic and simplified representation excludes, however, the fact that at low temperatures another change in slope occurs due to the formation of impurity-vacancy complexes.[72]

Point defects of any kind are usually written in the so-called *Kröger-Vink notation*. A defect can be described by the combination of three symbols. The kind of defect, either a vacancy or an ion which is not on a regular lattice position, is written with

---

<sup>4</sup>The term F-centre originates from the the German word *Farbzentrum*, which means colour centre.

its net charge in superscript and the regular lattice position in subscript. A positive net charge is written with a  $\bullet$ , neutral net charge with  $\times$  and negative net charge is indicated by  $'$ . An example is  $V_{\text{Cl}}^{\bullet}$ , which describes a vacancy on a lattice site normally occupied by Cl ions in *e.g.* NaCl with a net charge of +1. The positive net charge originates from the absence of negative Cl and leads to the maintenance of electroneutrality. Ions on an interstitial site are written with an  $i$  subscripted; *e.g.*  $F_i'$  indicates an  $F^-$  ion, which occupies an interstitial site in  $\text{CaF}_2$  with a net charge of  $-1$ . [77]

**Extended defects.** Defects of higher dimensionality, *i.e.* 1D, 2D and 3D, are called extended defects. *Dislocations* are line defects with a dimensionality of 1. As metals are always softer than it is predicted theoretically, the existence of dislocations was proposed long before they were experimentally found. The class of dislocations includes edge dislocations and screw dislocations. An edge dislocation has to be characterized by an additional half-plane in parallel to the regular lattice plane. Although the defect has the form of a plane, they are classified as line defects as the center of distortion is a line, that stretches through the material. The plane that separates two regions of the crystal with regular lattice order is called slip plane. The centre of distortion in screw dislocation works, as the name already implies, as a screw. Along the defect line atoms of the regular lattice are aligned accordingly like in a spiral staircase. It is often referred to further types of dislocations, which are in fact a combination of edge and screw dislocations. Since dislocations are energetically not stable they tend to glide along the slip plane and annihilate. Therefore, dislocations do not terminate in the bulk of a crystal but are found rather on the edge of the crystal. If they are in fact found inside the material, an interaction of dislocations takes place, whereby gliding becomes more difficult and a process called climbing occurs more frequently. Interactions of dislocations with each other, *i.e.* dislocation loops, as well as the interaction of dislocations with point (0D) and planar (2D) defects continuously happen in crystals, which, in addition, leads to climbing of dislocations. [73, 75, 77]

Similar to line defects, *planar defects* or 2D defects have a significant impact on the material's strength and ductility, respectively. Furthermore, planar defects do play an important role in terms of chemical reactivity, since most reactions with solids strongly depend on the surface area. These types of defects include internal boundaries, such as grain boundaries, twin boundaries and antiphase boundaries as well as stacking faults. The latter one is frequently seen in layered materials

that exhibit polytypism. A famous battery-related example that shows stacking faults is graphite. Internal boundaries in general are usually prone to aggregation of both, intrinsic and extrinsic point defects. Grain boundaries are usually considered as preferred diffusion pathways for ions with lower activation energies than in the bulk of the material. Planar defects occur even in single crystals, where they are understood as a boundary between different domains of the crystal. Here, the term low-angle grain boundary is used. Low-angle grain boundaries consist of a number of dislocations; being either edge or screw dislocations or a mixture of them.[73, 75, 77]

Impurities such as foreign phases or precipitates are considered 3D defects or *volume defects*. Although all defects are, in a broader definition, volume defects, impurities and precipitates as well as voids, cracks, inclusion and pores cannot be described from any other point of view than from a 3-dimensional. Volume defects can be separated into two categories regarding their influence on the mechanical strength of a material. In *e.g.* precipitation hardening the introduction of volume defects leads to an increase in mechanical strength. These artificially created inclusions serve as barriers for dislocation movement. The presence of cracks, voids and pores, however, is usually disadvantageous for the material's strength. Moreover, 3D defects influence thermal, electronic and optical properties of the material.[73, 75]

### 3.1.4. Diffusion Mechanisms

As already mentioned defects significantly influence the diffusion behaviour of a material. With point defects we can describe a number of different self-diffusion mechanisms that frequently occur in solid materials. The two most important mechanisms are the *vacancy mechanism* and the *interstitial mechanism* (Figure 9). The vacancy mechanism can be viewed from the perspective of the atoms, that hop into a vacancy, leaving a vacancy behind, which serves as possible site for further atoms in the crystal lattice. On the other hand, it is often easier to consider the mechanisms as movement of vacancies, especially when dealing with mathematical problems.[79] A related mechanism is the *divacancy mechanism*, where two vacancies agglomerate with a certain bonding energy. At higher temperatures, the contribution of divacancy mechanism to the total diffusion is usually higher than the contribution of monovacancies. Trivacancies are, in principle, also possible, but their contribution to the total diffusion process is limited.[67, 72, 73, 79]

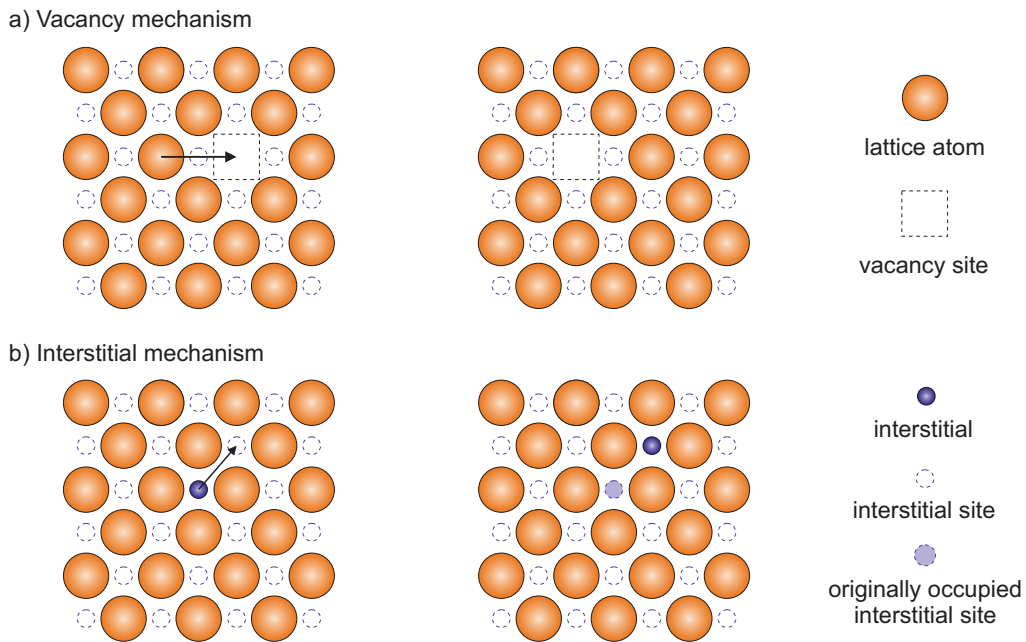


**Figure 9.** Schematic representation of a) the vacancy mechanism and b) the interstitial mechanism which are the most frequently occurring diffusion mechanisms in solids. (inspired by [73])

The diffusion mechanism called *interstitial diffusion* has already been introduced to describe the random walk theory (see subsection 3.1.2). Here, particles on interstitial sites of the lattice hop to a neighbouring interstitial site. This can happen even only due to thermal vibrations.[73] The moving species in interstitial diffusion is smaller than the atoms in the host lattice. The small size of the moving species, together with the fact that theoretically no defects are necessary in interstitial diffusion, is the reason for the comparably low activation energy and high diffusion coefficients of this mechanism.[72] A practical application of the interstitial mechanisms is steel hardening where nitrogen or carbon is introduced into the structure.[79]

The third fundamental diffusion mechanism is the *interstitialcy mechanism*. Here, a regular lattice atom is replaced by an interstitial atom. In further consequence, the lattice atom occupies a different interstitial site in the crystal. Obviously, this mechanism has a noticeable higher activation energy than the interstitial mechanism, since large lattice atoms occupy rather small interstitial sites.[72, 79] If interstitial diffusion takes place prior to the interstitialcy mechanism, the mechanism is called *knock-out mechanism*. When, on the other hand, the interstitially diffusing species

occupies a vacancy, it is referred to as *dissociative mechanism*.<sup>[72]</sup>

For the sake of completeness two additional mechanisms are introduced at the end of this subsection. The mechanisms called *direct exchange* and *ring diffusion* cause significant distortions in the lattice since the particles which contribute to these mechanisms are of similar size. The contributors are either regular lattice atoms or substitutionals. Direct exchange means that two neighbouring atoms exchange their regular positions in the crystal lattice, while in ring diffusion a number of atoms sequentially occupy the position of their neighbouring atoms in a circular way.<sup>[72]</sup>

## 3.2. Determination of Diffusion Parameters

In this section two indispensable characterization techniques of solid-state electrolytes will be presented. Impedance spectroscopy (IS) and nuclear magnetic resonance (NMR) offer together a broad picture of diffusion mechanisms of the observed material. IS, often referred to as alternating current (AC) conductivity spectroscopy, is sensitive to long-range diffusion and is able to distinguish between diffusion in the bulk of the material and diffusion through grain boundaries. Furthermore, IS is the technique of choice when it comes to the analysis of interfaces between electrodes and the solid electrolyte. Due to the fact that IS measures a total conductivity of all charge carriers (positive and negative ions as well as electrons), a complementary method is necessary to gain a definite picture of the diffusion mechanisms of a certain material. Polarization experiments are used to distinguish between electronic and ionic conductivity. These experiments enable the determination of the electronic conductivity, which can be subtracted from the total conductivity to obtain the ionic conductivity. If the determined electronic conductivity is negligibly small, it is still unclear which ion or ions are responsible for the the ionic conductivity. NMR is an element-specific method revealing a definite result, if the probed element is mobile in the observed material. NMR studies in the field of battery research particularly focus on Li and Na diffusion. Early studies dealing with both IS and NMR were wondering about differences in the results of diffusion parameters obtained via the two techniques. The difference originates in the sensitivity of the methods. While in NMR spin fluctuations influence the results, electrical relaxation is sensed by conductivity spectroscopy.<sup>[47]</sup> It has been the focus of many studies and different models were proposed to connect the results of both methods.<sup>[80–82]</sup> As prominent examples, the jump relaxation model by Funke <sup>[83]</sup> and the coupling model by Ngai <sup>[84, 85]</sup> proved their suitability in a variety of different systems.<sup>[47, 86]</sup> Years after

they proposed their models, both published detailed studies presenting experimental evidences for their models.[87, 88] In the following subsections the techniques IS and NMR will be explained and data interpretations of measurement results will be shown.

### 3.2.1. Impedance Spectroscopy

If new solid-state electrolytes are characterized, there is hardly any study which does not include impedance spectroscopy (IS). Due to the large amount of applications, representations and interpretations a number of books are dealing with IS (*e.g.* [89–91]). The measurement requires sample preparation where powder samples are usually pressed into cylindrical shaped pellets. The surface of the pellet is covered with electrodes on both sides, which can be either blocking (*e.g.* gold) or non-blocking (*e.g.* lithium metal for Li ions) for ions. The sample with a known geometry (surface  $A$  and thickness  $d$ ) is connected to the impedance spectrometer and an alternating voltage  $V(t)$  is applied (Figure 10.a).  $V(t)$  can be expressed through its amplitude  $V_A$  and frequency  $\nu$  as given by Eq. 3.9:

$$V(t) = V_A \cdot \sin(2\pi\nu t) = V_A \cdot \sin(\omega t) \quad (3.9)$$

The radial frequency is additionally used to express  $V(t)$  and is obtained through the relation  $\omega = 2\pi\nu$ . The resulting current has the same frequency but differs in amplitude  $I_A$  and is phase shifted ( $\phi$ ) (Figure 10.b):

$$I(t) = I_A \cdot \sin(\omega t + \phi) \quad (3.10)$$

Impedance can be expressed as the "*complex electrical resistance*" and includes not only "*the ability of a circuit to resist the flow of electrical current*", which is further referred to as the the real part of the impedance, but also the "*ability of a circuit to store electrical energy*", which will be denoted as the imaginary part of the impedance. As mentioned, impedance  $Z^*$  is a complex quantity which is measured in electrical circuits composed of a number of resistors, capacitors and inductors.[89] Using Ohm's law ( $R = \frac{U}{I}$ ) and Eq. 3.9 and 3.10 the impedance is given by:

$$Z^* = \frac{V(t)}{I(t)} = \frac{V_A \cdot \sin(\omega t)}{I_A \cdot \sin(\omega t + \phi)} = Z_A \frac{\sin(\omega t)}{\sin(\omega t + \phi)} \quad (3.11)$$

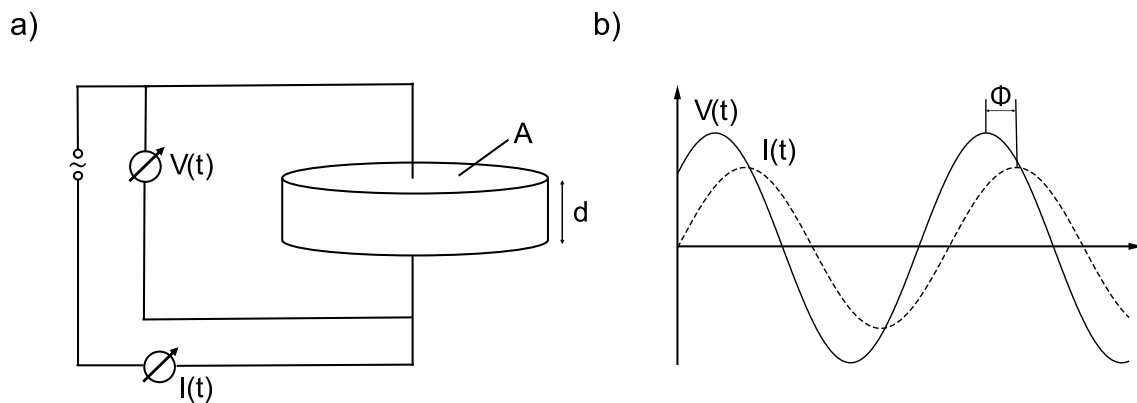


**Figure 10.** a) Schematic of an impedance spectroscopy experiment with a pellet sample. A voltage  $V(t)$  is applied to a cylindrical pellet sample with surface  $A$  and thickness  $d$ . The resulting current response  $I(t)$  is measured. b) Sinusoidal voltage and current response at a single frequency with a phase shift  $\phi$ . [92]

To express the impedance as a complex function with a real part  $Z_{\text{real}}$  and an imaginary part  $Z_{\text{im}}$ , the Euler's formula<sup>5</sup> ( $e^{i\phi} = \cos \phi + i \sin \phi$ ) is applied. The impedance  $Z^*$  as it is given in Eq. 3.11 is now expressed as follows:

$$Z^* = \frac{V(t)}{I(t)} = \frac{V_A \cdot e^{i\omega t}}{I_A \cdot e^{i\omega t - i\phi}} = Z_A \cdot e^{i\phi} = Z_A \cdot (\cos \phi + i \sin \phi) = Z_{\text{real}} + iZ_{\text{im}} \quad (3.12)$$

If the measured  $Z_{\text{real}}$  is plotted against the negative value of  $Z_{\text{im}}$ , a characteristic semicircle is obtained when solid-state electrolytes are analysed. The resulting plot, the so-called Nyquist plot (Figure 11.a), allows to distinguish between different diffusion regions. At higher frequencies a semicircle appears, which is attributed to bulk diffusion. In a number of materials a second semicircle is observed at lower frequencies, which points to grain boundary (g.b.) diffusion. This semicircle is usually higher in resistance. If non-blocking electrodes are applied, a third semicircle is observed, whereas with blocking electrodes the Nyquist plot shows a straight line pointing to electrode polarization. The various semicircles can be fit with equivalent circuits. For each semicircle a resistor and a capacitor are connected in parallel, which results in a full semicircle in an ideal system. Solid-electrolytes, however, do not always behave ideal leading to depressed semicircles. Therefore, the capacitor is replaced by a constant phase element (CPE) in the equivalent circuit. Such a circuit

<sup>5</sup>The Euler's formula relates trigonometric functions with complex exponential functions.

element is characterized by a phase angle which is independent from AC frequency. The equivalent circuit with a capacitor and a CPE in parallel is used to simulate the semicircles obtained from IS measurements.[89]

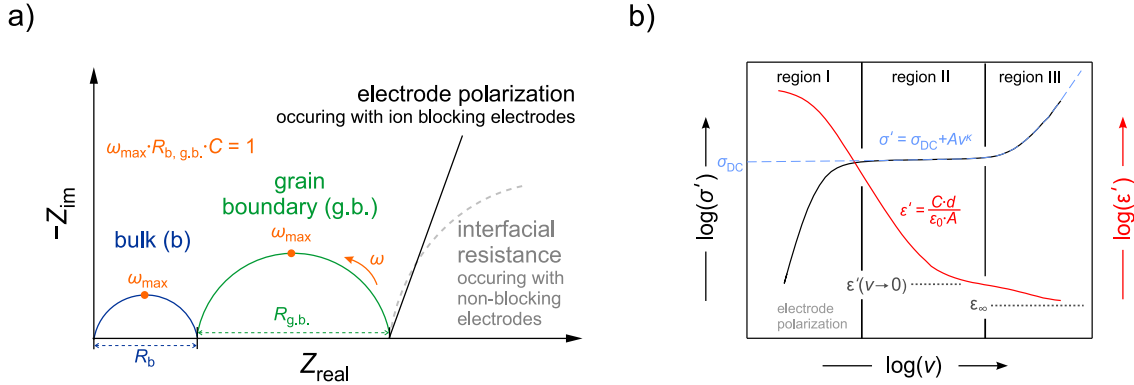


**Figure 11.** a) Schematic Nyquist representation of impedance spectroscopy data: The blue semi-circle shows bulk diffusion, whereas grain boundary diffusion is usually observed at lower frequencies and higher resistances (green). Depending on the kind of electrode, an additional semi-circle appears for non-blocking electrodes and a spike for blocking electrodes. (inspired by [93]) b) Results from an impedance measurement of  $\text{LiBH}_4\text{-LiI}/\text{Al}_2\text{O}_3$  at  $0^\circ\text{C}$  are shown exemplarily to illustrate typical conductivity and permittivity isotherms. For further details see text. (inspired by [94])

The frequency value, where  $-Z_{im}$  reaches its maximum ( $\omega_{max}$ , see Figure 11.a) and the capacitance of the constant phase element  $C$  are related through  $\omega_{max} \cdot R_{b, g.b.} \cdot C = 1$ , where  $R$  is the diameter of the semicircle (Figure 11.a). Irvine, Sinclair and West tabulated different phenomenons responsible for semicircles in the Nyquist representation and the capacitances of their corresponding CPE. The assignment of a certain range of capacitance to diffusion phenomenons allows an additional interpretation of the data. The obtained capacitance tells whether the semicircle is observed due to (i) diffusion of the ions in the bulk, (II) through the grain boundaries or (iii) the interface of electrode and sample (in measurements with non-blocking electrodes). In addition, different phenomenons are listed, where they attributed the semicircle to a second phase, bulk ferroelectric behaviour or a surface layer. Capacitances as low as  $10^{-4}$  point to electrochemical reactions, according to the interpretation of Irvine *et al.*[95] Alternatively,  $Z_{real}$  can be plotted against the frequency. This data representation is called the Bode plot, which includes also the

phase angle plotted against the frequency on a second y-axis.

While Nyquist plots are used to get a first impression of diffusion behaviour of a material, solid-state electrolytes are usually compared according to their ionic conductivity  $\sigma'$ .  $\sigma'$  is obtained by taking into account the dimensions of the sample (thickness  $d$  and area  $A$ ) and  $Z_{\text{real}}$  via the relation:

$$\sigma' = \frac{1}{Z_{\text{real}}} \cdot \frac{d}{A} \quad (3.13)$$

Usually impedance spectroscopy measurements are realized in a certain frequency range, measuring the impedance at certain points in this range and repeating the measurement at various temperatures. If the resulting conductivity obtained via Eq. 3.13 at a certain temperature is plotted versus the frequency a so-called conductivity isotherm is obtained. In Figure 11.b an impedance spectroscopy measurement of  $\text{LiBH}_4\text{-LiI}/\text{Al}_2\text{O}_3$  at 0 °C is exemplarily shown to illustrate a conductivity and permittivity isotherm. In the usual measurement range between 10 mHz and 10 MHz three region are observed in the conductivity isotherms of solid-state electrolytes (Figure 11.b, black curve).

At lower frequencies the conductivity isotherm runs through a regime where conductivity is decreasing with decreasing frequency (region I). When blocking electrodes are used, ions are accumulating at the electrodes and built a depletion layer leading to a drop in conductivity at low frequencies. Depending on the conductivity of the sample and the measurement temperature, the conductivity isotherm passes through a plateau over a certain frequency range (region II). The conductivity value at this plateau is called DC-conductivity ( $\sigma_{\text{DC}}$ ), since at this plateau (DC-plateau) the conductivity is independent from frequency. In general, different solid-state electrolytes are compared according to their  $\sigma_{\text{DC}}$  at room temperature.  $\sigma_{\text{DC}}$  follows an Arrhenius behaviour:

$$\sigma_{\text{DC}} = \frac{A}{T} \cdot e^{\frac{-E_a T}{k_B}} \quad (3.14)$$

The factor  $A$  in Eq. 3.14 is a pre-exponential factor,  $T$  is the absolute temperature of the measurement,  $k_B$  denotes the Boltzmann's constant and  $E_a$  is the average activation energy of long-range ionic transport. The third region (region III), at higher frequencies, is governed by correlated motions of interacting ions, which is accompanied by a significant rise in conductivity with increasing frequency.[94] Region II and Region III follow a power law (Figure 11.b, dashed blue curve) which was

introduced by Andrzej K. Jonscher in 1977:[96]

$$\sigma' = \sigma_{\text{DC}} + A\nu^\kappa \quad (3.15)$$

$A$  and  $\kappa$  are constant values for a certain material. The exponent  $\kappa$  allows a valid speculation about the dimensionality of conduction. Most ionic conductors show values for  $\kappa$  between 0.6 and 0.9 pointing to 3D ion transport. 2D diffusion and 1D diffusion has to be characterized by  $\kappa = 0.5$  and  $\kappa < 0.4$ , respectively.[97–99] At higher frequencies the conductivity enters a region called the nearly constant loss (NCL), where  $\sigma' \propto \nu^1$  and although it is not completely clear, it is believed that ion motion in this region is mainly governed by localized motions.[100] Going to even higher frequencies the dependence is  $\sigma' \propto \nu^2$ , which is the result of lattice vibrations and phononic contributions.

Another important parameter which can be extracted through  $\sigma_{\text{DC}}$  is the diffusion coefficient  $D^\sigma$ . The Nernst-Einstein equation (Eq. 3.16) relates  $\sigma_{\text{DC}}$ , the number of charge carriers ( $N$ ) and their charge ( $q$ ) with the diffusion coefficient. A usual attempt is to estimate the number of charge carriers by assuming that all charge carriers per unit cell of a certain material contribute to the diffusion process. The obtained  $D^\sigma$  can be related to the tracer diffusion coefficient  $D^T$  via the Haven-ratio ( $H_{\text{R}} = \frac{D^T}{D^\sigma}$ ).  $H_{\text{R}}$  tells, if  $D^\sigma$  rather reflects the diffusion of a single charge carrier ( $H_{\text{R}} = 1$ ) or if it is influenced by more than a single contribution. While  $H_{\text{R}} < 1$  gives rise to correlation effects or electronic conductivity being part of the total conductivity,  $H_{\text{R}} > 1$  allows to draw the conclusion that holes are contributing to the diffusion process.[72, 91, 101]

$$D^\sigma = \frac{\sigma_{\text{DC}} \cdot k_{\text{B}}T}{N \cdot q^2} \quad (3.16)$$

In Figure 11.b an alternative representation of an IS measurement is shown. The red curve shows a permittivity isotherm of  $\text{LiBH}_4\text{-LiI/Al}_2\text{O}_3$  at 0 °C. The real part of the permittivity  $\epsilon'$  at a certain temperature and frequency is obtained by:

$$\epsilon' = \frac{C \cdot d}{\epsilon_0 \cdot A} \quad (3.17)$$

Here,  $C$  denotes the capacitance,  $\epsilon_0$  is the permittivity in vacuum and  $A$  and  $d$  are again the dimensions of the pellet sample. The permittivity runs through 2 plateau-like regimes, where the frequency dependence is almost zero.[94]  $\epsilon'$ , however,

denotes only the real part of the permittivity. In general,  $\epsilon$  is a complex quantity and is related to the measured impedance as follows:

$$\epsilon = (j\omega \cdot C_C)^{-1} \cdot Z^{-1} \quad (3.18)$$

$C_C$  is the capacitance of the empty measurement cell and  $j$  indicates the complex nature of  $\epsilon$ . [91] Two additional quantities are often used to represent IS data. Together with impedance and permittivity, admittance ( $Y$ ) and the electric modulus ( $M$ ) are defined as the four immittance functions and are related through the equations below [91]:

$$Y = Z^{-1} \quad (3.19)$$

$$M = \epsilon^{-1} \quad (3.20)$$

### 3.2.2. Nuclear Magnetic Resonance

While IS reveals information about long-range ionic transport, with solid-state nuclear magnetic resonance (SSNMR) diffusion processes on an atomic scale can be analysed as well. NMR is element specific and via different measurements settings, it is possible to observe diffusion processes over different length scales. Atomic diffusion jump rates  $\tau^{-1}$  between  $10^{-2}$  to  $10^{10}$  are sensed with SSNMR. The analysis of solid ionic conductors involves mainly techniques sensitive to fast ionic motion like spin-lattice relaxation (SLR) experiments, which determine relaxation times  $T_1$  and  $T_{1\rho}$  by sensing longitudinal relaxation. SLR covers jump rates from  $10^4$  to  $10^{10}$ . Alternative experiments to observe slow jump processes are spin-spin relaxation experiments, which determine the time constant  $T_2$  and sense transverse magnetization. Even slower processes are covered with the so-called stimulated echo NMR, which is also referred to as spin-alignment echo NMR. [102]

In the frame of this thesis mainly three experiments have been performed to observe the diffusion processes in ionic conductors. The analysis of line shapes at different temperatures is the simplest technique, which also serves as fast screening for potential ion conductors. The determination of SLR rates ( $1/T_1$  and  $T_{1\rho}$ ) at variable temperature requires more complex pulse sequences and longer measurement times. Experimental details as well as theoretical background with explanation of

pulse sequences of the applied techniques are provided in the appendix B.2.3. Solid-state NMR is a comprehensive technique and therefore the textbooks of Abragam [103], Keeler [104] and Heitjans [70] as well as chapter 5 in *Handbook of Solid State Batteries* [102], chapter 1 in *Annual Reports on NMR Spectroscopy* [105] and chapter 15 in *Diffusion in Solids* [72] are highly recommended for further reading.

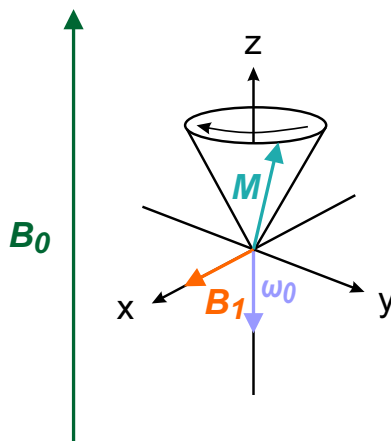


**Figure 12.** Simplified vector model of nuclear magnetic resonance. An external magnetic field  $\mathbf{B}_0$  in z-direction forces a magnetization  $\mathbf{M}$  in a precession about z. The frequency of this Larmor precession is  $\omega_0$ , which points in the opposite direction.  $\mathbf{B}_1$  is the direction of the oscillating magnetic field originating from the coil, in which the sample is placed.

**Basics - the vector model.** For NMR experiments, samples are prepared in NMR tubes under protective atmosphere. The NMR tube is placed inside a coil, which is able to apply an oscillating magnetic field. In the first place, the coil is at rest and the sample experiences only the magnetic field  $\mathbf{B}_0$  of the magnet, which surrounds the probe head. This strong magnetic field is usually in the order of 5 to 10 Tesla.  $\mathbf{B}_0$  forces the magnetic moments  $\boldsymbol{\mu}$  of the observed nuclei, with a spin vector  $\mathbf{I}$  other than 0, in the direction of the magnetic field (vectors are written in bold letters).

$$\boldsymbol{\mu} = \gamma \cdot \mathbf{I} \quad (3.21)$$

The gyromagnetic ratio  $\gamma$  is a proportionality factor and is specific for a certain nucleus. The sum of all magnetic moments is the magnetization  $\mathbf{M}$ . The consequence of the applied magnetic field  $\mathbf{B}_0$  is a precession of  $\mathbf{M}$  about the z-axis, as the

magnetic moments experiences a torque (see Figure 12 for the vector model). This precession is called Larmor precession and is observed when spectral lines of atoms are split due to the applied magnetic field (Zeeman effect). The angular frequency at which  $\mathbf{M}$  is precessing is called Larmor frequency  $\omega_0$ :

$$\omega_0 = -\gamma \cdot \mathbf{B}_0 \quad (3.22)$$

The Larmor frequency is pointing towards the opposite direction of  $\mathbf{B}_0$ . In a simple NMR experiments a radio frequency (rf) pulse is used to force the magnetization away from its equilibrium position. The rf pulse originates from the coil surrounding the sample and is applied perpendicular to  $\mathbf{B}_0$ . The frequency of the magnetization from the coil ( $\mathbf{B}_1$ ) is set close to the Larmor frequency, in order to obtain resonance. This enables  $\mathbf{B}_1$ , even due to significantly weaker field strength compared to  $\mathbf{B}_0$ , to force  $\mathbf{M}$  into the  $x$ - $y$  plane. In addition, the coil detects the signal, which is the so-called free induction decay (FID). The FID is a voltage signal that includes information about how the magnetization relaxes back to its equilibrium position, after the excitation through the rf pulse.[72] To obtain the most intense signal a  $90^\circ$  or  $\pi/2$  pulse has to be applied. To find such a  $\pi/2$  pulse the pulse length is increased until a point is reached where the signal is zero; this is the  $180^\circ$  or  $\pi$  pulse. Simply by halving the pulse length, the  $\pi/2$  pulse is obtained.[104]

**Data processing.** As already mentioned the coil detects the magnetization in the form of induced voltage in the coil. Since the magnetization and the signal experience a relaxation or decay it is referred to as the free induction decay (FID). A conversion of the time dependent signal is necessary to obtain common frequency dependent NMR spectra. This is done by applying a mathematical process on the FID; the *Fourier transformation*. The FID as well as the Fourier transformed frequency dependent signal contains a real and an imaginary part. Usually only the real part is plotted, which is known as the *absorption mode Lorentzian lineshape*. In the usual case, the displayed spectrum does not contain only the absorption mode. Therefore, processing of NMR data involves phase corrections. A zero order phase correction is, simply put, the adjustment of the baseline and influences several signals of the spectrum to the same extend as it is frequency independent. There is, however, another phase error which is frequency dependent and therefore, its effect is different for signals with different offsets. For spectra with more than one signal, a first order phase correction might be necessary. Such zero and first order

phase corrections are supported by the software provided by the manufacturers of the spectrometer.[104]

**Relaxation times.** The time, the spin ensembles need to relax back in their equilibrium position, is called relaxation time. A distinction is made here between longitudinal relaxation, that is spin-lattice relaxation (SLR), and transverse relaxation, that is spin-spin relaxation(SSR). The corresponding relaxation times are referred to as  $T_1$ , in the case of SLR, and  $T_2$  in the case of SSR. The Bloch equations relate the relaxation times with the measured magnetization and the diffusion coefficient. While  $T_1$  is a measure of how fast diffusion processes in a material occur,  $T_2$  is closely related to the width of the NMR signal  $\Delta\omega'$  by:

$$\Delta\omega' = \frac{1}{T_2} = \Delta\omega_0^2 \cdot \tau \quad (3.23)$$

The mean residence time of an atom in a certain lattice position  $\tau$  is a measure of diffusivity and as Eq. 3.23 implies, lines appear narrower when  $\tau$  is small and  $T_2$  is large. If NMR lines appear narrower with increasing temperature, this phenomenon is called *motional narrowing*. [72]

As already mentioned before, experimental details as well as additional theoretical background with explanation of pulse sequences used in  $1/T_1$  and  $1/T_{1\rho}$  experiments are provided in the appendix B.2.3. In short, a number of  $\pi/2$  pulses are used to make sure all initial magnetization in z-direction ( $M_z$ ) vanishes. After a certain period of time the relaxation of  $M_z$  is detected with another  $\pi/2$  pulse. By varying the waiting time in a range where  $M_z$  is still close to zero and where  $M_z$  is fully recovered, it is possible to determine the  $T_1$  relaxation time with stretched exponential fits. Similar, but by applying a locking field  $\mathbf{B}_1$ , the  $SLR_\rho$  rate is determined by sensing  $M_\rho$  in the rotating frame of reference. Worth mentioning, the applied locking field  $\mathbf{B}_1$  is perpendicular to  $\mathbf{B}_0$  and is able to fix the magnetization in the  $x$ - $y$  plane with a locking frequency  $\omega_1$ . In this case the locking time  $t_{lock}$  is varied and  $T_{1\rho}$  is again determined with a stretched exponential fit through the detected  $M_\rho$  at the applied  $t_{lock}$ .

**Data representation - the BPP model.** To gain information about diffusion processes in the observed solid materials, the  $T_1$  time constant is determined at various temperatures. This gives, if the sample contains mobile ions, a so-called *diffusion induced rate peak*. The Arrhenius plot arises from plotting various relaxation

rates ( $1/T_1$  or  $1/T_{1\rho}$ ) at the measured temperatures on a logarithmic scale against the inverse temperature ( $1000/T$ ). Bloembergen, Purcell and Pound [106] described a model that applies to isotropic media. The model results in a symmetric rate peak and is valid for uncorrelated 3D-diffusion. At the diffusion induced rate peak, it is possible to determine jump rates ( $\tau \approx 1/\tau_c$ ) through the condition  $\omega_0 \cdot \tau_c \approx 1$ , with the Larmor frequency  $\omega_0$  and the correlation time  $\tau_c$ . In the case of  $1/T_{1\rho}$  relaxation rates, the condition at the rate peak changes to  $\omega_1 \cdot \tau_c \approx 0.5$ , with  $\omega_1$  being the locking frequency.

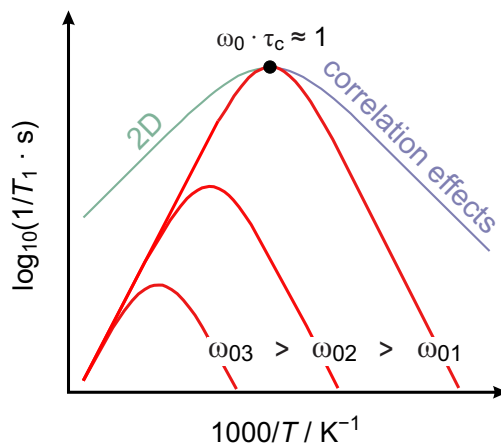


**Figure 13.** Schematic Arrhenius plot at different Larmor frequencies  $\omega_{01}$ ,  $\omega_{02}$ ,  $\omega_{03}$  (red). Deviations from the symmetric diffusion induced rate peak, as predicted by the BPP model, are lower dimensional diffusion processes *e.g.* 2D at the high-temperature flank (green) and correlation effects at the low-temperature flank (blue). At the rate peak the condition  $\omega_0 \cdot \tau_c \approx 1$  is valid when  $1/T_1$  rates are observed. (inspired by [70])

The position of the peak in the Arrhenius plot depends on the Larmor frequency. With higher Larmor frequencies the peak shifts towards higher temperatures and lower values for  $1000/T$ , respectively (Figure 13). At very high temperatures, relaxation rates get independent from frequency and the high temperature flanks recorded at different Larmor frequencies run into each other. If samples are governed by low dimensional diffusion processes, *i.e.* 1D or 2D, a decreased slope of the high temperature flank is observed. If, on the other hand, the corresponding low temperature flank exhibit a flatter slope, this is attributed to correlated motion. Correlated motion is caused by Coulomb interactions and/or structural disorder in the sample. The slopes of the high- and low-temperature flanks give the activation energy of the jump process. Hereby, the high-temperature flank represents long-range ionic transport and therefore, its activation energy can be well compared with activation

energies obtained by impedance spectroscopy. The low-temperature flank, however, reflects short-range ion transport, because at lower temperatures mobile particles move on a shorter length scale in the probed time frame.[102, 107]

**Diffusion coefficients from NMR.** Field-gradient (FG) NMR is a special NMR method, that is able to directly determine the tracer diffusion coefficient  $D^T$ . Here, a magnetic field gradient is applied to the sample in addition to the external magnetic field, which leads to an inhomogeneous magnetic field. The method uses the so-called stimulated spin-echo (SSE) technique and senses the decay of transversal magnetization. The variation of the constant field gradient with the strength  $g$  and the length  $\delta$  and the diffusion delay  $\Delta$  of the SSE pulse sequence allows a valid estimation of the tracer diffusion coefficient. This, however, enables only the determination of rather high diffusion coefficients. For the observation of diffusion coefficients in the order  $10^{-12} \text{ m}^2 \text{ s}^{-1}$ , pulsed magnetic-field gradients (PFG) are used. PFG NMR was introduced by Stejskal and Tanner [108], who proposed also the Stejskal-Tanner equation for stimulated echo pulse sequences:

$$M(g) = M_0 \cdot e^{-(\gamma\delta g)^2 D^T (\Delta - \frac{\delta}{3})} \quad (3.24)$$

$M$  denotes the echo attenuation which represents the measurable quantity of the experiment. At the pre-exponential factor  $M_0$ , the relation  $g \cdot \delta = 0$  is valid. In addition, the gyromagnetic constant  $\gamma$  is needed for the determination of  $D^T$ . A problem in PFG NMR are eddy currents produced by large pulsed gradients that interfere the measurement. This requires sophisticated techniques like *e.g.* longitudinal eddy current delays (LECD).

A second diffusion coefficient can be calculated from NMR. Here, the jump distance is approximated by the nearest neighbour distance  $a$ . In addition  $\tau_c$ , determined via the diffusion induced rate peak of SLR experiments, is used to determine the diffusion coefficient from NMR ( $D^{\text{NMR}}$ ). This diffusion coefficient equals the self-diffusion coefficient  $D^{\text{SD}}$ , as correlation effects are neglected. It is obtained according to Eq. 3.6 as given in subsection 3.1.2. The Diffusion coefficients from PFG NMR ( $D^{\text{PFG}}$ ), spin-relaxation NMR ( $D^{\text{NMR}}$ ) and IS ( $D^\sigma$ ) are related through the correlation factor  $f$  and the Haven ratio  $H_r$  via:

$$D^{\text{PFG}} = f \cdot D^{\text{NMR}} \quad (3.25)$$

$$D^{\text{PFG}} = H_r \cdot D^\sigma \quad (3.26)$$

$$D^{\text{NMR}} = \frac{H_r}{f} \cdot D^\sigma \quad (3.27)$$

Note again, that here the self diffusion coefficient  $D^{\text{SD}}$  is written as  $D^{\text{NMR}}$  and  $D^{\text{PFG}}$  denotes the tracer diffusion coefficient  $D^{\text{T}}$  in order to refer to the methods through which the diffusion coefficients were determined.[72, 109]

**Magic angle spinning.** A common issue in solid-state NMR is limited resolution of the obtained spectra. Especially measurements of nuclei with strong nuclear magnetic dipolar interactions result in broad spectra. Other anisotropic interactions of nuclei like indirect electron coupling, electric quadrupolar interactions (when  $I > \frac{1}{2}$ ) or electron shielding contribute to broad lines in static solid-state NMR. A lot of information is lost due to the extended width of the detected signals compared to NMR observation in liquids. Magic angle spinning (MAS) is a widespread and well sophisticated technique to overcome broad lines in solid-state NMR and to obtain high resolution spectra. In MAS NMR measurements, the sample is rotated at a certain frequency ( $\omega_r$ ) about an axis which is tilted at an angle of  $54.74^\circ$  regarding to the applied magnetic field  $\mathbf{B}_0$  of the spectrometer; this is called the *magic angle*<sup>6</sup>. [110]

The idea behind applying this specific angle is, however, far from magic. Homo- or heteronuclear magnetic dipolar interactions are described by a Hamiltonian<sup>7</sup>  $\mathcal{H}_d$  of the following form:

$$\mathcal{H}_d = \sum_{i < j} \frac{1}{2} \gamma_i \gamma_j \hbar^2 r_{ij}^{-3} (\mathbf{I}_i \cdot \mathbf{I}_j - 3\mathbf{I}_{iz}\mathbf{I}_{jz}) (3\cos^2\theta_{ij} - 1) \quad (3.28)$$

The indices  $i$  and  $j$  denote a pair of nuclei with the gyromagnetic ratios  $\gamma_i$  and  $\gamma_j$ , the spin vectors  $\mathbf{I}_i$  and  $\mathbf{I}_j$  and the internuclear displacement  $\mathbf{r}_{ij}$ . The angle between  $\mathbf{B}_0$  and  $\mathbf{r}_{ij}$  is  $\theta_{ij}$ . In MAS NMR experiments the sample is rotated about an axis (r) inclined to  $\mathbf{B}_0$  at an angle  $\beta$  with a frequency  $\omega_r$ . (Figure 14) The rotation of the

<sup>6</sup>The term was introduced by Andrew, after he was asked about the *magic* properties of the angle they applied in their experiments.

<sup>7</sup>A Hamiltonian is the total energy of a system of particles as a function of location and momentum, if there are no time constraints.

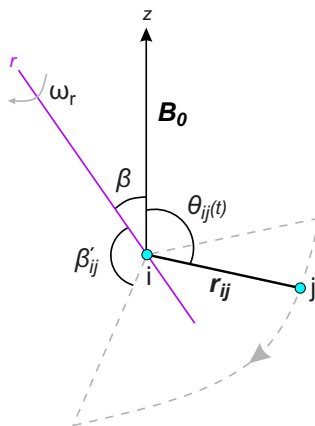


**Figure 14.** MAS NMR experimental setup - vector model and angles. The rotation axis  $r$  is shown in purple colour. The sample rotates about this axis with the rotation speed  $\omega_r$ . The axis is inclined to  $\mathbf{B}_0$  at an angle  $\beta$ ; the so-called *magic angle*. (inspired by [110])

sample about  $r$  leads to a time dependence of  $\theta_{ij}$  and reduces Eq. 3.28 by the factor  $F(\beta) = |\frac{1}{2}(3\cos^2\beta - 1)|$  as given by Eq. 3.29:

$$\overline{\mathcal{H}_d} = \frac{1}{2}(3\cos^2\beta - 1) \sum_{i < j} \frac{1}{2} \gamma_i \gamma_j \hbar^2 r_{ij}^{-3} (\mathbf{I}_i \cdot \mathbf{I}_j - 3\mathbf{I}_{iz}\mathbf{I}_{jz}) (3\cos^2\beta'_{ij} - 1) \quad (3.29)$$

If  $\beta$  is set to its *magic* value of  $54.74^\circ$ ,  $\theta_{ij}(t)$  takes positive and negative values, with an average of zero ( $\beta = \arccos \frac{1}{\sqrt{3}} = 54.74^\circ$ ,  $F(\beta) = 0$ ). If the sample is rotated about the  $z$ -axis ( $\beta = 0$ ) no reduction of the magnetic dipolar interaction would be observed, while if  $\beta = \frac{\pi}{2}$  the dipolar interactions are halved as  $F(\beta) = \frac{1}{2}$ .

The rotation speed  $\omega_r$  determines the side bands occurring in MAS spectra. The isotropic chemical shift is the main signal and it appears at the centre of the spectrum and does not change its position with the rotation speed. Side bands of the isotropic chemical shift are observed on both sides of the main signal. The distance of the side bands to the isotropic chemical shift signal is as large as  $\omega_r$ . Side bands can occur multiple times. To exclude any side bands,  $\omega_r$  has to take values 3 or 4 times larger than the anisotropy. A usual rotation speed is 25 kHz, but *e.g.* 60 kHz is achievable with standard NMR spectrometers that are equipped with a MAS probe head. For smaller nuclei usually little and less pronounced side bands are observed. As nuclei are getting bigger with a large number of associated electrons, side bands occur more frequently and appear larger.[111]

# 4 | Results

## Contents

---

|       |  |     |
|-------|--|-----|
| 4.1   | Electrode Materials for a Hybrid Solar Cell Battery System . . .                         | 53  |
| 4.1.1 | A New Solar Cell – Battery Hybrid Energy System . . .                                    | 54  |
| 4.1.2 | Magnetometric Observations on Sodium Vanadium Phosphate . . . . .                        | 70  |
| 4.2   | Ion Dynamics in Porous Materials . . . . .   | 77  |
| 4.2.1 | Introduction . . . . .   | 77  |
| 4.2.2 | Combining Ion Substitution and Nanoconfinement in Complex Hydrides . . . . .             | 79  |
| 4.2.3 | NMR Observations on Combined Ion Substituted and Nanoconfined Complex Hydrides . . . . . | 92  |
| 4.2.4 | Outlook on LiBH <sub>4</sub> /Oxide Composites . . . . .                                 | 108 |
| 4.2.5 | Hybrid Liquid-Solid Electrolytes Based on Metal-Organic Frameworks . . . . .             | 110 |

---

## 4.1. Electrode Materials for a Hybrid Solar Cell Battery System

As stated in the introductory part (chapter 1), the development of new battery technologies is vital. In the following, a sodium ion battery is presented, that proves its suitability in combination with an organic solar cell. This novel device combines the renewable energy conversion property of a solar cell with the efficient energy storage property of alkali-ion batteries. In this section the proof of principle of a new solar cell - battery hybrid energy system (4.1.1) will be described. The cathode material of the sodium ion battery of the hybrid device, *i.e.* sodium vanadium phosphate (NVP), will additionally serve as a model system for magnetometric observations on sodium intercalation compounds (4.1.2). For the first time magnetic susceptibility measurements were used to analyse the redox behaviour of sodium intercalation

compounds. Results of the mentioned research topics are shown in the form of a submitted manuscript (4.1.1) and a peer reviewed publication (4.1.2).

#### 4.1.1. A New Solar Cell – Battery Hybrid Energy System

The following study reports on the integration of a photo-rechargeable battery system composed of a solar cell and alkali-ion batteries. This setup enables simultaneous conversion of renewable energy and storage in efficient battery systems. One potential application of such a device is in portable electronics. Besides expected higher efficiency as well as increased stability and predictability of solar energy with its intermittent character, the limited number of parts leads to decreased complexity, enhanced safety and potentially lower production costs. The organic solar cell, in a tandem configuration, was composed of non-fullerene acceptors. In a hybrid device, the solar cell was combined with both a Li- and a Na-ion battery. A proof of concept included testing the device in a sealed case enabling also direct charge upon illumination. Prior to this, the individual systems were tested accordingly and compatibility tests showed satisfactory results. A carbonate based liquid electrolyte with  $\text{LiPF}_6$  showed excellent compatibility with the solar cell parts. As focus was laid on overall energy conversion and storage efficiency, battery materials were chosen in order to match the potential provided by the solar cell. Lithium vanadium phosphate (LVP) and vanadium disulfide ( $\text{VS}_2$ ) were the electrodes of choice in the Li-ion battery. In the sodium battery, sodium vanadium phosphate (NVP) and sodium titanium phosphate (NTP) were applied. After the final assembly of the hybrid device, the energy storage efficiency was as high as 40 %, while the overall efficiency of the device reached values up to 1.4 %.

## **A New Solar Cell – Battery Hybrid Energy System: Integrating Organic Photovoltaics with Li-Ion and Na-Ion Technologies**

Sebastian F. Hoefler, Roman Zettl, Daniel Knez, Georg Haberfehlner, Ferdinand Hofer, Thomas Rath, Gregor Trimmel, Martin Wilkening and Ilie Hanzu. *Sustain. Energ. Fuels*, **2020**  
*in peer review*

### **Author contributions**

S.H. fabricated the organic solar cells and performed the individual characterizations of the solar cells. R.Z. synthesized the electrode materials and performed the electrochemical characterizations of half cells and full cells. Electron microscopy characterizations were carried out by G.H. and D.K. The integrated system was assembled by S.H. and T.R. under protective atmosphere. S.H. and I.H. wrote the paper together with T.R., G.T. and R.Z. and the contribution of all authors. All authors participated in the discussions of the results in the frame of regular meetings within the project.

# A New Solar Cell – Battery Hybrid Energy System: Integrating Organic Photovoltaics with Li-Ion and Na-Ion Technologies

Sebastian F. Hoefler <sup>a,b</sup>, Roman Zettl <sup>a</sup>, Daniel Knez <sup>c,d</sup>, Georg Haberfehlner <sup>c</sup>, Ferdinand Hofer <sup>c</sup>, Thomas Rath <sup>a</sup>, Gregor Trimmel <sup>a,†</sup>, Martin Wilkening <sup>a,e</sup>, and Ilie Hanzu <sup>a,e,\*</sup>

Received 00th January 20xx,  
Accepted 00th January 20xx

DOI: 10.1039/x0xx00000x

**Abstract:** A solar energy conversion (organic tandem solar cell) and an electrochemical energy storage system (alkali metal ion battery) are designed and implemented in an integrated hybrid photo-rechargeable battery for simultaneous energy conversion and storage. As a proof of concept, the integrated power pack is successfully realized in a three-terminal hybrid assembly featuring two negative and a shared positive electrode. The device can be directly charged upon illumination (photo-charging) and discharged on the external load for many cycles. Aspects and requirements related to materials design, their specific properties and the encapsulation issues are presented and discussed. Data on compatibility of solar cell and battery materials is presented for the first time. We also report on the efficiency of the solar cell part, the battery part as well as the overall energy efficiency of the system. From the behaviour of this first-of-a-kind device, we were able to derive its relevant characteristics that can guide future work in this field.

## Introduction

Energy storage and conversion are intensely researched topics today. Li-ion batteries are already part of our everyday life – their performance is continuously improving.<sup>1</sup> Sustainable energy production from renewable resources, such as photovoltaic power generation, is undergoing major advances. For instance, one such notable breakthrough is the recent demonstration of tandem solar cells using non-fullerene acceptors that have an outstanding power conversion efficiency (PCE) of more than 17 %.<sup>2</sup> In many cases, when practical renewable energy systems are designed, i.e. for a household, there are at least two aspects that have to be implemented: i) an energy harvesting and conversion function and ii) an energy storage function.

A single device that can harvest solar energy, store it and then be able to release it on demand would present some practical advantages. As solar radiation tends to have an intermittent character, the hybrid device acts as an energy buffer.<sup>3</sup> Depending on the installed capacity, such a device can compensate unavoidable light flux variations. Then, thanks to its storage function, a hybrid device would also be able to dampen temporary peaks of high demand that exceed the power capability of the photovoltaic part alone. From Internet of Things (IoT) devices and small portable electronics, to medium- and large-scale systems, such characteristics could

increase stability and predictability of energy supply. Last, but not least, the reduced number of parts that such a system would feature has the potential of increasing the safety margins and reliability characteristics.

Combining the harvesting and storage functions in one simple hybrid device is indeed seducing and this crude idea was patented early on.<sup>4-6</sup> In spite of this disclosure, there was no commercial development and only very little academic research follow-up on this topic for the next 25 years or more.<sup>7,8</sup>

The renewed and fast growing interest in these topics during the past 5 years<sup>9-11</sup> appears to be catalysed by the advent of new and affordable nanotechnologies making the, otherwise complicated, preparation of functional structures relatively straightforward. For instance, in one report on hybrid devices, a nanowire-based dye-sensitized solar cell (DSSC) operating with an organic electrolyte was coupled to a supercapacitor operating with an aqueous electrolyte.<sup>12</sup> Only in the past three years, a plurality of hybrid combinations of photovoltaic devices of various types<sup>13</sup> (silicon,<sup>14</sup> DSSC,<sup>15,16</sup> perovskite solar cells<sup>17-19</sup> etc.) with Li-ion batteries,<sup>20-24</sup> Li-oxygen batteries<sup>25</sup> as well as various types of supercapacitors<sup>26-36</sup> or even simple capacitors<sup>37,38</sup> have been demonstrated at a proof of principle level. For instance, Paoletta et al. reported the light-assisted delithiation of the well-known LiFePO<sub>4</sub> positive electrode battery material.<sup>39</sup> Some other groups are revisiting the aqueous electrolytes for the pseudo-capacitive storage of energy.<sup>40</sup> Solar rechargeable redox flow batteries,<sup>41,42</sup> self-powered hybrid sensors<sup>43-45</sup> and electronics<sup>46</sup> have also been recently communicated. Additional properties and functionality are commonly reported and developed, for instance the mechanical flexibility of the hybrid energy conversion and storage device.<sup>47-49</sup> Some efforts are dedicated to the achievement of fibre and textile-based energy harvesting<sup>50</sup> and storage hybrid devices<sup>51,52</sup> that are wearable.<sup>53,54</sup>

The materials used for the realization of the hybrid devices include various forms of nanocarbons such as graphene and

<sup>a</sup> Institute for Chemistry and Technology of Materials, Graz University of Technology, Stremayrgasse 9, 8010 Graz, Austria.

<sup>b</sup> Infineon Technologies Austria AG, Siemensstraße 2, 9500 Villach, Austria

<sup>c</sup> Graz Centre for Electron Microscopy, Steyrergasse 17, 8010 Graz, Austria

<sup>d</sup> CNR-IOM, TASC Laboratory, Area Science Park, Basovizza, 34149, Trieste, Italy

<sup>e</sup> ALISTORE – European Research Institute, CNRS FR3104, Hub de l'Énergie, Rue Baudelocque, 80039 Amiens, France

\* Corresponding author: hanzu@tugraz.at

† See also for correspondence: gregor.trimmel@tugraz.at

Electronic Supplementary Information (ESI) available: [details of any supplementary information available should be included here]. See DOI: 10.1039/x0xx00000x

carbon nanotubes, a multitude of polymers and sensitizing dyes as well as various other composite oxide or polymer based fibres, films and nanomaterials. However, Li-ion storage materials have been chosen mostly in a rather conservative manner, the choice being limited to just a few, such as  $\text{TiO}_2$ ,  $\text{MnO}_2$ ,  $\text{LiCoO}_2$ ,  $\text{LiFePO}_4$  and metallic lithium. Significant improvements, however, need to be achieved to reach a reasonable technology readiness level which, in turn, requires new approaches and the incorporation of novel materials. For instance, in an audacious attempt, the use of materials for perovskite solar cells have been investigated for their lithium insertion properties<sup>55</sup> and, very recently, perovskite solar cells – battery hybrids have been demonstrated to function in the half-cell configuration.<sup>56</sup>

A common characteristic of the very recent literature on hybrid energy devices is in most cases its limitation to proof-of-concept demonstrators and very rarely more advanced functional details and practical design principles are provided. For instance, the compatibility of the photovoltaic materials with the battery materials is hardly discussed, in spite of the obvious importance of this aspect.<sup>57</sup> Moreover, there are many other questions related to the interplay of ionic and electronic transport phenomena in these complex devices – these are largely unaddressed. Thus, both, the design of new devices based on carefully selected functional materials as well as the understanding of their operation and their particularities within the complex environment of a hybrid device, are crucial milestones in the further development of a new generation of hybrid devices.

Hereby, we demonstrate a new organic tandem solar cell – battery hybrid configuration that can fulfill both the conversion and storage functions expected from such a hybrid device. In this current studies we focus on small devices for isolated sensor systems. Since we departed with a clean design, we first tested and discuss our solar cell and battery materials separately. Aspects related to the required materials properties are discussed from both a conceptual and practical point of view. While we initially focus on Li-ion storage solutions, we also address Na-ion cell configurations that may present some advantages. The hybrid cell assembly challenges are presented

and the solutions found are detailed. Finally, we evaluate the overall efficiency of the hereby reported hybrid energy device.

## Results and Discussion

### Concept and Initial Design Considerations

From a principle point of view, a hybrid device consists of a solar cell directly connected to an integrated rechargeable battery. Directly connecting a solar cell to a storage battery has been explored before, however only recently functional hybrid integrated devices were developed. This simple concept leads, however, to some practical requirements and significant restrictions on the materials used within the device. First, the voltage generated by the solar cell must match the voltage of the battery part so that charging of the battery is achieved. This translates into two opposite voltage requirements for the solar cell part and for the battery part. On the one hand, a high voltage solar cell is required. With the majority of single junction solar cells not significantly exceeding 1 V, the necessity of designing a relatively high voltage solar cell is obvious. Thus, we oriented towards tandem solar cells that are able to reach higher voltages (*vide infra*). On the other hand, a low voltage rechargeable battery would be required even when used with a tandem solar cell. Indeed, Li-ion batteries are typically charged to 3.6 - 4.2 V while even a high performance tandem solar cell will only reach 1.8 - 2.1 V at open circuit,<sup>58-61</sup> the voltage under load being lower. To this, we also have to add some ohmic drops and the over-potentials that develop during charging of the rechargeable cell – this would require an even lower battery voltage. A rough estimation leads to the conclusion that the voltage supplied by the solar cell has to be at least 0.2 V above the nominal battery voltage so that the battery can actually accept energy from the solar cell part. Thus, we looked for tandem solar cell configurations that reach 1.8 - 2.1 V and for battery materials that lead to a nominal voltage between 1.2 - 1.6 V.

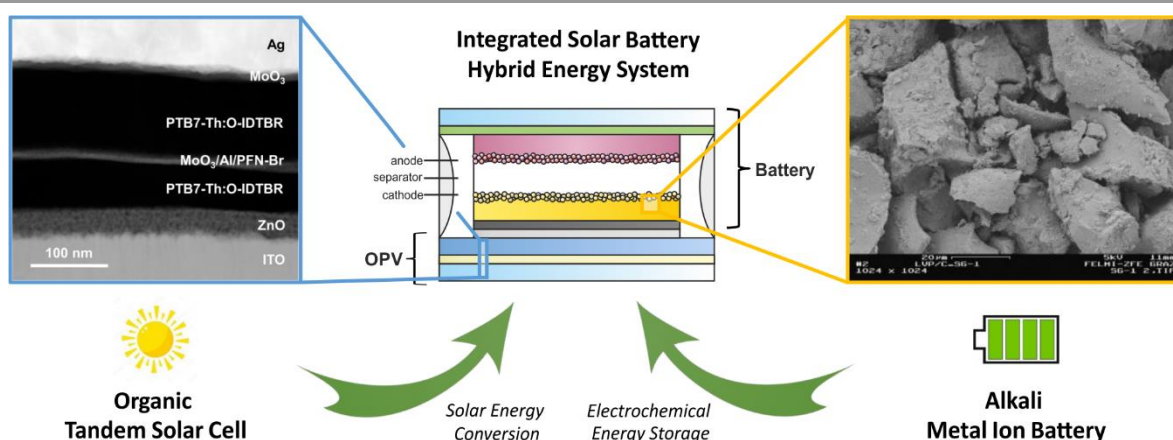


**Figure 1.** Synoptic representation of the hybrid energy conversion and storage system consisting of a non-fullerene organic homo-tandem solar cell (OPV) and an alkali metal ion battery. The insets show a STEM-HAADF image of a FIB-prepared lamella of the organic tandem solar cell (left) and a SEM image of the surface morphology of a LVP-C composite electrode (right).

It has to be noted that although such battery materials exist, very few of them were properly investigated and adequately characterized. Indeed, a battery with a high voltage anode and a low voltage cathode can only offer meagre energy densities due to the reduced cell voltage. Until very recently, such materials were perceived as scientific curiosities rather than serious battery materials. This view is currently changing under the impetus generated by the development of the Internet-of-Things (IoT) technologies – batteries required for such devices are fully acceptable even when supplying only a low voltage at the terminals<sup>62</sup> and thus having lower than usual energy densities is not an impediment at this point. For these applications, stability and long cycle life would be critical selection criteria. A conceptual representation of a parallel configuration hybrid device, as developed and investigated in this work is given in Figure 1.

### Materials Selection and Compatibility

**Non-Fullerene Organic Tandem Solar Cells.** In order to provide a high photo-voltage for charging the alkali metal ion battery within the integrated solar–battery hybrid energy device, non-fullerene organic homo-tandem solar cells were used as the photovoltaic system comprising of two blends of the low bandgap donor polymer PTB7-Th (poly[4,8-bis(5-(2-ethylhexyl)thiophen-2-yl)benzo[1,2-*b*;4,5-*b'*]dithiophene-2,6-diyl-*alt*-(4-(2-ethylhexyl)-3-fluorothieno[3,4-*b*]thiophene-)-2-carboxylate-2,6-diyl)) and the non-fullerene acceptor O-IDTBR (((5Z,5'Z)-5,5'-(((4,4,9,9-tetraoctyl-4,9-dihydro-*s*-indaceno[1,2-*b*:5,6-*b'*]dithiophene-2,7-diyl)bis(benzo[*c*][1,2,5]thiadiazole-7,4-diyl))bis-(methanylylidene))bis(3-ethyl-2-thioxothiazolidin-4-one))) which are serially connected via a MoO<sub>3</sub>/Al/PFN-Br (poly[(9,9-bis(3'-(*N,N*-dimethyl)-*N*-ethylammonium)-propyl)-2,7-fluorene)-*alt*-2,7-(9,9-dioctylfluorene)] dibromide) recombination layer.<sup>59, 63</sup> This material combination was selected since it provides some favourable material properties and characteristics in terms of recombination dynamics and charge carrier mobility, and exhibit a good performance and high open-circuit voltage ( $V_{OC}$ ) values in organic solar cells, as reported in the literature.<sup>59, 63–65</sup> Tandem solar cells were fabricated in inverted architecture consisting of glass/ITO (indium tin oxide, ca. 130–140 nm)/ZnO (ca. 30–40 nm)/PTB7-Th:O-IDTBR (ca. 70 nm)/MoO<sub>3</sub> (8 nm)/Al (3 nm)/PFN-Br (< 5 nm)/PTB7-Th:O-IDTBR (ca. 120 nm)/MoO<sub>3</sub> (10 nm)/Ag (100 nm), as shown in Figure S1 of ESI. Current density–voltage ( $J$ – $V$ ) characteristics of tandem solar cells are depicted in Figure 2 and compared to single-junction solar cells, while the photovoltaic performance parameters are summarized in Table S1. The open-circuit voltage ( $V_{OC}$ ) of the organic tandem solar cells with an active area of 9 mm<sup>2</sup> (square, 3 mm × 3 mm) of 1.92 V is almost equal to the sum of the individual subcells, showing only a small voltage loss of about 60 mV, which

corresponds to a loss of about 3% according to Kirchhoff's law for series-connected tandem solar cells. Due to not fully optimized layer thicknesses and the homo-tandem approach, lower short-circuit current density ( $J_{SC}$ ) values of 6.6 mA cm<sup>-2</sup> were obtained compared to the single-junction solar cells, which limits the PCE (power conversion efficiency) to 6.79% (max. 7.01%).

However, the electrode area of the organic tandem solar cells has to be increased in order to match the area of the photovoltaic device and the battery. Therefore, the geometry was changed from small, square electrodes (9 mm<sup>2</sup>) to larger, circular electrodes (10 mm diameter, 79 mm<sup>2</sup>) with dimensions slightly larger than the used circular battery electrodes with a diameter of 7.9 mm. The efficiency of the large-area organic tandem solar cells decreased considerably from 6.79 ± 0.15% to 5.19 ± 0.32%, which is mainly due to reduced  $J_{SC}$  and fill factor (FF) values; however, the  $V_{OC}$  values remain almost the same. The decrease of the FF values can be explained by the slightly S-shaped characteristics of the  $J$ – $V$  curves under illumination, along with a higher series resistance  $R_S$  (137 Ω cm<sup>2</sup> vs. 59 Ω cm<sup>2</sup>) and a lower shunt resistance  $R_{SH}$  (2.26 kΩ cm<sup>2</sup> vs. 2.65 kΩ cm<sup>2</sup>). In addition, the unbalanced photocurrent generation in both subcells might cause charge carrier accumulation in the subcells, which increases recombination losses and therefore reduces FF values.<sup>61, 66</sup> Nevertheless, the results show that even with this large electrode area, high  $V_{OC}$  values and reasonable PCE values of over 5% can be obtained. This proves the viability of this photovoltaic system for the implementation of the integrated hybrid energy system.<sup>61, 66</sup>

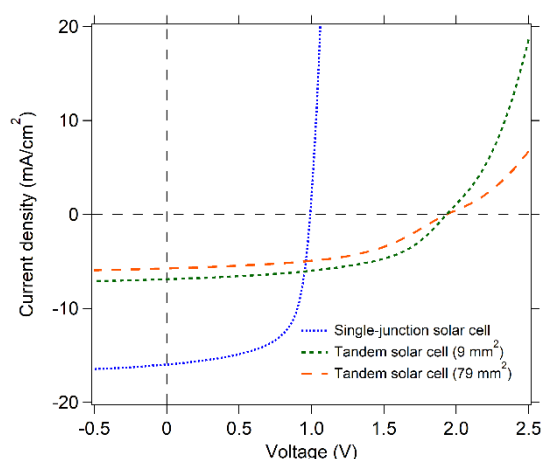


**Figure 2.**  $J$ – $V$  curves of PTB7-Th:O-IDTBR single-junction and tandem solar cells with different electrode area under illumination.

**Li-Ion and Na-Ion Batteries.** Since the charging voltage of the battery system within the integrated hybrid energy device is limited by the photo-voltage of the organic tandem solar cell (about 1.9 V), the battery voltage needs to be matched to the output voltage of the solar cell. For this purpose, a battery

system that can be fully charged at a relatively low voltage was developed. This was obviously accomplished by the combination of two battery electrode materials with a low potential difference, giving a low charging voltage of up to ca. 1.6 V. For the lithium-ion battery, we selected carbon-coated lithium vanadium phosphate ( $\text{Li}_3\text{V}_2(\text{PO}_4)_3$ , LVP-C) for the positive electrode (cathode) and vanadium disulfide ( $\text{VS}_2$ ) for the negative electrode (anode), respectively. For the sodium-ion battery, we used carbon-coated sodium vanadium phosphate ( $\text{Na}_3\text{V}_2(\text{PO}_4)_3$ , NVP-C, cathode) and sodium titanium phosphate ( $\text{NaTi}_2(\text{PO}_4)_3$ , NTP-C, anode). The materials were synthesised according to the literature using either a sol-gel method or hydrothermal method for  $\text{VS}_2$ .<sup>67</sup> (see Experimental section). Results on the structural, morphological, and electrochemical characterisations of the battery electrode materials are provided in detail in the ESI (see Figures S2–S6). Plots of charge-discharge curves of a typical Cu |  $\text{VS}_2$  | LP30 | LVP-C | Al full cell and its cycling behaviour are presented in Figure 3 a) and b), respectively. This cell configuration presents a mostly sloped charge-discharge characteristic curve, *i.e.* there is a clearly visible and exploitable correspondence between the voltage of the battery and its state of charge. This can be traced to the sloped potential response of the  $\text{VS}_2$  negative active material that is obviously superimposed on the well-defined potential plateaus of the LVP-C positive active material (ESI, Figure S5), resulting in an overall sloped voltage response of the battery during cycling. While this feature is obviously leading to a lower energy density, there are also advantages in this particular case. As any photovoltaic cell will undergo aging and degradation during normal operation, the supplied voltage is expected to decrease with the number of cycles. In such conditions, a sloped charge curve would be an obvious benefit since the minimum voltage required for the start of charge would be low and the system would still be able to function even at reduced supplied voltages, of course, with a reduction in capacity. We also found such a system useful for initial development purposes. Indeed, it is sometimes very difficult to estimate from the beginning if the photovoltaic materials are compatible with the battery materials. As a result, the voltage supplied is lower than in the ideal case. Being able to choose lower cut-off voltages is a useful feature that enabled us to achieve a working device while allowing a direct glimpse into the overall device stability. The cycling stability of the low voltage Li-ion battery was found to be satisfactory (Figure 3 b)). While the initial capacity is lower, it was found that the capacity increased during the first 15 cycles. This can probably be explained by the slow wetting of the porous electrode when brought into contact with the electrolyte. This is actually supported by the very good coulombic efficiency recorded in the first 15 cycles. Had degradation been present at this stage, it would have had lowered the coulombic efficiency values. Nevertheless, we would like to highlight the importance of electrolyte wetting characteristics of the active layers, which would have to be considered for any future developments.

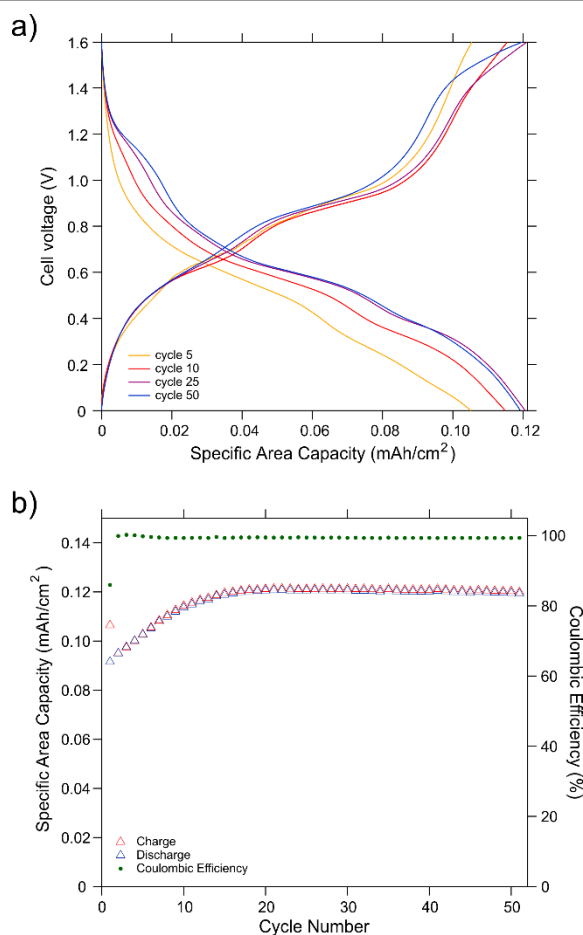


**Figure 3.** a) Charge-discharge curves of the Li-ion low voltage full cell Cu |  $\text{VS}_2$  | LP30 | LVP-C | Al showing a fairly sloped characteristic. This kind of discharge curve is expected to benefit a system in which the charge voltage will also depend on the state-of-charge of the hybrid device – such a battery would still be able to partially charge even at reduced voltage b) Cycle life of the Cu |  $\text{VS}_2$  | LP30 | LVP-C | Al low voltage cell at a current density of  $0.11 \text{ mA cm}^{-2}$ . The initial capacity increase can be ascribed to a less than optimal initial wetting of the electrodes (see text for further explanation).

The Na-ion battery that we selected can be conventionally represented as Cu | NTP-C | NaFSI in EC:DEC 4:6 | NVP-C | Al. While the overall areal capacities are slightly higher than for the Li-ion system, this battery features a different charge-discharge characteristic curve (Figure 4). In this case, we see some clearly defined voltage plateaus around 1.2 V in discharge and 1.3 V in charge. These voltage plateaus are inherent to the electrochemical behaviour of materials used (see Figure S6 for additional information about the working potentials with respect to a reference electrode). This voltage plateau characteristic would require a solar cell to supply a minimum of 1.4–1.5V in order to charge the battery, a lower voltage being insufficient to achieve any charging of the Na-ion battery. While this is clearly a disadvantage during development (see above), the existence of a plateau would result in a much more predictable battery voltage during operation, while also the energy density (*i.e.* effectively the area under the graph in Figure 4 a)) is considerably improved. In addition, a constant voltage supply would be a benefit for the design of any small device powered by such a hybrid device – the electronics would

be simpler. While the coulombic efficiency (Figure 4 b)) is very good, we see some capacity decay during cycling. However, for the current demonstration of the hybrid device the cycle life is more than sufficient and we decided to use the system without further optimization.

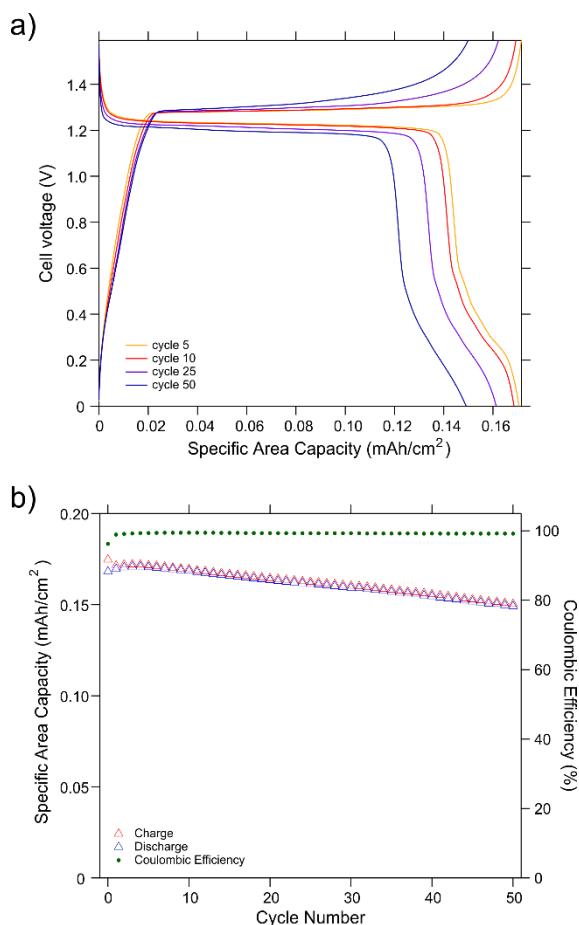


**Figure 4.** a) Charge-discharge curves of the Na-ion low voltage full cell Cu | NTP-C | NaFSI in EC:DEC 4:6 | NVP-C | Al showing a plateau characteristic. While this kind of curve requires the photovoltaic system to supply a minimum voltage, it maximizes the energy stored and the voltage supplied is fairly constant. b) Cycle life of the Cu | NTP-C | NaFSI in EC:DEC 4:6 | NVP-C | Al low voltage cell at a current density of  $0.12 \text{ mA cm}^{-2}$ .

**Compatibility of Solar Cell and Battery Materials.** Since the solar cell and battery are sharing the same enclosure, there are important chemical and/or electrochemical materials compatibility questions that require evaluation. On the one hand, since the solar cells that we used are generally very thin and contain no or a very low amount of solvents, we can consider that the solar cell materials do not have the potential of significantly affecting the functioning of the battery. On the other hand, the battery contains a significant quantity of liquid electrolyte that may actually have an impact of the functioning of the solar cell. Thus, we focussed our attention on investigating the chemical compatibility of the tandem solar cell, in particular the active layers, with the liquid electrolyte used in the battery part of the hybrid device. This is important since non-fullerene acceptors typically show a good solubility in common organic solvent which limits the usability of the liquid electrolyte, especially upon long-term contact. For example, the

liquid organic electrolyte Selectilyte LP 30 (used for lithium-ion based hybrid devices) shows a good compatibility with PTB7-Th and O-IDTBR without any dissolution or swelling effects of both compounds upon direct contact, and macroscopically no changes of the silver electrode (e.g. corrosion) were observed. Moreover, the electrolyte does not considerably deteriorate the photovoltaic performance of the non-fullerene organic solar cells (see Figure S7, ESI), implying an adequate material compatibility between the photovoltaic system and the liquid electrolyte of the lithium-ion battery.

A detailed description on the material compatibility including main hurdles and issues as well as electrochemical aspects and principal design considerations are provided in the Electronic Supplementary Information.

### Integrated Solar Cell-Battery Hybrid Energy System

The photo-rechargeable battery was fabricated by the combination of a photovoltaic system and a battery system in a single electronic component. This power pack consists of an organic homo-tandem solar cell (based on PTB7-Th as donor and O-IDTBR as acceptor, see above) connected in parallel with the alkali metal ion battery. The battery components (e.g. electrodes, separators, current collectors) are stacked layer-by-layer onto the already fabricated organic tandem solar cell in an inert atmosphere using a thin conductive carbon paper-type gas diffusion layer (SIGRACET® GDL 28 BC) used here as conductive interlayer to avoid direct contact between the Ag top contact of the solar cell and the aluminium current collector of the positive electrode of the battery (assembling), followed by the encapsulation to provide an air- and moisture-tight packaging and to improve the mechanical stability of the power pack (Figure S10, S11). In order to be able to evaluate separately the two parts (solar cell and battery), we draw two separate connections from both negative electrodes of the solar cell and the battery. The result is a three-terminal hybrid assembly with two separate negative electrodes and a common positive electrode. A schematic representation of the cross-section and a photographic image of the fully assembled hybrid energy device are shown Figure 5. We have to note from the beginning that the operation regimes of the battery and photovoltaic part are quite different from the operation envelope used in practice. For instance, a commercial battery is usually charged according to a constant current – constant voltage protocol (CC–CV), while a photovoltaic cell would be preferably operated close to its maximum power point. The internal resistance of a battery would increase non-linearly with increasing the state of charge. Thus, a fully discharged battery may absorb a higher power and thus take a higher current when charging than an almost fully charged battery. The solar cell also shows a non-linear characteristic  $J$ – $V$  curve (see Figure 2). At high loads, it will tend to deliver an almost constant current, while at lower loads, the current and voltage will show a pronounced non-linear response. Consequently, when a battery and photovoltaic cell are directly connected, one can expect a more complex current and voltage characteristic resulting from the convoluted behaviour of the two sub-systems of the device.

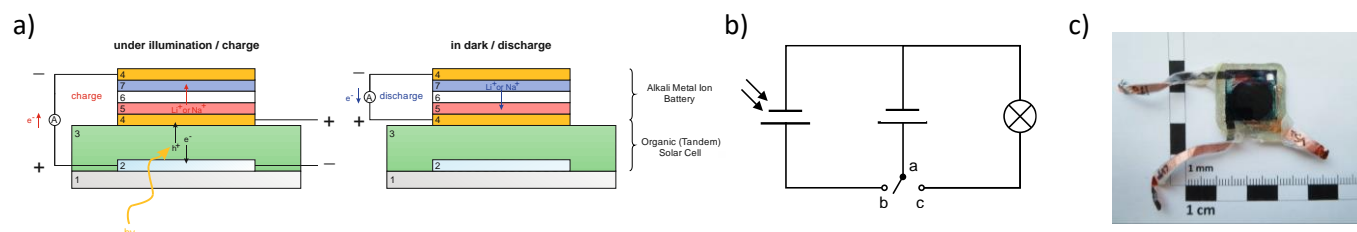


**Figure 5.** a) Schematic representation of the working mechanism of the integrated hybrid photo-rechargeable battery under illumination/charge and in dark/discharge (without packaging): (1) substrate, (2) transparent, conductive electrode, (3) organic tandem solar cell, (4) conductive interlayer, (5) positive electrode, (6) separator soaked with liquid electrolyte, and (7) negative electrode. b) Electrical circuit during charging (illumination, a-b) and discharging (dark, a-c), and c) photographic image of the integrated hybrid energy system in the three-terminal assembly.

The working mechanism of this integrated hybrid energy system is schematically shown in Figure 5 a). In principle, the photo-rechargeable battery is directly charged upon illumination of the organic tandem solar cell and discharged on the external load. In order to charge the solar battery, an over-voltage needs to be applied, which should be accomplished by the photo-voltage provided by the organic tandem solar cell. Upon illumination of the photovoltaic device, electrostatically bound electron-hole pairs (excitons) are created within the photo-active layer, which are separated at the donor/acceptor interface by the electric field. The photo-generated electrons and holes are transported to the negative and positive electrode of the solar cell, respectively. The over-voltage provided by the organic tandem solar cell forces electrons from the photovoltaic device to move, via the external circuit, to the negative electrode of the battery, concomitant with the movement of alkali metal ions via the electrolyte to the negative electrode (charging). Under dark conditions, the battery can be discharged on the external load and alkali metal ions move via the electrolyte from the negative to the positive electrode, whereas electrons move via the external circuit to the positive electrode. In dark, the photovoltaic device would ideally behave like a diode biased in the blocking direction.

**Voltage and Current Characteristics.** Typical battery voltage and solar cell current characteristics are shown in Figure 6 a) for the previously presented Li-based systems and b) for the Na-based system. While the battery part of the hybrid device was charged by directly connecting it to the illuminated solar cell, the discharging of the battery was carried out in dark at a constant current of 50  $\mu\text{A}$  for each of the two systems and with the photovoltaic cell disconnected from the battery. This was done to avoid any discharge of the battery through the solar cell that may allow the passage of a small leakage current in the dark.

For both Li- and Na-based systems the current and voltage increase immediately under illumination. In both cases, we see the voltage tendency to stabilize after the initial very steep

increase and reach a region with a significantly smaller slope corresponding to charging of the battery. As expected, we see that the slope of the charge curve of the Li-system is somewhat larger than the slope of the charge curve of the Na-system. This is also apparent on the constant current discharge part that follows the charge: the discharge curve of the Li-system has a much more pronounced slope, while the Na-system shows a sloped plateau at the beginning of discharge. Another difference between the lithium and the sodium system are the ohmic drops. Following a sudden drop in voltage when switching from photo-charging to constant-current discharge, we record approximately 0.4 V voltage drop for the Li-system and only 0.2 V for the Na-system. These first results suggest the Na-system being more suitable to this application than a functionally equivalent Li-system.

The current response of the hybrid device under illumination (Figure 6 a) and b)) shows similarities for the Li- and Na-system. With the cell fully discharged, the current spikes to approximately 1 mA upon illumination and then it decays exponentially as the battery charges. Please note that we do not see a region of an almost constant current at the beginning of charge, as it would be the case if the solar cell delivered power onto a low impedance load, such as a battery at low state-of-charge. We conclude that, at all times, the internal resistance of the battery is higher than the internal resistance of the solar cell. Had the internal resistance of the battery been very low at the beginning, we should have seen an almost constant current response in accordance to the  $J$ - $V$  curve of the solar cell (see Figure 2). Indeed, since the integrated battery device has not been optimized, we see higher ohmic drops recorded for both integrated Li and Na systems, when compared with separately tested batteries.

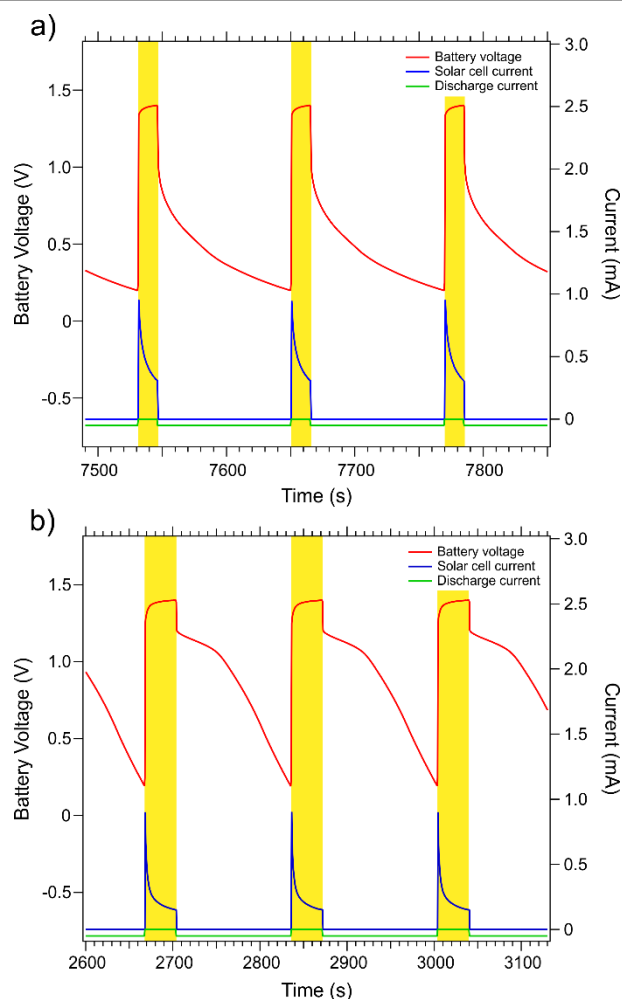


**Figure 6.** Typical voltage and current characteristic response of the a) Li-based hybrid device and b) Na-based hybrid device. The charging of the battery part is carried out under illumination, symbolized by the yellow vertical stripes, with the solar cell part directly connected to the battery. The discharge is carried out in dark with the solar cell disconnected and at a constant current of 50  $\mu\text{A}$ . The set voltage limits were 1.4 V for the end of charge and 0.2 V for the end of discharge with a surface area of the battery of 0.49  $\text{cm}^2$ .

**Capacity and Coulombic Efficiency.** The useful capacity of an electrochemical storage device is also known to be dependent on the cycling rate at which the battery is operated – the faster the cycling, the lower the capacity. The direct integration and connection of the generating solar cell with the low voltage storage battery lead to a system that charges at a variable rate (*vide supra*). While the charging rate is very high at the beginning (approx. 1 mA for both systems), it is still high at the end of the charge (0.15 mA and 0.30 mA for the Li- and Na-system respectively). Thus, a charge process takes only 15 s in the case of Li-system and 36 s in the case of Na-system. In these conditions, we can only reach relatively low capacities as shown in Figure 7 a) and b) for most of the cycles. We found that setting an upper voltage limit for the end of charge is not fully satisfactory and it leads to the device cycling either too fast, in case the limit is low, or, too slow, in case the limit is high. The exact voltage limit was difficult to establish in practice also

because both the solar cell and the battery part will undergo some slow ageing under illumination.

The decrease of the photo-current (or charging current) provided by the solar cell over time (e.g. from above 1 mA to approximately 400  $\mu\text{A}$  (see Fig. S12), indicates a degradation of the photovoltaic device. Such a decay of the solar cell current (or performance) is commonly observed in organic solar cells, for example, as an initial exponential decay (known as burn-in degradation) or over longer periods due to photo- or temperature-induced degradation effects.<sup>68, 69</sup> While IDTBR-based non-fullerene organic solar cells have been reported to show a burn-in free behavior,<sup>68, 69</sup> interface effects or morphological changes within the active layer due to light-induced phenomena are expected to reduce the photo-current generation as well as the solar cell performance and stability. More details on the device stability are provided in the ESI. The lower photo-currents lead to longer charging times of the solar battery, corresponding to lower charging rates (albeit still exceeding 1 C, on average, see below), and result in an apparent increase of the capacity, Coulombic efficiency and battery energy efficiency (Figure 7). The drop of the photo-current values (as seen in Fig. S12 b, d, f, h) explains the considerable increase of the Coulombic efficiency and battery energy efficiency thanks to the lower effective charging rates.

Ageing and degradation will also increase the time required to reach the end-of-charge voltage values, a situation that is clearly illustrated in Fig. S13. For instance in the case of Na-system we see (Fig. S13 b)) that under identical illumination conditions, after about 35 cycles, it takes longer and longer to reach the set 1.4 V limit while the battery is still adsorbing a certain current. This will have the effect of lowering the charging rate resulting in charging the battery to a higher capacity with every successive cycle as shown in Figure 7 d). In approximately 1 hour of photo-charging a value of 65  $\mu\text{Ah cm}^{-2}$  can be reached, a value that approaches half of the nominal 150  $\mu\text{Ah cm}^{-2}$  achieved in a test cell. Considering that the battery integrated in the hybrid device has not been optimized for small internal resistance and that, at least at the beginning, the charging rate is significantly higher than in the nominal test battery, this result is highly encouraging. When we lowered the end-of-charge voltage limit to 1.37 V (see Figure 7 d) ), the useful capacities returned to low values corresponding to fast charging rates, as explained above.

It has to be noted that the voltage limit is in this case an experimental shortcoming that should have no relevance in a practical hybrid device. Indeed, in such a device the battery and solar cell are always connected with no external separate leads – albeit an additional low opening voltage diode, e.g. a Schottky diode, would be required to prevent battery discharge through the photovoltaic device in the dark. As long as the voltage of the solar cell matches reasonably (*i.e.* slightly exceeds) the battery voltage, the device can be left under illumination with no risk of battery overcharge as the charging current will naturally decrease to a trickle when the battery is approaching the fully charged state. This operation mode is similar to the voltage floating in which a constant voltage is continuously applied to a charged battery in stand-by.

Indeed, we found that it is actually possible to abandon the voltage limit and rely for instance on a, much simpler to implement, time limitation. This would actually translate in a capacity limitation but it has the advantage of being immune to unavoidable variations and scatter of the voltage value at the terminals of the device. For instance, by setting a charge time limitation of 10 minutes we can achieve much higher capacities as illustrated in Figure S14.

The fast charging rates that were generally used are also affecting the efficiency of energy storage. We can see in Figure 7 that the coulombic efficiency of the battery is only about 80 % when charging is done at very fast rates. The coulombic efficiency increases as soon as the charging rate is lowered to approximately 1 to 2 C on average, and decreases again when the charging rate is increased again, a situation clearly illustrated in Figure 7 e). High ohmic drops and fast charging rates are the most likely cause for the low coulombic efficiency. While the coulombic efficiency is low, we note its relative stability upon cycling as well as the good correlation with the recorded capacity values. Practically, we see very little degradation and then only in the first cycles. Thus, the low but relatively stable coulombic efficiency values are an expression of the inherent fast charging rates used rather than the degradation of the battery sub-system.

In addition, at the current hybrid device characteristics, assuming a required average current of 1  $\mu\text{A}$ , as would be the case for state-of-the-art MEMS motion and pressure sensors, a light exposure of 10 minutes would be sufficient to power the sensor for roughly 35-38 hours. As the device was not optimized, this result is highly encouraging and proves the viability of this hybrid device concept.

**Energy Efficiency.** The energy efficiency is by definition the ratio between the useful energy and the consumed energy. In our case, to evaluate the overall efficiency of the hybrid device we have to consider the ratio between the useful energy delivered by the hybrid device and the incident light energy that reached the device. Since the hybrid device contains both a conversion part and a storage part, having very different characteristics, we believe it is useful to differentiate between these two parts and discuss also partial energy efficiencies of the two sub-systems before evaluating the overall device energy efficiency.

Thus, the *power conversion efficiency* (PCE or  $\eta_{\text{conversion}}$ ) of the photovoltaic device is defined as the ratio of the maximum power output of the solar cell ( $P_{\text{max}}$ ) divided by the average incident solar irradiance ( $P_{\text{in}}$ ). The power output is given by the product of the voltage ( $V_{\text{mpp}}$ ) and current density ( $J_{\text{mpp}}$ ) at the maximum power point (mpp), and can be represented as:

$$\eta_{\text{conversion}} = \frac{P_{\text{max}}}{P_{\text{in}}} = \frac{V_{\text{mpp}} \times J_{\text{mpp}}}{P_{\text{in}}} = \frac{V_{\text{OC}} \times J_{\text{SC}} \times \text{FF}}{P_{\text{in}}}$$

(Eq. 1)

where  $V_{\text{OC}}$  is the open-circuit voltage,  $J_{\text{SC}}$  is the short-circuit current density, and FF is the fill factor. The *energy storage efficiency* ( $\eta_{\text{storage}}$ ) of the energy storage unit relates the energy

output of the battery system during discharging ( $E_{\text{Batt.}}^{\text{discharge}}$ ) with the energy input, *i.e.* the energy consumed to charge the battery ( $E_{\text{Batt.}}^{\text{charge}}$ )

$$\eta_{\text{storage}} = \frac{E_{\text{Batt.}}^{\text{discharge}}}{E_{\text{Batt.}}^{\text{charge}}} = \frac{\int_0^{Q_{\text{discharge}}} U \cdot dQ}{\int_0^{Q_{\text{charge}}} U \cdot dQ}$$

(Eq. 2)

where  $U$  and  $Q$  are the battery voltage and the battery capacity, respectively.<sup>15, 17, 28</sup> The overall (solar-energy-conversion-and-storage) *energy efficiency* ( $\eta_{\text{overall}}$ ) of the hybrid energy system can be calculated by multiplying the conversion efficiency ( $\eta_{\text{conversion}}$ ) of the photovoltaic system and energy storage efficiency ( $\eta_{\text{storage}}$ ) of the battery unit.

$$\eta_{\text{overall}} = \eta_{\text{conversion}} \times \eta_{\text{storage}}$$

(Eq. 3)

While this mathematical implementation neglects the losses due to ohmic drops on the electrical connections between solar cell and the battery, we found it fully satisfactory as the contact resistance between the two sub-systems was very low.

Alternately, the overall energy efficiency can be defined as the ratio of the electrical energy delivered by the integrated hybrid energy system, which corresponds to the energy output of the battery during discharge ( $E_{\text{Batt.}}^{\text{discharge}}$ ), and the incident solar energy ( $E_{\text{in}}$ ), as follows:

$$\eta_{\text{overall}} = \frac{E_{\text{Batt.}}^{\text{discharge}}}{E_{\text{in}}} = \frac{\int_0^{Q_{\text{discharge}}} U \cdot dQ}{P_{\text{in}} \times t_{\text{charge}} \times A_{\text{PV}}}$$

(Eq. 4)

where  $U$  is the battery voltage,  $t_{\text{charge}}$  is the illumination time during photo-charging, and  $A_{\text{PV}}$  is the effective surface area of the photovoltaic device.<sup>8, 14, 15</sup> However, this expression is not always given in its integral form and many of the already reported energy efficiencies are actually rather crude approximations for instance when only average voltage is considered<sup>20</sup> or when only the upper and lower voltage limits are taken into account,<sup>15</sup> thus completely neglecting the practical discharge curve which is, in most of the cases, far from linear.

The above expression has the advantage of leading to the most accurate results since it can also adjust for the variations in energy conversion efficiency for solar cells not operating at their maximum power point. More often than not, this is a situation that occurs in practice. As we can easily see from the current and voltage characteristics of the hybrid device in charge, the hybrid device is almost never operating with the solar cell at its maximum power point (see Figure 6). Thus, the efficiency given by Eq. 3 should be considered as the highest practically achievable value from which there can be significant deviations of the efficiency as a function of the operation envelope. Various effects such as burn-in (see above) and inherent shifts

in operation point of the solar cell due to charging of the battery would result in actually lower values that can better and more accurately be accounted for by using Eq. 4.

In practice, we found that it would be useful to determine and report the partial energy efficiencies of the two sub-systems as this offers a quick overview on the practical efficiency bottlenecks within the hybrid device. The energy storage efficiency for the two storage systems considered (Li-ion and Na-ion) are shown in Figure 7 b) and e). We can see that the energy storage efficiency correlates well with the coulombic efficiency. As expected for very fast cycling, we see relatively low values in both cases. However, in spite of the harsh charging regime, the energy efficiency values are fairly stable, an indication of a relatively good behaviour of the battery part.

The overall efficiency determined using Eq. 4 is shown in Figure 7 c) and f). This represents the efficiency with which the solar radiation is converted to electric energy, chemically stored in the battery and then re-converted to electrical energy during the discharge of the battery. As we can see, the overall efficiency depends on the higher voltage limit set for the charge of the battery, the lower the voltage limit the higher the overall efficiency. This can be understood by noting that in these conditions the solar cell operates closer to its maximum power point where it has the best energy conversion efficiency - when the voltage limit is set low then relatively high current would flow, albeit for a short while during the photo-charging of the battery. On the other hand, a higher voltage setting would lead to a lower current on average thus reducing the overall efficiency because of reduced effective energy conversion efficiency in the solar cell. We can in fact see that the longer the charging time and the higher the capacity (see Figure S13 and Figure 7 a) and d), respectively) the lower the overall efficiency as seen in Figure 7 c) and f). For the Li-based hybrid device we measured an overall efficiency ranging between 0.6 and 1.4 % while for the Na-based hybrid device the overall efficiency values are between 0.1 and 0.6 %. However, for most of the testing the efficiency stays within a narrower range, between 1 – 1.4 % in the lithium case and between 0.4 – 0.6 % in the sodium case.

At a first glance, these values appear rather small. However, when we compare them with the maximum achievable efficiency for this system, they look in fact very reasonable. To estimate the maximum achievable efficiency we have to consider the efficiency of energy transfer between the sub-systems and to the load. For this, we can start by considering the maximum power transfer theorem, well known in electrical engineering, which states that in order to achieve the maximum power transfer from a source to a load, the internal resistance of the load must equal the internal resistance of the power source. It follows, that for any power source at maximum power transfer, only half of the energy is received by the load, the other half being dissipated on the internal resistance of the power source (and thus not useful). If the resistance of the load is lower than the internal resistance of the power source, then the energy transfer efficiency is lower than 50%, more is dissipated on the internal resistance than on the load. In the case of a solar cell operating at the maximum power point

(where the PCE is achieved), the maximum power is also transferred when the internal resistance of the solar cell equals the resistance of the load. Also in this case, the energy transfer efficiency is 50%. One could of course use a load having a higher resistance, and in this case, the energy transfer efficiency will increase – on a high resistance load, the energy transfer efficiency would even approach 100%. Obviously, on high resistance loads, the electrical current is smaller. Thus much of the incident light flux energy is actually lost, as the device delivers energy at low power, much lower than the maximum power point of the solar cell. While light is harvested, most of the electrons and holes generated will recombine when only low currents are drawn. Thus, even with the cell operating at the maximum power point, only half of the energy converted (the conversion ratio being the PCE) is actually transferred to the load. Therefore, we can conclude that, under illumination, the light-to-load energy conversion and transfer efficiency can reach a maximum of half of the PCE value. In our hybrid device, we also have losses in the battery, its energy storage efficiency is less than 50 % due to fast cycling, so the overall efficiency is actually expected to be lower.

In our studied hybrid systems, we have a photovoltaic cell with a 5% PCE. Assuming that solar cell operates at the maximum achievable energy conversion efficiency (which is the PCE at maximum power point) then the energy transfer efficiency is 50%. This will result in a 2.5 % light-to-solar-cell-output, where, in our case we have the battery. In practice, we achieved an overall efficiency (light-to-external-load, but passing through an additional integrated storage battery sub-system) mostly between 1 - 1.4 % for the lithium variant and between 0.4 – 0.6 % for the sodium variant. In conclusion, when measured efficiencies are compared with what is maximum achievable, we see that we already have an efficient device. With these materials, the efficiency can only be improved further by a maximum of 2-3 times for the lithium system and 4-6 times for the sodium system.

While overall efficiencies of hybrid devices are not always reported<sup>22, 46, 70</sup>, it is not unusual to have very low overall conversion and storage efficiencies. For instance, overall efficiencies between 0.02 – 0.08 %<sup>12, 39, 56</sup> are common, especially for proof-of-principle hybrid device concepts. Our new device having typical overall energy efficiencies between 0.4 – 1.6 %, compares well with other planar hybrid devices where values between 1-3 %<sup>28, 30, 31</sup> are reported. The highest value reported so far (11.5 %<sup>16</sup>) corresponds to a more complex type of hybrid device based on a dye-sensitized solar cell. However, this overall efficiency value is questionable as the determination method leads to systematically overestimated values. It must not be overlooked that only a method based on a precise integration protocol, as we and many other groups<sup>15, 19, 36</sup> have implemented, would deliver true and accurate overall energy efficiency values. Any other methods are estimations and not direct determinations.

Thus, in order for a hybrid device to function close to its best efficiency we can identify additional operation conditions and new design rules. First, it is mandatory that the impedance of the battery part matches the solar cell part – this will allow the

solar cell to harvest energy close to its maximum power point where it is most efficient. While this characteristic can be achieved with current battery materials operating with liquid electrolytes, it will be far more challenging for cells with solid electrolytes due to their current lower power capability. Second, as the battery is charged, the internal resistance of the battery will inherently increase, the current will drop and the solar cell functioning point will depart significantly from the maximum power point. This means that, in the current hybrid device configuration, it would be significantly more efficient to operate it at only a fraction of its storage capacity – completely

charging the battery will result in a much lower energy efficiency. Based on efficiency considerations alone, it would be better to have active materials with a high power capability and flat discharge plateaus. For instance, manganese spinels would fulfil these criteria and are likely to be further developed for such applications. Indeed, a battery with flat charge/discharge voltage plateau would result in a relatively constant internal resistance and, when the voltage and impedance are matched with that of the solar cell would lead to the most efficient operation.

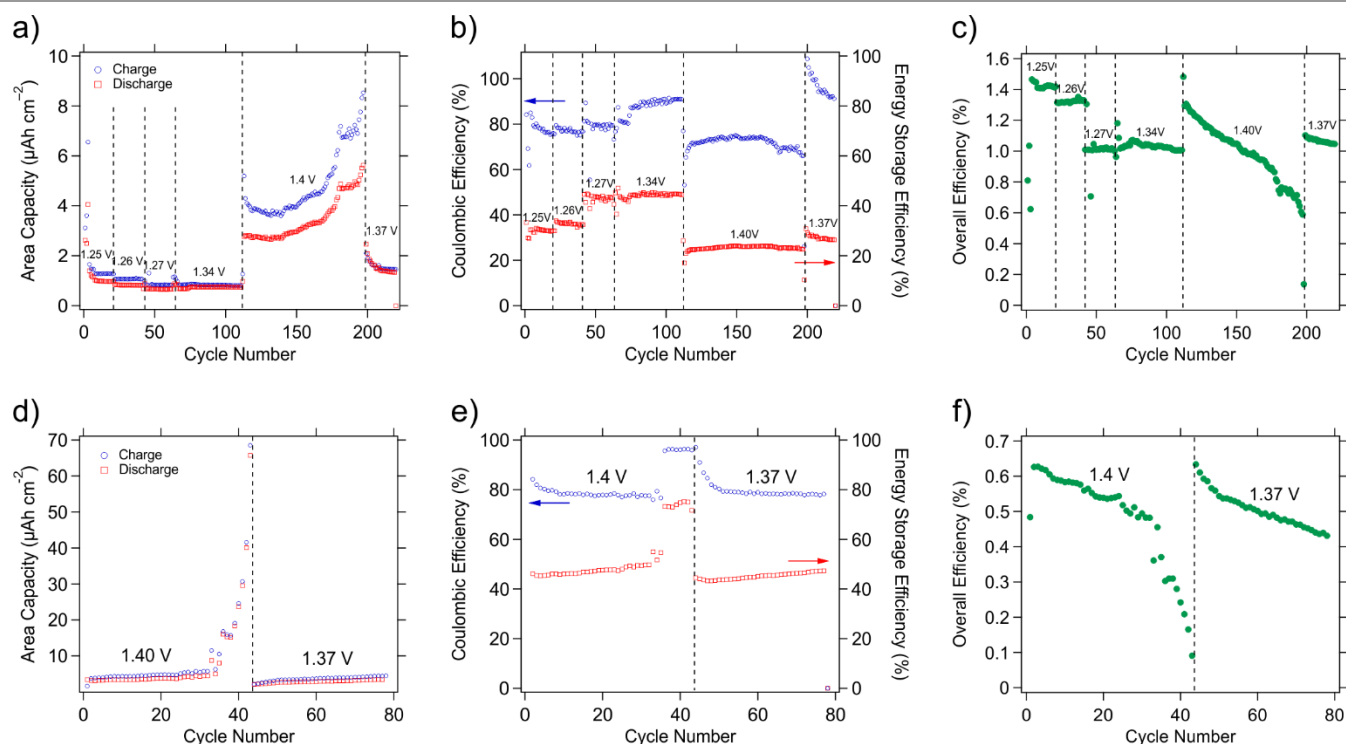


**Figure 7.** Specific area capacity of the hybrid device for the a) Li-based system d) Na-based system. The numerical values on the graphs represent the high cut-off voltage limit. The lower limit was always 0.2 V. There are significant differences in terms of stability and behaviour between the Li and Na based systems, see text for further information. Coulombic efficiency and energy storage efficiency of the battery part of the b) Li-based hybrid device and e) Na-based hybrid device. Overall efficiency of the c) Li-based hybrid device and f) Na-based hybrid device. The efficiencies were determined in accordance with Eq. 4 and represent the overall energy-conversion-and-storage efficiency.

## Conclusions

In this report we demonstrate a first-of-its-kind hybrid energy device integrating a non-fullerene organic tandem photovoltaic cell with either a lithium or a sodium ion battery. Photovoltaic cells having a sufficiently large area were successfully developed and tested. Battery materials with matched electrochemical potentials were prepared and tested in both half-cell and full-cell configurations. We investigated the compatibility of the solar cell materials with common battery materials that may interfere, such as the liquid electrolyte. We found a good compatibility between the usual liquid carbonate-based lithium and sodium electrolytes with little influence of the liquid electrolytes on the photovoltaic cell performance. Finally, we were able to develop a successful encapsulation method. The hybrid devices are able to charge very fast (under 1 minute), albeit with reduced capacity. Higher capacities are

achieved whenever the illumination time is extended with a reduction of the overall efficiency. Our first results indicate a better performance of the sodium-based device, most likely due to the lower ohmic drops that were achieved in this device. Nevertheless, it is very plausible that with some optimisation the lithium system would out-perform the sodium one. Also, because of some degradation of the photovoltaic device under illumination, we found the usual voltage limit set to signal the end-of-charge is difficult to use in practice when testing the hybrid device. Instead, a time limitation would be a much simpler and better practice. We accurately determined the efficiencies by an integration method. Under very fast charging conditions, we can achieve an energy storage efficiency in the order of 40% and an overall efficiency between 0.1 % and 1.4 %, depending on the operation point of the hybrid device. These values are only few times smaller than the theoretical efficiency estimated for these hybrid systems and represent a good and

encouraging starting point for any future development of organic photovoltaics – battery hybrids.

## Experimental

### Non-Fullerene Organic Tandem Solar Cells

**Tandem Solar Cell Fabrication.** Pre-patterned ITO-coated glass substrates were cleaned by sonication in 2-propanol (60 min, 40–50 °C) and oxygen plasma treatment (3 min, FEMTO, Diener electronics). ZnO thin films (ca. 30–40 nm) were derived from a sol-gel reaction of a zinc oxide precursor solution,<sup>71</sup> which was spin-coated (4000 rpm, 30 s) and annealed under ambient atmosphere (15 min, 150 °C). For the front subcell, PTB7-Th was dissolved in *ortho*-dichlorobenzene at 70 °C (10 mg mL<sup>-1</sup>), blended with O-IDTBR in a donor:acceptor ratio of 1:1.5 by weight (total concentration: 25 mg mL<sup>-1</sup>), and spin-coated to achieve layer thicknesses of about 70 nm. The recombination layer was deposited by thermal evaporation of MoO<sub>3</sub> (8 nm, deposition rate: ca. 0.1–0.2 Å s<sup>-1</sup>) and Al (3 nm, ca. 0.5–1.0 Å s<sup>-1</sup>), followed by spin coating of PFN-Br (< 5 nm) from a solution in methanol (0.5 mg mL<sup>-1</sup>, filtrated through a 0.45 µm polytetrafluoroethylene (PTFE) syringe filter). For the rear subcell, a PTB7-Th:O-IDTBR blend solution in chlorobenzene was prepared with a donor:acceptor ratio of 1:1.5 by weight (total concentration: 22.5 mg mL<sup>-1</sup>) as described above, and spin-coated to give a layer thickness of approx. 120 nm. A MoO<sub>3</sub> anode interfacial layer (10 nm, ca. 0.2 Å s<sup>-1</sup>) and an Ag anode (100 nm, 0.1–1.0 Å s<sup>-1</sup>) were deposited by thermal evaporation under reduced pressure (ca. 10<sup>-5</sup> mbar) using a shadow mask with square (3 × 3 mm) or circular (10 mm diameter) configuration to define the active area (9 mm<sup>2</sup> or 79 mm<sup>2</sup>).

**Solar Cell Characterization.** *J*-*V* curves were recorded under illuminated and dark conditions in inert atmosphere using a Keithley 2400 source meter, and a Dedolight DLH400D metal halide lamp (1000 W m<sup>-2</sup>, similar to AM 1.5G), which was calibrated with a standard reference silicon solar cell (Fraunhofer ISE). Photovoltaic performance parameters were averaged over five individual devices. *R*<sub>S</sub> and *R*<sub>SH</sub> values were extracted from the *J*-*V* curves under illumination.

### Li-Ion and Na-Ion Batteries

**Lithium Vanadium Phosphate ( Li<sub>3</sub>V<sub>2</sub>(PO<sub>4</sub>)<sub>3</sub> ).** Carbon-coated LVP (LVP-C) was synthesized according to a sol-gel route.<sup>72</sup> Citric acid (Sigma-Aldrich) and ammonium metavanadate (NH<sub>4</sub>VO<sub>3</sub>, Sigma-Aldrich) were separately dissolved in deionized water, mixed together in a beaker and the reaction mixture was slowly heated to 60 °C. During heating the solution changed its color from orange to green, to dark green and finally to black. Ammonium di-hydrogen phosphate (LiH<sub>2</sub>PO<sub>4</sub>, Sigma-Aldrich), dissolved in deionized water was slowly added (in approx. 1 h) through a dropping funnel at 60 °C. After heating up to 80 °C, which led to another color change of the solution to dark blue, the mixture was transferred into a wider beaker to accelerate

the evaporation of water. The reaction mass temperature was controlled with a temperature sensor during the whole procedure. The obtained gel (color changed again to green) was placed to an oven in air at 80 °C to dry overnight. The dry gel product was ground in a mortar and it was heat treated in a quartz tube in a tubular oven under Ar atmosphere by heating at 4°C/min and then held at 720 °C for 8h. Afterwards, the obtained LVP was ground again in a mortar and the final product was obtained. Although pure LVP should be pale green, the obtained sample was black due to the carbon that it purposely contained.

**Vanadium Disulfide ( VS<sub>2</sub> ).** A hydrothermal synthesis route was used for VS<sub>2</sub>.<sup>73</sup> Sodium orthovanadate (Na<sub>3</sub>VO<sub>4</sub>), thioacetamide (C<sub>2</sub>H<sub>5</sub>NS) in excess and 175 mL of distilled water were added to a Teflon beaker suited for a 250 mL autoclave for a hydrothermal synthesis. The solution was stirred for 1 h and the colour of the solution appeared green. The autoclave was closed and heated to 160 °C with a rate of 2 °C min<sup>-1</sup> and held for 24 h. Black needle-like VS<sub>2</sub> sheets were obtained and the VS<sub>2</sub> layered structure was confirmed by XRD (see Fig. S2). The liquid was removed by centrifugation for 2 min and 2400 rpm. The product was washed several times with deionized water and dried overnight under air at 80 °C.

**Sodium Vanadium Phosphate ( Na<sub>3</sub>V<sub>2</sub>(PO<sub>4</sub>)<sub>3</sub> ).** Carbon-coated NVP (NVP-C) was synthesized in the same way as LVP-C through a sol-gel synthesis route<sup>72</sup> with the lithium source being replaced by the sodium source. Citric acid (at a molar ratio of citric acid to vanadium ions 1:1) as gel-forming agent and NH<sub>4</sub>VO<sub>3</sub> were separately dissolved in deionized water and added in a beaker. The reaction mixture was slowly heated to 60 °C. During heating the solution changed its colour from orange to green, to dark green and finally to black. NaH<sub>2</sub>PO<sub>4</sub> in stoichiometric amounts (dissolved in deionized water) was added through a dropping funnel (for approx. 1 h) at 60 °C. The solution was heated to 80 °C to evaporate the water. The gel-forming reaction temperature was controlled with a temperature sensor during the whole procedure. After the gel was formed (colour changed again to green), it was dried overnight at 80 °C under ambient atmosphere. The gel was ground in a mortar and then heat-treated (700 °C, 8 h, heat up at 4 °C min<sup>-1</sup>, Ar atmosphere). After thermal treatment the material was ground again in a mortar and the final black product was used without further modifications.

**Sodium Titanium Phosphate ( NaTi<sub>2</sub>(PO<sub>4</sub>)<sub>3</sub> ).** Carbon-coated NTP (NTP-C) was prepared according to a sol-gel route.<sup>74</sup> 8.448 mL (24.8 mmol) titanium butoxide were added to a mixture of 50 mL H<sub>2</sub>O<sub>2</sub> (30 %) and 20 mL NH<sub>3</sub> (30 %) in 1 mL steps in a beaker under stirring. The solution turned yellow. 9.528 g (49.5 mmol) citric acid were added to the solution. 4.274 g (37.2 mmol) NH<sub>4</sub>H<sub>2</sub>(PO<sub>4</sub>) were dissolved in 20 mL deionized water and 1.772 g of Na<sub>2</sub>CO<sub>3</sub> were dissolved in 15 mL HNO<sub>3</sub> (60%). Both solutions were added to the butoxide solution. When adding the NaNO<sub>3</sub>, heat was generated and the solution turned orange. Afterwards, 2.77 mL (49.5 mmol) ethylene glycol were added; the resulting mixture was heated to 80°C and kept at this temperature for two hours under stirring. The resulting orange gel was put in the oven at 140°C for two hours and then at 350°C

for three hours under air. Both steps led to an enormous volume expansion of the gel resulting in a threefold volume expansion. The obtained black powder was annealed at 800 °C under argon atmosphere. The resulting black powder was ground in an agate mortar and used for the preparation of the slurries without further modifications.

**Electrode preparation.** All the electrodes were prepared by the slurry cast method. The components were mixed together by ball milling (Fritsch, Pulverisette 7 Premium Line) at 400 rpm, four times 15 min each. The slurry contained the active material (80% wt.), a conductive material (Super C65, 10% wt.) and a binding material (Kynar 761, 10% wt.). Additionally, a solvent for the binder (1-Methyl-2-Pyrrolidinone (NMP)) was incorporated until a suitable slurry was obtained. The positive materials slurries were cast on aluminum foil (50 μm thick, Goodfellow), which serves as current collector. The aluminum foil was first etched for 20 s in 5 % KOH solution at 40 °C to remove the oxide layer and any rests from Al-foil manufacturing by rolling. For the negative electrodes a battery-grade electrodeposition-roughened Cu-foil (20 μm, Schlenk) was used for the current collector. Using a doctor blade with a gap of 100 μm the slurry was cast onto the foils with a velocity of 5 mm/s. The foil with the active layer was dried overnight under air in an oven at 60 °C. The active material mass loads were approximately 1.5–2 mg cm<sup>-2</sup>. The next step was to cut the disk electrodes and continue with another drying step at 60 °C in a Büchi drying system first under Ar atmosphere and then under vacuum (10<sup>-3</sup> mbar). The electrodes were weighed after this step to determine the mass of active material per electrode. Finally, one last drying step again in a Büchi drying system at 60 °C and under high vacuum (1.4 × 10<sup>-6</sup> mbar) was carried out and afterwards the samples were transferred into an Ar- or N<sub>2</sub>-filled glove box without any further exposure to ambient atmosphere. The final thicknesses of the active layers were 37–55 μm.

### Material Characterization

**Surface Profilometry.** Layer thicknesses were determined using a DektakXT stylus profiling system (Bruker) equipped with a 12.5 μm-radius stylus tip. Line scans were recorded over a length of 1000 μm, with a stylus force of 3 mg, and a resolution of 0.33 μm pt<sup>-1</sup>. Layer thickness values were derived from surface profiles using the Vision 64 software (Bruker).

**Scanning Electron Microscopy (SEM) and Scanning Transmission Electron Microscopy (STEM).** A cross-section of the organic homo-tandem solar cells was prepared using a slope-cutter (for SEM), and the FIB technique performed on an FEI Nova 200 FIB/SEM dual-beam system (for STEM). A platinum protection layer was deposited on the photovoltaic device prior to the FIB preparation of the cross-section. STEM images were taken on an FEI Titan 60-300 at an acceleration voltage of 300 kV equipped with a HAADF detector. SEM images of the battery electrode materials were acquired on a Zeiss Ultra55 SEM at an acceleration voltage of 3 kV equipped with an in-lens secondary electron detector.

**X-Ray Diffraction (XRD).** X-ray diffraction was routinely carried out on the as-prepared battery materials in order to identify the phases formed and check for any crystalline foreign phase major contamination. A Bruker D8 Advance diffractometer operating with Bragg Brentano geometry and CuKα radiation (1.5406 Å) was used.

**Electrode characterization.** Dried electrode disks (10 mm in diameter) were assembled in three-electrode Swagelok-type cells. Lithium or sodium were used as reference electrodes in both half-cells and full cells. A disk of GF/B glass microfiber Whatman paper was used as the separator. The electrolyte used for lithium cells was a commercial Selectilyte LP 30 (BASF) consisting of a mixture of ethylene carbonate (EC):dimethyl carbonate (DMC) 1:1 with 1 M lithium hexafluorophosphate (LiPF<sub>6</sub>). For sodium cells, a solution of 1 M sodium bis(fluorosulfonyl)imide (NaFSI) in ethylene carbonate (EC):diethyl carbonate (DEC) (4:6, v/v) was used as electrolyte. MPG2 and VPM3 multichannel potentiostat/galvanostats from Bio-Logic were used to carry out the electrochemical measurements.

### Integrated Solar Cell-Battery Hybrid Energy System

**Assembling and Electrochemical Characterization.** The integrated photo-rechargeable battery was assembled and sealed in a nitrogen-filled glovebox by directly placing the Al-supported carbon-coated LVP (LVP-C) cathode (7.9 mm diameter) onto the organic tandem solar cell (with a thin carbon paper-type gas diffusion layer (SIGRACET® GDL 28 BC, Ion Power)), followed by glass microfiber separators (8 mm diam., Whatman GF/B) soaked with the Selectilyte LP 30 electrolyte and the Cu-supported VS<sub>2</sub> anode (7.9 mm diameter). In analogy to the lithium-ion battery, NVP-C and NTP-C were used as cathode and anode material for the sodium-ion battery using a 1 M sodium bis(fluorosulfonyl)imide (NaFSI) in ethylene carbonate (EC):diethyl carbonate (DEC) (4:6, v/v) as the electrolyte. The solar cell-battery hybrid assembly was encapsulated with an O-ring and a two-component epoxy resin. The electrical contacts required for measuring the performance were provided by copper/nickel stripes mounted to the electrodes of the hybrid device with a conductive epoxy resin prior to the assembling procedure. For the electrochemical characterization, the photo-rechargeable battery was illuminated with a white-light LED with an intensity of approx. 750 W m<sup>-2</sup>, and the battery voltage (within the potential limits of 0.2 V and 1.4 V) as well as the charging/discharging current were monitored over time using a Keithley 2400 source meter. The hybrid energy system was galvanostatically discharged with a fixed discharge current of 50 μA. Photo-charging measurements were performed with a time limitation of 5 min, followed by galvanostatic discharging sequences (50 μA discharge current). The specific area capacity was extracted from the current profiles over time considering the electrode area (0.49 cm<sup>2</sup>).

## Conflicts of interest

There are no conflicts to declare.

## Acknowledgements

This work was carried out within the project “SolaBat – Solar cell meets battery – Realization of a hybrid energy system” funded by the Austrian “Climate and Energy Fund” within the program Energy Emission Austria (FFG No. 853 627). The authors thank Lukas Troi and Kathrin Fellner for experimental support.

## References

1. G. E. Blomgren, *Journal of The Electrochemical Society*, 2017, **164**, A5019-A5025.
2. L. Meng, Y. Zhang, X. Wan, C. Li, X. Zhang, Y. Wang, X. Ke, Z. Xiao, L. Ding, R. Xia, H.-L. Yip, Y. Cao and Y. Chen, *Science*, 2018, **361**, 1094.
3. V. Vega-Garita, L. Ramirez-Elizondo, N. Narayan and P. Bauer, *Progress in Photovoltaics: Research and Applications*, 2019, **27**, 346-370.
4. M. Ezawa, A. Misumi, K. Suzuki and M. Kumada, 1984, US Pat. 4481265 A.
5. R. G. Little, 1988, US Pat. 4740431 A.
6. T. Uda, K. Miyauchi, E. Maruyama, T. Shimada and Y. Murayama, 1983, EP 0108492 A0108492.
7. G. Dennler, S. Bereznev, D. Fichou, K. Holl, D. Ilic, R. Koeppel, M. Krebs, A. Labouret, C. Lungenschmied, A. Marchenko, D. Meissner, E. Mellikov, J. Méot, A. Meyer, T. Meyer, H. Neugebauer, A. Öpik, N. S. Sariciftci, S. Taillemite and T. Wöhrlé, *Solar Energy*, 2007, **81**, 947-957.
8. T. L. Gibson and N. A. Kelly, *Journal of Power Sources*, 2010, **195**, 3928-3932.
9. A. Gurung and Q. Qiao, *Joule*, 2018, **2**, 1217-1230.
10. R. Liu, Y. Liu, H. Zou, T. Song and B. Sun, *Nano Research*, 2017, **10**, 1545-1559.
11. B. Luo, D. Ye and L. Wang, *Adv Sci (Weinh)*, 2017, **4**, 1700104.
12. J. Bae, Y. J. Park, M. Lee, S. N. Cha, Y. J. Choi, C. S. Lee, J. M. Kim and Z. L. Wang, *Adv Mater*, 2011, **23**, 3446-3449.
13. H. Liu, M. Li, R. B. Kaner, S. Chen and Q. Pei, *ACS Appl Mater Interfaces*, 2018, **10**, 15609-15615.
14. H.-D. Um, K.-H. Choi, I. Hwang, S.-H. Kim, K. Seo and S.-Y. Lee, *Energy & Environmental Science*, 2017, **10**, 931-940.
15. X. Chen, H. Sun, Z. Yang, G. Guan, Z. Zhang, L. Qiu and H. Peng, *J. Mater. Chem. A*, 2014, **2**, 1897-1902.
16. B.-M. Kim, M.-H. Lee, V. S. Dilimon, J. S. Kim, J. S. Nam, Y.-G. Cho, H. K. Noh, D.-H. Roh, T.-H. Kwon and H.-K. Song, *Energy & Environmental Science*, 2020, DOI: 10.1039/C9EE03245B.
17. J. Xu, Y. Chen and L. Dai, *Nat Commun*, 2015, **6**, 8103.
18. S. Yun, Y. Qin, A. R. Uhl, N. Vlachopoulos, M. Yin, D. Li, X. Han and A. Hagfeldt, *Energy & Environmental Science*, 2018, **11**, 476-526.
19. G.-M. Weng, J. Kong, H. Wang, C. Karpovich, J. Lipton, F. Antonio, Z. S. Fishman, H. Wang, W. Yuan and A. D. Taylor, *Energy Storage Materials*, 2020, **24**, 557-564.
20. S. N. Agbo, T. Merdzhanova, S. Yu, H. Tempel, H. Kungl, R.-A. Eichel, U. Rau and O. Astakhov, *physica status solidi (a)*, 2016, **213**, 1926-1931.
21. W. Guo, X. Xue, S. Wang, C. Lin and Z. L. Wang, *Nano Lett*, 2012, **12**, 2520-2523.
22. V. Chakrapani, F. Rusli, M. A. Filler and P. A. Kohl, *Journal of Power Sources*, 2012, **216**, 84-88.
23. T. Kim, W. Song, D.-Y. Son, L. K. Ono and Y. Qi, *Journal of Materials Chemistry A*, 2019, **7**, 2942-2964.
24. A. Gurung, K. Chen, R. Khan, S. S. Abdulkarim, G. Varnekar, R. Pathak, R. Naderi and Q. Qiao, *Advanced Energy Materials*, 2017, **7**, 1602105.
25. M. Yu, X. Ren, L. Ma and Y. Wu, *Nat Commun*, 2014, **5**, 5111.
26. X. Wang, B. Liu, R. Liu, Q. Wang, X. Hou, D. Chen, R. Wang and G. Shen, *Angew Chem Int Ed Engl*, 2014, **53**, 1849-1853.
27. X. B. Xu, S. H. Li, H. Zhang, Y. Shen, S. M. Zakeeruddin, M. Graetzel, Y. B. Cheng and M. K. Wang, *Acs Nano*, 2015, **9**, 1782-1787.
28. T. Chen, L. Qiu, Z. Yang, Z. Cai, J. Ren, H. Li, H. Lin, X. Sun and H. Peng, *Angew Chem Int Ed Engl*, 2012, **51**, 11977-11980.
29. T. Chen, Z. Yang and H. Peng, *Chemphyschem*, 2013, **14**, 1777-1782.
30. C. T. Chien, P. Hiralal, D. Y. Wang, I. S. Huang, C. C. Chen, C. W. Chen and G. A. Amaratunga, *Small*, 2015, **11**, 2929-2937.
31. B. P. Lechêne, M. Cowell, A. Pierre, J. W. Evans, P. K. Wright and A. C. Arias, *Nano Energy*, 2016, **26**, 631-640.
32. J. Liang, G. Zhu, Z. Lu, P. Zhao, C. Wang, Y. Ma, Z. Xu, Y. Wang, Y. Hu, L. Ma, T. Chen, Z. Tie, J. Liu and Z. Jin, *Journal of Materials Chemistry A*, 2018, **6**, 2047-2052.
33. A. Takshi, H. Yaghoubi, T. Tevi and S. Bakhshi, *Journal of Power Sources*, 2015, **275**, 621-626.
34. A. S. Westover, K. Share, R. Carter, A. P. Cohn, L. Oakes and C. L. Pint, *Applied Physics Letters*, 2014, **104**, 213905.
35. Z. Yang, L. Li, Y. Luo, R. He, L. Qiu, H. Lin and H. Peng, *J. Mater. Chem. A*, 2013, **1**, 954-958.
36. C. Li, S. Cong, Z. Tian, Y. Song, L. Yu, C. Lu, Y. Shao, J. Li, G. Zou, M. H. Rummeli, S. Dou, J. Sun and Z. Liu, *Nano Energy*, 2019, **60**, 247-256.
37. X. Huang, X. Zhang and H. Jiang, *J Power Sources*, 2014, **248**.
38. X. Zhang, X. Huang, C. Li and H. Jiang, *Adv Mater*, 2013, **25**, 4093-4096.
39. A. Paolella, C. Faure, G. Bertoni, S. Marras, A. Guerfi, A. Darwiche, P. Hovington, B. Commarieu, Z. Wang, M. Prato, M. Colombo, S. Monaco, W. Zhu, Z. Feng, A. Vijh, C. George, G. P. Demopoulos, M. Armand and K. Zaghbi, *Nat Commun*, 2017, **8**, 14643.
40. F. Podjaski, J. Kroger and B. V. Lotsch, *Adv Mater*, 2018, **30**.
41. P. Liu, Y. L. Cao, G. R. Li, X. P. Gao, X. P. Ai and H. X. Yang, *ChemSusChem*, 2013, **6**, 802-806.
42. W. Li, H. C. Fu, L. Li, M. Caban-Acevedo, J. H. He and S. Jin, *Angew Chem Int Ed Engl*, 2016, **55**, 13104-13108.
43. K. L. Agrawal and M. Shtein, *Nanoscale*, 2014, **6**, 11019-11023.

44. X. Hou, B. Liu, X. Wang, Z. Wang, Q. Wang, D. Chen and G. Shen, *Nanoscale*, 2013, **5**, 7831-7837.
45. J. Xu and G. Shen, *Nano Energy*, 2015, **13**, 131-139.
46. P. Du, X. Hu, C. Yi, H. C. Liu, P. Liu, H.-L. Zhang and X. Gong, *Advanced Functional Materials*, 2015, DOI: 10.1002/adfm.201500335, DOI: 10.1002/adfm.201500335.
47. X. Wang, X. Lu, B. Liu, D. Chen, Y. Tong and G. Shen, *Adv Mater*, 2014, **26**, 4763-4782.
48. X. Wang, K. Jiang and G. Shen, *Materials Today*, 2015, **18**, 265-272.
49. X. Wang and G. Shi, *Energy & Environmental Science*, 2015, **8**, 790-823.
50. M. Peng, B. Dong and D. Zou, *Journal of Energy Chemistry*, 2018, **27**, 611-621.
51. Y. Fu, H. Wu, S. Ye, X. Cai, X. Yu, S. Hou, H. Kafafy and D. Zou, *Energy & Environmental Science*, 2013, **6**, 805.
52. Z. Zhang, X. Chen, P. Chen, G. Guan, L. Qiu, H. Lin, Z. Yang, W. Bai, Y. Luo and H. Peng, *Adv Mater*, 2014, **26**, 466-470.
53. X. Pu, W. Hu and Z. L. Wang, *Small*, 2018, **14**.
54. T. Song and B. Sun, *ChemSusChem*, 2013, **6**, 408-410.
55. N. Vicente and G. Garcia-Belmonte, *J Phys Chem Lett*, 2017, **8**, 1371-1374.
56. S. Ahmad, C. George, D. J. Beesley, J. J. Baumberg and M. De Volder, *Nano Lett*, 2018, **18**, 1856-1862.
57. G. Bouteau, A. N. Van-Nhien, M. Sliwa, N. Sergent, J. C. Lepretre, G. Gachot, I. Sagaidak and F. Sauvage, *Sci Rep*, 2019, **9**, 135.
58. W. Liu, S. Li, J. Huang, S. Yang, J. Chen, L. Zuo, M. Shi, X. Zhan, C.-Z. Li and H. Chen, *Advanced Materials*, 2016, **28**, 9729-9734.
59. S. F. Hoefler, G. Haberehner, T. Rath, R. Canteri, M. Barozzi, F. Hofer and G. Trimmel, *Advanced Materials Interfaces*, **0**, 1901053.
60. Y. Cui, H. Yao, B. Gao, Y. Qin, S. Zhang, B. Yang, C. He, B. Xu and J. Hou, *Journal of the American Chemical Society*, 2017, **139**, 7302-7309.
61. S. Chen, G. Zhang, J. Liu, H. Yao, J. Zhang, T. Ma, Z. Li and H. Yan, *Advanced Materials*, 2017, **29**, 1604231.
62. J. Sather, in *Enabling the Internet of Things: From Integrated Circuits to Integrated Systems*, ed. M. Alioto, Springer International Publishing, Cham, 2017, DOI: 10.1007/978-3-319-51482-6\_15, pp. 409-440.
63. S. F. Hoefler, T. Rath, N. Pastukhova, E. Pavlica, D. Scheunemann, S. Wilken, B. Kunert, R. Resel, M. Hobisch, S. Xiao, G. Bratina and G. Trimmel, *Journal of Materials Chemistry A*, 2018, **6**, 9506-9516.
64. S. Zhang, L. Ye, W. Zhao, D. Liu, H. Yao and J. Hou, *Macromolecules*, 2014, **47**, 4653-4659.
65. S. Holliday, R. S. Ashraf, A. Wadsworth, D. Baran, S. A. Yousaf, C. B. Nielsen, C.-H. Tan, S. D. Dimitrov, Z. Shang, N. Gasparini, M. Alamoudi, F. Laquai, C. J. Brabec, A. Salleo, J. R. Durrant and I. McCulloch, *Nature Communications*, 2016, **7**, 11585.
66. J. A. Bartelt, D. Lam, T. M. Burke, S. M. Sweetnam and M. D. McGehee, *Advanced Energy Materials*, 2015, **5**, 1500577.
67. C. S. Rout, B. H. Kim, X. Xu, J. Yang, H. Y. Jeong, D. Odkhuu, N. Park, J. Cho and H. S. Shin, *J Am Chem Soc*, 2013, **135**, 8720-8725.
68. N. Gasparini, M. Salvador, S. Strohm, T. Heumueller, I. Levchuk, A. Wadsworth, J. H. Bannock, J. C. de Mello, H.-J. Egelhaaf, D. Baran, I. McCulloch and C. J. Brabec, *Advanced Energy Materials*, 2017, **7**, 1700770.
69. H. Cha, J. Wu, A. Wadsworth, J. Nagitta, S. Limbu, S. Pont, Z. Li, J. Searle, M. F. Wyatt, D. Baran, J.-S. Kim, I. McCulloch and J. R. Durrant, *Advanced Materials*, 2017, **29**, 1701156.
70. A. E. Ostfeld, A. M. Gaikwad, Y. Khan and A. C. Arias, *Sci Rep*, 2016, **6**, 26122.
71. Y. Sun, J. H. Seo, C. J. Takacs, J. Seiffter and A. J. Heeger, *Advanced Materials*, 2011, **23**, 1679-1683.
72. C. Huang, D. Chen, Y. Huang and Y. Guo, *Electrochimica Acta*, 2013, **100**, 1-9.
73. C. S. Rout, B.-H. Kim, X. Xu, J. Yang, H. Y. Jeong, D. Odkhuu, N. Park, J. Cho and H. S. Shin, *Journal of the American Chemical Society*, 2013, **135**, 8720-8725.
74. S. I. Park, I. Gocheva, S. Okada and J.-i. Yamaki, *Journal of The Electrochemical Society*, 2011, **158**, A1067-A1070.

### 4.1.2. Magnetometric Observations on Sodium Vanadium Phosphate

In the following publication *operando* magnetic magnetometry was used to observe redox processes in a cathode material for sodium-ion batteries. Carbon-coated sodium vanadium phosphate (NVP/C) proved to be a promising candidate amongst sodium intercalation compounds. This was already known from the study presented earlier on the hybrid solar-cell battery system (4.1.1). Electrochemical characterization was performed to demonstrate the suitability of NVP/C as a cathode material. Cyclic voltammetry showed the typical oxidation and reduction peaks for NVP at 3.5 V *vs.* Na/Na<sup>+</sup>. Galvanostatic cycling with potential limitation revealed a specific capacity of 52 mAh g<sup>-1</sup> even at a relatively fast cycling rate of 5 C with a maximum capacity of over 70 mAh g<sup>-1</sup> at C/10. As magnetometry was already widely used to study oxidation and reduction processes upon charging and discharging of Li intercalation compounds, here, we applied this technique to the Na intercalation compound, NVP/C. The magnetic susceptibility was measured during electrochemical cycling of the electrode. The parameter provides information about the oxidation state of transition metals. We could clearly show that the charge compensation process exclusively happens as a consequence of the redox reaction during charging or discharging of the cell ( $V^{3+}(S = 1) \longleftrightarrow V^{4+}(S = 1/2)$ ).[112]

## Redox processes in sodium vanadium phosphate cathodes – insights from *operando* magnetometry

Gregor Klinser, [Roman Zettl](#), Martin Wilkening, Heinz Krenn, Ilie Hanzu and Roland Würschum. *Phys. Chem. Chem. Phys.*, **2019**, 21, 20151

DOI: 10.1039/c9cp04045e

### Author contributions

R.Z. performed the synthesis of NVP/C and the electrochemical experiments. G.K. performed the magnetometry experiments. G.K. and R.Z. wrote the paper together with R.W. and I.H. and the contribution of all authors. All authors participated in the discussion of the results.



Cite this: *Phys. Chem. Chem. Phys.*,  
2019, 21, 20151

# Redox processes in sodium vanadium phosphate cathodes – insights from *operando* magnetometry†

Gregor Klinser,<sup>a</sup> Roman Zettl,<sup>b</sup> Martin Wilkening,<sup>bd</sup> Heinz Krenn,<sup>c</sup>  
Ilie Hanzu<sup>bd</sup> and Roland Würschum<sup>a</sup>

Received 19th July 2019,  
Accepted 29th August 2019

DOI: 10.1039/c9cp04045e

rsc.li/pccp

*Operando* magnetic susceptibility measurements of sodium ion cathode materials during repetitive electrochemical cycling enable a continuous and bulk sensitive monitoring of the transition metal oxidation states. Such measurements on  $\text{Na}_x\text{V}_2(\text{PO}_4)_3$  identified vanadium to be the only ion undergoing oxidation/reduction processes upon battery operation. For the initial battery charging–discharging cycle as well as for the first cycle after prolonged room temperature storage, however, peculiarities within the magnetic susceptibility measurements indicate parasitic side reactions, likely on the cathode surface.

## 1 Introduction

Transition metal compounds, such as oxides and phosphates, are universally used as positive electrode (cathode) materials in advanced batteries. For instance, lithium vanadium phosphate (LVP,  $\text{Li}_3\text{V}_2(\text{PO}_4)_3$ ) was proven as a highly stable, very fast cycling active material with applications ranging from high-power batteries to battery-supercapacitor hybrid devices.<sup>1–3</sup> Its sodium analogue, the sodium vanadium phosphate (NVP,  $\text{Na}_3\text{V}_2(\text{PO}_4)_3$ ) shows good performance as cathode material in sodium ion batteries.<sup>4</sup> As with most transition metal oxides used for lithium or sodium storage, the transition metal center undergoes oxidation or reduction upon charging or discharging of the battery electrode.

Magnetometry has proven to be a powerful tool for studying such oxidation/reduction processes in layered cathode materials with Li as the mobile ionic species (e.g. ref. 5–15). Combining magnetic measurements with *operando* techniques enables a continuous and bulk sensitive monitoring of the oxidation and reduction processes during electrochemical cycling.<sup>16–19</sup> As the magnetic susceptibility serves as highly sensitive fingerprint to the oxidation state of the transition metal, irrespectively of the

ion species, the technique of magnetometry will also give valuable insights for the sodium analogue.

The present study aims at *operando* magnetic susceptibility measurements of sodium ion cathode materials. In particular, the oxidation and reduction processes in sodium vanadium phosphate upon electrochemical cycling are studied.

## 2 Results

The electrochemical behavior of the prepared NVP carbon composite (NVP/C) was investigated by cyclic voltammetry (CV) and galvanostatic cycling with potential limitation (GCPL). CV accurately shows the characteristic oxidation peak at 3.5 V vs.  $\text{Na}/\text{Na}^+$  as well as the reduction peak at 3.3 V vs.  $\text{Na}^+/\text{Na}$  (Fig. 1a). These values fit nicely to previous studies on NVP.<sup>20,21</sup> The electrochemical process is clearly reversible since almost symmetrical peaks occur at the oxidation and reduction side. The small visible shoulders in the oxidation and reduction peaks (indicated by arrows in Fig. 1a) indicate structural reorganization<sup>22</sup> which is related to a change in sodium ion occupancy.<sup>23</sup>

In the potential range of 2.8–4.0 V (vs.  $\text{Na}/\text{Na}^+$ ) a fully reversible two-phase electrochemical reaction occurs where two sodium ions can be extracted and inserted, respectively.‡ Nevertheless, the first cycle is slightly different compared to the subsequent cycles (see Fig. 1a). On the one hand, there is a small shift in potential towards more negative values. On the other hand, the CV slope significantly deviates for the first cycle (more pronounced in the oxidation peak) (see Fig. S2, ESI† for

‡ The remaining sodium ion, residing on a different crystallographic position, is much stronger bound and its electrochemical extraction is not possible in this potential range.<sup>24</sup>

<sup>a</sup> Institute of Material Physics, Graz University of Technology, Petersgasse 16, A-8010 Graz, Austria. E-mail: wuerschum@tugraz.at, g.klinser@tugraz.at; Fax: +43 316 873 108480; Tel: +43 316 873 8481

<sup>b</sup> Institute for Chemistry and Technology of Materials, Christian Doppler Laboratory for Lithium Batteries, Graz University of Technology, Stremayrgasse 9, A-8010 Graz, Austria

<sup>c</sup> Institute of Physics, University of Graz, Universitätsplatz 5, A-8010 Graz, Austria

<sup>d</sup> ALISTORE – European Research Institute, CNRS FR3104, Hub de l’Energie, Rue Baudelocque, 80039 Amiens, France

† Electronic supplementary information (ESI) available. See DOI: 10.1039/c9cp04045e



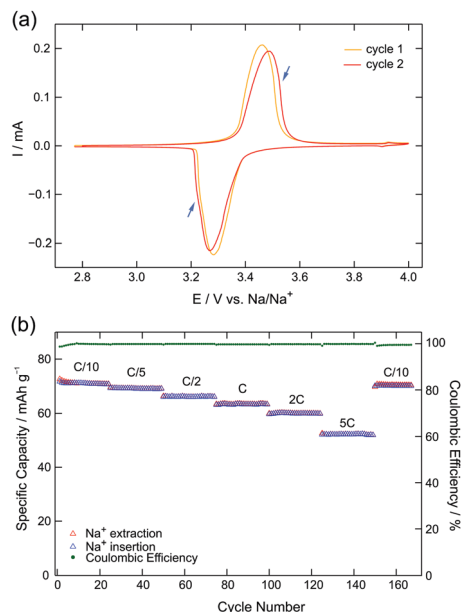


**Fig. 1** (a) Cyclic voltammety of NVP carbon composite (NVP/C) with a cycling rate of  $0.05 \text{ mV s}^{-1}$ . A different behavior in the first cycle is observed in CV, see text for further explanation. (b) Specific capacity and coulombic efficiency of NVP/C during galvanostatic cycling between 2.8 and 4.0 V for 175 cycles at different C-rates: C/10, C/5, C/2, C, 2C and 5C. Note: the voltage profiles for these measurements can be found in Fig. S1, ESI†

different sweep rates). This could be related to a slightly lower stoichiometry of sodium in NVP as revealed by inductively coupled plasma mass spectrometry (see Table S1, ESI†). However, deviations within the first charging cycle are also seen in magnetic susceptibility measurements which cannot be explained with a lower stoichiometry of sodium in NVP (see below).

Fig. 1b shows the cycling behavior of NVP/C half-cell. After each 25 cycles the C-rates were increased from C/10, C/5, C/2, C, 2C to finally 5C. The last 15 cycles serve as a control as they are conducted again with a slow C-rate of C/10. GCPL revealed that NVP/C shows almost no capacity loss within a certain cycling rate. The drop in capacity upon increasing the cycling rate is related to the increase of ohmic drops at higher currents. The drops, however, are relatively small, a sign of the good electronic conductivity introduced by the carbon phase of the NVP/C composite. Interestingly the capacity is still as high as  $52 \text{ mA h g}^{-1}$  even for cycling the cell at the highest rate of 5C.

The electrode electrochemical potential  $E$  and the change in the magnetic susceptibility  $\Delta\chi$  (with respect to the magnetic signal of the pristine sample) as a function of charging time  $t$  for two independent measurements are shown in Fig. 2. In Fig. 2a and b the first three cycles of a freshly prepared cell are shown. With the onset of charging,  $\chi$  immediately starts to decrease. This decrease prevails monotonously until the upper cut-off potential of 4.0 V is reached after 8.0 h of charging. Reversing the current flow results in an instantaneous linear re-increase of  $\chi$ , which lasts until the end of the discharging cycle at  $t = 15.6 \text{ h}$ . The second and third cycle qualitatively show the same linear variation of the magnetic susceptibility. While Fig. 2a and b display the first three cycles of a battery cell,

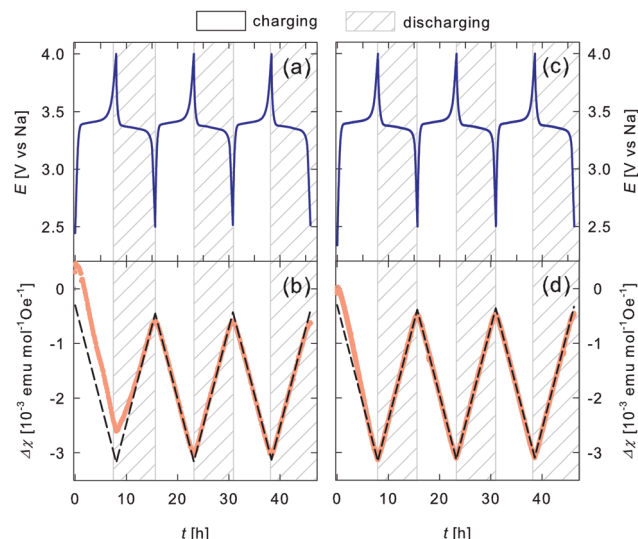


**Fig. 2** (a) Electrochemical electrode potential  $E$  with the cut off potentials 4.0 and 2.5 V and (b) change in the magnetic susceptibility  $\Delta\chi$  as a function of charging time  $t$  for three consecutive cycles of charging and discharging of the cathode material  $\text{Na}_x\text{V}_2(\text{PO}_4)_3$  (C/8 rate). (c), (d) same as (a), (b) for a cell which has been cycled 24 times before the magnetic measurement. The straight dashed line in (b) and in (d) are calculated according to eqn (1) and (2) assuming pure  $\text{V}^{3+}(S = 1) \rightarrow \text{V}^{4+}(S = 1/2)$  oxidation.

Fig. 2c and d show cycles 25 to 28 of a different cell. It should be noted that the cell rested under open circuit conditions for 6 days between cycle 24 and 25. The observed susceptibility variation in Fig. 2d can be described as above (Fig. 2b). The susceptibility immediately starts to decrease with the onset of charging. This decrease prevails linearly until the end of charging and re-increases instantaneously as soon as discharging starts.

The data represented in Fig. 2a and b are replotted in Fig. 3 as a function of the sodium content  $x$ , which is calculated for the nominal cathode mass using Faraday's law and the assumption that the entire current is consumed for Na extraction and insertion, respectively. While the electrode potential curve of different charging and discharging cycles overlaps (see Fig. 3a), the change in the magnetic susceptibility (displayed in Fig. 3b) differs between the first and second cycle. However, from the second cycle onwards  $\Delta\chi$  perfectly overlaps for the subsequent charging and discharging cycles.

*Ex situ* magnetic susceptibility measurement on the same cathode material,  $\text{Na}_x\text{V}_2(\text{PO}_4)_3$  with  $x = 2$  (Fig. S3, ESI†) show a linear variation of  $1/\chi$  as a function of temperature as characteristic for pure Langevin paramagnetism.

### 3 Discussion

As *ex situ* magnetic susceptibility measurement revealed pure Langevin paramagnetism at room temperature, charging induced variation of the susceptibility  $\chi(t)$  can be calculated according to the Curie-Weiss law:<sup>17,19</sup>

$$\chi(t) = \frac{N_A \mu_{\text{eff}}(t)^2}{3k_B(T + \Theta)} \quad (1)$$



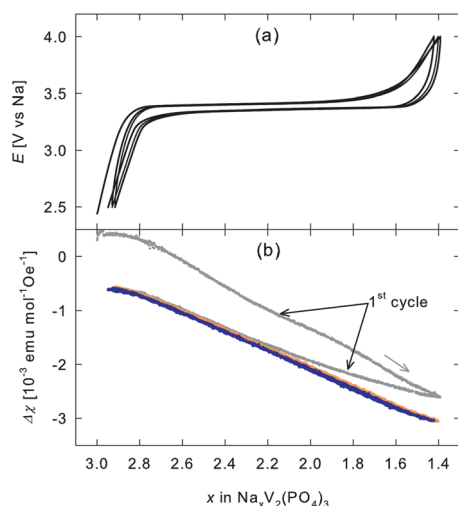


Fig. 3 (a) Electrode potential  $E$  (cut off potentials 4.0 and 2.5 V) and (b) change in the magnetic susceptibility  $\Delta\chi$  as a function of Na-content  $x$  of the cathode material  $\text{Na}_x\text{V}_2(\text{PO}_4)_3$ .

Herein,  $N_A$  and  $k_B$  denote the Avogadro and Boltzmann constant, respectively,  $T$  the temperature,  $\Theta$  the Curie–Weiss temperature, and  $\bar{\mu}_{\text{eff}}$  the mean effective magnetic moment. For  $\Theta$  a value of 50 K was determined by the *ex situ* magnetic susceptibility measurement.  $\bar{\mu}_{\text{eff}}$  can be calculated from the effective magnetic moment of the transition metal ions in its respective oxidation state  $\mu_i$  and their corresponding concentration  $c_i$ .<sup>17,19</sup>

$$\bar{\mu}_{\text{eff}}^2 = \sum_i c_i(t) \mu_i^2 \quad \text{with} \quad \sum_i c_i(t) = 1. \quad (2)$$

As vanadium is the only transition metal ion in this compound, the  $\chi$ -variation is considered to arise from  $\text{V}^{3+}$  ( $S = 1$ ,  $\mu_i = 2.83 \mu_B$ )  $\leftrightarrow$   $\text{V}^{4+}$  ( $S = 1/2$ ,  $\mu_i = 1.73 \mu_B$ ) oxidation/reduction during charging/discharging. The variation of the magnetic susceptibility, as predicted according to eqn (1) and (2) for pure vanadium oxidation/reduction, is plotted as a function of charging time in Fig. 2b and d as black dashed line. Apart from the first cycle, the experimentally observed  $\chi$ -variation can indeed be well described by the  $\chi$ -variation expected for the  $\text{V}^{3+}/\text{V}^{4+}$  oxidation/reduction (Fig. 2b and d). Deviations within the first cycle are only seen in the magnetic susceptibility data but not within the electrode potential during galvanostatic cycling (Fig. 3). However, some small deviations of the electrochemical response occur in the first cycle of a cyclic voltammetry experiment (Fig. 1a).

It seems likely that the observed deviations in the magnetic susceptibility measurements are related to some chemical reactions (potential assisted) at the surface of the electrode/electrolyte, e.g. the formation of a passivation layer. Indeed an unstable passivation layer on the same cathode material in 1 M NaFSI in EC/PC (volume ratio 1:1) was reported by Manohar *et al.* ref. 25. Upon such a reaction, Na ions may be extracted from the cathode which do not contribute to battery charging similar to the formation of surface layer compounds proposed

for  $\text{LiMn}_2\text{O}_4$ .<sup>26</sup> Due to charge neutrality conditions, Na ions which are lost in the passivation layer formation process will cause  $\text{V}^{3+} \rightarrow \text{V}^{4+}$  oxidation. Thus, during the first charging cycle this parasitic effects contributes to vanadium oxidation which results in a more pronounced  $\chi$ -decrease compared to the predicted model (see Fig. 2b dashed lines). The less pronounced increase at the beginning of the first discharging cycle could be due to the same reason. Here, the reduction of vanadium ions due to battery discharging is superimposed by oxidation process caused by the passivation layer formation. After around 12 hours of battery operation (see Fig. 2b) the measured and predicted  $\chi$ -variation according to eqn (1) and (2) agree, indicating that the reaction not contributing to the battery cycling has vanished (is in equilibrium). The deviations at the beginning of the 25th cycle in Fig. 2d may arise for the very same reason. The cell was under open circuit condition for 6 days before measured within the SQUID magnetometer. It is reasonable to think that after 6 days the material relaxes toward a different equilibrium state that, to some extent, involves a return to the original situation (before any cycling) as the passivation layer is found to be unstable in organic electrolytes.<sup>25</sup> It should be noted that magnetic ordering was reported on the similar Li NASICON phase  $\text{Li}_3\text{Fe}_2(\text{PO}_4)_3$ .<sup>27</sup> As this ordering phenomena occur at low temperatures it is not believed to have any influence on the observed room temperature  $\chi$ -variation of this work.

## 4 Conclusion and summary

*Operando* magnetic susceptibility measurements can serve as highly sensitive fingerprint for the charge compensation process in battery cathodes as the magnetic moment of the transition metal ions is directly related to its oxidation state. For the cathode material  $\text{Na}_x\text{V}_2(\text{PO}_4)_3$  the charge compensation process was confirmed to be entirely due to  $\text{V}^{3+}$  ( $S = 1$ )  $\leftrightarrow$   $\text{V}^{4+}$  ( $S = 1/2$ ) oxidation/reduction during charging/discharging. Cyclic voltammetry and magnetic measurements clearly revealed deviations for the first charging cycle which could be related to the formation of an electrode–electrolyte interphase layer on the NVP cathode.

## 5 Experimental

### Synthesis of NVP/C

Sodium vanadium phosphate–carbon composite (NVP/C) was synthesized *via* a sol–gel synthesis analogous to the synthesis of LVP/C (lithium vanadium phosphate,  $\text{Li}_3\text{V}_2(\text{PO}_4)_3$ –carbon composite).<sup>28</sup> Here, the precursor  $\text{LiH}_2\text{PO}_4$  was replaced with  $\text{NaH}_2\text{PO}_4$ . Citric acid as gel-forming agent and  $\text{NH}_4\text{VO}_3$  were separately dissolved in 50 ml of deionized water and then mixed in a beaker. The molar ratio of citric acid to vanadium was 1:1. The reaction mixture was slowly heated to 60 °C.  $\text{NaH}_2\text{PO}_4$  in stoichiometric amounts was dissolved in 50 ml deionized water and was added slowly (drop-wise in approximately 1 h) from a separation funnel to the solution of  $\text{NH}_4\text{VO}_3$  and citric acid at 60 °C. The solution was then heated to 80 °C to evaporate the water on a hot plate until a gel formed. The obtained gel was

§ In the spin only case  $\mu_i = g\sqrt{S_i(S_i + 1)}$  with the spin state  $S_i$  and  $g = 2$ .



subsequently dried overnight in an oven at 80 °C under air. Afterward, it was first ground in an agate mortar and then thermally treated under argon in a quartz tube placed in a tube oven at 700 °C for 8 h. The heating ramp was set at 4 °C min<sup>-1</sup>, the cooling ramp being the natural cooling rate of the oven, which is approximately 8–12 °C min<sup>-1</sup> above 350 °C. In these synthesis conditions, the citric acid converts to conductive carbon and forms a composite with the NVP. At last two grounding processes of the NVP carbon composite (using an agate mortar) were performed with an sintering step in between. The XRD pattern of the obtained crystalline black powder can be seen in Fig. S4 (ESI<sup>†</sup>).

### Electrochemical characterization

The electrodes were prepared by the slurry cast method. The slurry contained the active material (NVP/C, 800 mg), conductive carbon (Super C65, 100 mg) and a binder (Kynar 761, 100 mg) resulting in a mass ratio of 8 : 1 : 1 respectively. Additionally, 3 g of solvent (1-methyl-2-pyrrolidinone (NMP)) were added. The components were mixed together by ball milling at 400 rpm 4 times for 15 minutes. The well dispersed slurry was cast on an Al current collector which was, before casting, etched with a 5 wt% KOH solution at 40 °C. The doctor blade casting was carried out at a velocity of 5 mm s<sup>-1</sup> and using a casting gap of 150 μm. The cast films were then dried at 60 °C in air, electrode disks were cut (10 mm in diam.), vacuum dried in a Büchi oven and then transferred to an Ar-filled glovebox with water and oxygen contents smaller than 0.5 ppm. The electrodes, with a mass loading of 1.68 mg cm<sup>-2</sup>, were assembled in Swagelok-type cells with metallic Na as reference and counter electrode. The electrolyte used in all experiments was 1 M NaFSI in EC:DEC (volume ratio 4 : 6). Electrochemical measurements were carried out on VMP3 or MPG2 potentiostat/galvanostat instruments from Bio-Logic controlled by the EC-Lab software. Cyclic voltammetry (CV) was performed at different increasing scan rates, *i.e.* 0.05 mV s<sup>-1</sup>, 0.1 mV s<sup>-1</sup>, 0.2 mV s<sup>-1</sup> and 0.5 mV s<sup>-1</sup>. The samples were cycled between 2.8 V to 4.0 V *vs.* Na/Na<sup>+</sup>. Galvanostatic cycling with potential limitation was carried out between 2.8 V to 4.0 V *vs.* Na/Na<sup>+</sup>. The cycling rates were C/10, C/5, C/2, C, 2C, 5C (each 25 cycles) and again C/10 (15 cycles). The currents corresponding to the chosen C-rates were calculated considering the theoretical capacity of NVP, which is 118 mA h g<sup>-1</sup>.

### Operando magnetometry

The cathodes for the *operando* magnetic measurements were prepared from the same electrode slurry used for electrochemical characterization (see above). A flattened end of an aluminum wire was first dip-coated, then pre-dried in air and subsequently dried at 370 K under vacuum conditions (10<sup>-5</sup> mbar) for 24 hours. The dip-coated cathodes were mounted in a self-developed purpose-built electrochemical cell suitable for the use in a SQUID magnetometer.<sup>16,29</sup> This cell enables an electrochemical measurement in a 3-electrode geometry and ensures that the measured magnetic signal variation arise originate solely from the cathode material. Please note that with the developed cell design the magnetic signal of both the anode and cathode is actually measured. However, sodium plating and dissolving stripping on

the anode side contributes less than 1% to the total magnetic signal variation. Thus, the variation of the magnetic susceptibility can entirely be attributed to the variation of the susceptibility of the cathode material. In the present case, the cell compartment was a polyethylene tube. Metallic sodium pressed on copper wires served as anode and reference electrode. The electrolyte was the same as for the electrochemical characterization (*vide supra*). Charging and discharging was performed with a constant current of 18.4 μA (Fig. 2a and b) and 25.7 μA (Fig. 2c and d) corresponding to a C-rate of about C/8 based on the specific theoretical cathode capacity of 118 mA h g<sup>-1</sup> and the coating masses of 1.56 mg and 2.73 mg using a single channel potentiostat/galvanostat instrument potentiostat (Autolab PGSTAT 128N).

The cathode electrode film for the *ex situ* magnetometry measurement was prepared in the same way as for the electrochemical measurements. A pouch cells was used in which the reference electrode and the counter electrode was made of metallic sodium foil. The square 4 cm<sup>2</sup> electrode containing 8.5 mg of NVP/C active mass was cycled between 2.8 V and 3.8 V *vs.* Na/Na<sup>+</sup> and subsequently stopped in the 4th charging cycle at an approximate sodium content of  $x = 2$  (Na<sub>x</sub>V<sub>2</sub>(PO<sub>4</sub>)<sub>3</sub>). Afterward the cell was dismantled, the NVP-containing cathode rinsed with dimethyl carbonate (DMC) and dried under in vacuum conditions at room temperature before placing it in an airtight SQUID sample holder with minimized magnetic contribution. In addition, the measured signal was also corrected for the magnetic signal of the additives (carbon and binder) and the aluminum substrate both of which in sum contribute by about 9% to the overall signal. The whole process of cathode preparation, handling and transfer to the SQUID magnetometer was performed under protective Ar-atmosphere.

Magnetic susceptibility measurements were performed at an applied magnetic field of 5000 Oe using a SQUID magnetometer (Quantum Design MPMS-XL-7) in the same manner as described elsewhere.<sup>18</sup> In the case of *operando* studies, the temperature was controlled and kept at 300 K, whereas the *ex situ* samples were measured as a function of temperature (field-cooling, 300 K to 10 K).

### Conflicts of interest

There are no conflicts to declare.

### Acknowledgements

This work was performed in the framework of the inter-university cooperation of TU Graz and Uni Graz on natural science (NAWI Graz). This work was financially supported by the Austrian Research Promotion Agency (FFG) through the project SolaBat (grant no. 853627).

### References

- 1 N. Böckenfeld and A. Balducci, *J. Power Sources*, 2013, **235**, 265–273.



- 2 X. Rui, N. Ding, J. Liu, C. Li and C. Chen, *Electrochim. Acta*, 2010, **55**, 2384–2390.
- 3 M. Secchiarioli, G. Giuli, B. Fuchs, R. Marassi, M. Wohlfahrt-Mehrens and S. Dsoke, *J. Mater. Chem. A*, 2015, **3**, 11807–11816.
- 4 Q. Wang, J. Xu, W. Zhang, M. Mao, Z. Wei, L. Wang, C. Cui, Y. Zhu and J. Ma, *J. Mater. Chem. A*, 2018, **6**, 8815–8838.
- 5 A. Mauger, F. Gendron and C. Julien, *J. Alloys Compd.*, 2012, **520**, 42–51.
- 6 Z. Li, N. A. Chernova, M. Roppolo, S. Upreti, C. Petersburg, F. M. Alamgir and M. S. Whittingham, *J. Electrochem. Soc.*, 2011, **158**, A516.
- 7 M. Labrini, I. Saadoune, F. Scheiba, A. Almaggoussi, J. Elhaskouri, P. Amoros, H. Ehrenberg and J. Brötz, *Electrochim. Acta*, 2013, **111**, 567.
- 8 D. Mohanty and H. Gabrisch, *J. Power Sources*, 2012, **220**, 405.
- 9 G. Klinser, S. Topolovec, H. Kren, S. Koller, H. Krenn and R. Würschum, *Solid State Ionics*, 2016, **293**, 64.
- 10 D. Kellerman, V. Galakhov, A. Semenova, Y. Blinovskov and O. Leonidova, *Phys. Solid State*, 2006, **48**, 548–556.
- 11 J. T. Hertz, Q. Huang, T. McQueen, T. Klimczuk, J. W. G. Bos, L. Viciu and R. J. Cava, *Phys. Rev. B: Condens. Matter Mater. Phys.*, 2008, **77**, 075119.
- 12 K. Miyoshi, C. Iwai, H. Kondo, M. Miura, S. Nishigori and J. Takeuchi, *Phys. Rev. B: Condens. Matter Mater. Phys.*, 2010, **82**, 075113.
- 13 J. Sugiyama, H. Nozaki, J. H. Brewer, E. J. Ansaldo, G. D. Morris and C. Delmas, *Phys. Rev. B: Condens. Matter Mater. Phys.*, 2005, **72**, 144424.
- 14 K. Mukai, Y. Ikedo, H. Nozaki, J. Sugiyama, K. Nishiyama, D. Andreica, A. Amato, P. L. Russo, E. J. Ansaldo, J. H. Brewer, K. H. Chow, K. Ariyoshi and T. Ohzuku, *Phys. Rev. Lett.*, 2007, **99**, 087601.
- 15 T. Motohashi, T. Ono, Y. Sugimoto, Y. Masubuchi, S. Kikkawa, R. Kanno, M. Karppinen and H. Yamauchi, *Phys. Rev. B: Condens. Matter Mater. Phys.*, 2009, **80**, 165114.
- 16 S. Topolovec, H. Kren, G. Klinser, S. Koller, H. Krenn and R. Würschum, *J. Solid State Electrochem.*, 2016, **20**, 1491–1496.
- 17 G. Klinser, S. Topolovec, H. Kren, S. Koller, W. Goessler, H. Krenn and R. Würschum, *Appl. Phys. Lett.*, 2016, **109**, 213901.
- 18 G. Klinser, M. Stückler, H. Kren, S. Koller, W. Goessler, H. Krenn and R. Würschum, *J. Power Sources*, 2018, **396**, 791–795.
- 19 G. Klinser, S. Topolovec, H. Krenn and R. Würschum, in *Encyclopedia of Interfacial Chemistry*, ed. K. Wandelt, Elsevier, Oxford, 2018, pp. 849–855.
- 20 L. Si, Z. Yuan, L. Hu, Y. Zhu and Y. Qian, *J. Power Sources*, 2014, **272**, 880–885.
- 21 N. Böckenfeld and A. Balducci, *J. Solid State Electrochem.*, 2014, **18**, 959–964.
- 22 E. Wang, M. Chen, X. Liu, Y. Liu, H. Guo, Z. Wu, W. Xiang, B. Zhong, X. Guo, S. Chou and S.-X. Dou, *Small Methods*, 2019, **3**, 1800169.
- 23 W. Song, X. Ji, Z. Wu, Y. Zhu, Y. Yang, J. Chen, M. Jing, F. Li and C. E. Banks, *J. Mater. Chem. A*, 2014, **2**, 5358–5362.
- 24 Y. Fang, J. Zhang, L. Xiao, X. Ai, Y. Cao and H. Yang, *Adv. Sci.*, 2017, **4**, 1600392.
- 25 C. Manohar, A. Raj K, M. Kar, M. Forsyth, D. R. MacFarlane and S. Mitra, *Sustainable Energy Fuels*, 2018, **2**, 566–576.
- 26 T. Eriksson, A. M. Andersson, C. Gejke, T. Gustafsson and J. O. Thomas, *Langmuir*, 2002, **18**, 3609–3619.
- 27 G. Rousse, J. Rodríguez-Carvajal, C. Wurm and C. Masquelier, *Chem. Mater.*, 2001, **13**, 4527–4536.
- 28 C. Huang, D. Chen, Y. Huang and Y. Guo, *Electrochim. Acta*, 2013, **100**, 1–9.
- 29 S. Topolovec, H. Krenn and R. Würschum, *Rev. Sci. Instrum.*, 2015, **86**, 063903.



## 4.2. Ion Dynamics in Porous Materials

### 4.2.1. Introduction

Similar to section 4.1, results in this section are presented mainly in a cumulative way by showing peer reviewed papers and a manuscripts in the final stage before submission. At the beginning, a brief introduction about the key materials is given. First,  $\text{LiBH}_4$  is introduced by explaining the interest in the material as solid state electrolyte together with the link to porous materials. Secondly, MIL-121 as pristine porous metal-organic framework (MOF) with its properties and modification strategies are briefly reviewed. Detailed information, however, can be found in the introductory part of the papers and the manuscript presented below.

**$\text{LiBH}_4$ .** As mentioned in the subsection 2.3.2, the class of hydride based solid electrolytes exhibit interesting properties like good mechanical stability and chemical stability in contact with Li metal. Its most famous representative, lithium boron hydride ( $\text{LiBH}_4$ ), however, suffers from low room temperature conductivity. On the other hand, at high temperatures, above approximately 110 °C,  $\text{LiBH}_4$  is highly conductive. At the transition temperature the material undergoes a structural change from hexagonal (high-temperature phase) to orthorhombic (low-temperature phase). In Figure 15.a, X-ray diffractograms of  $\text{LiBH}_4$  are shown. The lower one represents the orthorhombic phase (blue) and the pattern shown in orange reflects the hexagonal phase. The corresponding crystal structures are attached to the patterns. Another experiment was carried out to observe this structural change by means of  $^2\text{D}$  MAS NMR. For this purpose  $\text{LiBD}_4$ , *i.e.* deuterated  $\text{LiBH}_4$ , was analysed. In Figure 15.b the corresponding spectra are shown. The line shapes clearly narrow from lower (blue) to higher (orange) temperatures. This is a valid indication for higher mobility of the species of interest ( $^2\text{D}$ ), as expected for the high temperature phase. If the measurement above the transition temperature is carried out without any resting period, residual orthorhombic  $\text{LiBD}_4$  is still detected (yellow spectrum), which can be identified by a broad contribution to the narrow NMR line (marked with an arrow in Figure 15.b).

The transition of  $\text{LiBH}_4$  and the limited conductivity of its orthorhombic phase, respectively, is the cause of intensive research on  $\text{LiBH}_4$  composites. It was found that not only the substitution of halogens stabilizes the hexagonal phase of  $\text{LiBH}_4$ , but also nanoconfinement of  $\text{LiBH}_4$  in porous supports creates diffusion pathways ben-

eficial for Li-ion transport in the composites. The fact that different phenomena are responsible for higher conductivity at room temperature catalysed the interest in combining these approaches aiming in even better conductivities. In the following three subsections results of this research is presented.

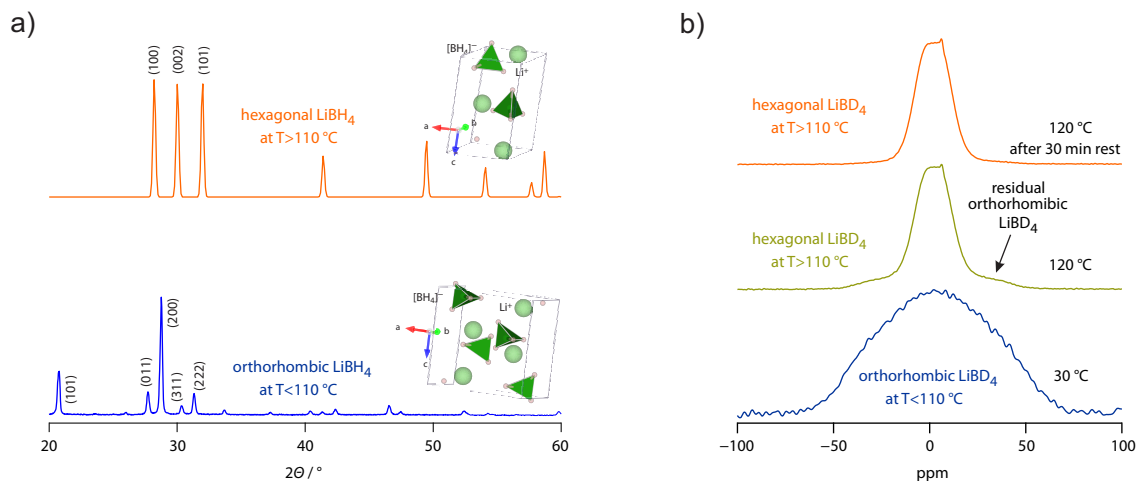


**Figure 15.** a) XRD of  $\text{LiBH}_4$  at room temperature (blue) and above  $110^\circ\text{C}$  (orange) and the corresponding structure attached. Above the transition temperature of  $110^\circ\text{C}$ ,  $\text{LiBH}_4$  appears in a hexagonal structure, whereas below this temperature an orthorhombic structure is observed. The high temperature diffractogram was recorded by Soulie *et al.* [113] b)  $^2\text{D}$  MAS NMR spectra of  $\text{LiBD}_4$  at temperatures above and below the transition temperature. Samples were measured on a spectrometer connected to a 11.4 Tesla cryomagnet, which corresponds to a resonance frequency of 76.753 MHz for  $^2\text{D}$ . The measurement was carried out with pulse lengths between 3 and  $5\ \mu\text{s}$  at 100 W and with a recycle delay of 5 s.

**MIL-121.** The metal-organic framework (MOF) MIL-121 is the starting material of the second group of porous compounds modified to obtain alkali-ion conductors. The modifications of MIL-121 included introducing mobile ions and soaking with a liquid electrolyte. A variety of properties of MIL-121 arouse the interest in this material for the application as solid-state electrolyte. First, the fact that only two of four carboxylic groups are needed to built the network of the MOF is highly interesting. Those free functional groups are rarely found in this MOF family of Al-centred MOFs. To introduce alkali-ions to the structure of MIL-121, we took advantage of the free carboxylic groups and applied an acid-base reaction with Li and Na containing bases. Secondly, the porosity of the material is suspected to provide diffusion channels and beneficial interfaces for ions to move. The surface

area of MIL-121 is  $162\text{ m}^2\text{ g}^{-1}$  with 1D channels along the structure. Thirdly, its thermal stability up to at least  $400\text{ }^\circ\text{C}$  makes MIL-121 accessible to a variety of modification approaches involving high-temperature treatments.[114, 115]

### 4.2.2. Combining Ion Substitution and Nanoconfinement in Complex Hydrides

In the first study of this section, we used porous materials  $\text{SiO}_2$  with a hierarchical structure, namely MCM-41 and SBA-15, as well as  $\text{Al}_2\text{O}_3$ . After the analysis of structural details by means of  $\text{N}_2$ -physisorption, SEM and XRD the materials were filled with a hydride based solid electrolyte. For this purpose, melt infiltration was used, as it is highly effective in filling the solid pores of the supports with the melted ionic conductor. After natural cooling and re-solidification of the complex hydride, this procedure leads to the formation of a highly conductive solid-solid interface. This method called nanoconfinement was already well-known in literature to increase the room temperature ionic conductivity of these materials by several orders of magnitude. Furthermore, it was found that anion substitution in *e.g.*  $\text{LiBH}_4$  is an effective approach to reach again highly enhanced room temperature conductivities. Our aim was to combine the two strategies to further increase the room temperature conductivity of  $\text{LiBH}_4$ . We analysed the synthesis product composed of the porous support,  $\text{LiBH}_4$  and an anion substitute ( $\text{LiI}$  or  $\text{LiNH}_2$ ) with XRD and DRIFTS and confirmed the filling of the pores with  $\text{N}_2$ -physisorption.

Finally, samples were compared according to their ionic conductivity. Results from impedance spectroscopy revealed that our new approach is effective in enhancing room temperature conductivity of metal hydride composites. In addition, the activation energy was decreased in samples synthesized via the combined approach. By testing our idea on various materials, we showed that this approach can be applied to different combinations of porous materials and metal hydride electrolytes.  $^7\text{Li}$  solid-state NMR showed that indeed the mobility of Li ions is significantly higher in the composite where both approaches, *i.e.* nanoconfinement and anion substitution, were combined.[116]

## Combined Effects of Anion Substitution and Nanoconfinement on the Ionic Conductivity of Li-Based Complex Hydrides

Roman Zettl, Laura de Kort, Maria Gombotz, H. Martin R. Wilkening, Petra E. de Jongh and Peter Ngene. *J. Phys. Chem. C*, **2020**, 124, 5, 2806-2816

DOI: 10.1021/acs.jpcc.9b10607

### Author contributions

R.Z. and L.d.K. performed the experiments (synthesis, XRD, DRIFTS and impedance spectroscopy measurements) and analysed the associated data. M.G. carried out the NMR measurements and the analysis of the data. R.Z. and L.d.K. wrote the paper together with H.M.R.W. and P.N with the contribution of all authors. All authors participated in the discussion of the results.

# Combined Effects of Anion Substitution and Nanoconfinement on the Ionic Conductivity of Li-Based Complex Hydrides

Roman Zettl, Laura de Kort, Maria Gombotz, H. Martin R. Wilkening, Petra E. de Jongh,\* and Peter Ngene\*

Cite This: <https://dx.doi.org/10.1021/acs.jpcc.9b10607>

Read Online

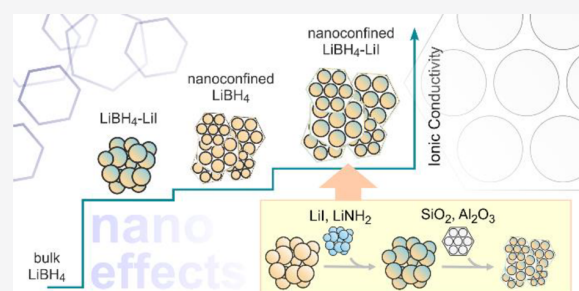
ACCESS |

Metrics & More

Article Recommendations

Supporting Information

**ABSTRACT:** Solid-state electrolytes are crucial for the realization of safe and high capacity all-solid-state batteries. Lithium-containing complex hydrides represent a promising class of solid-state electrolytes, but they exhibit low ionic conductivities at room temperature. Ion substitution and nanoconfinement are the main strategies to overcome this challenge. Here, we report on the synthesis of nanoconfined anion-substituted complex hydrides in which the two strategies are effectively combined to achieve a profound increase in the ionic conductivities at ambient temperature. We show that the nanoconfinement of anion substituted  $\text{LiBH}_4$  ( $\text{LiBH}_4\text{-LiI}$  and  $\text{LiBH}_4\text{-LiNH}_2$ ) leads to an enhancement of the room temperature conductivity by a factor of 4 to 10 compared to nanoconfined  $\text{LiBH}_4$  and nonconfined  $\text{LiBH}_4\text{-LiI}$  and  $\text{LiBH}_4\text{-LiNH}_2$ , concomitant with a lowered activation energy of 0.44 eV for Li-ion transport. Our work demonstrates that a combination of partial ion substitution and nanoconfinement is an effective strategy to boost the ionic conductivity of complex hydrides. The strategy could be applicable to other classes of solid-state electrolytes.



## 1. INTRODUCTION

Solid-state electrolytes are indispensable for the realization of safe batteries offering high energy densities<sup>1,2</sup> crucial for the development of both mobile applications and large-scale stationary systems that can effectively store electricity from renewable but intermittent energy sources such as solar, wind, or tidal. Current battery systems, especially those designed for electric vehicles, may suffer from flammable and volatile organic based liquid electrolytes. In many cases, this narrow electrochemical stability window of conventional aprotic electrolytes prevents the use of anode materials providing high energy densities like metallic lithium. These disadvantages have led to a renewed interest in inorganic solid-state electrolytes, because they are potentially safer than liquid electrolytes and chemically compatible with Li metal. In addition, if sulfur-based cathode materials are considered, they prevent the dissolution and shuttling of polysulfides, which is one of the most serious hurdles that needs to be overcome in these type of batteries that promise high energy densities.<sup>3</sup>

Various classes of materials have been investigated as solid-state ion conductors for all-solid-state batteries.<sup>4–8</sup> These materials include garnets,<sup>9</sup> perovskites,<sup>10</sup> and polymers<sup>11</sup> as well as glass type electrolytes.<sup>12</sup> The complex metal hydrides, particularly those containing Li and Na, such as  $\text{LiBH}_4$ ,  $\text{Li}_2\text{B}_{12}\text{H}_{10}$ ,  $\text{NaB}_{10}\text{H}_{10}$ , and  $\text{NaCB}_{11}\text{H}_{12}$  constitute a relatively new class of solid electrolytes.<sup>13–17</sup> Due to their lightweight and high hydrogen content, these materials have been

intensively investigated over the last 20 years for reversible hydrogen storage. The hydrogen could be used for fuel cells with polymer electrolyte membranes.<sup>18–21</sup> Over a decade ago, it was shown that they also exhibit fast ionic conductivity and some also show good electrochemical stability windows up to 3 V versus  $\text{Li/Li}^+$ .<sup>22–24</sup>

The main challenge for solid-state electrolytes in general has been the inherently low room temperature ionic conductivity, compared to liquid electrolytes. Therefore, most research effort has been focused on enhancing the ionic conductivities by structural modifications. For instance, the high ionic conductivity in complex hydrides is often a result of structural phase transition at high temperatures. A typical example is  $\text{LiBH}_4$ , which exhibits an ionic conductivity of  $1 \times 10^{-3} \text{ S cm}^{-1}$  above 110 °C,<sup>14,23</sup> due to the formation of the hexagonal phase, whereas at room temperature, the compound crystallizes into the orthorhombic structure, which shows poor ion conductivity.<sup>25–27</sup>

Two main approaches, which have separately been introduced in literature, have proved to be successful in boosting the room temperature ionic conductivity of solid

Received: November 12, 2019

Revised: January 14, 2020

Published: January 21, 2020

electrolytes, especially complex hydrides. The first approach takes advantage of the partial substitution of the complex anion (e.g.,  $\text{BH}_4^-$  in  $\text{LiBH}_4$ ) by halides such as  $\text{Cl}^-$  and  $\text{I}^-$  or by amides.<sup>28–30</sup> Iso- or aliovalent replacement of the  $\text{Li}^+$  cations by  $\text{Na}^+$ ,  $\text{Ca}^{2+}$  or  $\text{Ce}^{3+}$  has been reported as well.<sup>31–33</sup> Partial ion substitution is generally achieved by high-energy ball milling<sup>34</sup> or by heating a physical mixture of the compounds at temperatures of 200 to 300 °C; note that the melting point of  $\text{LiBH}_4$  is 278 °C.<sup>35</sup> For instance, solid solutions of  $\text{LiBH}_4\text{--LiX}$  ( $\text{X} = \text{Cl}, \text{Br}, \text{I}$ ) and  $\text{LiBH}_4\text{--Li}_3\text{N}$  or new compounds like in  $\text{LiBH}_4\text{--LiNH}_2$  with room temperature ionic conductivities that are much higher than the individual compounds have been reported. Several studies have been conducted to investigate the effect of heat treatment,<sup>36</sup> the influence of  $\text{LiX}$  contents,<sup>35</sup> and the influence of the kind of the substituting anion.<sup>37</sup>

It is generally believed that anion substitution leads to an increase in distance between neighboring  $\text{BH}_4^-$  units which is associated with weaker Coulomb interactions in  $\text{LiBH}_4$  and hence a decrease of the transition temperature at which the compound changes from orthorhombic to hexagonal symmetry.<sup>38</sup> Indeed, substitution with larger halide anions leads to stabilization of the hexagonal phase of  $\text{LiBH}_4$  at near ambient temperatures as clearly seen in the most investigated anion substituted complex hydride  $\text{LiBH}_4\text{--LiI}$ .<sup>14</sup> Alternatively, treatment at elevated temperatures (150 °C) of  $\text{LiBH}_4$  together with  $\text{LiNH}_2$  leads to the formation of a new phase,  $\text{Li}_2(\text{BH}_4)(\text{NH}_2)$ . The formation of a new phase causes a conductivity enhancement and a relatively low phase transition temperature of approximately 50 °C.<sup>30,39</sup> A main disadvantage of this method is, however, that the resulting compounds suffer from poor electrochemical and thermal cycling stability because of phase segregation.

The second approach, which has led to a large increase in the ionic conductivity in several classes of solid electrolytes, is interface engineering by forming nanocomposites with oxides such as  $\text{SiO}_2$  and  $\text{Al}_2\text{O}_3$ .<sup>40–43</sup> This approach, especially when using carbon scaffolds, was originally proposed to enhance the hydrogen sorption properties of complex hydrides,<sup>44–48</sup> but it was additionally shown to influence the ion mobility in the materials as well. The increase in ionic conductivity is currently believed to be caused by interactions of the hydride with the scaffold surface leading to either interfacial space charge zones<sup>49</sup> or to the formation of highly conducting compounds at this interface<sup>50</sup> due to changes in structure or defect density. The exact nature of the hydride/oxide interface is still a subject of intensive investigation. Alternatively, it has been shown that nanocrystalline  $\text{LiBH}_4$  has an enhanced ionic conductivity compared to the microcrystalline form.<sup>51</sup> Interface engineering of  $\text{LiBH}_4$  is normally achieved by nanoconfinement, e.g., via melt infiltration<sup>52</sup> of  $\text{LiBH}_4$  in the nanopores of the oxides<sup>40,42</sup> or by ball milling<sup>41–43</sup> a mixture of  $\text{LiBH}_4$  and the metal oxide. The two preparation methods have been reported to lead to comparable effects. Results from testing all-solid-state Li–S batteries using  $\text{LiBH}_4/\text{SiO}_2$  nanocomposites as electrolytes showed that this approach enhances the ionic conductivity of  $\text{LiBH}_4$  and leads to better electrochemical and cycling stability.<sup>53–55</sup>

It has been shown that in these so-called dispersed ionic conductors, only the conductor or electrolyte (e.g.,  $\text{LiBH}_4$ ) near the interface with the oxide (within 1–2 nm) exhibits very high ion mobility at room temperature.<sup>48,55</sup> Nevertheless, the volume fraction far from the interface is crucial to achieve interconnected  $\text{LiBH}_4$  particles as the silica or alumina particles

do not contribute to the ionic conductivity. Only a percolating network of fast  $\text{Li}^+$  diffusion pathways will guarantee facile Li ion transport over long distances. We hypothesize that the overall long-range ionic conductivity of the nanocomposite can be further improved if the conductive regions are interconnected via highly conductive  $\text{Li}^+$  diffusion pathways rather than just bulk  $\text{LiBH}_4$ .

For this purpose, we prepared nanoconfined anion substituted  $\text{LiBH}_4$ . In these nanocomposites, the combined effects of partial anion substitution, either with  $\text{I}^-$  or  $\text{NH}_2^-$ , and nanoconfinement in metal oxides ( $\text{SiO}_2$  and  $\text{Al}_2\text{O}_3$ ) indeed leads to high room temperature Li-ion conductivities. In agreement with this observed enhancement, the activation energy for Li ion transport is lower than those probed for nanoconfined  $\text{LiBH}_4$  and the unconfined anion-substituted ( $\text{LiBH}_4\text{--LiI}$ ,  $\text{LiBH}_4\text{--LiNH}_2$ ) systems. By using different preparation methods, we show that the enhancement seen for nanoconfined  $\text{LiBH}_4\text{--LiI}$  and  $\text{LiBH}_4\text{--LiNH}_2$  is indeed due to the combined effects of interfacial interactions with the metal oxide surface groups and the presence of highly conducting anion-substituted  $\text{LiBH}_4$  located further away from the  $\text{SiO}_2$  or  $\text{Al}_2\text{O}_3$  surfaces.  $\text{LiBH}_4$  was used as an excellent model system to demonstrate the effect of combining anion substitution and nanoconfinement, and we believe that this approach and outcome are applicable to a wide variety of solid-state electrolytes.

## 2. EXPERIMENTAL SECTION

**Synthesis of Silica Supports.** MCM-41 was synthesized using the procedure described by Cheng et al.<sup>56</sup> In brief, hexadecyltrimethylammonium bromide (Sigma-Aldrich,  $\geq 96.0\%$ ) and tetramethylammonium hydroxide solution (Sigma-Aldrich, 25 wt % in  $\text{H}_2\text{O}$ ) were mixed with deionized water. After the addition of the silica source (Aerosil 380), the white suspension was stirred for 2 h at 30 °C and kept at this temperature for another 24 h unstirred in a closed polypropylene bottle. The composition of the mixture was 1.00  $\text{SiO}_2$ : 0.19 (TMA)OH: 0.27 (CTA)Br: 40  $\text{H}_2\text{O}$ . The jelly like product was heated to 140 °C in stainless steel autoclaves and kept there for 48 h. After being naturally cooled to room temperature, the mixture was thoroughly washed, filtered, and dried at 120 °C for approximately 12 h. The final calcination step (550 °C, 12 h) was carried out after heating the sample first to 100 °C for 1 h as an additional drying step.

SBA-15 was prepared according to Zhao et al.<sup>57</sup> Poly(ethylene glycol)-*block*-poly(propylene glycol)-*block*-poly(ethylene glycol) (Sigma-Aldrich, PEG–PPG–PEG, Pluronic, P-123), hydrochloric acid fuming 37% (Merck, for analysis), and deionized water were stirred at 35 °C. Tetraethyl orthosilicate (Sigma-Aldrich,  $\geq 99.0\%$  GC, TEOS) was added dropwise to the solution, and the solution was then stirred for 24 h at 40 °C resulting in a composition of 0.015 P123:5.2 HCl: 129  $\text{H}_2\text{O}$ : 1 TEOS. This mixture was kept at 100 °C in a closed polypropylene bottle for 48 h, followed by extensive washing and filtration. Subsequently, the product was predried (60 °C, 24 h, air), dried (120 °C, 8 h, air), and calcined (1.2 °C  $\text{min}^{-1}$ , 550 °C, 6 h, air).

**Electrolyte Preparation.** Alumina ( $\text{Al}_2\text{O}_3$ ) was purchased from Sasol (product brand Puralox SCCa-5/200), while lithium amide (95% pure), lithium iodide (98% pure), and lithium borohydride (95% pure) were purchased from Sigma-Aldrich. The metal oxide supports (MCM-41, SBA-15 and  $\text{Al}_2\text{O}_3$ ) were first dried under a vacuum at 220 °C overnight;

then we stored them in an Ar purified glovebox (MBraunLab-master, typically  $\text{H}_2\text{O}$  and  $\text{O}_2 < 1$  ppm). All subsequent sample handling and transfer were carried out in the glovebox to avoid contamination with air or traces of moisture. The  $\text{LiBH}_4$ -LiI/oxide nanocomposites were prepared using two different methods. In the first method,  $\text{LiBH}_4$  and LiI were *physically mixed* in molar ratios of 10, 20, 30, and 40 mol % LiI with respect to  $\text{LiBH}_4$ . Subsequently, the materials were mixed with the desired amount of the oxide and placed in a quartz reactor which was then inserted inside a stainless-steel high-pressure autoclave (Parr). The amounts were calculated in order to fill the oxide pores by 130%, meaning that all pores were filled and voids between particles and space between grains were filled additionally. Melt infiltration was carried out at 50 bar  $\text{H}_2$  pressure and a temperature of 295 °C for 30 min; the heating rate was approximately 3 °C  $\text{min}^{-1}$ .<sup>48</sup> During this process, Li-Li $\text{BH}_4$  forms a solid solution  $((1-x)\text{LiBH}_4 \cdot x\text{LiI}$  with  $x = 0.1, 0.2, 0.3, 0.4$ ) which melts and infiltrates the pores of the oxide. Upon cooling, the molten solid solution solidifies in the pores of the support material, and the excess amount remains at the external surface of the support.

In the second approach, the samples were prepared by combining *solution impregnation* and melt infiltration. A solution of LiI and water or ethanol was prepared. The desired amount of the solution was added dropwise, using a syringe and a septum, to the metal oxide support contained in a round-bottom flask. This was done outside the glovebox but by using a Schlenk line to avoid contamination. The impregnated oxide was kept at room temperature for 3 h, after which the solvent was removed. Subsequently, the mixture was dried at 250 °C overnight under a dynamic vacuum. In order to reach the desired amount of LiI in the pores, the procedure was repeated twice. The LiI/metal oxide nanocomposite was mixed with  $\text{LiBH}_4$  to reach a molar ratio LiI/ $\text{LiBH}_4$  of 20:80 with the volume of  $\text{LiBH}_4$ -LiI corresponding to 130% of the total pore volume of the silica (or alumina). The mixture was then inserted into a sample holder placed inside a stainless-steel high-pressure autoclave, pressurized to 50 bar  $\text{H}_2$  and heated at 3 °C  $\text{min}^{-1}$  to 295 °C. The dwell time was 30 min. The molten  $\text{LiBH}_4$  infiltrates the oxide pores and reacts with the nanoconfined LiI to form  $\text{LiBH}_4$ -LiI.

Reference samples of  $\text{LiBH}_4$ -LiI solid solutions and nanoconfined  $\text{LiBH}_4$  were prepared under the same autoclave conditions as outlined above. Solid solutions were synthesized by heating mixtures of  $\text{LiBH}_4$  and LiI without adding the metal oxide support; nanoconfined  $\text{LiBH}_4$  was obtained without adding LiI to the mixture. A third reference sample was bulk  $\text{LiBH}_4$ , which was ground and melted under the same autoclave conditions and recrystallized.

$\text{LiBH}_4$ - $\text{LiNH}_2$ /oxide nanocomposites were prepared using a two-step preparation method. First,  $\text{LiBH}_4$  and  $\text{LiNH}_2$  were physically mixed in a molar ratio of 50%  $\text{LiNH}_2$  with respect to  $\text{LiBH}_4$ . Afterward, the physical mixture was placed in a stainless-steel reactor which was then inserted into a stainless-steel high-pressure autoclave. The solid-state reaction was carried out at 50 bar  $\text{H}_2$  pressure and at 150 °C (heating rate 2.5 °C  $\text{min}^{-1}$ ) for 30 min to form a solid solution with the composition 0.5 $\text{LiBH}_4$ -0.5 $\text{LiNH}_2$ . Subsequently, the solid solution was mixed with the desired amount of oxide in order to fill the pores by 130%. Melt infiltration was carried out at 50 bar  $\text{H}_2$  pressure at 120 °C (2.5 °C  $\text{min}^{-1}$ ) for 30 min. Upon cooling, the molten solid solution recrystallized in the

pores of the support material to form nanoconfined  $\text{LiBH}_4$ - $\text{LiNH}_2$ .

**Characterization of Pristine Materials and Composites.** X-ray diffraction was performed with a Bruker-AXS D-8 Advance X-ray diffractometer with Co  $K\alpha_{1,2}$  radiation ( $\lambda = 1.79026$  Å). The samples were placed in an airtight sample holder, and diffractograms were recorded at room temperature covering a  $2\theta$  range of 10° to 100° for alumina-based samples and of 20 to 80°  $2\theta$  for the silica containing samples as well as the crystalline samples. The increment and scan duration per point was 0.12°  $2\theta$  and 4 s, respectively, for the alumina samples; 0.06°  $2\theta$  and 2 s, respectively, for the silica samples; and 0.03°  $2\theta$  and 1 s, respectively, for the crystalline samples. Rietveld refinement was carried out using the software X'PertHighScore Plus. A Le-Bail fit was applied to analyze the pattern; literature patterns of hexagonal  $\text{LiBH}_4$  taken from the Inorganic Crystal Structure Database served as reference. To refine the patterns, we used the lattice parameters of hexagonal  $\text{LiBH}_4$  as starting values ( $a = 4.28$  Å,  $b = 4.28$  Å,  $c = 6.98$  Å).

Diffuse reflectance infrared Fourier transform spectra (DRIFTS) were obtained by a PerkinElmer 2000 spectrometer and a MCT detector. Sixteen scans were accumulated with a resolution of 4  $\text{cm}^{-1}$  in the range of 500 to 4500  $\text{cm}^{-1}$ . An airtight sample holder (KBr background) guaranteed no air contamination during the measurements. Data acquisition was realized by recording absorbance versus wavenumber. The absorbance is directly converted to K-M units, introduced by Kubleka and Munk, which includes a scattering component and is, therefore, typically used for the analysis of powder samples.

**Conductivity Measurement.** Alternating current (AC) impedance spectroscopy measurements were performed using a Princeton Applied Research Parstat 2273. Lithium foil (Sigma-Aldrich, 99.9%, 0.38 mm thick and 12 mm in diameter leading to a surface of 1.33  $\text{cm}^2$ ) was firmly placed on top of two 13 mm stainless steel dies. A 100–300 mg portion of the electrolyte was placed between the two lithium foils in a standard pellet die set. The sample was pressed using a pressure of 2 tons, resulting in a final electrolyte thickness of 1 to 2 mm, excluding the Li foil. With the weight of the samples, we calculated that the void fraction of the pellets is below 20%. The pressed sample pellet, which is tightly connected to the Li foils and stainless-steel dies, was placed in a custom-made impedance cell housed in a Büchi B-585 glass oven that was placed in an Ar-filled glovebox. The voltage amplitude of the AC signal was 1 V; we measured complex impedances over a frequency range from 1 MHz to 1 Hz. Generally, the pellets were heated from room temperature to 50 or 130 °C (depending on the sample), and then the samples were cooled down to room temperature. During this temperature cycle, impedance scans were acquired in steps of 5 or 10 °C. Before the acquisition of each scan, the measurement cell was allowed to equilibrate at the desired temperature for 45 min (while heating), 90 min (while cooling), and 150 min (for measurements at room temperature). The entire sequence was repeated for 2 to 3 cycles to investigate any hysteresis behavior and to detect any changes of the samples. Matlab and ZView software were used to fit the raw data by using Nyquist plots. A constant phase element (CPE) and a resistor connected in parallel were used as appropriate equivalent circuit to parametrize the data. Capacitances,  $C$ , were calculated according to  $C = R^{(1-n)/n} \times Q^{1/n}$ .  $R$  is the resistance

in  $\Omega$ , i.e., it denotes the real part of the complex impedance;  $Q$  has the numerical value of the admittance at  $\omega = 1 \text{ rad s}^{-1}$ .  $n$  is a dimensionless variable characterizing the deviation of the CPE from the behavior of an ideal RC unit, which would yield  $n = 1$ .

**NMR Line Shape Measurement.** To underpin the findings by conductivity spectroscopy, we recorded  $^7\text{Li}$  (spin-3/2) nuclear magnetic resonance (NMR) spectra at a magnetic field of 7 T, corresponding to a Larmor frequency of 116 MHz, by employing a Bruker Advance III solid-state spectrometer. We used a standard broadband probe to acquire variable-temperature NMR spectra with a one pulse sequence under static, i.e., nonrotating conditions. The  $\pi/2$  pulse length slightly depended on temperature and ranged from 2.1 to 2.3  $\mu\text{s}$ . Such short pulse lengths ensured nonselective excitation of the whole spectra. Up to 16 scans were accumulated to form an average free induction decay, which, after Fourier transformation, yield the  $^7\text{Li}$  NMR spectra. The temperature in the sample chamber was monitored by a Eurotherm controller. Temperature adjustment was achieved, with an accuracy of  $\pm 2\text{K}$ , with a heater that was constantly flushed with a stream of dry nitrogen gas.

### 3. RESULTS AND DISCUSSION

**Structure of  $((1-x)\text{LiBH}_4-x\text{LiI})$  and Its Nanoconfined Counterpart As Seen by XRD and DRIFTS.** First, we discuss the structural properties of (i) the  $\text{LiBH}_4\text{-LiI}$  solid solutions  $((1-x)\text{LiBH}_4-x\text{LiI})$  containing 10 to 40 mol % I ( $x = 0.1, 0.2, 0.3$  and  $0.4$ ) and (ii) the nanocomposites with different oxides viz.  $\gamma\text{-Al}_2\text{O}_3$ , SBA-15, and MCM-41. The compositions of the samples in wt % are given in Table S1. Structural details of the hydrides, oxides, and nanocomposite materials are shown in Figure 1 as well as in Table S2 and Figures S1 to S6. Figure 1 shows the XRD powder pattern of a 20 mol %  $\text{LiI-LiBH}_4$  solid solution and the patterns of the nanocomposites prepared using two different routes, i.e., comet infiltration and impregnation with  $\text{LiI}$  followed by melt infiltration with  $\text{LiBH}_4$ . For comparison, the XRD pattern of  $\text{LiI}$  and the patterns of orthorhombic and hexagonal  $\text{LiBH}_4$  are also included. The influence of  $\text{LiI}$  on the on XRD patterns of the solid solutions and the composites is illustrated in Figures S7 and S8. The patterns shown here are normalized to the highest intensities;  $hkl$  values are added to distinct reflections of  $\text{LiBH}_4$ <sup>58,59</sup> and  $\text{LiI}$ ,<sup>60–62</sup> respectively. The XRD patterns of the  $\text{LiBH}_4\text{-LiI}$  samples with 10 and 20 mol %  $\text{LiI}$  (Figure S7) clearly differ from those of orthorhombic  $\text{LiBH}_4$  and  $\text{LiI}$ . Instead they resemble the pattern of hexagonal  $\text{LiBH}_4$  being the stable phase at elevated temperatures. The reflections in the range from  $27^\circ$  to  $32^\circ$   $2\theta$  are shifted toward lower  $2\theta$  values by approximately  $1^\circ$   $2\theta$ . This shift reveals successful incorporation of  $\text{LiI}$  and is caused by lattice expansion because  $\text{I}^-$  is larger than  $\text{BH}_4^-$ .<sup>35</sup> A similar shift has been reported in literature.<sup>14</sup> Rietveld refinement of the diffraction data for the  $0.8\text{LiBH}_4\text{-}0.2\text{LiI}$  solid solution yielded an hcp unit cell with the following lattice parameters  $a = 4.44 \text{ \AA}$ ,  $b = 4.44 \text{ \AA}$ , and  $c = 7.19 \text{ \AA}$ . Simultaneously with lattice expansion, the density increased from  $0.67 \text{ g/cm}^3$  for bulk  $\text{LiBH}_4$  to  $1.20 \text{ g/cm}^3$  for  $0.8\text{LiBH}_4\text{-}0.2\text{LiI}$ . Samples with more than 20 mol %  $\text{LiI}$  revealed reflections of pure  $\text{LiI}$  indicating a solubility limit for the  $\text{LiBH}_4\text{-LiI}$  system (Figure S7).

Confinement of the  $\text{LiBH}_4\text{-LiI}$  solid solutions in the oxide nanopores led to both broadening and a decrease in intensity of the diffraction peaks (see Figures 1 and S8). Peak

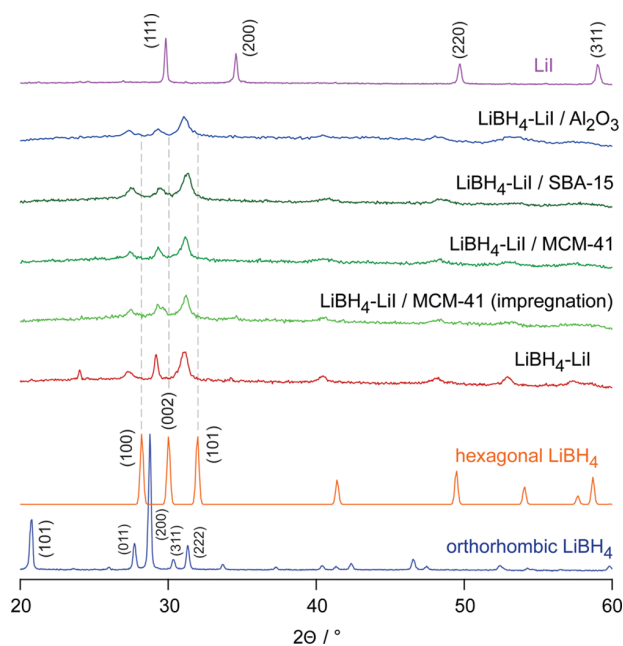


**Figure 1.** XRD powder patterns of the various  $\text{LiBH}_4\text{-LiI}/\text{oxide}$  nanocomposites investigated. For comparison, the positions of the reflection of  $\text{LiBH}_4$  in its hexagonal form are included as well. In addition, the pattern of  $\text{LiBH}_4\text{-LiI}$  (20 mol % of  $\text{LiI}$ ) and  $\text{LiI}$  are also shown. Values in brackets refer to  $hkl$  indices. The shift of the reflections toward lower diffraction angles indicates successful incorporation of  $\text{LiI}$  that stabilizes the hexagonal form of  $\text{LiBH}_4$ .

broadening is expected because of size effects and lattice strain, whereas the decrease in intensity suggests a decrease in the long-range order. Note, however, that the composites shown here contain 30 vol % more  $\text{LiBH}_4\text{-LiI}$  than is required to fill all the pores of the scaffold. This is essential for interconnectivity between the  $\text{LiBH}_4$  particles. For the nanocomposites with  $\text{LiBH}_4\text{-LiI} \leq 100\%$  of the total pore volume of the scaffold, no crystalline phase was observed. Thus, we conclude that nanoconfinement led to a significant decrease in crystallinity of the samples. The similarity in the diffraction patterns of the nanocomposites prepared using the different methods (Figure 1) suggests that both methods are useful for the preparation of  $\text{LiBH}_4\text{-LiI}/\text{metal oxide}$  solutions. Moreover, the use of different oxide supports did not lead to major differences in the XRD patterns of the nanocomposites.

Further evidence for successful incorporation of the solid solutions into the oxide pores is provided by nitrogen physisorption measurements. The measurements showed that only a negligible amount of nitrogen was adsorbed by the nanocomposites. This finding proved that the pores were occupied by the electrolyte  $\text{LiBH}_4\text{-LiI}$ .

DRIFTS was used to investigate the nature of chemical bonding in the different samples prepared. In Figure 2 the spectrum of the  $\text{LiBH}_4\text{-LiI}/\text{Al}_2\text{O}_3$  nanocomposite is compared to spectra of bulk  $\text{LiBH}_4$ ,  $\text{LiBH}_4\text{-LiI}$ , and pristine  $\text{Al}_2\text{O}_3$ . The spectra are presented in arbitrary K-M units (for further explanation see the Experimental Section). Macrocrystalline, that is, bulk  $\text{LiBH}_4$ , shows characteristic bands between  $1000$  and  $1500 \text{ cm}^{-1}$  which correspond to  $[\text{BH}_4]^-$  bending vibrations; bands appearing in the range from  $2000$  to  $2800 \text{ cm}^{-1}$  can be associated with stretching vibrations in  $[\text{BH}_4]^-$ .<sup>63,64</sup> The most preeminent bands of  $\text{LiBH}_4$  are marked

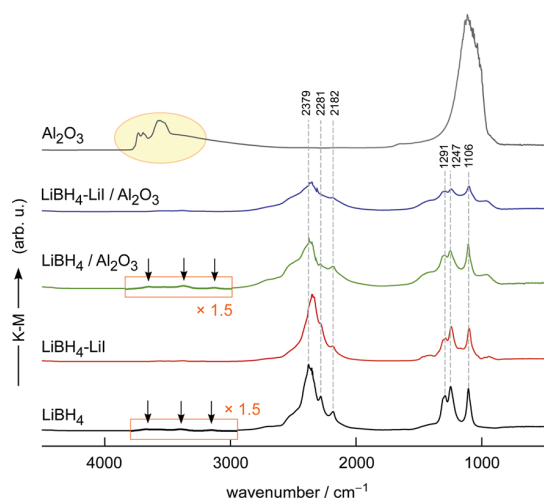


**Figure 2.** DRIFT spectra of  $\text{Al}_2\text{O}_3$ , nanoconfined  $\text{LiBH}_4\text{-LiI}/\text{Al}_2\text{O}_3$ , nanoconfined  $\text{LiBH}_4/\text{Al}_2\text{O}_3$ , and  $\text{LiBH}_4\text{-LiI}$  (20 mol % of LiI). For comparison, the spectrum of  $\text{LiBH}_4$  is also shown. Main peaks are marked by vertically drawn dashed lines with the wavenumbers indicated. K-M intensities (see the ordinate axis) are in arbitrary units. See text for further explanation.

with dashed lines in gray color; the corresponding wavenumbers are indicated. The spectrum of the  $\text{LiBH}_4\text{-LiI}$  solution resembles that of  $\text{LiBH}_4$ , the band characterizing the stretching vibrations ( $2379\text{ cm}^{-1}$ ) is, however, slightly shifted toward a lower wavenumber. Most likely, this shift is due to the effect of negative chemical pressure resulting from an increased unit cell by addition of I, as previously observed for halide-substituted  $\text{BH}_4$ .<sup>65</sup> Also, a stronger electronic interaction between iodine and Li, because of the higher electronegativity of the halides compared to  $\text{BH}_4^-$ , can lead to such a change in vibration frequencies.<sup>66</sup> For  $\text{LiBH}_4\text{-LiI}/\text{Al}_2\text{O}_3$ , the bands are clearly broadened due to nanoconfinement. A similar broadening effect is also observed for  $\text{LiBH}_4/\text{Al}_2\text{O}_3$ . It suggests that the structure of the confined materials is different from the bulk compound. This observation is in line with previous studies on nanoconfined  $\text{LiBH}_4$ .<sup>67–69</sup>

Interestingly, the bands of  $\text{Al}_2\text{O}_3$  in the region from  $3400$  to  $3800\text{ cm}^{-1}$ , representing OH surface groups,<sup>70</sup> almost disappear after the pores are filled with electrolyte; see the vertical arrows in Figure 2. The same behavior is found for the characteristic vibrations of the surface OH-silanol groups of silica<sup>71,72</sup> in the samples  $\text{LiBH}_4/\text{SiO}_2$ ,  $\text{LiI}/\text{SiO}_2$ , and  $\text{LiBH}_4\text{-LiI}/\text{SiO}_2$  (see Figures S9 and S10). Interaction of  $\text{LiBH}_4$  with the surface is the origin of the high ionic conductivity of  $\text{LiBH}_4/\text{oxide}$  nanocomposites.

**Ionic Conductivity of Nanoconfined  $\text{LiBH}_4\text{-LiI}$ .** To evaluate the effects of different LiI concentrations on ionic conductivity, we recorded complex impedance data at different temperatures and analyzed the results in the Nyquist representation; see Figure 3. An overview of results from impedance spectroscopy of the  $\text{LiBH}_4\text{-LiI}$  solid solutions and the nanocomposites is given in Table S3 and Figure S11. The overall ionic conductivity of the confined and pure solid solutions increased with increasing amounts of added LiI. At LiI contents higher than 20 mol %, the conductivity started to decrease (Figure S12). This is in line with results from XRD pointing to crystalline (unreacted) LiI above this composi-

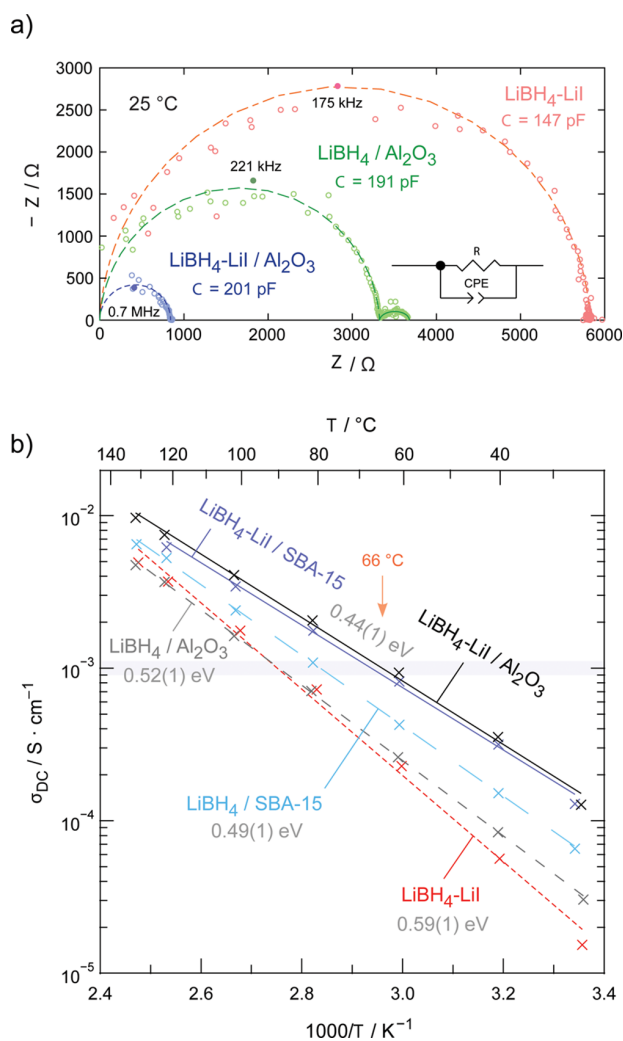


**Figure 3.** (a) Nyquist plots, that is, the imaginary part,  $-Z''$ , of the complex impedance plotted versus the real part  $Z'$ , of nanoconfined  $\text{LiBH}_4\text{-LiI}/\text{Al}_2\text{O}_3$  and  $\text{LiBH}_4/\text{Al}_2\text{O}_3$ . The  $\text{LiBH}_4\text{-LiI}$  sample (20 mol % LiI) is also shown. Values in pF show the capacitances obtained after parametrizing the main (nondepressed) semicircles with the equivalent circuit shown; see also Experimental section. The line approximating the second semicircle of the curve belonging to  $\text{LiBH}_4/\text{Al}_2\text{O}_3$ , which shows up at higher frequencies, is drawn to guide the eye. (b) Arrhenius plot (half-logarithmic plot of  $\sigma'$  vs  $1000/T$ ) to illustrate the change of conductivity with increasing temperature. Dashed and solid lines represent linear fits to determine activation energies  $E_A$ , which range from  $0.44(1)\text{ eV}$  to  $0.59(1)\text{ eV}$ . Nanoconfined  $\text{LiBH}_4\text{-LiI}/\text{Al}_2\text{O}_3$  shows the highest conductivities. At room temperature ( $25\text{ °C}$ ), its ion conductivity is slightly larger than  $10^{-4}\text{ S cm}^{-1}$ ; a conductivity of  $10^{-3}\text{ S cm}^{-1}$ , needed to realize Li-ion batteries, is reached at  $66\text{ °C}$ .

tional limit. Hence, the sample  $\text{LiI-LiBH}_4$  with 20 mol % LiI was chosen for a more detailed study.

Figure 3a shows the corresponding Nyquist plot recorded at  $25\text{ °C}$ ; in Figure 3b, the temperature dependence of the ionic conductivity is displayed using an Arrhenius plot. For comparison, the Nyquist plots and conductivity data referring to  $\text{LiBH}_4\text{-LiI}$  and nanoconfined  $\text{LiBH}_4$  are also shown. Capacitances  $C$  ranged from 147 to 210 pF; values larger than 100 pF typically indicate electrical relaxation processes influenced by interfacial regions.<sup>73</sup> For nanoconfined compo-

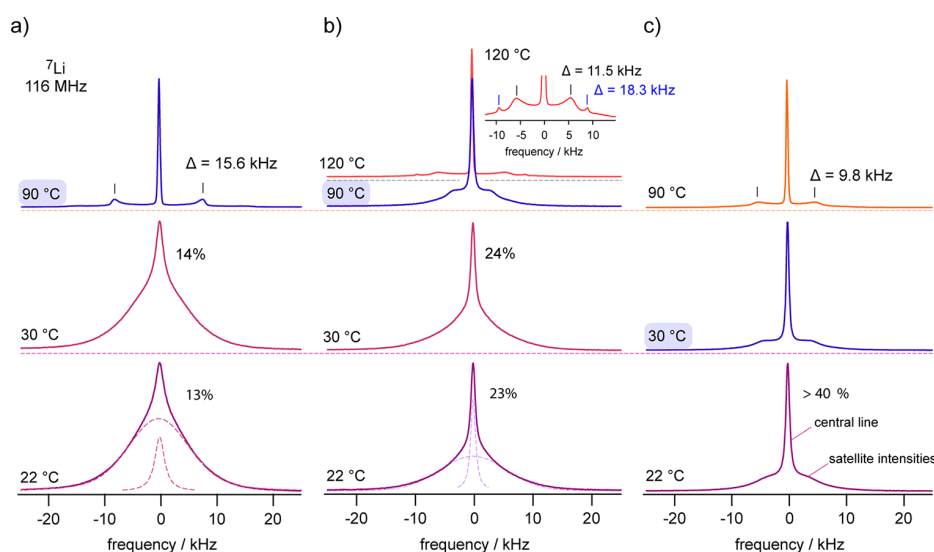


**Figure 4.**  $^7\text{Li}$  NMR spectra of (a)  $\text{LiBH}_4\text{-LiI}$ , (b) nanoconfined  $\text{LiBH}_4/\text{Al}_2\text{O}_3$  without  $\text{LiI}$ , and (c) nanoconfined  $\text{LiBH}_4\text{-LiI}/\text{Al}_2\text{O}_3$ . Spectra were recorded at a Larmor frequency of 116 MHz at the temperatures indicated. Dashed lines in parts a and b show the deconvolution of the entire line with appropriate Gaussian and Lorentzian functions to estimate the number fraction of mobile Li ions in these compounds. For  $\text{LiBH}_4\text{-LiI}/\text{Al}_2\text{O}_3$ , the spectrum has almost adopted its final form at temperatures as low as 30 °C. While the sharp line represents fast Li ions, the broader foot comprises both the central line of a fraction of slower Li ions and quadrupole intensities. The latter become visible as a sharp powder pattern at elevated temperature where dipole–dipole interactions are effectively averaged out due to rapid  $\text{Li}^+$  exchange. See text for further information.

sites, it is widely believed that ion transport mainly occurs along the heterogeneous solid–solid interphase, that is, at the interface between the insulating oxide and the electrolyte.<sup>41–43</sup> The exponents  $n$  turned out to take values close to 1 meaning that the corresponding CPEs (constant phase elements) of all three samples behaved almost like an ideal RC unit. This observation is in line with the interpretation that the semicircle seen in the complex plane plot is governed by a response strongly influenced by grain boundary effects.

For  $\text{LiBH}_4/\text{Al}_2\text{O}_3$ , a second semicircle is seen at lower frequencies, which is either too small to be detected or is absent in  $\text{LiBH}_4\text{-LiI}$  and  $\text{LiBH}_4\text{-LiI}/\text{Al}_2\text{O}_3$ . The presence of the second semicircle suggests two different conducting phases. We attribute the main semicircle with the higher electrical relaxation rate to  $\text{LiBH}_4$  interacting with the oxide surface and the semicircle appearing at lower frequencies to  $\text{LiBH}_4$ , which is farther away from the interface. This feature is also seen in  $^7\text{Li}$  NMR spectroscopy; see Figure 4. We suppose that the addition of  $\text{LiI}$  led to both an increase of the high conducting regions and an enhancement of interfacial conductivity. Thus, for  $\text{LiBH}_4\text{-LiI}/\text{Al}_2\text{O}_3$ , the two contributions could not be resolved any longer when data recorded at 25 °C were analyzed.

The Arrhenius plot shown in Figure 3b shows that ion transport at temperatures lower than 100 °C is clearly faster in the nanocomposites  $\text{LiBH}_4\text{-LiI}/\text{Al}_2\text{O}_3$  and  $\text{LiBH}_4\text{-LiI}/\text{SiO}_2$  than in  $\text{LiBH}_4\text{-LiI}$  and the nanoconfined samples  $\text{LiBH}_4/\text{Al}_2\text{O}_3$  and  $\text{LiBH}_4/\text{SiO}_2$ . For instance, at room temperature (25 °C), the ionic conductivity of  $\text{LiBH}_4\text{-LiI}/\text{Al}_2\text{O}_3$  (0.1 mS  $\text{cm}^{-1}$ ) was four times higher than that of  $\text{LiBH}_4/\text{Al}_2\text{O}_3$  and eight times higher than that of  $\text{LiBH}_4\text{-LiI}$ . In agreement with the trend for the increase in ionic conductivity, the activation energy for long-range ion transport decreased from 0.52(1) eV for  $\text{LiBH}_4/\text{oxide}$  to 0.44(1) eV for  $\text{LiBH}_4\text{-LiI}/\text{oxide}$ .  $\text{LiBH}_4\text{-LiI}$  showed a rather high activation energy of 0.59 eV. These

values are similar to those reported in literature for  $\text{LiBH}_4/\text{Al}_2\text{O}_3$  and  $\text{LiI-LiBH}_4$  systems.<sup>35,41</sup>

$^7\text{Li}$  NMR line shapes of these samples, which have been recorded at room temperature and above, clearly revealed that  $\text{Li}^+$  acts as mobile charge carrier.<sup>74</sup> Selected lines are shown in Figure 4. For the  $\text{LiBH}_4\text{-LiI}$  solid solution (see Figure 4a), the line at room temperature is composed of two contributions. The narrow line on top of the broader signal reflects the mobile Li spins whose jump rates exceed the line widths of this line in the rigid lattice, which turns out to be approximately 13 kHz. Narrow NMR lines are caused by sufficiently fast  $\text{Li}^+$  exchange processes able to average local dipole–dipole interactions that lead to line broadening at low temperatures. In the case of  $\text{LiBH}_4\text{-LiI}$ , the line shape did not change much when going to 30 °C; however, a significant change was seen at 90 °C where a fully narrowed central line appeared, that is, on top of a quadrupole powder pattern. This distinct pattern, showing sharp 90° singularities separated by  $\Delta = 15.6$  kHz, is characteristic for hexagonal  $\text{LiBH}_4\text{-LiI}$ . A similar situation is seen for nanoconfined  $\text{LiBH}_4/\text{Al}_2\text{O}_3$  (see Figure 4b). However, the number fraction of rapid  $\text{Li}^+$  ions was higher at 22 and 30 °C (24%) compared to that seen for nonconfined  $\text{LiBH}_4\text{-LiI}$ . This difference is in line with the slightly higher conductivity seen for  $\text{LiBH}_4/\text{Al}_2\text{O}_3$ . It is worth noting that the motionally narrowed spectra recorded at 90 °C and at 120 °C were governed by electric quadrupole intensities being different than those of bulk  $\text{LiBH}_4$  and bulk  $\text{LiBH}_4\text{-LiI}$ . The spectra of nonconfined  $\text{LiBH}_4$  and nonconfined  $\text{LiBH}_4\text{-LiI}$  reveal patterns produced by a symmetric electric field gradient (EFG) the ions were subjected to. They agree with those of similar systems studied earlier.<sup>40</sup>

In contrast to the nonconfined samples, the NMR line of nanoconfined  $\text{LiBH}_4/\text{Al}_2\text{O}_3$  recorded at 90 °C shows a nonsymmetric EFG. Its shape points to structural disorder and strain which the Li spins sense.  $\Delta$  reduces from 15.6 to 11.5 kHz. Careful inspection of the powder pattern shows that

another set of singularities is present (see inset of Figure 4b), which is characterized by  $\Delta = 18.3$  kHz. Assuming axial symmetry for this pattern, we obtained a quadrupole coupling constant  $\delta_q$  of ca. 36.6 kHz which was identical to that of bulk  $\text{LiBH}_4$  ( $\delta_q = 37$  kHz).<sup>75</sup> The two quadrupole patterns represent the Li ions near the insulator surface ( $\Delta = 11.5$  kHz) and the ions farther away, that is, located in the bulk regions ( $\Delta = 18.3$  kHz). NMR revealed that these two species are exposed to different electric interactions. Two sources of electrical relaxation have also been seen in the corresponding Nyquist plot, vide supra.

For nanoconfined  $\text{LiBH}_4\text{-LiI}/\text{Al}_2\text{O}_3$  (Figure 4c), we also observed a quadrupole powder pattern that is characterized by a lower  $\Delta$  ( $= 9.5$  kHz) than that expected for bulk  $\text{LiBH}_4(-\text{LiI})$ . However, a pronounced pattern attributable to Li ions in bulk  $\text{LiBH}_4\text{-LiI}$ , as seen for  $\text{LiBH}_4/\text{Al}_2\text{O}_3$ , was missing. Instead, already at temperatures as low as 30 °C, an almost fully narrowed <sup>7</sup>Li NMR line was observed which clearly points to very fast ion dynamics in this nanocomposite.<sup>74</sup> We conclude that the majority of ions in this nanocomposite take part in rapid  $\text{Li}^+$  exchange, which perfectly agrees with the conductivity trend seen in Figure 3b. From a structural point of view, the single EFG pattern observed points to a homogeneous sample as compared to nanoconfined  $\text{LiBH}_4/\text{Al}_2\text{O}_3$ . Presumably, if the ions reside in areas farther away from the surface of the oxide, they are subjected to a structurally stressed  $\text{LiBH}_4\text{-LiI}$  phase with high ionic conductivity. This modified region, e.g., influenced by space charge zones, regions with higher defect density or increased structural disorder, may extend over almost the whole  $\text{LiBH}_4\text{-LiI}$  phase leading to the enhancement in conductivity observed.

Note that all our samples were prepared under the same conditions and, therefore, the remarkable increase in ionic conduction for  $\text{LiBH}_4\text{-LiI}/\text{Al}_2\text{O}_3$  seen by impedance spectroscopy and <sup>7</sup>Li NMR is mainly attributed to the combined effects of anion substitution and interface engineering by nanoconfinement. Table 1 compares conductivities, activation

energies, and Arrhenius prefactors of the samples investigated. The slight differences in ionic conductivity of the nanocomposites prepared with different oxides (SBA-15, MCM-41, or  $\text{Al}_2\text{O}_3$ ) are most likely due to differences in properties of these materials (see Figures S1 to S6 and Table S2). For example, the oxides differ in morphology, pore size, and pore size distribution, surface area, surface/interface energy, density of the surface groups, and the nature of the pores (e.g., pore corrugations). Detailed elucidation of the exact influence of these properties on ionic conductivity is, however, beyond the scope of the present work.

**Importance of  $\text{LiBH}_4(-\text{LiI})/\text{Oxide}$  Interface.** To further demonstrate that both the interaction of  $\text{LiBH}_4$  with the oxide interface and partial anion substitution are important for the enhancement in ionic conductivity, we employed a preparation technique that is supposed to hinder the interaction of  $\text{LiBH}_4$  with the oxide interface but still form  $\text{LiBH}_4\text{-LiI}$  in the pores. This comparison showed that the nanocomposites prepared by coinfiltration of a physical mixture of  $\text{LiBH}_4$  and  $\text{LiI}$  exhibited much higher conductivities than those which were prepared via solution impregnation (Table 1). If we first add  $\text{LiI}$  to fill the pores via impregnation with  $\text{LiI}/\text{H}_2\text{O}$  or  $\text{LiI}/\text{C}_2\text{H}_5\text{OH}$  solution and then add  $\text{LiBH}_4$  by melt infiltration as a second step, we see that the resulting ionic conductivity is significantly lower. At first glance, this difference is surprising as results from XRD and IR (DRIFTS) suggest that both samples have similar structures (cf. Figure 1 and Figure S9). We attribute the marked change seen in conductivity to the fact that if  $\text{LiI}$  is added first, we do not have the original  $\text{SiOH}$  groups present at the interface anymore (see Figure S9 for the loss of silanol groups in  $\text{LiI}/\text{SiO}_2$ ). This changed the properties of the interface with the  $\text{LiBH}_4$ , and as a result, the conductivity is not as high as that with the other preparation technique.

**$\text{LiBH}_4\text{-LiNH}_2$  System.** To demonstrate the general applicability of the strategy outlined above, we measured also the conductivity of another nanoconfined electrolyte containing two complex anions, i.e., nanoconfined  $\text{LiBH}_4\text{-LiNH}_2$ . XRD revealed the formation of two new phases, namely,  $\text{Li}_2(\text{BH}_4)(\text{NH}_2)$  and  $\text{Li}_4(\text{BH}_4)(\text{NH}_2)_3$  (see Figure 5a). This is unlike the  $\text{LiBH}_4\text{-LiX}$  systems where the high temperature phase of  $\text{LiBH}_4$  was stabilized through the replacement of  $\text{BH}_4^-$  by halides causing lattice strain but no change in crystal structure. For nanoconfined  $\text{LiBH}_4\text{-LiNH}_2/\text{MCM-41}$ , XRD points to a loss of crystallinity, that is, long-range order. As mentioned above, the same feature was observed for the  $\text{LiBH}_4\text{-LiI}$  solid solutions. In addition, results from DRIFTS measurements (see Figure 5b) revealed that the characteristic vibrations related to  $\text{LiBH}_4\text{-LiNH}_2$ , (1000 to 1500  $\text{cm}^{-1}$  and 2000 to 2800  $\text{cm}^{-1}$  ( $\text{BH}_4^-$ ), 1500 to 1600  $\text{cm}^{-1}$  and 3200 to 3300  $\text{cm}^{-1}$  ( $\text{NH}_2^-$ ), shifted toward lower wavenumbers and became significantly broader upon nanoconfinement. The bands related to the surface silanol groups (3700  $\text{cm}^{-1}$ ) were absent, as seen for nanoconfined  $\text{LiBH}_4\text{-LiI}$ . Hence, we conclude that the  $\text{LiBH}_4\text{-LiNH}_2$  composite was successfully infiltrated into the nanopores of MCM-41 leading to profound changes of its structure.<sup>66</sup>

In Figure 6, the ionic conductivities of selected  $\text{LiBH}_4\text{-LiNH}_2$  samples are shown. First, when compared to  $\text{LiBH}_4$ , it is clear that the addition of  $\text{LiNH}_2$  to  $\text{LiBH}_4$  increases the room temperature ionic conductivity by approximately 2 orders of magnitude. This increase is ascribed to the formation of  $\text{Li}_2(\text{BH}_4)(\text{NH}_2)$ .<sup>39</sup> The sudden increase in conductivity of  $\text{Li}_2(\text{BH}_4)(\text{NH}_2)$  at approximately 35 °C originates from a

**Table 1. Room Temperature Conductivities ( $\sigma$ ) of the Samples Studied by Impedance Spectroscopy<sup>a</sup>**

| sample   | $\sigma$ (25 °C) (S $\text{cm}^{-1}$ ) | $E_A$ (eV)                                   | $\log_{10}(A)$ (S $\text{cm}^{-1}\text{K}$ ) |
|--|--|--|--|
| $\text{LiBH}_4/\text{MCM-41}$  | $2.29 \times 10^{-5}$                  | 0.49(2)                                      | 6.0(3)                                       |
| $\text{LiBH}_4\text{-LiI}/\text{MCM-41}$ comelt infiltration                   | $3.86 \times 10^{-5}$                  | 0.43(1)                                      | 5.3(1)                                       |
| $\text{LiBH}_4\text{-LiI}/\text{MCM-41}$ impregnation ( $\text{H}_2\text{O}$ ) | $1.63 \times 10^{-5}$                  | 0.52(2)                                      | 6.5(3)                                       |
| $\text{LiBH}_4\text{-LiI}/\text{MCM-41}$ impregnation ( $\text{EtOH}$ )        | $4.57 \times 10^{-6}$                  | 0.47(0)                                      | 5.2(1)                                       |
| $\text{LiBH}_4\text{-LiI}/\text{SBA-15}$ comelt infiltration                   | $1.29 \times 10^{-4}$                  | 0.44(1)                                      | 6.0(2)                                       |
| $\text{LiBH}_4\text{-LiI}/\text{Al}_2\text{O}_3$ comelt infiltration           | $1.27 \times 10^{-4}$                  | 0.44(1)                                      | 6.1(1)                                       |
| $\text{LiBH}_4\text{-LiI}$   | $1.54 \times 10^{-5}$                  | 0.59(2)                                      | 7.8(3)                                       |
| $\text{LiBH}_4\text{-LiNH}_2$  | $2.92 \times 10^{-6}$                  | 1.03(1) <sup>a</sup><br>0.19(1) <sup>b</sup> | 1.8(1) <sup>a</sup><br>13(1) <sup>b</sup>    |
| $\text{LiBH}_4\text{-LiNH}_2/\text{MCM-41}$                                    | $1.16 \times 10^{-4}$                  | 0.43(1) <sup>c</sup>                         | 5.5(2)                                       |

<sup>a</sup> $E_A$  determined in the temperature range from 30 to 50 °C. <sup>b</sup> $E_A$  determined in the temperature range from 60 to 85 °C. <sup>c</sup> $E_A$  determined in the temperature range from 30 to 85 °C. <sup>d</sup>The table also includes activation energies ( $E_A$ ) and pre-factors ( $\log_{10}(A)$ ) of the Arrhenius laws used to approximate the temperature dependence of the ionic conductivity. If not stated otherwise,  $E_A$  has been determined in the temperature range from 25 to 130 °C.

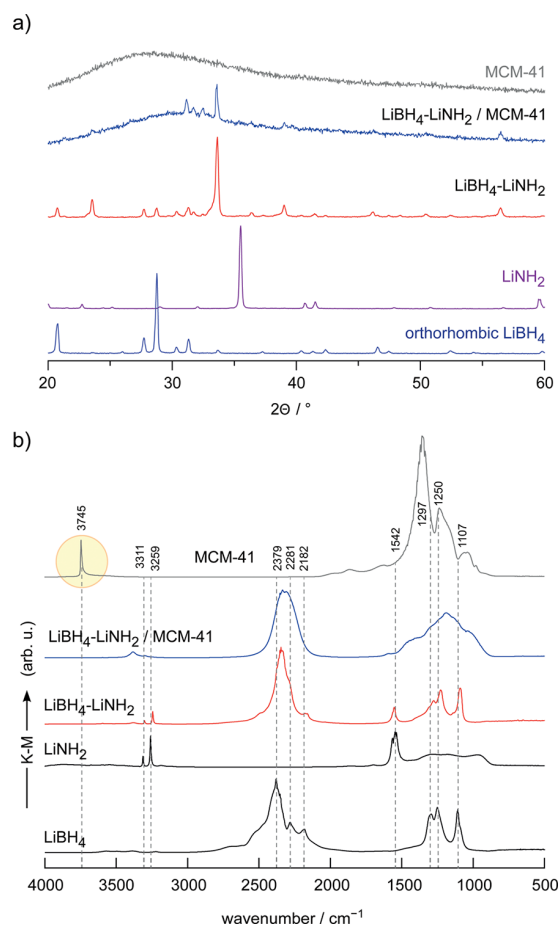


**Figure 5.** (a) X-ray powder diffraction patterns of nanoconfined and nonconfined  $\text{LiBH}_4\text{-LiNH}_2$ . For comparison, the expected patterns of orthorhombic  $\text{LiBH}_4$  and  $\text{LiNH}_2$  are also shown. The pattern at the top represents that of the oxide substrate,  $\text{SiO}_2$ . (b) DRIFT spectra of the samples shown in part a; the spectra reveal broadening of the signals, which shift toward lower wavenumbers upon nanoconfinement. Those bands which result from silanol OH groups are absent for  $\text{LiBH}_4\text{-LiNH}_2/\text{SiO}_2$  indicating surface reactions between the electrolyte and the surface of the oxide. See text for further explanation.

structural phase change leading to a highly conducting phase at temperature higher than  $40^\circ\text{C}$ . Nanoconfined  $\text{LiBH}_4\text{-LiNH}_2/\text{MCM-41}$  showed an even better ionic conductivity at this temperature; remarkably, this high ionic conductivity was also preserved at lower temperatures. When compared to  $\text{LiBH}_4$  and  $\text{LiBH}_4\text{-LiNH}_2$ , the room temperature ionic conductivity of nanoconfined  $\text{LiBH}_4\text{-LiNH}_2/\text{MCM-41}$  was higher by 4 and 2 orders of magnitude, respectively. It also exceeded that of nanoconfined  $\text{LiBH}_4/\text{MCM-41}$  by a factor of 2 if conductivities at  $T = 30^\circ\text{C}$  were considered (cf. Figure 6). At approximately  $50^\circ\text{C}$ ,  $\text{LiBH}_4\text{-LiNH}_2/\text{MCM-41}$  reached a conductivity of  $1\text{ mS cm}^{-1}$ . Below  $45^\circ\text{C}$ , the overall activation energy governing ion transport in  $\text{LiBH}_4\text{-LiNH}_2/\text{MCM-41}$  ( $0.43\text{ eV}$ ) is comparable to that of bulk  $\text{LiBH}_4$  and significantly lower than that of  $\text{LiBH}_4\text{-LiNH}_2$  at room temperature. For  $\text{LiBH}_4/\text{MCM-41}$  and  $\text{LiBH}_4\text{-LiNH}_2$  at higher temperatures, we see that  $E_A$  is somewhat lower,  $0.26$  and  $0.19\text{ eV}$ , respectively; see Figure 6 and Table 1. On the basis of the results from the DRIFTS measurements, the remarkable

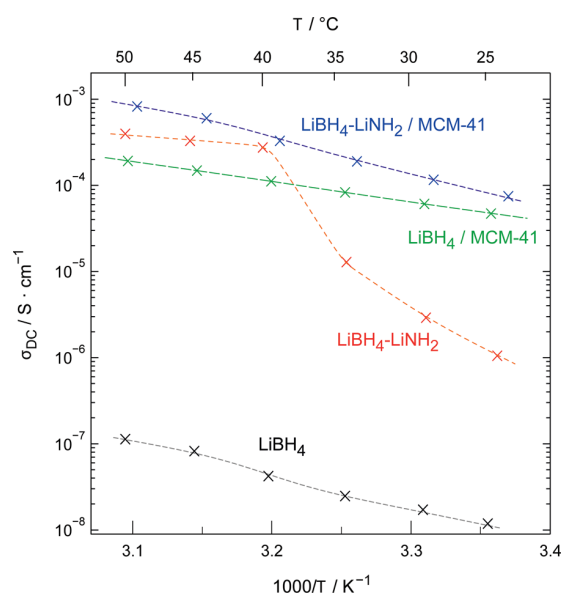


**Figure 6.** Ionic conductivity of nanoconfined  $\text{LiBH}_4\text{-LiNH}_2/\text{SiO}_2$  as a function of the inverse temperature. For comparison, data on  $\text{LiBH}_4/\text{SiO}_2$ , nonconfined  $\text{LiBH}_4\text{-LiNH}_2$  and bulk  $\text{LiBH}_4$  are also included. The lines are to guide the eye.

increase in ionic conductivity is again attributed to the combined effect of anion substitution and interface effects, as observed for nanoconfined  $\text{LiBH}_4\text{-LiI}$ . These results illustrate that the synergistic effects of nanoconfinement, that is, interface engineering, and partial ion substitution is applicable to different Li-based electrolytes in various nonconducting nanoporous scaffolds.

#### 4. CONCLUSION

We have shown how two routes, namely, ion substitution and interface engineering, can be effectively combined to enhance the ionic conductivity of solid-state electrolytes. Using complex hydrides as model systems, we developed an approach where anion substituted  $\text{LiBH}_4$  ( $\text{Li}_2(\text{BH}_4)_x\text{I}_{1-x}$  and  $\text{Li}_2(\text{BH}_4)_x(\text{NH}_2)_{1-x}$ ) are confined in nanoporous  $\text{SiO}_2$  or  $\text{Al}_2\text{O}_3$  in order to exploit both the effect of ion substitution and nanoconfinement or interface engineering to boost the Li-ion conductivities of  $\text{LiBH}_4$  at ambient conditions. Indeed, the ionic conductivity of the nanocomposites of  $\text{LiBH}_4\text{-LiI}/\text{Al}_2\text{O}_3$  reached  $0.1\text{ mS cm}^{-1}$  at room temperature. The room temperature conductivities of nonsubstituted  $\text{LiBH}_4/\text{Al}_2\text{O}_3$  and  $\text{LiBH}_4\text{-LiI}$  without nanoconfinement were 1 order of magnitude lower. Activation energies are in line with this trend, with  $0.44$ ,  $0.52$ , and  $0.59\text{ eV}$  for the  $\text{LiBH}_4\text{-LiI}/\text{Al}_2\text{O}_3$ ,  $\text{LiBH}_4/\text{Al}_2\text{O}_3$ , and  $\text{LiBH}_4\text{-LiI}$ , respectively. Detailed structural investigations and  $^7\text{Li}$  NMR line shape measurements show that the combined effects of interaction with the interface of the oxides and phase stabilization due to partial anion substitution (by the iodide anion) produces faster  $\text{Li}^+$  diffusion pathways in  $\text{LiBH}_4\text{-LiI}/\text{oxide}$  than those in the case of  $\text{LiBH}_4/\text{oxide}$  and  $\text{LiBH}_4\text{-LiI}$ . Results on  $\text{LiBH}_4\text{-LiNH}_2$  confined in mesoporous silica (MCM-41) show that this concept is also applicable to other Li-bearing hydrides. The enhancement effect depends also on the type and property of the scaffold. Our study clearly shows that combining partial anion substitution and nanoconfinement is a very promising

approach to achieve high room temperature ionic conductivities in solid-state ion conductors.

## ■ ASSOCIATED CONTENT

### Supporting Information

The Supporting Information is available free of charge at <https://pubs.acs.org/doi/10.1021/acs.jpcc.9b10607>.

Calculation of the amount of material needed for melt infiltration to reach the desired pore filling; physisorption data; high-resolution scanning electron microscopy images; additional XRD patterns and DRIFTS data; further conductivity Arrhenius plot comparing different supports; comparison of room temperature conductivity values of samples with varying LiI content (0 to 40 mol %) (PDF)

## ■ AUTHOR INFORMATION

### Corresponding Authors

**Petra E. de Jongh** – *Inorganic Chemistry and Catalysis, Debye Institute for Nanomaterials Science, Utrecht University, 3584 CG Utrecht, Netherlands*; [orcid.org/0000-0002-2216-2620](https://orcid.org/0000-0002-2216-2620); Email: [P.E.deJongh@uu.nl](mailto:P.E.deJongh@uu.nl)

**Peter Ngene** – *Inorganic Chemistry and Catalysis, Debye Institute for Nanomaterials Science, Utrecht University, 3584 CG Utrecht, Netherlands*; [orcid.org/0000-0003-3691-0623](https://orcid.org/0000-0003-3691-0623); Email: [P.ngene@uu.nl](mailto:P.ngene@uu.nl)

### Authors

**Roman Zettl** – *Institute for Chemistry and Technology of Materials, and Christian Doppler Laboratory for Lithium Batteries, Graz University of Technology (NAWI Graz), 8010 Graz, Austria; Inorganic Chemistry and Catalysis, Debye Institute for Nanomaterials Science, Utrecht University, 3584 CG Utrecht, Netherlands*

**Laura de Kort** – *Inorganic Chemistry and Catalysis, Debye Institute for Nanomaterials Science, Utrecht University, 3584 CG Utrecht, Netherlands*

**Maria Gombotz** – *Institute for Chemistry and Technology of Materials, and Christian Doppler Laboratory for Lithium Batteries, Graz University of Technology (NAWI Graz), 8010 Graz, Austria*

**H. Martin R. Wilkening** – *Institute for Chemistry and Technology of Materials, and Christian Doppler Laboratory for Lithium Batteries, Graz University of Technology (NAWI Graz), 8010 Graz, Austria*; [orcid.org/0000-0001-9706-4892](https://orcid.org/0000-0001-9706-4892)

Complete contact information is available at: <https://pubs.acs.org/doi/10.1021/acs.jpcc.9b10607>

### Author Contributions

R.Z. and L.d.K. contributed equally to this work.

### Notes

The authors declare no competing financial interest.

## ■ ACKNOWLEDGMENTS

We greatly appreciate funding from the NWO materials for sustainability (Mat4Sus-739.017.009) and NWO-ECHO (712.015.005) grants. P.N. received funding from the European Research Council (ERC) under the European Union's Horizon 2020 research and innovation programme (ERC-2014-CoG No 648991). R.Z. and H.M.R.W. thank the Austrian Federal Ministry for Science, Research and Economy

as well as the Christian-Doppler Forschungsgesellschaft for financial support; further support by the FFG (The Austrian Research Promotion Agency) in the frame of the project Safe Battery is also acknowledged. R.Z. thanks the project SOLABAT (project no. 853627) funded by the Klima- und Energiefonds of FFG for additional support. Furthermore, we thank Sander Lambregts and Hans Meeldijk for physisorption and SEM measurements as well as Oscar Brandt Corstius for the synthesis of MCM-41.

## ■ REFERENCES

- (1) Manthiram, A.; Yu, X. W.; Wang, S. F. Lithium battery chemistries enabled by solid-state electrolytes. *Nat. Rev. Mater.* **2017**, *2* (4), 16103.
- (2) Janek, J.; Zeier, W. G. A solid future for battery development. *Nat. Energy* **2016**, *1*, 16141.
- (3) Mikhaylik, Y. V.; Akridge, J. R. Polysulfide shuttle study in the Li/S battery system. *J. Electrochem. Soc.* **2004**, *151* (11), A1969–A1976.
- (4) Kim, J. G.; Son, B.; Mukherjee, S.; Schuppert, N.; Bates, A.; Kwon, O.; Choi, M. J.; Chung, H. Y.; Park, S. A review of lithium and non-lithium based solid state batteries. *J. Power Sources* **2015**, *282*, 299–322.
- (5) Sun, C. W.; Liu, J.; Gong, Y. D.; Wilkinson, D. P.; Zhang, J. J. Recent advances in all-solid-state rechargeable lithium batteries. *Nano Energy* **2017**, *33*, 363–386.
- (6) Knauth, P. Inorganic solid Li ion conductors: An overview. *Solid State Ionics* **2009**, *180* (14–16), 911–916.
- (7) Takada, K. Progress and prospective of solid-state lithium batteries. *Acta Mater.* **2013**, *61* (3), 759–770.
- (8) Li, J. C.; Ma, C.; Chi, M. F.; Liang, C. D.; Dudney, N. J. Solid electrolyte: the key for high-voltage lithium batteries. *Adv. Energy Mater.* **2015**, *5* (4), 1401408.
- (9) Thangadurai, V.; Narayanan, S.; Pinzaru, D. Garnet-type solid-state fast Li ion conductors for Li batteries: Critical review. *Chem. Soc. Rev.* **2014**, *43* (13), 4714–4727.
- (10) Bohnke, O.; Bohnke, C.; Fourquet, J. L. Mechanism of ionic conduction and electrochemical intercalation of lithium into the perovskite lanthanum lithium titanate. *Solid State Ionics* **1996**, *91*, 21–31.
- (11) Li, J.; Lin, Y.; Yao, H. H.; Yuan, C. F.; Liu, J. Tuning thin-film electrolyte for lithium battery by grafting cyclic carbonate and combed poly(ethylene oxide) on polysiloxane. *ChemSusChem* **2014**, *7* (7), 1901–1908.
- (12) Hayashi, A.; Sakuda, A.; Tatsumisago, M. Development of sulfide solid electrolytes and interface formation processes for bulk-type all-solid-state Li and Na batteries. *Front. Energy Res.* **2016**, *4*, 25.
- (13) de Jongh, P. E.; Blanchard, D.; Matsuo, M.; Udovic, T. J.; Orimo, S. Complex hydrides as room-temperature solid electrolytes for rechargeable batteries. *Appl. Phys. A: Mater. Sci. Process.* **2016**, *122*, 251.
- (14) Matsuo, M.; Orimo, S. Lithium fast-ionic conduction in complex hydrides: review and prospects. *Adv. Energy Mater.* **2011**, *1* (2), 161–172.
- (15) Lu, Z. H.; Ciucci, F. Metal borohydrides as electrolytes for solid-state Li, Na, Mg, and Ca batteries: A first-principles study. *Chem. Mater.* **2017**, *29* (21), 9308–9319.
- (16) Møller, K.; Sheppard, D.; Ravnsbæk, D.; Buckley, C.; Akiba, E.; Li, H.-W.; Jensen, T. Complex metal hydrides for hydrogen, thermal and electrochemical energy storage. *Energies* **2017**, *10* (10), 1645.
- (17) Yoshida, K.; Sato, T.; Unemoto, A.; Matsuo, M.; Ikeshoji, T.; Udovic, T. J.; Orimo, S. Fast sodium ionic conduction in Na<sub>2</sub>B<sub>10</sub>H<sub>10</sub>-Na<sub>2</sub>B<sub>12</sub>H<sub>12</sub> pseudo-binary complex hydride and application to a bulk-type all-solid-state battery. *Appl. Phys. Lett.* **2017**, *110* (10), 103901.
- (18) Sakituna, B.; Lamari-Darkrim, F.; Hirscher, M. Metal hydride materials for solid hydrogen storage: A review. *Int. J. Hydrogen Energy* **2007**, *32* (9), 1121–1140.

- (19) Zuttel, A.; Wenger, P.; Rentsch, S.; Sudan, P.; Mauron, P.; Emmenegger, C.  $\text{LiBH}_4$  a new hydrogen storage material. *J. Power Sources* **2003**, *118* (1–2), 1–7.
- (20) Umegaki, T.; Yan, J. M.; Zhang, X. B.; Shioyama, H.; Kuriyama, N.; Xu, Q. Boron- and nitrogen-based chemical hydrogen storage materials. *Int. J. Hydrogen Energy* **2009**, *34* (5), 2303–2311.
- (21) Schuth, F.; Bogdanovic, B.; Felderhoff, M. Light metal hydrides and complex hydrides for hydrogen storage. *Chem. Commun.* **2004**, *20*, 2249–2258.
- (22) Duchene, L.; Kuhnle, R.-S.; Stilp, E.; Cuervo Reyes, E.; Remhof, A.; Hagemann, H.; Battaglia, C. A stable 3 V all-solid-state sodium-ion battery based on a closo-borate electrolyte. *Energy Environ. Sci.* **2017**, *10* (12), 2609–2615.
- (23) Asakura, R.; Duchene, L.; Kuhnle, R. S.; Remhof, A.; Hagemann, H.; Battaglia, C. Electrochemical oxidative stability of hydroborate-based solid state electrolytes. *ACS Appl. Energy Mater.* **2019**, *2* (9), 6924–6930.
- (24) Kim, S.; Oguchi, H.; Toyama, N.; Sato, T.; Takagi, S.; Otomo, T.; Arunkumar, D.; Kuwata, N.; Kawamura, J.; Orimo, S. A complex hydride lithium superionic conductor for high-energy-density all-solid-state lithium metal batteries. *Nat. Commun.* **2019**, *10*, 1081.
- (25) Matsuo, M.; Nakamori, Y.; Orimo, S.; Maekawa, H.; Takamura, H. Lithium superionic conduction in lithium borohydride accompanied by structural transition. *Appl. Phys. Lett.* **2007**, *91* (22), 224103.
- (26) Soulié, J. P.; Renaudin, G.; Černý, R.; Yvon, K. Lithium borohydride  $\text{LiBH}_4$ : I. Crystal structure. *J. Alloys Compd.* **2002**, *346* (1), 200–205.
- (27) Aeberhard, P. C.; Refson, K.; David, W. I. F. Molecular dynamics investigation of the disordered crystal structure of hexagonal  $\text{LiBH}_4$ . *Phys. Chem. Chem. Phys.* **2013**, *15* (21), 8081–8087.
- (28) Matsuo, M.; Takamura, H.; Maekawa, H.; Li, H. W.; Orimo, S. Stabilization of lithium superionic conduction phase and enhancement of conductivity of  $\text{LiBH}_4$  by  $\text{LiCl}$  addition. *Appl. Phys. Lett.* **2009**, *94* (8), 084103.
- (29) Oguchi, H.; Matsuo, M.; Hummelshoj, J. S.; Vegge, T.; Norskov, J. K.; Sato, T.; Miura, Y.; Takamura, H.; Maekawa, H.; Orimo, S. Experimental and computational studies on structural transitions in the  $\text{LiBH}_4$ - $\text{LiI}$  pseudobinary system. *Appl. Phys. Lett.* **2009**, *94* (14), 141912.
- (30) Matsuo, M.; Remhof, A.; Martelli, P.; Caputo, R.; Ernst, M.; Miura, Y.; Sato, T.; Oguchi, H.; Maekawa, H.; Takamura, H.; et al. Complex hydrides with  $(\text{BH}_4)^-$  and  $(\text{NH}_2)^-$  anions as new lithium fast-ion conductors. *J. Am. Chem. Soc.* **2009**, *131* (45), 16389.
- (31) Yao, Z. P.; Kim, S.; Michel, K.; Zhang, Y. S.; Aykol, M.; Wolverton, C. Stability and conductivity of cation- and anion-substituted  $\text{LiBH}_4$ -based solid-state electrolytes. *Phys. Rev. Mater.* **2018**, *2* (6), 065402.
- (32) Mezaki, T.; Kuronuma, Y.; Oikawa, I.; Kamegawa, A.; Takamura, H. Li-ion conductivity and phase stability of Ca-doped  $\text{LiBH}_4$  under high pressure. *Inorg. Chem.* **2016**, *55* (20), 10484–10489.
- (33) Ley, M. B.; Jorgensen, M.; Cerny, R.; Filinchuk, Y.; Jensen, T. R. From  $\text{M}(\text{BH}_4)_3$  ( $\text{M} = \text{La}, \text{Ce}$ ) Borohydride frameworks to controllable synthesis of porous hydrides and ion conductors. *Inorg. Chem.* **2016**, *55* (19), 9748–9756.
- (34) Rude, L. H.; Groppo, E.; Arnbjerg, L. M.; Ravnsbaek, D. B.; Malmkjaer, R. A.; Filinchuk, Y.; Baricco, M.; Besenbacher, F.; Jensen, T. R. Iodide substitution in lithium borohydride,  $\text{LiBH}_4$ - $\text{LiI}$ . *J. Alloys Compd.* **2011**, *509* (33), 8299–8305.
- (35) Miyazaki, R.; Karahashi, T.; Kumatani, N.; Noda, Y.; Ando, M.; Takamura, H.; Matsuo, M.; Orimo, S.; Maekawa, H. Room temperature lithium fast-ion conduction and phase relationship of  $\text{LiI}$  stabilized  $\text{LiBH}_4$ . *Solid State Ionics* **2011**, *192* (1), 143–147.
- (36) Sveinbjornsson, D.; Myrdal, J. S. G.; Blanchard, D.; Bentzen, J. J.; Hirata, T.; Mogensen, M. B.; Norby, P.; Orimo, S. I.; Vegge, T. Effect of heat treatment on the lithium ion conduction of the  $\text{LiBH}_4$ - $\text{LiI}$  solid solution. *J. Phys. Chem. C* **2013**, *117* (7), 3249–3257.
- (37) Maekawa, H.; Matsuo, M.; Takamura, H.; Ando, M.; Noda, Y.; Karahashi, T.; Orimo, S. I. Halide-stabilized  $\text{LiBH}_4$ , a room-temperature lithium fast-ion conductor. *J. Am. Chem. Soc.* **2009**, *131* (3), 894.
- (38) Stephenson, C. C.; Rice, D. W.; Stockmayer, W. H. Order-disorder transitions in the alkali borohydrides. *J. Chem. Phys.* **1955**, *23* (10), 1960–1960.
- (39) Yan, Y. G.; Kuhnle, R. S.; Remhof, A.; Duchene, L.; Reyes, E. C.; Rentsch, D.; Lodziana, Z.; Battaglia, C. A lithium amide-borohydride solid-state electrolyte with lithium-ion conductivities comparable to liquid electrolytes. *Adv. Energy Mater.* **2017**, *7* (19), 1700294.
- (40) Blanchard, D.; Nale, A.; Sveinbjornsson, D.; Eggenhuisen, T. M.; Verkuijlen, M. H. W.; Suwarno; Vegge, T.; Kentgens, A. P. M.; de Jongh, P. E. Nanoconfined  $\text{LiBH}_4$  as a fast lithium ion conductor. *Adv. Funct. Mater.* **2015**, *25* (2), 184–192.
- (41) Epp, V.; Wilkening, M. Motion of  $\text{Li}^+$  in nanoengineered  $\text{LiBH}_4$  and  $\text{LiBH}_4$ - $\text{Al}_2\text{O}_3$  comparison with the microcrystalline form. *ChemPhysChem* **2013**, *14* (16), 3706–3713.
- (42) Choi, Y. S.; Lee, Y. S.; Oh, K. H.; Cho, Y. W. Interface-enhanced Li ion conduction in a  $\text{LiBH}_4$ - $\text{SiO}_2$  solid electrolyte. *Phys. Chem. Chem. Phys.* **2016**, *18* (32), 22540–22547.
- (43) Choi, Y. S.; Lee, Y. S.; Choi, D. J.; Chae, K. H.; Oh, K. H.; Cho, Y. W. Enhanced Li ion conductivity in  $\text{LiBH}_4$ - $\text{Al}_2\text{O}_3$  mixture via interface engineering. *J. Phys. Chem. C* **2017**, *121* (47), 26209–26215.
- (44) Gutowska, A.; Li, L. Y.; Shin, Y. S.; Wang, C. M. M.; Li, X. H. S.; Linehan, J. C.; Smith, R. S.; Kay, B. D.; Schmid, B.; Shaw, W.; et al. Nanoscaffold mediates hydrogen release and the reactivity of ammonia borane. *Angew. Chem., Int. Ed.* **2005**, *44* (23), 3578–3582.
- (45) Berube, V.; Radtke, G.; Dresselhaus, M.; Chen, G. Size effects on the hydrogen storage properties of nanostructured metal hydrides: A review. *Int. J. Energy Res.* **2007**, *31* (6–7), 637–663.
- (46) de Jongh, P. E.; Adelhelm, P. Nanosizing and nanoconfinement: new strategies towards meeting hydrogen storage goals. *ChemSusChem* **2010**, *3* (12), 1332–1348.
- (47) Ngene, P.; van Zwiene, M.; de Jongh, P. E. Reversibility of the hydrogen desorption from  $\text{LiBH}_4$ : a synergetic effect of nanoconfinement and Ni addition. *Chem. Commun.* **2009**, *46* (43), 8201–8203.
- (48) Suwarno; Ngene, P.; Nale, A.; Eggenhuisen, T. M.; Oschatz, M.; Embs, J. P.; Remhof, A.; de Jongh, P. E. Confinement effects for lithium borohydride: comparing silica and carbon scaffolds. *J. Phys. Chem. C* **2017**, *121* (8), 4197–4205.
- (49) Maier, J. Ionic-conduction in space charge regions. *Prog. Solid State Chem.* **1995**, *23* (3), 171–263.
- (50) Verdal, N.; Udovic, T. J.; Rush, J. J.; Liu, X. F.; Majzoub, E. H.; Vajo, J. J.; Gross, A. F. Dynamical perturbations of tetrahydroborate anions in  $\text{LiBH}_4$  due to nanoconfinement in controlled-pore carbon scaffolds. *J. Phys. Chem. C* **2013**, *117* (35), 17983–17995.
- (51) Breuer, S.; Uitz, M.; Wilkening, H. M. R. Rapid Li ion dynamics in the interfacial regions of nanocrystalline solids. *J. Phys. Chem. Lett.* **2018**, *9* (8), 2093–2097.
- (52) de Jongh, P. E.; Eggenhuisen, T. M. Melt infiltration: an emerging technique for the preparation of novel functional nanostructured materials. *Adv. Mater.* **2013**, *25* (46), 6672–6690.
- (53) Unemoto, A.; Yasaku, S.; Nogami, G.; Tazawa, M.; Taniguchi, M.; Matsuo, M.; Ikeshoji, T.; Orimo, S. Development of bulk-type all-solid-state lithium-sulfur battery using  $\text{LiBH}_4$  electrolyte. *Appl. Phys. Lett.* **2014**, *105* (8), 083901.
- (54) Das, S.; Ngene, P.; Norby, P.; Vegge, T.; de Jongh, P. E.; Blanchard, D. All-solid-state lithium-sulfur battery based on a nanoconfined  $\text{LiBH}_4$  electrolyte. *J. Electrochem. Soc.* **2016**, *163* (9), A2029–A2034.
- (55) Lefevr, J.; Cervini, L.; Griffin, J. M.; Blanchard, D. Lithium conductivity and ions dynamics in  $\text{LiBH}_4/\text{SiO}_2$  solid electrolytes studied by solid-state NMR and quasi-elastic neutron scattering and applied in lithium sulfur batteries. *J. Phys. Chem. C* **2018**, *122* (27), 15264–15275.
- (56) Cheng, C.-F.; Zhou, W.; Ho Park, D.; Klinowski, J.; Hargreaves, M.; Gladden, L. F. Controlling the channel diameter of the

mesoporous molecular sieve MCM-41. *J. Chem. Soc., Faraday Trans.* **1997**, *93* (2), 359–363.

(57) Zhao, D. Y.; Feng, J. L.; Huo, Q. S.; Melosh, N.; Fredrickson, G. H.; Chmelka, B. F.; Stucky, G. D. Triblock copolymer syntheses of mesoporous silica with periodic 50 to 300 angstrom pores. *Science* **1998**, *279* (5350), 548–552.

(58) Hartman, M. R.; Rush, J. J.; Udovic, T. J.; Bowman, R. C.; Hwang, S. J. Structure and vibrational dynamics of isotopically labeled lithium borohydride using neutron diffraction and spectroscopy. *J. Solid State Chem.* **2007**, *180* (4), 1298–1305.

(59) Filinchuk, Y.; Chernyshov, D.; Cerny, R. Lightest borohydride probed by synchrotron X-ray diffraction: Experiment calls for a new theoretical revision. *J. Phys. Chem. C* **2008**, *112* (28), 10579–10584.

(60) Hanawalt, J. D.; Rinn, H. W.; Frevel, L. K. Chemical analysis by X-ray diffraction - Classification and use of X-ray diffraction patterns. *Ind. Eng. Chem., Anal. Ed.* **1938**, *10*, 0457–0512.

(61) Posnjak, E. W. R. Crystal structure of alkali halogenides. *J. Wash. Acad. Sci.* **1922**, *12*, 248–251.

(62) Royer, L. Sur les accolements reguliers de cristaux d'especes differentes. *C. R. Hebd. Seances Acad. Sci.* **1925**, *180*, 2050.

(63) Harvey, K. B.; Mcquaker, N. R. Low temperature infrared and raman spectra of lithium borohydride. *Can. J. Chem.* **1971**, *49* (20), 3282.

(64) D'Anna, V.; Spyratou, A.; Sharma, M.; Hagemann, H. FT-IR spectra of inorganic borohydrides. *Spectrochim. Acta, Part A* **2014**, *128*, 902–906.

(65) D'Anna, V.; Daku, L. M. L.; Hagemann, H. Quantitative spectra-structure relations for borohydrides. *J. Phys. Chem. C* **2015**, *119* (38), 21868–21874.

(66) Coates, J. Interpretation of infrared spectra, a practical approach. *Encycl. Anal. Chem.* **2006**, *1*, 10815–10837.

(67) Sun, T.; Liu, J.; Jia, Y.; Wang, H.; Sun, D. L.; Zhu, M.; Yao, X. D. Confined LiBH<sub>4</sub>: Enabling fast hydrogen release at similar to 100 degrees C. *Int. J. Hydrogen Energy* **2012**, *37* (24), 18920–18926.

(68) Plerdsranoy, P.; Utke, R. Confined LiBH<sub>4</sub>-LiAlH<sub>4</sub> in nanopores of activated carbon nanofibers. *Int. J. Hydrogen Energy* **2015**, *40* (22), 7083–7092.

(69) Javadian, P.; Sheppard, D. A.; Buckley, C. E.; Jensen, T. R. Hydrogen storage properties of nanoconfined LiBH<sub>4</sub>-NaBH<sub>4</sub>. *Int. J. Hydrogen Energy* **2015**, *40* (43), 14916–14924.

(70) Laiti, E.; Persson, P.; Ohman, L. O. Balance between surface complexation and surface phase transformation at the alumina/water interface. *Langmuir* **1998**, *14* (4), 825–831.

(71) Hiyoshi, N.; Yogo, K.; Yashima, T. Adsorption characteristics of carbon dioxide on organically functionalized SBA-15. *Microporous Mesoporous Mater.* **2005**, *84* (1–3), 357–365.

(72) Zhao, X. S.; Lu, G. Q. Modification of MCM-41 by surface silylation with trimethylchlorosilane and adsorption study. *J. Phys. Chem. B* **1998**, *102* (9), 1556–1561.

(73) Irvine, J. T. S.; Sinclair, D. C.; West, A. R. Electroceramics: Characterization by impedance spectroscopy. *Adv. Mater.* **1990**, *2*, 132–138.

(74) Verkuijlen, M. H. W.; Ngene, P.; de Kort, D. W.; Barre, C.; Nale, A.; van Eck, E. R. H.; van Bentum, P. J. M.; de Jongh, P. E.; Kentgens, A. P. M. Nanoconfined LiBH<sub>4</sub> and enhanced mobility of Li<sup>+</sup> and BH<sub>4</sub><sup>-</sup> studied by solid-state NMR. *J. Phys. Chem. C* **2012**, *116* (42), 22169–22178.

(75) Epp, V.; Wilkening, M. Fast Li diffusion in crystalline LiBH<sub>4</sub> due to reduced dimensionality: Frequency-dependent NMR spectroscopy. *Phys. Rev. B: Condens. Matter Mater. Phys.* **2010**, *82* (2), 020301.

### 4.2.3. NMR Observations on Combined Ion Substituted and Nanoconfined Complex Hydrides

It was found that nanoconfinement of ion substituted  $\text{LiBH}_4$ , *e.g.*  $\text{LiBH}_4\text{-LiI}/\text{Al}_2\text{O}_3$ , leads to beneficial properties of the material. Thus, the combination of well-established methods in stabilizing the room temperature phase of  $\text{LiBH}_4$  was found to result in even better conductivities. The exact origin of this behaviour was still unclear. We conducted a detailed study to probe diffusion coefficients over 6 orders of magnitude and compared  $^7\text{Li}$  PFG NMR and static  $^7\text{Li}$  SLR NMR results with those from conductivity and electrical modulus spectroscopy. Even though these methods determine the diffusion coefficient either macroscopically or microscopically and are either influenced by correlated motions or consider totally random walks, we see good agreement in the observed diffusion coefficients over 6 orders of magnitude.

With  $^{27}\text{Al}$  MAS NMR we could show that signals from penta-coordinated Al, seen in the starting material  $\text{Al}_2\text{O}_3$ , vanished in the composites. The penta-coordinated Al is attributed to surface groups in  $\text{Al}_2\text{O}_3$ . This circumstance gave rise to the interaction of  $\text{LiBH}_4$  and  $\text{LiBH}_4\text{-LiI}$ , respectively, with surface groups of  $\text{Al}_2\text{O}_3$ . This indicates that these interactions at the interface  $\text{LiBH}_4(-\text{LiI})/\text{oxide}$  play a major role in the diffusion of  $\text{Li}^+$  through the material. It is sophisticatedly speculated that the origin of the high ionic conductivity is due to space charge effects. Additionally, the study revealed that in the bulk, *i.e.*  $\text{LiBH}_4\text{-LiI}$ , ionic transport is governed by a 2D process, whereas on a larger length scale, 3D ionic transport was observed. Evidence for the 2D diffusion process was obtained by applying a Jonscher's power law on conductivity isotherms, which lead to an exponent of 0.5, pointing to 2D ionic transport in the bulk of the material. We could show that the conductor/insulator interplay is the key factor of diffusion processes in these materials.[109]

## Li-Ion Diffusion in Nanoconfined $\text{LiBH}_4\text{-LiI}/\text{Al}_2\text{O}_3$ : From 2D Bulk Transport to 3D Long-Range Interfacial Dynamics

Roman Zettl, Maria Gombotz, David Clarkson, Steven G. Greenbaum, Peter Ngene, Petra E. de Jongh, H. Martin R. Wilkening. *ACS Appl. Mater. Interfaces*, **2020**, 12, 38570-38583

DOI: 10.1021/acsami.0c10361

### Author contributions

R.Z. synthesized the samples and performed MAS NMR, conductivity spectroscopy and static NMR experiments and analysed the data. D.C. performed the PFG NMR experiments for the determination of the tracer diffusion coefficient and analysed the data. M.G. carried out data analysis on NMR line spectra and FIDs. R.Z., M.G. and H.M.R. illustrated the data. R.Z. and H.M.R. wrote the paper together with the contribution of all authors. All authors participated in the discussion of intermediate and final results.

# Li-Ion Diffusion in Nanoconfined $\text{LiBH}_4\text{-LiI}/\text{Al}_2\text{O}_3$ : From 2D Bulk Transport to 3D Long-Range Interfacial Dynamics

Roman Zettl,\* Maria Gombotz, David Clarkson, Steven G. Greenbaum, Peter Ngene, Petra E. de Jongh, and H. Martin R. Wilkening\*

Cite This: *ACS Appl. Mater. Interfaces* 2020, 12, 38570–38583

Read Online

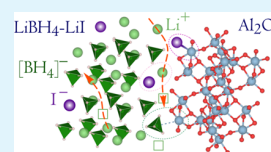
ACCESS |

Metrics & More

Article Recommendations

Supporting Information

**ABSTRACT:** Solid electrolytes based on  $\text{LiBH}_4$  receive much attention because of their high ionic conductivity, electrochemical robustness, and low interfacial resistance against Li metal. The highly conductive hexagonal modification of  $\text{LiBH}_4$  can be stabilized via the incorporation of LiI. If the resulting  $\text{LiBH}_4\text{-LiI}$  is confined to the nanopores of an oxide, such as  $\text{Al}_2\text{O}_3$ , interface-engineered  $\text{LiBH}_4\text{-LiI}/\text{Al}_2\text{O}_3$  is obtained that revealed promising properties as a solid electrolyte. The underlying principles of  $\text{Li}^+$  conduction in such a nanocomposite are, however, far from being understood completely. Here, we used broadband conductivity spectroscopy and  $^1\text{H}$ ,  $^6\text{Li}$ ,  $^7\text{Li}$ ,  $^{11}\text{B}$ , and  $^{27}\text{Al}$  nuclear magnetic resonance (NMR) to study structural and dynamic features of nanoconfined  $\text{LiBH}_4\text{-LiI}/\text{Al}_2\text{O}_3$ . In particular, diffusion-induced  $^1\text{H}$ ,  $^7\text{Li}$ , and  $^{11}\text{B}$  NMR spin–lattice relaxation measurements and  $^7\text{Li}$ -pulsed field gradient (PFG) NMR experiments were used to extract activation energies and diffusion coefficients.  $^{27}\text{Al}$  magic angle spinning NMR revealed surface interactions of  $\text{LiBH}_4\text{-LiI}$  with pentacoordinated Al sites, and two-component  $^1\text{H}$  NMR line shapes clearly revealed heterogeneous dynamic processes. These results show that interfacial regions have a determining influence on overall ionic transport ( $0.1 \text{ mS cm}^{-1}$  at 293 K). Importantly, electrical relaxation in the  $\text{LiBH}_4\text{-LiI}$  regions turned out to be fully homogenous. This view is supported by  $^7\text{Li}$  NMR results, which can be interpreted with an overall (averaged) spin ensemble subjected to uniform dipolar magnetic and quadrupolar electric interactions. Finally, broadband conductivity spectroscopy gives strong evidence for 2D ionic transport in the  $\text{LiBH}_4\text{-LiI}$  bulk regions which we observed over a dynamic range of 8 orders of magnitude. Macroscopic diffusion coefficients from PFG NMR agree with those estimated from measurements of ionic conductivity and nuclear spin relaxation. The resulting 3D ionic transport in nanoconfined  $\text{LiBH}_4\text{-LiI}/\text{Al}_2\text{O}_3$  is characterized by an activation energy of 0.43 eV.



**KEYWORDS:** lithium borohydride, nanoconfinement, electrolytes, dynamics, conductivity, NMR

## 1. INTRODUCTION

The increase of anthropogenic  $\text{CO}_2$  in the atmosphere is responsible for the global warming observed; this warming is generally known as the greenhouse effect. Burning of fossil fuels belongs to one of the main sources of energy-related  $\text{CO}_2$  emissions. Cutting our dependency on hydrocarbons, such as coal, fuel oil, or natural gas, and finding alternatives to convert energy, e.g., from solar or wind power, to electricity is one of the most important challenges that humans need to face within the 21st century. As electricity from solar power is generated from a nondispatchable source of energy and, thus, highly intermittent, we have to develop high-performance and sustainable energy storage devices that are connected to the electricity grid in a mainly decentralized way.<sup>1</sup> Secondary batteries, which either use  $\text{Li}^+$  or  $\text{Na}^+$  ions as ionic charge carriers, are suitable devices for this purpose.<sup>2–5</sup> While Na-based batteries are envisaged to play a pivotal role in stationary energy storage,<sup>5</sup>  $\text{Li}^+$ -ion batteries offering both considerably higher energy densities and higher power densities are the devices of choice for automotive applications.<sup>3,6</sup> Currently, these systems use flammable, aprotic liquid electrolytes. To increase both safety and longevity, solid electrolytes attracted great attention. Highly conducting solids, that is, polymers or

ceramics, are at the heart of all-solid-state systems as they ensure the facile transport of the ions between the two compartments of a battery, viz., the anode and cathode.<sup>4,7–9</sup>

Over the last years, many ceramic materials that show ionic conductivities with values reaching or even exceeding a benchmark of  $1 \text{ mS cm}^{-1}$  have been presented.<sup>7,9,10</sup> Each material, regardless of whether being an oxide, sulfide, thiophosphate, or hydride, has its own advantages and disadvantages with respect to, for example, electrochemical stability, interfacial resistance, chemical robustness, synthesis costs, and sustainability.<sup>7</sup>

Highly conducting anion-substituted hydrides based on lithium borohydride ( $\text{LiBH}_4$ ) especially when prepared in nanostructured forms that benefit from interfacial properties belong to the core group of sustainable materials composed of elements with high natural abundance. Quite recently, some of

Received: June 9, 2020  
Accepted: August 5, 2020  
Published: August 5, 2020



us reported on enhanced ion dynamics in nanoconfined  $\text{LiBH}_4\text{-LiI}$ .<sup>11</sup> Nanoconfinement was achieved by melt infiltration of  $\text{LiBH}_4\text{-LiI}$  in the nanopores of alumina,  $\text{Al}_2\text{O}_3$ . The combination of both (i) substitutions of iodide anions for the  $\text{BH}_4^-$  units and (ii) spatial confinement resulted in a composite material with promising ion conductivities at room temperature. The underlying transport mechanism in this interface-controlled or surface-dominated material remains, however, unclear. Here, we used time domain and magic angle spinning (MAS) nuclear magnetic resonance (NMR) spectroscopy to shed light on both structural features and ion dynamics in nanoconfined  $\text{LiBH}_4\text{-LiI}$ .

Numerous publications, which appeared over the last decades, pointed out that various NMR techniques represent crucial and powerful analysis methods also in metal hydrides research. Already in 1987, Jarrett et al.<sup>12</sup> used solid-state  $^2\text{H}$  NMR to identify bridging and terminal metal hydride sites. In  $\text{LiZn}_2(\text{BD}_4)_5$ ,  $^{11}\text{B}$  MAS NMR and multiple quantum MAS NMR helped identify four different boron sites in the  $[\text{Zn}_2(\text{BD}_4)_5]^-$  anion.<sup>13</sup> Furthermore,  $^1\text{H}$ ,  $^7\text{Li}$ , and  $^{11}\text{B}$  NMR, including spin–lattice relaxation rate measurements in particular, were used to characterize the translational and rotational dynamics in this compound.<sup>14</sup>

Before complex metal hydrides received considerable attention from the battery research community, lithium borohydride,  $\text{LiBH}_4$ , and its relatives were intensively investigated as hydrogen storage materials;<sup>15–18</sup> NMR played a central role in characterizing both local structures and ion dynamics.<sup>19,20</sup> As an example,  $\text{Mg}(\text{BH}_4)_2(\text{NH}_3\text{BH}_3)_2$ , that is, a metal borohydride–ammonia borane complex, was proposed as a good candidate for hydrogen storage. Results from  $^{11}\text{B}$  MAS NMR were compared with those from DFT calculations to validate the crystal structure.<sup>21</sup> It turned out that the excellent hydrogen-sorption properties found could be further enhanced by synthesizing composites with nanoscaffolds.<sup>22–24</sup> Gutowska et al.<sup>25</sup> used solid-state  $^{11}\text{B}$  NMR to underline their hypothesis that nanoconfinement of the complex metal hydrides decreases the temperature for hydrogen release from ammonia borane together with an increase in hydrogen purity. Conradi and co-workers<sup>26,27</sup> presented an elegant NMR-based study using  $^1\text{H}$  NMR and  $^7\text{Li}$  NMR on  $\text{LiBH}_4$  and  $\text{LiBH}_4$  confined in carbon aerogel. They observed pronounced changes in Li mobility when going from bulk materials to nanoconfined samples.

Nanoconfinement is, in general, an elegant approach to increase the room-temperature conductivity of  $\text{LiBH}_4$ .<sup>28–31</sup> Bulk  $\text{LiBH}_4$  undergoes a reversible structural change at approximately  $T_{\text{pt}} = 110$  °C and changes from the highly conductive hexagonal phase to the poorly conductive orthorhombic phase.<sup>32</sup> The scaffolds of the nanoconfined complex hydrides are ionic insulators. In such conductor/insulator composites,<sup>33–37</sup> enhanced ion transport along the heterointerfaces can occur due to both structural disorder<sup>38–40</sup> and/or space charge effects.<sup>35,41–43</sup>

The first NMR studies on  $\text{LiBH}_4$ , which was confined in silica, were realized in 2012 by Kentgens and co-workers.<sup>44</sup> In the following years, solid-state NMR, especially  $^7\text{Li}$  NMR, proved itself as a powerful technique to study Li diffusion in these compounds that were envisaged as solid electrolytes for Li batteries.<sup>28,29,45</sup> Quite recently, the same group<sup>46</sup> reported on the phase behavior and Li ion dynamics of nanoconfined  $\text{LiBH}_4$  in silica. Furthermore, the second approach to increase ionic conductivity, which is anion substitution with, e.g., LiI

(vide supra), was successfully studied via solid-state NMR.<sup>47,48</sup> As mentioned above, replacing  $[\text{BH}_4]^-$  partly by halogen anions such as  $\text{I}^-$  stabilizes the highly conducting hexagonal phase of  $\text{LiBH}_4$  at room temperature.

Despite the various studies,<sup>26,28–31,46</sup> the role of the interface of the pore walls and complex hydride is not completely clear yet. A reaction or at least an interaction of the surface groups of the porous supports ( $\text{Al}_2\text{O}_3$  or  $\text{SiO}_2$ ) with the metal hydride could be the key factor to explain the origin of the significant increase in ionic conduction upon nanoconfinement. Most of these studies deal with silica supports. It was, however, shown that the surface groups in alumina beneficially affected ion diffusion too;<sup>36</sup> similar effects were found with other oxides such as  $\text{MgO}$ ,  $\text{CaO}$ ,  $\text{TiO}_2$ , and  $\text{ZrO}_2$ .<sup>49</sup> These surface groups can, in ideal cases, be identified via  $^{27}\text{Al}$  MAS NMR. Besides the well-known NMR signals for octahedrally and tetrahedrally coordinated Al in nanostructured  $\gamma\text{-Al}_2\text{O}_3$ , another signal shows up. In terms of chemical shift values, this signal is located between these two main signals and points to pentacoordinated alumina near the surface regions.<sup>50–52</sup> Such sites might be involved in ion transport in nanoconfined, anion-stabilized  $\text{LiBH}_4\text{-LiI}/\text{Al}_2\text{O}_3$ .

In our recent study on this system,<sup>11</sup> we shed light on the correlation between morphology and Li-ion conductivity by means of X-ray diffraction, diffuse reflectance infrared Fourier transform spectra,  $\text{N}_2$  physisorption, and scanning electron microscopy. Impedance spectroscopy was used to characterize long-range ion transport in the nanoconfined composite. The present paper is aimed at giving insights into the mechanisms of  $\text{Li}^+$  diffusion in  $\text{LiBH}_4\text{-LiI}/\text{Al}_2\text{O}_3$ . For this purpose, we used solid-state NMR techniques including variable-temperature  $^1\text{H}$ ,  $^7\text{Li}$ , and  $^{11}\text{B}$  spin–lattice relaxation measurements and  $^7\text{Li}$  pulsed-field gradient (PFG) experiments to study ion dynamics on different length scales. We compare our results with transport parameters extracted from broadband conductivity measurements and electrical modulus spectroscopy. Structural features of the sample were probed by  $^1\text{H}$ ,  $^6\text{Li}$ ,  $^{11}\text{B}$ , and  $^{27}\text{Al}$  MAS NMR. Taken together, we show that nuclear spin relaxation, PFG NMR, and electrical relaxation provide consistent diffusion coefficients characterizing long-range ion dynamics. Via the combination of these techniques, we were able to study ion transport in the nanoconfined ion conductor over a dynamic range of 6–8 orders of magnitude.

## 2. EXPERIMENTAL SECTION

**2.1. Preparation of the  $\text{LiBH}_4\text{-LiI}/\text{Al}_2\text{O}_3$  Electrolyte.** Lithium boron hydride ( $\text{LiBH}_4$ , with a purity of 95%, Sigma Aldrich) and lithium iodide (LiI, 98%, Sigma Aldrich) were thoroughly mixed for several minutes in a ceramic mortar. The molar ratio  $\text{LiBH}_4/\text{LiI}$  was 80:20. A sufficient amount of physical mixture was added to the porous support material, alumina ( $\text{Al}_2\text{O}_3$ , Sasol Puralex SCCa-5/200, see ref 11 for detail), to fill the pores by 130%. The pore size was determined by  $\text{N}_2$  physisorption and turned out to be 8.7 nm.<sup>11</sup> The extra 30% was added to enable interconnectivity between the insulating alumina particles. The calculation was done after the specific pore volume has been determined via  $\text{N}_2$  physisorption. To finally obtain the melt-infiltrated alumina product, the mixture was filled in a quartz reactor and placed inside a stainless-steel high-pressure autoclave (Parr). After applying a pressure of 50 bar  $\text{H}_2$ , the sample was heated to  $\theta = 295$  °C with a heating rate of approximately  $3$  °C  $\text{min}^{-1}$ . During a dwell time of 30 min,  $\text{LiBH}_4$  and LiI built a solid solution and infiltrate the pores of the alumina support.<sup>53</sup> For a more detailed description, we refer to our recent study,<sup>11</sup> which also includes the characterization of the reference samples  $\text{LiBH}_4\text{-LiI}$ , i.e., a sample without alumina.

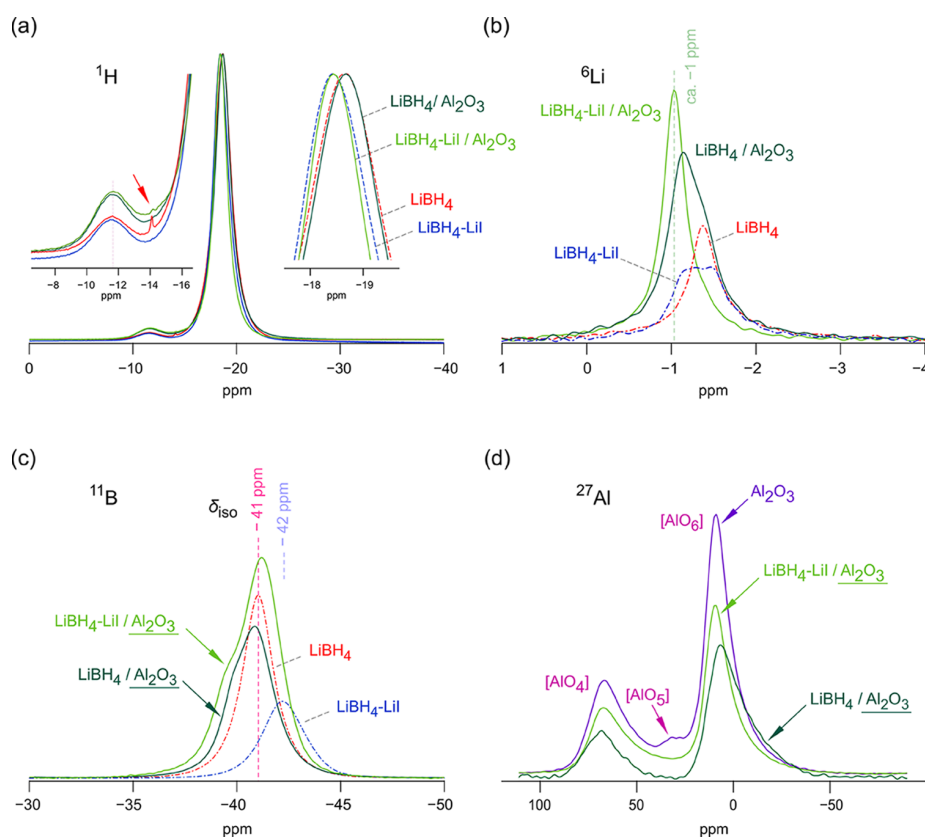


**Figure 1.**  $^1\text{H}$ ,  $^6\text{Li}$ ,  $^{11}\text{B}$ , and  $^{27}\text{Al}$  MAS NMR spectra of  $\text{LiBH}_4\text{-LiI}/\text{Al}_2\text{O}_3$ , the NMR spectra are compared with those of  $\text{LiBH}_4$ ,  $\text{LiBH}_4\text{-LiI}$ ,  $\text{LiBH}_4/\text{Al}_2\text{O}_3$ , and  $\text{Al}_2\text{O}_3$ , respectively. The spinning speed was 25 kHz. (a)  $^1\text{H}$  MAS NMR spectra, most likely, the small arrow indicates an impurity phase. (b)  $^6\text{Li}$  MAS NMR spectra, for  $\text{LiBH}_4/\text{Al}_2\text{O}_3$ , a line composed of two spectral components is observed. (c)  $^{11}\text{B}$  MAS NMR spectra, which also show a two-component line shape for the nanoconfined samples. (d)  $^{27}\text{Al}$  MAS NMR spectra of  $\text{Al}_2\text{O}_3$ , besides lines attributable to four- and six-fold Al species, we also recognize pentacoordinated Al centers,  $[\text{AlO}_5]$ . Most likely, as this signal does not show up in the spectra of  $\text{LiBH}_4/\text{Al}_2\text{O}_3$  and  $\text{LiBH}_4\text{-LiI}/\text{Al}_2\text{O}_3$ , we assume that six-fold coordinated surface species  $[\text{AlO}_5\text{X}]$  ( $\text{X} = \text{I}, \text{BH}_4^-$ ) have been formed.

**2.2. Nuclear Magnetic Resonance.** Samples for MAS NMR measurements were filled in Bruker MAS rotors ( $\text{ZrO}_2$ ) with a diameter of 2.5 mm and a length of 1 cm. The rotors were carefully filled portion by portion with the powder sample, which was pressed by hand after each filling step to prepare a dense-packed rotor. Various reference samples such as  $\text{LiBH}_4$ ,  $\text{Al}_2\text{O}_3$ ,  $\text{LiBH}_4\text{-LiI}$ , and  $\text{LiBH}_4/\text{Al}_2\text{O}_3$  were also investigated to interpret the results of the nanoconfined composite  $\text{LiBH}_4\text{-LiI}/\text{Al}_2\text{O}_3$  obtained via  $^1\text{H}$ ,  $^6\text{Li}$ ,  $^{11}\text{B}$ , and  $^{27}\text{Al}$  MAS NMR. To acquire the spectra, we used a Bruker Avance III 500 spectrometer that was connected to an 11.4 Tesla cryomagnet. This magnet field corresponds to the following resonance frequencies: 500.00 MHz ( $^1\text{H}$ ), 73.58 MHz ( $^6\text{Li}$ ), 160.42 MHz ( $^{11}\text{B}$ ), and 130.29 MHz ( $^{27}\text{Al}$ ). The MAS probe was operated at a spinning speed of 25 kHz. The temperature of the bearing gas was set to approximately  $\vartheta = 30^\circ\text{C}$ . Spectra were recorded with a single-pulse excitation sequence. Pulse lengths, delay times, and number of scans for each spectrum are listed in Table S1. Free induction decays were Fourier transformed to obtain spectra without any further manipulation except for zero- and first-order phase correction.

Information about ion dynamics, i.e., activation energies  $E_a$ , jump rates  $\tau^{-1}$ , was collected under static, that is, under non-MAS conditions with a Bruker Avance III 300 spectrometer. The spectrometer was connected to a 7.0 Tesla cryomagnet yielding the following resonance frequencies for the nuclei under investigation: 300.00 MHz ( $^1\text{H}$ ), 116.59 MHz ( $^7\text{Li}$ ), and 96.25 MHz ( $^{11}\text{B}$ ).  $\text{LiBH}_4\text{-LiI}/\text{Al}_2\text{O}_3$  was fire-sealed in Duran tubes for the  $^7\text{Li}$  and  $^1\text{H}$  measurements and in quartz tubes for the  $^{11}\text{B}$  experiments, respectively. The samples were placed in a commercially available probe head (Bruker) designed to be operated at temperatures  $\vartheta$  as

high as  $300^\circ\text{C}$ ; the probe was equipped with a ceramic sample chamber and a type T thermocouple to monitor the temperature which we adjusted with a stream of nitrogen gas that passed a heater beneath the sample chamber. The heater was connected to a Eurotherm temperature controller. We varied the temperature for the measurements of longitudinal NMR spin–lattice relaxation (SLR) rates  $R_1$  ( $1/T_1$ ) and for the measurement of the spin-lock rates  $R_{1\rho}$  ( $1/T_{1\rho}$ ) from  $-100^\circ\text{C}$  to  $160^\circ\text{C}$ .

The so-called saturation recovery pulse sequence was used to record the  $1/T_1$  rates in the laboratory frame of reference: a comb of closely spaced  $\pi/2$  pulses destroys any longitudinal magnetization  $M_z$ . The subsequent recovery curve of  $M_z$ , see the Supporting Information (Figure S1), is obtained by plotting the area under the free induction decays (FIDs) against the waiting time  $t_d$ . To parametrize the transients  $M_z(t_d)$ , stretched exponential fits were used,  $M_z(t_d) \propto 1 - \exp(-(t_d/T_1)^\gamma)$  with  $0 < \gamma \leq 1$ . Rotating-frame  $^7\text{Li}$  NMR SLR rates were acquired with the spin-lock technique at a locking frequency of 20 kHz. The spin-lock period  $t_{\text{lock}}$  was varied such that it takes values from 10  $\mu\text{s}$  to 1 s. Worth noting, it is crucial to ensure full longitudinal relaxation between each spin-lock scan. This is realized by paying attention to a recycle delay of  $5 \times T_1$ . Again, stretched exponential fits were used to analyze the transversal transients,  $M_\rho(t_{\text{lock}})$ :  $M_\rho(t_{\text{lock}}) \propto \exp(-(t_{\text{lock}}/T_{1\rho})^\varphi)$  with  $0 < \varphi \leq 1$ , see Figure S1, and obtain the  $R_{1\rho}$  rates ( $1/T_{1\rho}$ ). All sample preparation steps for MAS NMR and static NMR were carried out under a protective argon (Ar) atmosphere. Pulse lengths, delay times, and number of scans of the time-domain experiments are summarized in Table S1 also.

PFG diffusion-ordered spectroscopy (DOSY) NMR was conducted using a 300 MHz Varian direct drive spectrometer and Doty Scientific

closed-bore gradient probe capable of producing gradients of up to  $1200 \text{ G cm}^{-1}$ . The sample was packed under the Ar atmosphere into high-throughput NMR tubes (Wilmad) with a 5 mm outer diameter and sealed with tight-fitting caps and Parafilm.  $^7\text{Li}$  NMR experiments were then conducted to determine the relaxation and diffusion properties of the sample at different temperatures. For further information on the PFG DOSY experiment, we refer to the Supporting Information section. Results were fit using the Stejskal–Tanner equation for stimulated echo pulse sequences with square pulses, see Figure S2 and the Supporting Information for details.

Transverse relaxation times  $T_2$  were measured at three temperatures, viz., at 25, 60, and  $90^\circ\text{C}$  using a Hahn–Echo pulse sequence with variable delays; corresponding transients are shown in Figure S3. At  $25^\circ\text{C}$ , the spin–spin relaxation time was  $500 \mu\text{s}$ . At 60 and  $90^\circ\text{C}$ ,  $T_2$  increased, however, to 2.7 and 4.9 ms, respectively.  $T_1$  was approximated to be on the order of hundreds of milliseconds at all temperatures based on sample saturation observation at shorter delays between single-pulse experiments. In fact, independent measurements of  $T_1$  yielded  $T_1 = 590 \text{ ms}$  at  $60^\circ\text{C}$  (116.59 MHz) and  $T_1 = 510 \text{ ms}$  at  $\vartheta = 100^\circ\text{C}$ . This circumstance enabled sufficiently long diffusion times in  $^7\text{Li}$ -stimulated echo DOSY experiments and the measurement of diffusion coefficients on the order of  $10^{-12} \text{ m}^2 \text{ s}^{-1}$ . Diffusion coefficients were measured using a stimulated echo DOSY sequence with a longitudinal eddy current delay, varying the gradient strength between 0 and  $650 \text{ G cm}^{-1}$ . The attenuation curves measured and associated fits are presented in Figure S2.

**2.3. Impedance Spectroscopy.** For the impedance spectroscopy measurements, a sample of  $\text{LiBH}_4\text{-LiI}/\text{Al}_2\text{O}_3$  was pelletized with a load of 0.5 tons. The final two pellets (5 mm in diameter) were sputtered on both sides with gold. The Au layers (100 nm in thickness) acted as ion-blocking electrodes. The sample was placed in an active ZGS sample cell (Novocontrol), which was connected to a Concept 80 broadband impedance spectrometer (Novocontrol) using an Alpha-A analyzer. The cell was continuously flushed with a stream of freshly evaporated nitrogen to avoid any contamination or reaction with moisture. The sample was placed between two gold-sputtered spacer electrodes and a spring to ensure a sufficiently long contact throughout the measurements. We corrected the measured impedance for the cell stray and spacer capacity, which depends on the dimensions of the electrodes and the sample pellet itself. Conductivity isotherms were recorded at temperatures  $\vartheta$  ranging from  $-50$  to  $100^\circ\text{C}$  in a frequency range of 10 MHz to 10 mHz.

A second pellet of the same batch was used to carry out variable-temperature impedance measurements but at fixed frequencies of 100 Hz and 100 kHz ( $-140$  to  $160^\circ\text{C}$ , in steps of  $5^\circ\text{C}$ ). We analyzed the resistivity in the form of  $M''/\omega$  where  $M''$  is the imaginary part of the complex electric modulus, and  $\omega$  denotes the angular frequency. Such a plot reveals peaks being similar to those seen in  $^7\text{Li}$  NMR spin–lattice relaxation.

### 3. RESULTS AND DISCUSSION

**3.1. Structural Elucidation.** High-resolution (MAS) NMR was used to observe structural changes of the different  $\text{LiBH}_4$ -based composites.  $^1\text{H}$ ,  $^6\text{Li}$ ,  $^{11}\text{B}$ , and  $^{27}\text{Al}$  MAS NMR spectra are shown in Figure 1. Intensities are given in arbitrary units; the spectra are scaled such that it is easier to differentiate between the distinct spectral contributions. The  $^1\text{H}$  MAS NMR spectrum (Figure 1a) of  $\text{LiBH}_4\text{-LiI}/\text{Al}_2\text{O}_3$  reveals a main signal that is very similar to that of the  $\text{LiBH}_4\text{-LiI}$  sample. The spectra of the samples without LiI are shifted toward lower parts per million (ppm) values, that is, these lines are upfield or shielded. Obviously, because halides have a higher electronegativity than the borohydride anion,  $^1\text{H}$  in the direct neighborhood of I experiences, on average, a reduced electron density at its site, and it is therefore less magnetically shielded. Consequently, the corresponding lines appear in the downfield region, i.e., they are shifted toward the direction of positive ppm values. Interestingly, nanoconfinement of  $\text{LiBH}_4$  (or

$\text{LiBH}_4\text{-LiI}$ ) in  $\text{Al}_2\text{O}_3$  did not lead to a shift on the ppm scale of the corresponding NMR lines.

The small signal at more positive ppm values (isotropic shift  $\delta_{\text{iso}} = -11.5 \text{ ppm}$ , see Figure 1a) might be attributed to an H-containing impurity phase. This signal is anticipated to be related to the 95% purity of the sample. The same holds for the tiny line located at  $-14 \text{ ppm}$  (see arrow), which we also assign to a slight amount of impurities in pristine  $\text{LiBH}_4$ .<sup>54</sup> Most likely, these lines arise from compounds such as  $\text{Li}_2\text{B}_{10}\text{H}_{10}$  or  $\text{Li}_2\text{B}_{12}\text{H}_{12}$ . Alternatively, it has been suggested, at least for  $\text{LiBH}_4/\text{SiO}_2$ , that this line would be attributed to trapped  $\text{H}_2$ , which is released as a result of a surface reaction between  $\text{BH}_4^-$  and the silanol groups at the surface of the oxide.<sup>45,55</sup>

Compared to  $^1\text{H}$ ,  $^6\text{Li}$  MAS NMR revealed more distinct changes when going from  $\text{LiBH}_4$  to the final anion-stabilized nanocomposite, see Figure 1b. Coarse-grained  $\text{LiBH}_4$  shows a signal at approximately  $\delta_{\text{iso}} = -1.35 \text{ ppm}$ , the  $^6\text{Li}$  NMR spectra are referenced to an aqueous solution of LiCl (0 ppm, crystalline lithium acetate served as a secondary reference). If in contact with  $\text{Al}_2\text{O}_3$ , we see that more than approximately 50% of the Li ions, as estimated via deconvolution of the spectrum with Gaussian functions, experiences an NMR line shift toward positive ppm values. The original line, being reduced in intensity, is still seen. This feature reveals the important effect of  $\text{Al}_2\text{O}_3$  and its surface groups on the  $^6\text{Li}$  NMR signal of the composite.

Adding LiI to  $\text{LiBH}_4$  broadens the  $\text{LiBH}_4$  signal and shifts its center of gravity slightly to less negative ppm values; the NMR line of  $\text{LiBH}_4\text{-LiI}$  appears at ca.  $-1.3 \text{ ppm}$  (Figure 1b). Broadening of the line might be explained by site disorder introduced. For  $\text{LiBH}_4\text{-LiI}/\text{Al}_2\text{O}_3$ , a single line is seen at  $\delta_{\text{iso}} = -1 \text{ ppm}$  (see Figure 1b). This line and its position can be explained by two-accumulating effects. Obviously, the Li ions in nanoconfined  $\text{LiBH}_4\text{-LiI}/\text{Al}_2\text{O}_3$  experience a magnetic environment, which is similar but not identical with that in  $\text{LiBH}_4$  or  $\text{LiBH}_4\text{-LiI}$ . As indicated by the line of  $\text{LiBH}_4/\text{Al}_2\text{O}_3$ , a large amount of  $\text{Li}^+$  ions is influenced by the presence of  $\text{Al}_2\text{O}_3$ . For  $\text{LiBH}_4\text{-LiI}/\text{Al}_2\text{O}_3$ , this feature is even more pronounced. Second, as has been seen in a recent study,<sup>11</sup> compared to both  $\text{LiBH}_4\text{-Al}_2\text{O}_3$  and  $\text{LiBH}_4\text{-LiI}$ , ion dynamics, and thus the  $\text{Li}^+$  exchange rate, is noticeably higher in the nanoconfined composite. Hence, at room temperature, and above, the line already represents a motionally narrowed signal with the  $\text{Li}^+$  ions experiencing a magnetically homogeneous matrix (see also below). This view is supported by variable-temperature  $^7\text{Li}$  NMR line shape measurements revealing, from a dynamic point of view, a single, motionally narrowed central line. Moreover, the  $^7\text{Li}$  NMR lines do only reveal a single-electric quadrupole pattern pointing to an ensemble of Li ions experiencing the same electric field gradient. This observation is in line with a magnetically homogeneous environment to which the single  $^6\text{Li}$  MAS NMR line points.

For  $^{11}\text{B}$ , we observed a single line for  $\text{LiBH}_4$ ; the same is true for the line belonging to  $\text{LiBH}_4\text{-LiI}$ , which is shifted toward lower ppm values (see Figure 1c). The spectra were referenced to  $\text{LiBH}_4$  whose signal shows up at  $-41 \text{ ppm}$  when referenced to  $\text{BF}_3\cdot\text{O}(\text{CH}_2\text{CH}_3)_2$  (0 ppm), see Hwang et al.<sup>56</sup> While for the nonconfined samples, single lines are seen; those of the nanoconfined samples reveal two spectral components. For  $\text{LiBH}_4\text{-LiI}/\text{Al}_2\text{O}_3$ , we see that the original line, assigned to  $\text{LiBH}_4$ , is slightly shifted toward the position of the line of  $\text{LiBH}_4\text{-LiI}$ . In addition, a shoulder appeared that is also visible in the spectrum of  $\text{LiBH}_4/\text{Al}_2\text{O}_3$  (Figure 1c). Most likely,  $^{11}\text{B}$

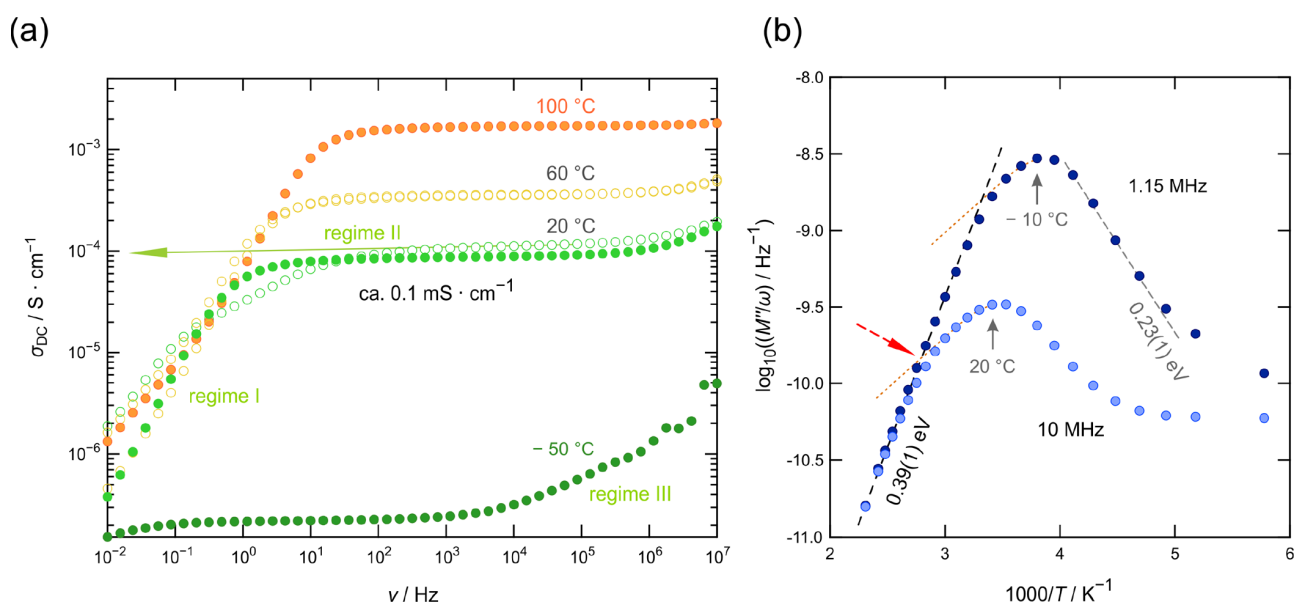


**Figure 2.** (a) Conductivity isotherms of nanoconfined  $\text{LiBH}_4\text{-LiI}/\text{Al}_2\text{O}_3$  recorded at the temperatures indicated (pellet 1, the results of a second pellet are shown in Figure 4) with duplicate measurements at 20 and 60 °C, proving the temperature stability of the sample with respect to ionic conductivity. The isotherms are composed of three regimes showing universal features in conductivity spectroscopy, see text for further explanation. (b) Change of  $M''/\omega$  as a function of inverse temperature, measured for the two frequencies indicated (fresh sample, pellet 2). The peaks obtained give rise to two different activation energies characterizing ion dynamics in  $\text{LiBH}_4\text{-LiI}/\text{Al}_2\text{O}_3$ . The high- $T$  flank corresponds to long-range ion dynamics (0.39 eV), whereas the low- $T$  flank (0.23 eV) points to electrical relaxation processes proceeding on a shorter length scale.  $M''/\omega$  peaks were recorded at 1.15 MHz and 10 MHz, respectively. The kink marked by the dashed arrow indicates that low-dimensional features are masked by the fact that, at sufficiently high temperature, the quantity  $M''/\omega$  is governed by DC conductivity values rather than by the dispersive regimes of the conductivity isotherms; see text for further details.

senses the presence of  $\text{Al}_2\text{O}_3$  causing this extra line in NMR spectroscopy.

Finally, we used  $^{27}\text{Al}$  NMR spectroscopy to visualize any unsaturated Al centers near or at the surface regions of the alumina scaffold, see Figure 1d. Indeed, pure  $\text{Al}_2\text{O}_3$ , which is here present in its  $\gamma$ -modification, produces a  $^{27}\text{Al}$  MAS NMR spectrum that is not only composed of the signals reflecting six- and four-fold-coordinated Al species, see the signals at 9 ppm and at ca. 65 ppm, but is also including a line at approximately 30 ppm (Figure 1d). Although the intensity of the line is low, we are certain that it represents unsaturated pentacoordinated Al ions near the surface of the oxide.<sup>50,52</sup> The generation of such pentacoordinated sites has been studied for nanocrystalline  $\gamma\text{-Al}_2\text{O}_3$ ,<sup>52</sup> which can be prepared by high-energy ball-milling. These sites can be saturated if foreign anions, such as  $\text{F}^-$  anions from  $\text{CaF}_2$  or  $\text{LiF}$ , are offered.<sup>36,52</sup> As a consequence, the signal disappears since  $[\text{AlO}_5\text{F}]$  will give rise to NMR lines with chemical shifts highly comparable to that of  $[\text{AlO}_6]$ . Indeed, this phenomenon is also seen in the present case, see Figure 1d. For both  $\text{LiBH}_4/\text{Al}_2\text{O}_3$  and  $\text{LiBH}_4\text{-LiI}/\text{Al}_2\text{O}_3$ , we observe only the main signals reflecting  $[\text{AlO}_6]$  and  $[\text{AlO}_4]$ . This comparison shows that, at least to a certain degree, the anions  $\text{I}^-$  and  $\text{BH}_4^-$  interact with the  $[\text{AlO}_5]$  surface groups, which serve as anchoring points for these anions. In nanocomposites of  $\text{LiF}/\text{Al}_2\text{O}_3$ , this interaction influences  $\text{Li}^+$  transport, as  $\text{Li}^+$  is assumed to be electrostatically bound to the  $[\text{AlO}_5\text{F}]$  sites.<sup>36</sup> The complex  $[\text{AlO}_5\text{F}]^- \text{Li}^+$  leaves behind  $\text{Li}^+$  vacancies being necessary for the other  $\text{Li}^+$  ions to perform hopping processes in the vicinity of the surface regions. Such a surface-controlled diffusion mechanism might be a universal feature of conductor/insulator composites with  $\gamma\text{-Al}_2\text{O}_3$  equipped with unsaturated species in interfacial

regions. As in the case of  $\text{LiF}/\text{Al}_2\text{O}_3$ <sup>36</sup> or  $\text{LiI}/\text{Al}_2\text{O}_3$ ,<sup>37</sup> percolating surface pathways would give rise to enhanced long-range Li ion transport. Here, also, hydroxyl surface groups might strongly influence  $\text{Li}^+$  interfacial ionic transport as has been suggested by us recently.<sup>11</sup>

Importantly, the asymmetry of the NMR signal belonging to  $[\text{AlO}_6]$  (and  $[\text{AlO}_4]$ ) showing a tail in the direction of low chemical shift values serves as a classical indication of disordering. As  $\text{LiBH}_4\text{-LiI}$  (and  $\text{LiBH}_4$  without  $\text{LiI}$ ) infiltrates the pores of the oxide support, we attribute disordering to the generation of strain and polyhedra distortions experienced by the Al species on or near the surface of the oxide.  $^{27}\text{Al}$  multiquantum MAS NMR might be helpful to characterize this effect in future studies.

**3.2. Impedance Spectroscopy and Resistivity Measurements at Fixed Frequency.** Figure 2a includes selected conductivity isotherms of  $\text{LiBH}_4\text{-LiI}/\text{Al}_2\text{O}_3$ , which show the real part,  $\sigma'$ , of the complex conductivity as a function of frequency  $\nu$ . The isotherms are composed of three regimes. Regime I is caused by polarization effects appearing at sufficiently low frequencies and high DC conductivity values. DC conductivities  $\sigma_{\text{DC}}$  can be read off from the frequency-independent plateaus spanning, at  $\vartheta = 20$  °C, a frequency range of six orders of magnitude (regime II). At this temperature, the ionic bulk conductivity  $\sigma_{\text{DC}}$  is in the order of  $0.1 \text{ mS cm}^{-1}$ , see the horizontal arrow in Figure 2a. With increasing frequency, the DC plateau passes into regime III, which is the dispersive region being characteristic for correlated, forward-backward jump processes and electrical relaxation processes proceeding on a shorter length scale. This regime is best seen at low temperatures and high frequencies, see Figure 2a.

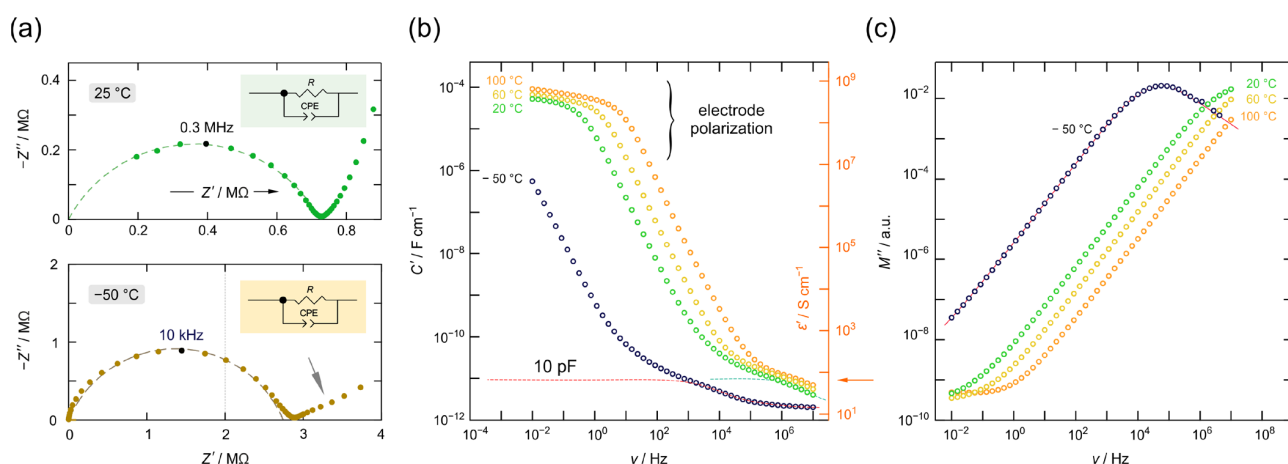


**Figure 3.** (a) Nyquist plots showing the electrical response of nanoconfined  $\text{LiBH}_4\text{-LiI}/\text{Al}_2\text{O}_3$  as the location curve of  $-Z''$  as a function of  $Z'$  at two different temperatures, viz., recorded at 25 °C and -50 °C. The dashed lines show simulations of the semicircle with the equivalent circuit shown. The response at low frequencies reflects electrode polarization, see also (b). In contrast to the spike seen at 25 °C, the flat response of the location curve referring to -50 °C (see arrow) might indicate the influence of interfacial electrical relaxation processes. (b) Real part of the capacitance as a function of frequency. The curves correspond to the conductivity isotherms shown in Figure 2a; the right axis shows the change of  $\epsilon'$  with frequency. (c) Modulus spectra of nanoconfined  $\text{LiBH}_4\text{-LiI}/\text{Al}_2\text{O}_3$  recorded at the temperatures indicated.

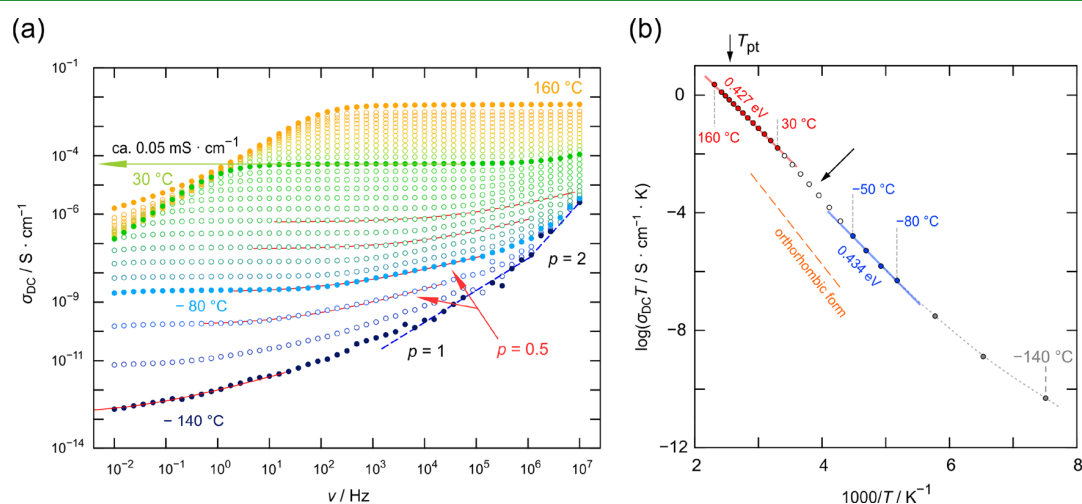


**Figure 4.** (a) Full set of conductivity isotherms recorded at temperatures ranging from -140 to 160 °C. The solid lines show power law fits revealing that the dispersive regime directly associated with the DC response has to be characterized by an exponent  $p = 0.5$ , which points to 2D ionic conduction. The DC response corresponds to the conductivities in the limit  $\nu \rightarrow 0$  excluding polarization effects. At lower temperatures, the frequency dependence in the dispersive regime changes from  $p = 1/2$  to  $p = 1$  and further to  $p = 2$ . While  $p = 1$  is consistent of nearly constant loss behavior of the imaginary part of the complex permittivity,  $p = 2$  indicates the influences of phonons on  $\sigma'$ . (b) Change of the DC conductivity with temperature, plotted as  $\log_{10}(\sigma_{\text{DC}} T)$  vs  $1000/T$ . The position  $\sigma_{\text{DC}} T$  of microcrystalline  $\text{LiBH}_4$  (orthorhombic modification) is also shown;<sup>29</sup> data reproduced with permission from ref 29. Copyright 2010 John Wiley and Sons.

The DC plateau together with its dispersive regime produces a single depressed, i.e., non Debye, semicircle in the complex plane plot; two of these plots are exemplarily shown in Figure 3a. They show the imaginary part,  $-Z''$ , of the complex impedance as a function of the real part,  $Z'$ . Simulating the main electrical response with an equivalent circuit consisting of a resistor connected in parallel with a constant phase element, as shown in the inset of Figure 3a, yields a capacity of 6.5 pF, which lies in the expected range for values of bulk processes. Values in the order of 10 pF are also estimated for this electrical process if we take a look at the change of the real part of the complex capacitance  $C'$  as a function of frequency, see the first step of the  $C'(\nu)$  when coming from high frequencies, which is marked by the dashed lines drawn. In terms of  $\epsilon'$ ,

which is the real part of the complex permittivity, this values corresponds to  $\epsilon'(\nu \rightarrow 0) \approx 80$ , see the right axis of Figure 3b. The shape of the corresponding complex modulus  $M''(\nu)$  is shown in Figure 3c. At  $\vartheta = -50$  °C, the characteristic relaxation frequency reaches values in the order of  $10^5$  Hz. In all three plots (Figure 3a–c), neglecting the effect of polarization of the ion blocking electrodes, a single electrical response characterizes the overall behavior. Hence, from the point of view of electrical relaxation, nanoconfined  $\text{LiBH}_4\text{-LiI}/\text{Al}_2\text{O}_3$  behaves like a homogenous matrix. Considering the small pore size of 9 nm, see above, this result seems to be quite reasonable as the inner regions of the pores are expected to be affected by space charge or surface effects. Here, we cannot see distinct responses that exclusively reflect relaxation in or near

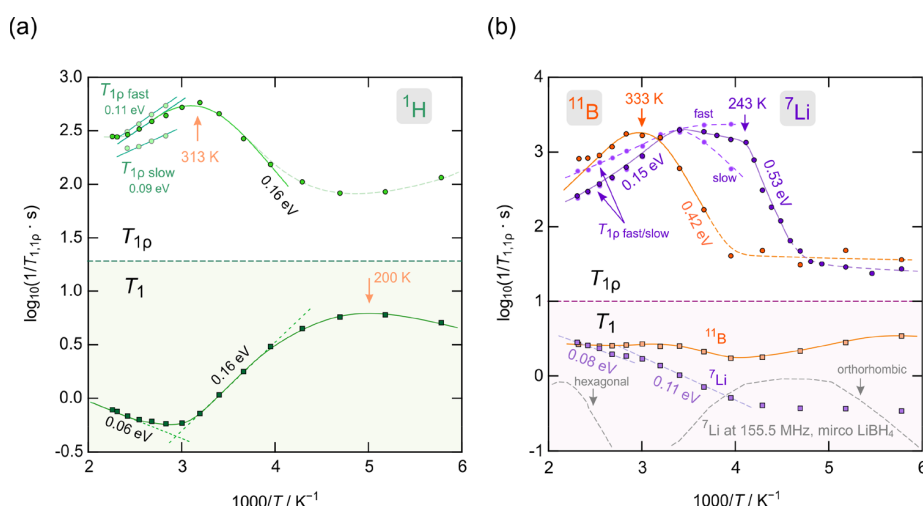


**Figure 5.** (a) Arrhenius plot revealing the temperature behavior of the  $^1\text{H}$  NMR spin–lattice relaxation rates  $1/T_1$  of  $\text{LiBH}_4\text{-LiI/Al}_2\text{O}_3$  (lower graph). The corresponding rates  $1/T_{1\rho}$  recorded in the rotating frame of the reference 20 kHz locking frequency are also shown, see the upper graph. Above 330 K, a separation of two rates according to their distinct  $T_2$  spin–spin relaxation times is possible. (b)  $^7\text{Li}$  and  $^{11}\text{B}$  NMR spin–lattice relaxation rates as a function of the inverse temperature. Spin-lock NMR rates (20 kHz) are shown in the upper part of the Figure; again, a separation into two sub-ensembles is possible indicated by the rates  $1/T_{1\rho,\text{slow}}$  and  $1/T_{1\rho,\text{fast}}$ . Dashed and dotted lines are drawn to guide the eye. Values show activation energies calculated from the slopes of the lines drawn. The behavior of  $1/T_1$  of  $^7\text{Li}$  of coarse-grained (microcrystalline)  $\text{LiBH}_4$  is indicated by dashed lines (155 MHz), data reproduced with permission from ref 29. Copyright 2010 John Wiley and Sons.

interfacial regions and regions farther away from the surface. This observation is in agreement with the  $^6\text{Li}$  MAS NMR and, partly, also with the  $^7\text{Li}$  NMR line shapes, see below. These lines, because of sufficiently rapid  $\text{Li}^+$  exchange, do not point to strongly dynamically distinct Li ions. This dynamic homogeneity seen does also agree with the shape of the resistivity peaks recorded, see Figure 2b.

In Figure 2b, the change of the resistivity expressed as  $M''$  divided by frequency  $\omega$  is shown.  $M''$  is the imaginary part of the electrical modulus.  $\rho'_M = M''/\omega$  is given by  $\rho'_M = \tau_\rho/(1 + (\tau_\rho\omega)^\beta)$  with  $1 < \beta \leq 2$  where  $\tau_\rho$  denotes the electrical relaxation time, and  $\beta$  is a parameter that quantifies the deviation of the Lorentzian-shaped peak  $\log_{10}(\rho'_M)$  versus  $1/T$  from symmetric behavior. For  $\beta = 2$ , symmetric rate peaks would be obtained.  $E_{a,\text{high}} = 0.39$  eV and  $E_{a,\text{low}} = 0.23$  eV are related to each other via  $E_{a,\text{low}} = (\beta - 1)E_{a,\text{high}}$  yielding  $\beta \approx 1.6$ . This view on  $\rho'_M$  is comparable to that of NMR spin–lattice relaxation measurements, see below. The shape of the  $\rho'_M(1/T)$  peak, which points to length-scale-dependent heterogeneous electrical relaxation, agrees with the observation of a depressed, non Debye semicircle in the complex plot  $-Z''(Z')$  as well as with the dispersive signature of the conductivity isotherms  $\sigma'(\nu)$ , which is seen at sufficiently low temperatures (regime III in Figure 2a).

Importantly, we notice that the shape of the  $\rho'_M$  peaks near the maximum is composed of two contributions. The arrow in Figure 2b marks a kink (380 K) most likely showing the crossover from  $\rho'_M$  values being influenced by regime III and those governed by regime II. The latter influence is seen at higher temperatures where  $\rho'_M(1/T)$  follows an Arrhenius behavior with  $E_a = 0.39$  eV. This activation energy agrees well with that of  $\sigma_{\text{DC}}T(1/T)$ , see Figure 4b, characterizing long-range ion transport.  $\rho'_M$  values recorded below 380 K, see the curve measured at 10 MHz, reveal a frequency-dependent behavior if we compare the resistivity values measured at 10 Hz with those recorded at 1.2 MHz, cf. the dashed lines drawn.

Such a dispersive behavior is here interpreted as a result of 2D ionic conduction in the interior regions of  $\text{LiBH}_4\text{-LiI/Al}_2\text{O}_3$ .

The frequency dependence of the conductivity isotherms in regime III of Figure 2a supports this idea. They are composed of a dispersive regime that also points to low-dimensional ionic transport in  $\text{LiBH}_4\text{-LiI/Al}_2\text{O}_3$ . In general, for hexagonal  $\text{LiBH}_4$ , being stable at temperatures above 110 °C, 2D  $\text{Li}^+$  self-diffusion was proved by frequency-dependent  $^7\text{Li}$  and  $^6\text{Li}$  NMR relaxation.<sup>57</sup> If the hexagonal modification is, however, stabilized at sufficiently low temperatures, the dispersive regime of the  $\sigma'(\nu)$  becomes detectable, which should contain information about dimensionality effects. In Figure 4a, a full set of conductivity isotherms recorded over a much larger temperature range than that covered by Figure 2a is shown. For these variable-temperature  $\sigma'$  measurements, we used a second, fresh pellet to probe regime III in detail. Although  $\sigma_{\text{DC}}$  is somewhat lower for this pellet (0.05 mS  $\text{cm}^{-1}$  at 20 °C), the dispersive part is perfectly seen over a large frequency range. If it is approximated with Jonscher's power law<sup>58</sup>  $\sigma'(\nu) \propto \nu^p$ , we obtain  $p = 0.5$ . It has been shown earlier that an exponent  $p$  of 1/2 is a valid argument pointing to 2D ionic conduction.<sup>59</sup> For 3D ion transport,  $p$  is expected to take values of 0.6–0.9, while 1D (channel-like) transport should result in  $p < 0.4$ .<sup>59</sup>

Here, the idea of 2D ionic transport restricts to the  $\text{LiBH}_4\text{-LiI}$  regions of the sample. As mentioned above, at higher  $T$ , the resistivity values are mainly governed by  $\sigma_{\text{DC}}$  rather than by  $\sigma'(\nu) \propto \nu^p$ . Hence, we conclude that effectively 3D ionic conduction is established on a long-range length scale in  $\text{LiBH}_4\text{-LiI/Al}_2\text{O}_3$ , while 2D ion transport is seen on a shorter-length scale.

To further analyze long-range ionic transport, we read off  $\sigma_{\text{DC}}$  values from the isotherms presented in Figure 4a. In Figure 4b, the change of  $\sigma_{\text{DC}}T$  with  $1/T$  for pellet 2 is shown. In above ambient conditions, we see that the data points follow Arrhenius behavior with an activation energy of  $E_a = 0.427$  eV. At approximately  $\vartheta = -50$  °C, a slight curvature appears (see arrow) slightly reducing the ionic conductivity while almost

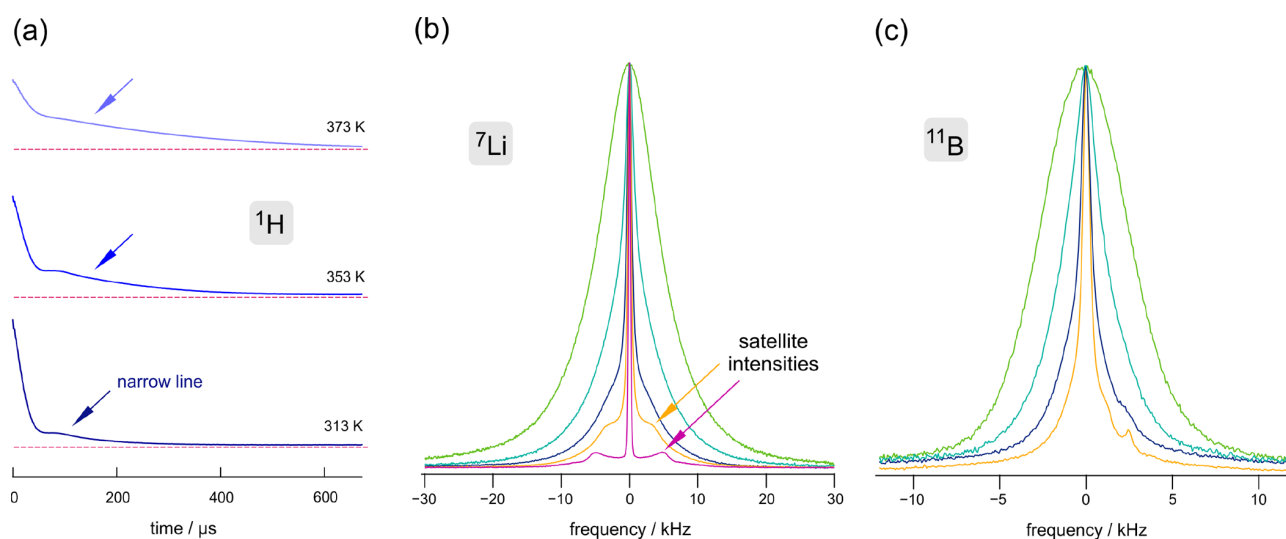


**Figure 6.** (a)  $^1\text{H}$  NMR FIDs (300 MHz) of  $\text{LiBH}_4\text{-LiI}/\text{Al}_2\text{O}_3$  measured at the temperatures indicated. The FIDs are composed of two contributions reflecting two  $^1\text{H}$  sub-ensembles that differ in spin–spin relaxation behavior. (b, c) Variable-temperature  $^7\text{Li}$  (116 MHz) and  $^{11}\text{B}$  NMR (96 MHz) spectra (173, 253, 294, 313, and 433 K) of nanoconfined  $\text{LiBH}_4\text{-LiI}/\text{Al}_2\text{O}_3$ . In the case of  $^7\text{Li}$  NMR, distinct satellite intensities show up at high temperatures.

unchanging the activation energy. Thus, this change is mainly caused by a slight reduction of the pre-exponential factor  $\sigma_0$  in  $\sigma_{\text{DC}}T = \sigma_0 \exp(-E_a/(k_{\text{B}}T))$  where  $k_{\text{B}}$  denotes Boltzmann's constant. The prefactor contains, among other quantities, the effective number of charge carriers, the attempt frequency, and an activation entropy term; thus, a range of factors can cause this slight difference. Below  $-100$  °C, the values seem to be influenced by further conduction processes because  $\sigma_{\text{DC}}T$  turned out to be higher than expected if the Arrhenius line, which is characterized by  $E_a = 0.434$  eV, is extrapolated toward lower  $T$ , see Figure 4b. Likely, electronic conduction might influence the overall DC conductivity of such a nanostructured sample in this low- $T$  range. Most importantly, even up to temperatures well below ambient, we do not find strong indications that the material transforms from its hexagonal modification, stabilized by the incorporation of LiI, to the orthorhombic form. The latter, if present in a coarse-grained form or being in contact with  $\text{Al}_2\text{O}_3$  in the sense of a dispersed ionic conductor, shows a much lower ionic conductivity.<sup>29</sup> For comparison, the ionic conductivity of microcrystalline orthorhombic  $\text{LiBH}_4$  with a crystallite diameter in the micrometer ( $\mu\text{m}$ ) range is indicated by a dashed line in Figure 4b. The original temperature  $T_{\text{pt}}$  at which the phase transition occurs (ca. 110 °C) is also indicated, see the arrow pointing at the upper axis. In conclusion, we do not find any evidence for a marked phase transition for  $\text{LiBH}_4\text{-LiI}/\text{Al}_2\text{O}_3$ . Quite the contrary, we assume that nanoconfinement supports the stabilization of the hexagonal phase of  $\text{LiBH}_4\text{-LiI}$  nanoconfined in alumina. 2D ionic conduction seems to be the prevailing transport mechanism in  $\text{LiBH}_4\text{-LiI}$  as revealed by the  $p^{0.5}$  frequency behavior seen in  $\sigma'(\nu)$  measurements, as has also been suggested by other methods and theory.<sup>57,60–62</sup>

**3.3.  $^1\text{H}$ ,  $^7\text{Li}$ , and  $^{11}\text{B}$  NMR Spin–Lattice Relaxation in  $\text{LiBH}_4\text{-LiI}/\text{Al}_2\text{O}_3$ .** In Figure 5, the temperature behaviors of the NMR spin–lattice relaxation rates  $^1\text{H}$ ,  $^{11}\text{B}$ , and  $^7\text{Li}$  of  $\text{LiBH}_4\text{-LiI}/\text{Al}_2\text{O}_3$  are shown. As nuclear spin relaxation is sensitive to both long-range and short-range ion dynamics, including translational processes, rotational motions, and even librations, we expect a wide range of activation energies probed by NMR.

Indeed, the diffusion-induced rates, if analyzed in the frame of Arrhenius representations, yield a couple of different flanks pointing to activation energies ranging from 0.06 to 0.53 eV. A similar situation has been met for cation-disordered fluorides.<sup>63</sup>

**3.3.1.  $^1\text{H}$  NMR Spin–Lattice Relaxation.** Starting with  $^1\text{H}$  NMR, see Figure 5a, we see that, below 300 K, the laboratory-frame  $1/T_1$  rates pass through a broad maximum. Most likely, this peak reflects rotational  $\text{BH}_4^-$  motions as a very similar behavior has been documented for  $\text{LiBH}_4$ . The slight increase in  $1/T_1$  above 300 K is attributed to either H-dynamics or localized  $\text{Li}^+$  motions indirectly sensed by the  $^1\text{H}$  probes or H-dynamics. The associated apparent activation energy of 0.06 eV points to correlated ionic motion proceeding on a local length scale. At even higher temperatures, one would expect the rate to pass through a diffusion-induced maximum. With decreasing Larmor frequency, this maximum would be shifted toward lower  $T$ . The corresponding peak  $1/T_1(1/T)$  should occur at  $T_{\text{max}}$  where the motional correlation rate  $1/\tau_c$  reaches the angular Larmor frequency  $\omega_0 (= \nu_0 \times 2\pi = 300 \text{ MHz} \times 2\pi)$  fulfilling the relationship  $\tau_c \omega_0 \approx 1$ .  $1/\tau_c$  is within a factor of 2 identical with the  $\text{Li}^+$  jump rate,<sup>64</sup> provided the peak is solely caused by  $\text{Li}^+$ -translational jumps. Replacing  $\omega_0$ , having values in the megahertz (MHz) range, by  $\omega_1$ , being the spin-lock frequency in the kilohertz (kHz) range, will shift this peak considerably toward lower  $T$ .<sup>64</sup> As can be seen in the upper graph of Figure 5a, such a peak indeed appears at  $T_{\text{max}} = 313$  K. This peak corresponds to a similar diffusion-induced peak seen in  $^{11}\text{B}$  NMR (333 K, Figure 5b), see below. The activation energy of the  $^1\text{H}$  NMR peak probed by  $1/T_{1\rho}$  is 0.16 eV. This value agrees with that from the  $M''/\omega$  analysis if we consider the low- $T$  flank of the  $\rho'_M(1/T)$  peak (0.21 eV, 100 kHz, see Figure 2b). We also observed that  $1/T_{1\rho}$  of  $^1\text{H}$  increases at temperatures lower than 200 K. At such low temperatures, the rate  $1/T_{1\rho}$  is expected to pass through another rate peak, which corresponds to the behavior of  $1/T_1$  ( $T_{\text{max}} = 200$  K), presumably characterizing fast rotational  $\text{BH}_4^-$  dynamics.

Noteworthy, the  $^1\text{H}$  (spin-1/2) NMR rates shown in Figure 5a were extracted from magnetization transients that were constructed by analyzing the full area under the corresponding

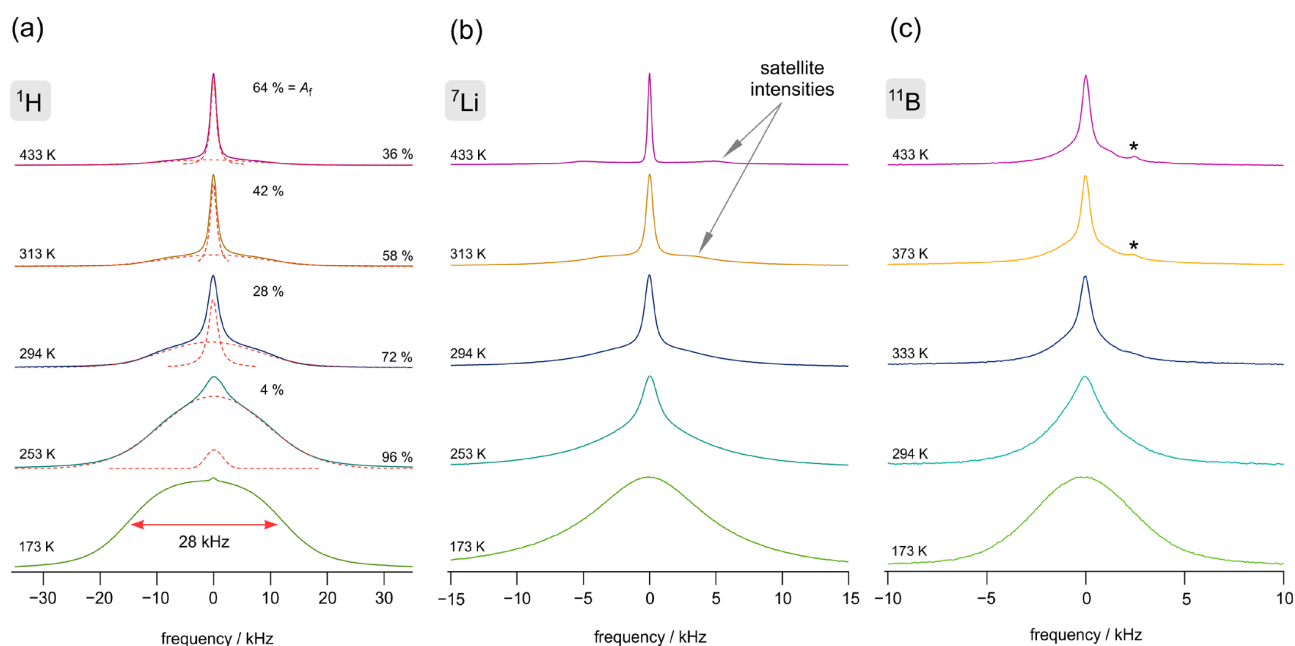


**Figure 7.** (a)  $^1\text{H}$  NMR spectra of  $\text{LiBH}_4\text{-LiI}/\text{Al}_2\text{O}_3$  being composed of two spectral components reflecting two dynamically distinct  $^1\text{H}$  spin ensembles. Dashed lines show deconvolutions of the spectra with Gaussian and Lorentzian functions. (b, c)  $^7\text{Li}$  and  $^{11}\text{B}$  spectra as in Figure 6 but shown in a stacked plot to highlight the Gaussian shape of the lines at low temperatures.

FIDs, see Figure 6a. The resulting transients show stretched exponential behavior, see Experimental Section. However, as can be seen in Figure 6a, we observed so-called two-component FIDs at temperatures above ambient. Such a two-component FID is composed of a slowly decaying part, which can be well separated from a fast-decaying contribution dominating the FID at short acquisition times. Consequently, Fourier transformation leads to  $^1\text{H}$  NMR spectra showing two contributions, as presented in Figure 7a.

The motionally narrowed contribution represents  $^1\text{H}$  spins sensing magnetic-dipolar fluctuations being fast on the NMR spectral time scale, i.e., the corresponding motional correlation greatly rate exceeds the rigid lattice line width (28 kHz at 173 K, see Figure 7a). With increasing temperature, the majority of the  $^1\text{H}$  spins benefit from this motional averaging process resulting in an overall line shape, which is mainly dominated by the narrow line. The change in area fraction  $A_f$  of this line, on top of the broad one, is indicated in Figure 6a;  $A_f$  reaches values as high as 64% at 433 K. At room temperature, approximately one third of the  $^1\text{H}$  spins participate in a rather fast dynamic process. In general, one would assign the narrow line to those H spins located in the interfacial regions. On the other hand, the two-component line shape could also originate from strongly heterogeneous dynamics of the whole spin ensemble, see below.

To test whether these two spectral contributions with individual spin–spin relaxation times are also characterized by distinct  $1/T_1$  rates, we analyzed parts of the underlying FIDs in the frame of a saturation recovery experiment. This procedure has been explained in detail elsewhere.<sup>65</sup> Here, no difference in  $1/T_1$  is observed between the rates obtained either by analyzing the full FID or the two differently decaying parts highlighted in Figure 7a. This finding points to fast-spin diffusion connecting the two  $^1\text{H}$  spin reservoirs with their distinct spin–spin relaxation behavior. Spin diffusion due to fast flip–flop processes results in a single, averaged spin–lattice

relaxation behavior. It is, however, in contrast for  $^1\text{H}$  spin-lock  $1/T_{1\rho}$ . The circles in light green in Figure 5a show that it is possible to obtain two rates, which we call  $1/T_{1\rho,\text{fast}}$  (0.11 eV) and  $1/T_{1\rho,\text{slow}}$  (0.06 eV). The rates differ by a factor of 2 to 3, at most. Importantly, they follow nearly the same temperature behavior (0.09 eV) as seen for the mean rates  $1/T_1$  in this  $T$  range. Thus, spin-diffusion seems to be present too; however, it turns out to be less effective as in the case of  $^1\text{H}$  NMR spin–lattice relaxation characterized by the rate  $1/T_1$ .

**3.3.2.  $^7\text{Li}$  and  $^{11}\text{B}$  NMR Spin–Lattice Relaxation.** The  $^7\text{Li}$  and  $^{11}\text{B}$  NMR spin–lattice relaxation NMR rates  $1/T_1$  and  $1/T_{1\rho}$  are shown in Figure 5b, the evolution of the corresponding spectra with temperature is again presented in Figures 6 and 7. In contrast to  $^1\text{H}$ , the  $^7\text{Li}$   $1/T_1$  NMR rates do not reveal a strong influence of  $\text{BH}_4^-$  rotations at low  $T$ . Rather, below 250 K, the rates are influenced by nondiffusive background relaxation. Above this temperature, they pass into a flank with an activation energy characterized by 0.11 eV. A slight curvature is seen at 340 K; above this temperature,  $E_a$  reduces to 0.08 eV. As for  $^1\text{H}$ , we assign these low values of  $E_a$  to short-range dynamics in nanoconfined  $\text{LiBH}_4\text{-LiI}/\text{Al}_2\text{O}_3$ . For comparison, in Figure 5b, the  $^7\text{Li}$  NMR rates of coarse-grained  $\text{LiBH}_4$  are also included.<sup>29,57</sup> While in hexagonal  $\text{LiBH}_4$ , present above  $T_{\text{pt}} \approx 100$  °C, the rates are induced by  $\text{Li}^+$  diffusion; below this temperature, they reflect  $\text{BH}_4^-$  rotational dynamics. The  $^7\text{Li}$  NMR response of  $\text{LiBH}_4\text{-LiI}/\text{Al}_2\text{O}_3$  turned out to be completely different to that seen for the source material showing that, from a dynamic point of view as seen by NMR, anion substitution and nanoconfinement have turned the ionic conductor into a completely different material.

$1/T_{1\rho}$  of  $^7\text{Li}$  reveals a more complex behavior compared to that observed for the corresponding  $1/T_1$  rates, Figure 5b. A nondiffusion-induced background appeared below  $T = 210$  K. Above this temperature, the rates, however, sharply increase. This increase is characterized by an activation energy of 0.53 eV, which is very similar to the activation energy extracted

from the  $\rho'_M(1/T)$  peak in the high- $T$  limit (0.57 eV, Figure 2b). Obviously, spin-lock  $^7\text{Li}$  NMR, if carried out at a locking frequency of 20 kHz, is able to sense long-range ion dynamics. The above-mentioned curvature seen in  $1/T_1$  might correspond to the maximum in  $T_{1\rho}$ , seen at 243 K. At higher temperature than 243 K (Figure 5b), the behavior of  $1/T_{1\rho}(^7\text{Li})$  can only be understood if we consider several relaxation rate peaks contributing to the overall response. Interestingly, the flank seen at high  $T$  is again characterized by an activation energy (0.15 eV, Figure 5b) that resembles those seen by  $1/T_1(^7\text{Li})$ ; it is also comparable to the values obtained from  $^1\text{H}$  NMR, see above.

Similar to  $^1\text{H}$  NMR, also, the FIDs of the  $^7\text{Li}$  nucleus are, at least to some extent, composed of several components if results above  $T = 230$  K are regarded (not shown for the sake of brevity). The corresponding spectra are displayed in Figures 6b and 7b. As  $^7\text{Li}$  is a spin-3/2 nucleus,<sup>66</sup> the sharply decaying part of its FID partly (or mainly) originates from electric quadrupole interactions, which are characteristic for  $\text{LiBH}_4$ , if present in its hexagonal modification.  $^7\text{Li}$  NMR spectra have been discussed in detail elsewhere;<sup>11</sup> worth noting, at each temperature, the lines are to be characterized by a single, averaged quadrupole powder pattern with distinct  $90^\circ$  singularities appearing at a distance of  $\pm 5$  kHz from the central line. They result in a quadrupole splitting of  $\Delta \approx 10$  kHz (Figures 6b and 7b). Hence, also from the point of view of quadrupolar electric interactions, the Li ions belong a single ensemble with electrically equivalent spins. We do not see the original electrical powder patterns of  $\text{LiBH}_4$  ( $\Delta \approx 18.5$  kHz) or  $\text{LiBH}_4\text{-LiI}$  ( $\Delta \approx 18.6$  kHz) any longer. In our earlier publication,<sup>11</sup> we speculated that both the ions near the  $\text{Al}_2\text{O}_3$  surface regions, possibly influenced by (residual) hydroxyl surface groups,<sup>11</sup> and those farther away are subjected to a structurally stressed  $\text{LiBH}_4\text{-LiI}$  phase with high ionic conductivity. Space charge zones,<sup>35,41</sup> high defect densities or increased structural disorder<sup>34</sup> may characterize these inner, interfacially influenced regions leading to a magnetically and electrically homogenous phase showing enhanced, but heterogeneous, ion dynamics.

The other part of the  $^7\text{Li}$  NMR FIDs, which forms the central NMR line after Fourier transformation, may also represent  $^7\text{Li}$  sub-ensembles differing in spin-spin-relaxation times. A clear separation as in the case of  $^1\text{H}$  NMR is, however, fraught with difficulties. Thus, we cannot precisely identify  $\text{Li}^+$  ions in the interfacial regions undergoing rapid exchange processes as those spins residing farther away from these regions are involved in rapid diffusion also. The same situation was met in  $\text{Li}_x\text{TiS}_2$  for which structural disorder did not lead to a significant enhancement of  $\text{Li}^+$  dynamics. In layer-structured  $\text{TiS}_2$ , the mobility of  $\text{Li}^+$  is already rather high.<sup>67</sup> Here, as in the case of  $^1\text{H}$  spin-lattice relaxation  $1/T_1$ , the different contributions to the  $^7\text{Li}$  FIDs undergo the same  $^7\text{Li}$  spin-lattice relaxation recovery. Again, we conclude that they belong to a magnetically homogeneous Li spin ensemble affected by rapid spin diffusion. Such an ensemble is also suggested by the thermally coalesced  $^6\text{Li}$  MAS NMR signal discussed above.

For comparison, this finding is in contrast for nanocrystalline, poorly conducting orthorhombic  $\text{LiBH}_4$  presented in literature quite recently.<sup>38</sup> Its  $^7\text{Li}$  NMR lines show well-defined two-component line shapes and biexponential magnetization transients at different temperatures. Note that in the orthorhombic modification,  $\text{Li}^+$ -translational ion dynamics is much lower than in the hexagonal form. Only in the interfacial

regions of nanocrystalline, orthorhombic  $\text{LiBH}_4$ -fast  $\text{Li}^+$  ions (0.18 eV) were found that could separately be studied by  $^7\text{Li}$  NMR spin-lattice relaxation.<sup>38</sup> A very similar result has been seen by  $^7\text{Li}$  NMR in  $\text{LiI}/\text{Al}_2\text{O}_3$  mixtures investigated by Ardel et al.<sup>37</sup> In such mixtures one  $\text{Li}^+$  site has been associated with surface or interface regions.

A separation, being similar to that discussed and carried out for  $^1\text{H}$  NMR, is only partly possible for the  $^7\text{Li}$  NMR spin-lock rates  $1/T_{1\rho}$ . While  $1/T_{1\rho,\text{slow}} = 1/T_1$ , the rates  $1/T_{1\rho,\text{fast}}$  reveal an even weaker temperature dependence than  $1/T_1$  (0.11 eV vs 0.15 eV), see Figure 5b. Again, we interpret such low activation energies as a signature for fast, but localized, dynamic processes, which do not necessarily lead to long-range  $\text{Li}^+$  ion transport. Alternatively, they might reflect fast  $\text{Li}^+$  dynamic processes near the conductor/insulator interface,<sup>42</sup> as also seen for nanocrystalline orthorhombic  $\text{LiBH}_4$  (0.18 eV).<sup>38</sup>

The  $^{11}\text{B}$  NMR spin-lattice relaxation rates, see Figure 5b, reveal two shallow NMR rate peaks. The one at lower  $T$  could again be assigned to rotational ion dynamics, while the exact origin of that seen at higher  $T$  remains unknown. In general, it is well known for  $\text{LiBH}_4$  that the  $\text{BH}_4^-$  units undergo fast rotational motions. Moreover, also, the presence of translational ion dynamics has been suggested on the basis of  $^{11}\text{B}$  NMR.<sup>26,68</sup> Interactions with the alumina scaffold might change this dynamic behavior of the anions. Here, in  $^{11}\text{B}$  spin-lock NMR, we observed a single peak located at  $T_{\text{max}} = 313$  K; it might indeed be caused by a slower Li translational process indirectly seen by the  $^{11}\text{B}$  spins or by  $\text{BH}_4^-$  translational motions, which were suggested for  $\text{LiBH}_4$ .<sup>27</sup> Interestingly, the activation energy extracted from the  $^{11}\text{B}$   $1/T_{1\rho}(1/T)$  NMR is very similar to that seen by  $\sigma_{\text{DC}}T$ ; hence, this agreement supports the idea that, at least from a quantitative point of view, the peak is influenced by  $\text{Li}^+$ -hopping processes.<sup>11</sup>  $^{11}\text{B}$  NMR spectra (spin-3/2) are shown in Figures 6c and 7c. A tiny line, which is marked by an asterisk in Figure 7c, points to a side phase that has already been discussed for  $^1\text{H}$  MAS NMR, see above.  $^{11}\text{B}$  NMR spectra are mainly governed by central lines that are flanked, at least at high temperatures, by satellite intensities. Alternatively, the broad spectral component could be interpreted as a signal arising from less mobile  $\text{BH}_4^-$  units.

**3.4. Long-Range Ion Transport and Diffusion Coefficients as Probed by NMR and Electrical Measurements.** NMR spin-lattice relaxation measurements reveal a rather complex picture of the magnetic fluctuations taking place in nanoconfined  $\text{LiBH}_4\text{-LiI}/\text{Al}_2\text{O}_3$ . Apart from rapid localized ion dynamics, a practical parameter being relevant for battery applications is the macroscopic (self-)diffusion coefficient  $D$  of the Li ions. Here, we took advantage of  $^7\text{Li}$  PFG NMR measurements to probe tracer diffusion coefficients  $D_{\text{PFG}}$  at two different temperatures, see the Arrhenius plot of Figure 8.

To compare the results from PFG NMR with those from conductivity spectroscopy, we used the Nernst-Einstein equation,  $D_\sigma = (\sigma_{\text{DC}}k_{\text{B}}T)/(Nq^2)$ , to convert  $\sigma_{\text{DC}}$  into solid-state diffusion coefficients; in Figure 8, the results for the two pellets are included. Here,  $N$  is the charge carrier density, which we estimated to be approximately  $1.8 \times 10^{27} \text{ m}^{-3}$ ,  $q$  denotes the charge of the  $\text{Li}^+$  ions. Here, we simply used the chemical formula of  $\text{LiBH}_4\text{-LiI}/\text{Al}_2\text{O}_3$  and assumed that all  $\text{Li}^+$  ions participate in diffusion. The effective number might be lower and should be related to the exact defect structure of the

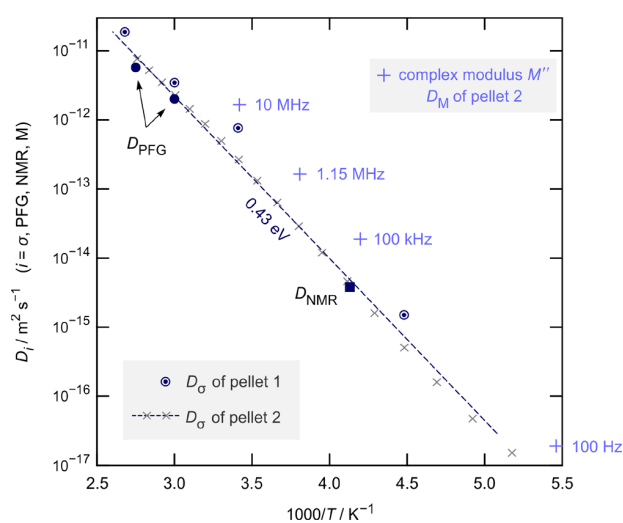


**Figure 8.** Arrhenius plot illustrating the temperature dependence of the diffusion coefficients  $D_i$  ( $i = \sigma$ , PFG, NMR, M) deduced from the various methods applied to study long-range ion dynamics in nanoconfined  $\text{LiBH}_4\text{-LiI}/\text{Al}_2\text{O}_3$ . Depending on temperature, the difference between  $D_\sigma$  values of pellets 1 and 2 turned out to be a factor of 3 (at most). The dashed line is a guide to the eye whose slope corresponds to an activation energy of 0.43 eV. Coefficients deduced from electric modulus spectroscopy (pellet 2) are also included. They run in parallel but are shifted toward larger values. Such a discrepancy can be described to length-scale-dependent dynamics. While  $\sigma_{\text{DC}}$  senses long-range ion dynamics, electric modulus data might already be influenced by short-range ion dynamics.

material. Moreover, this estimate holds only under the assumption of  $\text{Li}^+$  being the sole charge carrier.

In addition, to estimate  $D_{\text{NMR}}$  we used the result from  $^7\text{Li}$  NMR spin-lock measurements. As mentioned above, the relation  $\omega_1\tau_c \approx 1$  holds for spin-lock relaxation  $1/T_{1\rho}$ . To estimate  $D_{\text{NMR}} = a^2/(4\tau_c)$  we used the  $^7\text{Li}$  NMR peak  $1/T_{1\rho}$  that appears at  $T_{\text{max}} = 243$  K, see Figure 5b.  $a$  ( $= 4.26$  Å) is the nearest-neighbor distance of a  $\text{Li}^+$  ion in the hexagonal lattice. Finally, we estimated diffusion coefficients  $D_M$  from the  $M''/\omega$  peak maxima by assuming that at  $T_{\text{max}}$  the associated electrical relaxation time is given by  $\omega\tau_e \approx 1$  with  $\omega$  being the fixed measurement frequency.  $D_M$  was calculated by means of the Einstein–Smoluchowski equation,<sup>34</sup> which reads for 2D diffusion  $D_M = a^2/(4\tau_M)$ .

In general, differences between  $D_{\text{PFG}}$  and  $D_\sigma$  can be explained by the Haven ratio  $H_r$  deviating from  $H_r = 1$ . If we identify  $D_{\text{PFG}}$  with the tracer diffusion coefficient  $D_{\text{tracer}}$ , the two diffusion coefficients are related to each other via  $D_{\text{tracer}} = H_r D_\sigma$ . On the other hand,  $D_{\text{NMR}}$  and  $D_{\text{tracer}}$  are linked via the correlation factor  $f$  ( $0 < f \leq 1$ ):  $D_{\text{tracer}} = f D_{\text{NMR}}$ . Altogether, this leads to  $D_{\text{NMR}} = (H_r/f) D_\sigma$ . Hence, the factor  $H_r/f$  deviating from 1 can explain the rather small differences between the coefficients shown in Figure 8. Despite these differences, the results for  $D_\sigma$ ,  $D_{\text{PFG}}$ , and  $D_{\text{NMR}}$  shown in Figure 8 agree well with each other. As indicated by the straight line, which is used as a guide to the eye here, the data points follow an Arrhenius law with an activation energy of 0.43 eV; at ambient temperature, we estimated the mean diffusion coefficient to be in the order of ca.  $3 \times 10^{-13} \text{ m}^2 \text{ s}^{-1}$  (298 K, pellet 2). The shift of  $D_M$  toward larger coefficients might be explained by short-range ion dynamics already influencing the maxima of

the resistivity peaks recorded. Indeed, as has been shown by both  $^1\text{H}$ ,  $^7\text{Li}$ , and  $^{11}\text{B}$  NMR line shapes and NMR spin–lattice relaxation measurements quite complex, translational and rotational (and librational) dynamic processes are present including (strictly) localized events determined by much lower activation energies of only 0.06 eV.

#### 4. SUMMARY AND CONCLUSIONS

Overall, long-range ionic transport in nanoconfined  $\text{LiBH}_4\text{-LiI}/\text{Al}_2\text{O}_3$  as probed by conductivity spectroscopy follows Arrhenius behavior (0.43 eV) over a dynamic range of almost 8 orders of magnitude. Solid-state diffusion coefficients estimated from conductivity values and variable-temperature resistivity data recorded at fixed frequency agree very well with those obtained from macroscopic  $^7\text{Li}$  PFG NMR. At room temperature, a diffusion coefficient of  $3 \times 10^{-13} \text{ m}^2 \text{ s}^{-1}$  was obtained.  $^1\text{H}$ ,  $^7\text{Li}$ , and  $^{11}\text{B}$  NMR relaxation measurements revealed highly complex dynamics with a broad range of activation energies ranging from 0.06 to 0.57 eV.

Interfacial effects are seen by  $^{27}\text{Al}$  MAS NMR; most likely, pentacoordinated sites of the  $\text{Al}_2\text{O}_3$  scaffold become saturated through the formation of  $\text{Li}^+[\text{AlO}_3\text{I}]^-$  or  $\text{Li}^+[\text{AlO}_3\text{BH}_4]^-$  species; the participation of surface hydroxyl groups has to be considered also, as suggested recently.<sup>11</sup> This view is supported by  $^6\text{Li}$  MAS and  $^{11}\text{B}$  MAS NMR, the latter reveals two B sites slightly differing in the magnetic environment. At least for  $^1\text{H}$ , the corresponding variable-temperature, two-component NMR line shapes showed H spins subjected to quite different spin–spin fluctuations. Most likely, they reflect spins near interfacial regions and spins farther away from the surface, that is, located in the  $\text{LiBH}_4\text{-LiI}$  matrix. As shown by  $^7\text{Li}$  NMR line shapes and broadband conductivity spectroscopy, the Li spins participate in heterogeneous ion dynamics but; most likely, they belong to an electrically homogeneous ensemble. We speculate that interfacial effects also influence the inner regions of the nanometer-sized pores that are filled with  $\text{LiBH}_4\text{-LiI}$ . This situation is usually met for nanostructured ion conductors dominated by space charge effects, which are termed artificial ion conductors.<sup>69,70</sup> Specifically, the reaction with hydroxyl surface groups might play a crucial role too since insights into  $^{27}\text{Al}$  MAS NMR underpin this assumption.<sup>11</sup>

Finally, the dispersive regions in conductivity spectra follows Jonscher’s power law with an exponent of  $p = 1/2$ . This result points to low-dimensional (2D) ionic transport in the layer-structured, hexagonal  $\text{LiBH}_4\text{-LiI}$  regions. We were able to follow this 2D ion transport process down to temperatures as low as  $-80$  °C. On the other hand, NMR and electric modulus spectroscopy carried out at sufficiently high temperatures reveal long-range 3D ion transport, likely involving fast ion conduction also along the interfacial conductor/insulator regions. While for many highly conducting layer-structured materials, grain boundaries may act as regions blocking ion transport; in the case of nanoconfined  $\text{LiBH}_4\text{-LiI}/\text{Al}_2\text{O}_3$ , such limitations can be overcome by fast-conducting interfacial conductor/insulator regions.

#### ■ ASSOCIATED CONTENT

##### Supporting Information

The Supporting Information is available free of charge at <https://pubs.acs.org/doi/10.1021/acsami.0c10361>.

NMR parameters;  $^1\text{H}$ ,  $^7\text{Li}$ , and  $^{11}\text{B}$  NMR relaxation transients; and PFG NMR decay curves (PDF)

## AUTHOR INFORMATION

## Corresponding Authors

**Roman Zettl** – Institute for Chemistry and Technology of Materials, and Christian Doppler Laboratory for Lithium Batteries, Graz University of Technology, Graz 8010, Austria; Inorganic Chemistry and Catalysis, Debye Institute for Nanomaterials Science, Utrecht University, Utrecht 3584, Netherlands; Email: [zettl@tugraz.at](mailto:zettl@tugraz.at)

**H. Martin R. Wilkening** – Institute for Chemistry and Technology of Materials, and Christian Doppler Laboratory for Lithium Batteries, Graz University of Technology, Graz 8010, Austria; Alistore–ERI European Research Institute, CNRS FR3104, Hub de l’Energie, F-80039 Amiens, France; [orcid.org/0000-0001-9706-4892](https://orcid.org/0000-0001-9706-4892); Email: [wilkening@tugraz.at](mailto:wilkening@tugraz.at)

## Authors

**Maria Gombotz** – Institute for Chemistry and Technology of Materials, and Christian Doppler Laboratory for Lithium Batteries, Graz University of Technology, Graz 8010, Austria

**David Clarkson** – Department of Physics and Astronomy, Hunter College of the City University of New York, New York 10065 New York, United States

**Steven G. Greenbaum** – Department of Physics and Astronomy, Hunter College of the City University of New York, New York 10065 New York, United States; [orcid.org/0000-0001-5497-5274](https://orcid.org/0000-0001-5497-5274)

**Peter Ngene** – Inorganic Chemistry and Catalysis, Debye Institute for Nanomaterials Science, Utrecht University, Utrecht 3584, Netherlands; [orcid.org/0000-0003-3691-0623](https://orcid.org/0000-0003-3691-0623)

**Petra E. de Jongh** – Inorganic Chemistry and Catalysis, Debye Institute for Nanomaterials Science, Utrecht University, Utrecht 3584, Netherlands; [orcid.org/0000-0002-2216-2620](https://orcid.org/0000-0002-2216-2620)

Complete contact information is available at: <https://pubs.acs.org/10.1021/acsami.0c10361>

## Notes

The authors declare no competing financial interest.

## ACKNOWLEDGMENTS

We thank Veronika Pregartner for her help with sample preparation with NMR and impedance spectroscopy measurements. R.Z. and H.M.R.W. thank the Austrian Federal Ministry for Science, Research and Economy and the Christian-Doppler Forschungsgesellschaft for financial support; further support by the FFG (The Austrian Research Promotion Agency) in the frame of the project Safe Battery is also acknowledged. R.Z. and H.M.R.W. thank the project Solabat (project no. 853627), funded by the “Klima- und Energiefonds” of the FFG, for additional support. P.N. and P.E.J. received funding from the NWO materials for sustainability (Mat4Sus-739.017.009) and NWO-ECHO (712.015.005).

## REFERENCES

- (1) Larcher, D.; Tarascon, J.-M. Towards Greener and More Sustainable Batteries for Electrical Energy Storage. *Nat. Chem.* **2015**, *7*, 19–29.
- (2) Whittingham, M. S. Inorganic Nanomaterials for Batteries. *Dalton Trans.* **2008**, 5424–5431.
- (3) Goodenough, J. B. Evolution of Strategies for Modern Rechargeable Batteries. *Acc. Chem. Res.* **2013**, *46*, 1053–1061.
- (4) Zhou, W.; Li, Y.; Xin, S.; Goodenough, J. B. Rechargeable Sodium All-Solid-State Battery. *ACS Cent. Sci.* **2017**, *3*, 52–57.
- (5) Pan, H.; Hu, Y.-S.; Chen, L. Room-Temperature Stationary Sodium-Ion Batteries for Large-Scale Electric Energy Storage. *Energy Environ. Sci.* **2013**, *6*, 2338–2360.
- (6) Goodenough, J. B.; Kim, Y. Challenges for Rechargeable Li Batteries. *Chem. Mater.* **2010**, *22*, 587–603.
- (7) Zhang, Z.; Shao, Y.; Lotsch, B.; Hu, Y.-S.; Li, H.; Janek, J.; Nazar, L. F.; Nan, C.-W.; Maier, J.; Armand, M.; Chen, L. New Horizons for Inorganic Solid State Ion Conductors. *Energy Environ. Sci.* **2018**, *11*, 1945–1976.
- (8) Uitz, M.; Epp, V.; Bottke, P.; Wilkening, M. Ion Dynamics in Solid Electrolytes for Lithium Batteries. *J. Electroceram.* **2017**, *38*, 142–156.
- (9) Bachman, J. C.; Mui, S.; Grimaud, A.; Chang, H.-H.; Pour, N.; Lux, S. F.; Paschos, O.; Maglia, F.; Lupart, S.; Lamp, P.; Giordano, L.; Shao-Horn, Y. Inorganic Solid-State Electrolytes for Lithium Batteries: Mechanisms and Properties Governing Ion Conduction. *Chem. Rev.* **2016**, *116*, 140–162.
- (10) Thangadurai, V.; Narayanan, S.; Pinzaru, D. Garnet-Type Solid-State Fast Li Ion Conductors for Li Batteries: Critical Review. *Chem. Soc. Rev.* **2014**, *43*, 4714–4727.
- (11) Zettl, R.; de Kort, L.; Gombotz, M.; Wilkening, H. M. R.; de Jongh, P. E.; Ngene, P. Combined Effects of Anion Substitution and Nanoconfinement on the Ionic Conductivity of Li-Based Complex Hydrides. *J. Phys. Chem. C* **2020**, *124*, 2806–2816.
- (12) Jarrett, W. L.; Farlee, R. D.; Butler, L. G. Observation of Bridging and Terminal Metal-Hydrides by Solid-State Deuterium NMR Spectroscopy - Application to Bis(Cyclopentadienyl)Zirconium Dideuteride. *Inorg. Chem.* **1987**, *26*, 1381–1383.
- (13) Ravnsbaek, D. B.; Frommen, C.; Reed, D.; Filinchuk, Y.; Sørbj, M.; Hauback, B. C.; Jakobsen, H. J.; Book, D.; Besenbacher, F.; Skibsted, J.; Jensen, T. R. Structural Studies of Lithium Zinc Borohydride by Neutron Powder Diffraction, Raman and NMR spectroscopy. *J. Alloys Compd.* **2011**, *509*, S698–S704.
- (14) Skripov, A. V.; Solonin, A. V.; Ley, M. B.; Jensen, T. R.; Filinchuk, Y. Nuclear Magnetic Resonance Studies of  $\text{BH}_4^-$  Reorientations and Li Diffusion in  $\text{LiLa}(\text{BH}_4)_3\text{Cl}$ . *J. Phys. Chem. C* **2013**, *117*, 14965–14972.
- (15) Züttel, A.; Wenger, P.; Rentsch, S.; Sudan, P.; Mauron, P.; Emmenegger, C.  $\text{LiBH}_4$ , a New Hydrogen Storage Material. *J. Power Sources* **2003**, *118*, 1–7.
- (16) Schüth, F.; Bogdanović, B.; Felderhoff, M. Light Metal Hydrides and Complex Hydrides for Hydrogen Storage. *Chem. Commun.* **2004**, *20*, 2249–2258.
- (17) Sakintuna, B.; Lamari-Darkrim, F.; Hirscher, M. Metal Hydride Materials for Solid Hydrogen Storage: A Review. *Int. J. Hydrogen Energy* **2007**, *32*, 1121–1140.
- (18) Umegaki, T.; Yan, J.-M.; Zhang, X.-B.; Shioyama, H.; Kuriyama, N.; Xu, Q. Boron- and Nitrogen-Based Chemical Hydrogen Storage Materials. *Int. J. Hydrogen Energy* **2009**, *34*, 2303–2311.
- (19) Bowman, R. C., Jr.; Reiter, J. W.; Hwang, S.-J.; Kim, C.; Kabbour, H. Characterization of Complex Metal Hydrides by High-Resolution Solid State NMR Spectroscopy. *Mater. Issues Hydrogen Econ.* **2009**, 192.
- (20) Hwang, S.-J.; Bowman, R. C., Jr.; Kim, C.; Zan, J. A.; Reiter, J. W. Solid State NMR Characterization of Complex Metal Hydrides systems for Hydrogen Storage Applications. *J. Anal. Sci. Technol.* **2011**, *2*, A159–A162.
- (21) Jepsen, L. H.; Ban, V.; Møller, K. T.; Lee, Y.-S.; Cho, Y. W.; Besenbacher, F.; Filinchuk, Y.; Skibsted, J.; Jensen, T. R. Synthesis, Crystal Structure, Thermal Decomposition, and  $^{11}\text{B}$  MAS NMR Characterization of  $\text{Mg}(\text{BH}_4)_2(\text{NH}_3\text{BH}_3)_2$ . *J. Phys. Chem. C* **2014**, *118*, 12141–12153.
- (22) Bérubé, V.; Radtke, G.; Dresselhaus, M.; Chen, G. Size Effects on the Hydrogen Storage Properties of Nanostructured Metal Hydrides: A review. *Int. J. Energy Res.* **2007**, *31*, 637–663.
- (23) de Jongh, P. E.; Adelhelm, P. Nanosizing and Nanoconfinement: New Strategies Towards Meeting Hydrogen Storage Goals. *ChemSusChem* **2010**, *3*, 1332–1348.

- (24) Ngene, P.; van Zwienen, M. R.; de Jongh, P. E. Reversibility of the Hydrogen Desorption from  $\text{LiBH}_4$ : A Synergetic Effect of Nanoconfinement and Ni Addition. *Chem. Commun.* **2010**, *46*, 8201–8203.
- (25) Gutowska, A.; Li, L.; Shin, Y.; Wang, C. M.; Li, X. S.; Linehan, J. C.; Smith, R. S.; Kay, B. D.; Schmid, B.; Shaw, W.; Gutowski, M.; Autrey, T. Nanoscaffold Mediates Hydrogen Release and the Reactivity of Ammonia Borane. *Angew. Chem., Int. Ed.* **2005**, *44*, 3578–3582.
- (26) Shane, D. T.; Corey, R. L.; McIntosh, C.; Rayhel, L. H.; Bowman, R. C., Jr.; Vajo, J. J.; Gross, A. F.; Conradi, M. S.  $\text{LiBH}_4$  in Carbon Aerogel Nanoscaffolds: An NMR Study of Atomic Motions. *J. Phys. Chem. C* **2010**, *114*, 4008–4014.
- (27) Corey, R. L.; Shane, D. T.; Bowman, R. C., Jr.; Conradi, M. S. Atomic Motions in  $\text{LiBH}_4$  by NMR. *J. Phys. Chem. C* **2008**, *112*, 18706–18710.
- (28) Blanchard, D.; Nale, A.; Sveinbjörnsson, D.; Eggenhuisen, T. M.; Verkuijlen, M. H. W.; Suwarno; Vegge, T.; Kentgens, A. P. M.; de Jongh, P. E. Nanoconfined  $\text{LiBH}_4$  as a Fast Lithium Ion Conductor. *Adv. Funct. Mater.* **2015**, *25*, 184–192.
- (29) Epp, V.; Wilkening, M. Motion of  $\text{Li}^+$  in Nanoengineered  $\text{LiBH}_4$  and  $\text{LiBH}_4\cdot\text{Al}_2\text{O}_3$  Comparison with the Microcrystalline Form. *ChemPhysChem* **2013**, *14*, 3706–3713.
- (30) Choi, Y. S.; Lee, Y.-S.; Oh, K. H.; Cho, Y. W. Interface-Enhanced Li Ion Conduction in a  $\text{LiBH}_4\text{-SiO}_2$  Solid Electrolyte. *Phys. Chem. Chem. Phys.* **2016**, *18*, 22540–22547.
- (31) Choi, Y. S.; Lee, Y.-S.; Choi, D.-J.; Chae, K. H.; Oh, K. H.; Cho, Y. W. Enhanced Li Ion Conductivity in  $\text{LiBH}_4\text{-Al}_2\text{O}_3$  Mixture via Interface Engineering. *J. Phys. Chem. C* **2017**, *121*, 26209–26215.
- (32) Matsuo, M.; Orimo, S.-i. Lithium Fast-Ionic Conduction in Complex Hydrides: Review and Prospects. *Adv. Energy Mater.* **2011**, *1*, 161–172.
- (33) Knauth, P.; Schoonman, J. *Nanocomposites - Ionic Conducting Materials and Structural Spectroscopies*; Springer Science & Business Media: New York, 2007.
- (34) Heitjans, P.; Indris, S. Diffusion and Ionic Conduction in Nanocrystalline Ceramics. *J. Phys.: Condens. Matter* **2003**, *676*, Y6.6.
- (35) Maier, J. Nano-Ionics: Trivial and Non-Trivial Size Effects on Ion Conduction in Solids. *Z. Phys. Chem.* **2003**, *217*, 415–436.
- (36) Breuer, S.; Pregartner, V.; Lunghammer, S.; Wilkening, H. M. R. Dispersed Solid Conductors: Fast Interfacial Li-Ion Dynamics in Nanostructured  $\text{LiF}$  and  $\text{LiF}:\gamma\text{-Al}_2\text{O}_3$  Composites. *J. Phys. Chem. C* **2019**, *123*, 5222–5230.
- (37) Ardel, G.; Golodnitsky, D.; Peled, E.; Wang, Y.; Wang, G.; Bajue, S.; Greenbaum, S. Bulk and Interfacial Ionic Conduction in  $\text{LiF}/\text{Al}_2\text{O}_3$  Mixtures. *Solid State Ionics* **1998**, *113-115*, 477–485.
- (38) Breuer, S.; Uitz, M.; Wilkening, H. M. R. Rapid Li Ion Dynamics in the Interfacial Regions of Nanocrystalline Solids. *J. Phys. Chem. Lett.* **2018**, *9*, 2093–2097.
- (39) Prutsch, D.; Breuer, S.; Uitz, M.; Bottke, P.; Langer, J.; Lunghammer, S.; Philipp, M.; Posch, P.; Pregartner, V.; Stanje, B.; Dunst, A.; Wohlmuth, D.; Brandstätter, H.; Schmidt, W.; Epp, V.; Chadwick, A.; Hanzu, I.; Wilkening, M. Nanostructured Ceramics: Ionic Transport and Electrochemical Activity A Short Journey Across Various Families of Materials. *Z. Phys. Chem.* **2017**, *231*, 1361–1405.
- (40) Gadermaier, B.; Stanje, B.; Wilkening, A.; Hanzu, I.; Heitjans, P.; Wilkening, H. M. R. Glass in Two Forms: Heterogeneous Electrical Relaxation in Nanoglassy Petalite. *J. Phys. Chem. C* **2019**, *123*, 10153–10162.
- (41) Maier, J. Ionic Conduction in Space Charge Regions. *Prog. Solid State Chem.* **1995**, *23*, 171–263.
- (42) Maier, J. Space-Charge Regions in Solid 2-Phase Systems and Their Conduction Contribution - Conductance Enhancement in the System Ionic Conductor-'Inert' Phase and Application on  $\text{AgCl-Al}_2\text{O}_3$  and  $\text{AgCl-SiO}_2$ . *J. Phys. Chem. Solids* **1985**, *46*, 309–320.
- (43) Knauth, P.; Albinet, G.; Debierre, J.-M. Enhanced Electrical Conductivity of  $\text{CuBr-TiO}_2$  Composites: Dependence on Temperature, Volume Fractions and Grain Sizes. *Ber. Bunsenges. Phys. Chem.* **1998**, *102*, 945–952.
- (44) Verkuijlen, M. H. W.; Ngene, P.; de Kort, D. W.; Barré, C.; Nale, A.; van Eck, E. R. H.; van Benthum, P. J. M.; de Jongh, P. E.; Kentgens, A. P. M. Nanoconfined  $\text{LiBH}_4$  and Enhanced Mobility of  $\text{Li}^+$  and  $\text{BH}_4^-$  Studied by Solid-State NMR. *J. Phys. Chem. C* **2012**, *116*, 22169–22178.
- (45) Lefevr, J.; Cervini, L.; Griffin, J. M.; Blanchard, D. Lithium Conductivity and Ions Dynamics in  $\text{LiBH}_4/\text{SiO}_2$  Solid Electrolytes Studied by Solid-State NMR and Quasi-Elastic Neutron Scattering and Applied in Lithium Sulfur Batteries. *J. Phys. Chem. C* **2018**, *122*, 15264–15275.
- (46) Lambregts, S. F. H.; van Eck, E. R. H.; Suwarno; Ngene, P.; de Jongh, P. E.; Kentgens, A. P. M. Phase Behavior and Ion Dynamics of Nanoconfined  $\text{LiBH}_4$  in Silica. *J. Phys. Chem. C* **2019**, *123*, 25559–25569.
- (47) Maekawa, H.; Matsuo, M.; Takamura, H.; Ando, M.; Noda, Y.; Karahashi, T.; Orimo, S.-i. Halide-Stabilized  $\text{LiBH}_4$ , a Room-Temperature Lithium Fast-Ion Conductor. *J. Am. Chem. Soc.* **2009**, *131*, 894–895.
- (48) Matsuo, M.; Remhof, A.; Martelli, P.; Caputo, R.; Ernst, M.; Miura, Y.; Sato, T.; Oguchi, H.; Maekawa, H.; Takamura, H.; Borgschulte, A.; Züttel, A.; Orimo, S.-i. Complex Hydrides with  $\text{BH}_4^-$  and  $\text{NH}_2^-$  Anions as New Lithium Fast-Ion Conductors. *J. Am. Chem. Soc.* **2009**, *131*, 16389–16391.
- (49) Gulino, V.; Barberis, L.; Ngene, P.; Baricco, M.; de Jongh, P. E. Enhancing Li-Ion Conductivity in  $\text{LiBH}_4$ -Based Solid Electrolytes by Adding Various Nanosized Oxides. *ACS Appl. Energy Mater.* **2020**, *3*, 4941–4948.
- (50) Kwak, J. H.; Hu, J. Z.; Kim, D. H.; Szanyi, J.; Peden, C. H. F. Pentacoordinated  $\text{Al}^{3+}$  Ions as Preferential Nucleation Sites for BaO on  $\gamma\text{-Al}_2\text{O}_3$ : An Ultra-High-Magnetic field  $^{27}\text{Al}$  MAS NMR study. *J. Catal.* **2007**, *251*, 189–194.
- (51) Kwak, J. H.; Hu, J.; Lukaski, A.; Kim, D. H.; Szanyi, J.; Peden, C. H. F. Role of Pentacoordinated  $\text{Al}^{3+}$  Ions in the High Temperature Phase Transformation of  $\gamma\text{-Al}_2\text{O}_3$ . *J. Phys. Chem. C* **2008**, *112*, 9486–9492.
- (52) Düvel, A.; Romanova, E.; Sharifi, M.; Freude, D.; Wark, M.; Heitjans, P.; Wilkening, M. Mechanically Induced Phase Transformation of  $\gamma\text{-Al}_2\text{O}_3$  into  $\alpha\text{-Al}_2\text{O}_3$ : Access to Structurally Disordered  $\gamma\text{-Al}_2\text{O}_3$  with a Controllable Amount of Pentacoordinated Al Sites. *J. Phys. Chem. C* **2011**, *115*, 22770–22780.
- (53) Suwarno; Ngene, P.; Nale, A.; Eggenhuisen, T. M.; Oschatz, M.; Embs, J. P.; Remhof, A.; de Jongh, P. E. Confinement Effects for Lithium Borohydride: Comparing Silica and Carbon Scaffolds. *J. Phys. Chem. C* **2017**, *121*, 4197–4205.
- (54) Shane, D. NMR Study of Borohydrides for Hydrogen Storage Applications. Dissertation, Washington University in St. Louis, 2011.
- (55) Senadheera, L.; Carl, E. M.; Ivancic, T. M.; Conradi, M. S.; Bowman, R. C., Jr.; Hwang, S.-J.; Udovic, T. J. Molecular  $\text{H}_2$  trapped in  $\text{AlH}_3$  solid. *J. Alloys Compd.* **2008**, *463*, 1–5.
- (56) Hwang, S.-J.; Bowman, R. C.; Reiter, J. W.; Rijssenbeek; Soloveichik, G. L.; Zhao, J.-C.; Kabbour, H.; Ahn, C. C. NMR Confirmation for formation of  $[\text{B}_{12}\text{H}_{12}]^{2-}$  Complexes During Hydrogen Desorption from Metal Borohydrides. *J. Phys. Chem. C* **2008**, *112*, 3164–3169.
- (57) Epp, V.; Wilkening, M. Fast Li Diffusion in Crystalline  $\text{LiBH}_4$  due to Reduced Dimensionality: Frequency-Dependent NMR Spectroscopy. *Phys. Rev. B* **2010**, *82*, No. 020301.
- (58) Jonscher, A. K. The 'Universal' Dielectric Response. *Nature* **1977**, *267*, 673–679.
- (59) Sidebottom, D. L. Dimensionality Dependence of the Conductivity Dispersion in Ionic Materials. *Phys. Rev. Lett.* **1999**, *83*, 983–986.
- (60) Matsuo, M.; Nakamori, Y.; Orimo, S.-i.; Maekawa, H.; Takamura, H. Lithium Superionic Conduction in Lithium Borohydride Accompanied by Structural Transition. *Appl. Phys. Lett.* **2007**, *91*, 224103.
- (61) Aeberhard, P. C.; Williams, S. R.; Evans, D. J.; Refson, K.; David, W. I. F. Ab initio Nonequilibrium Molecular Dynamics in the

Solid Superionic Conductor  $\text{LiBH}_4$ . *Phys. Rev. Lett.* **2012**, *108*, 095901.

(62) Myrdal, J. S. G.; Blanchard, D.; Sveinbjörnsson, D.; Vegge, T. Li-ion Conduction in the  $\text{LiBH}_4\text{:LiI}$  System from Density Functional Theory Calculations and Quasi-Elastic Neutron Scattering. *J. Phys. Chem. C* **2013**, *117*, 9084–9091.

(63) Preishuber-Pflügl, F.; Bottke, P.; Pregartner, V.; Bitschnau, B.; Wilkening, M. Correlated Fluorine Diffusion and Ionic Conduction in the Nanocrystalline  $\text{F}^-$  Solid Electrolyte  $\text{Ba}_{0.6}\text{La}_{0.4}\text{F}_{2.4}$  -  $^{19}\text{F}$   $T_{1\rho}$  NMR Relaxation vs. Conductivity Measurements. *Phys. Chem. Chem. Phys.* **2014**, *16*, 9580–9590.

(64) Wilkening, M.; Heitjans, P. Li jump Process in  $h\text{-Li}_{0.7}\text{TiS}_2$  Studied by Two-Time  $^7\text{Li}$  Spin-Alignment Echo NMR and Comparison with Results on Two-Dimensional Diffusion from nuclear Magnetic Relaxation. *Phys. Rev. B* **2008**, *77*, No. 024311.

(65) Wilkening, M.; Indris, S.; Heitjans, P. Heterogeneous Lithium Diffusion in Nanocrystalline  $\text{Li}_2\text{O:Al}_2\text{O}_3$  Composites. *Phys. Chem. Chem. Phys.* **2003**, *5*, 2225–2231.

(66) Wilkening, M.; Heitjans, P. From Micro to Macro: Access to Long-Range  $\text{Li}^+$  Diffusion Parameters in Solids via Microscopic  $^6\text{Li}$ ,  $^7\text{Li}$  Spin-Alignment Echo NMR Spectroscopy. *ChemPhysChem* **2012**, *13*, 53–65.

(67) Winter, R.; Heitjans, P.  $\text{Li}^+$  Diffusion and its Structural Basis in the Nanocrystalline and Amorphous Forms of Two-Dimensionally Ion-Conducting  $\text{Li}_x\text{TiS}_2$ . *J. Phys. Chem. B* **2001**, *105*, 6108–6115.

(68) Liu, X.; Majzoub, E. H.; Stavila, V.; Bhakta, R. K.; Allendorf, M. D.; Shane, D. T.; Conradi, M. S.; Verdal, N.; Udovic, T. J.; Hwang, S.-J. Probing the Unusual Anion Mobility of  $\text{LiBH}_4$  Confined in Highly Ordered Nanoporous Carbon Frameworks via Solid State NMR and Quasielastic Neutron Scattering. *J. Mater. Chem. A* **2013**, *1*, 9935–9941.

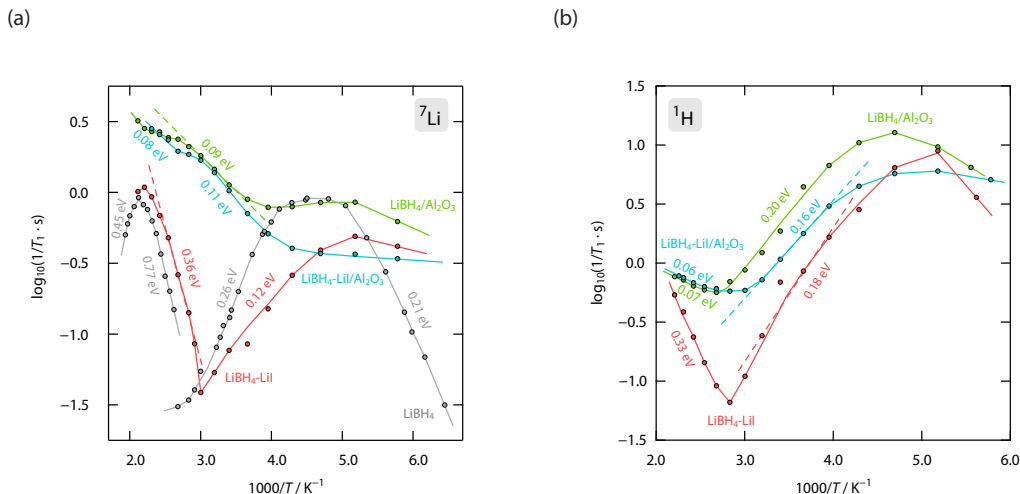
(69) Sata, N.; Eberman, K.; Eberl, K.; Maier, J. Mesoscopic Fast Ion Conduction in Nanometre-Scale Planar Heterostructures. *Nature* **2000**, *408*, 946–949.

(70) Maier, J. Nanoionics: Ion Transport and Electrochemical Storage in Confined Systems. *Nat. Mater.* **2005**, *4*, 805–815.

4.2.4. Outlook on  $\text{LiBH}_4/\text{Oxide}$  Composites

## Towards the origin of Li-Ion Diffusion in Nanoconfined and Anion-substituted Lithium Boron Hydride

Roman Zettl, Peter Ngene, Petra E. de Jongh, H. Martin R. Wilkening.

*manuscript in preparation*

**Figure R1.** Arrhenius representation of  $T_1$  spin-lattice relaxation times of  $\text{LiBH}_4\text{-LiI}/\text{Al}_2\text{O}_3$  (blue),  $\text{LiBH}_4/\text{Al}_2\text{O}_3$  (green),  $\text{LiBH}_4\text{-LiI}$  (red) and  $\text{LiBH}_4$  of nuclei a)  $^7\text{Li}$  and b)  $^1\text{H}$

The findings presented in 4.2.2 and 4.2.3 catalysed the research towards the origin of the diffusion behaviour. We were interested which approach, *i.e.* nanoconfinement or ion substitution, was mainly pivotal for the special behaviour of  $\text{LiBH}_4\text{-LiI}/\text{Al}_2\text{O}_3$ . Thus, we conducted  $^1\text{H}$  and  $^7\text{Li}$  NMR under static conditions and determined  $T_1$  and  $T_{1\rho}$  relaxations times for the individual systems  $\text{LiBH}_4\text{-LiI}$  and  $\text{LiBH}_4/\text{Al}_2\text{O}_3$  and compared the results with those obtained for both the combined composite and bulk  $\text{LiBH}_4$ . While  $^7\text{Li}$  NMR relaxation (Figure R1.a) of  $\text{LiBH}_4\text{-LiI}$  (red) is comparable to bulk  $\text{LiBH}_4$  (grey), the relaxation curve of  $\text{LiBH}_4/\text{Al}_2\text{O}_3$  (green) resembles rather that of  $\text{LiBH}_4\text{-LiI}/\text{Al}_2\text{O}_3$  (blue). The similarities are particularly present at high temperatures. Below  $-20^\circ\text{C}$  all samples show individual behaviour, but  $\text{LiBH}_4\text{-LiI}/\text{Al}_2\text{O}_3$  tends to be rather comparable to  $\text{LiBH}_4\text{-LiI}$  than to  $\text{LiBH}_4/\text{Al}_2\text{O}_3$ . In conclusion, at high temperatures the combined composite,  $\text{LiBH}_4\text{-LiI}/\text{Al}_2\text{O}_3$ , benefits from diffusion behaviour of  $\text{LiBH}_4/\text{Al}_2\text{O}_3$ , whereas diffusion properties of  $\text{LiBH}_4\text{-LiI}$  dominate at lower temperatures.

A similar picture is obtained when  $^1\text{H}$  SLR Arrhenius plots of the composites are compared (Figure R1.b). Again,  $\text{LiBH}_4\text{-LiI}/\text{Al}_2\text{O}_3$  and  $\text{LiBH}_4/\text{Al}_2\text{O}_3$  behave in a similar way in terms of spin-lattice relaxation rates at high temperatures above  $60^\circ\text{C}$ . This observations of the  $T_1$  rates clearly show that nanoconfinement plays the major role compared to ion substitution in  $\text{LiBH}_4\text{-LiI}/\text{Al}_2\text{O}_3$ . A deviation from the purely nanoconfined sample, *i.e.*  $\text{LiBH}_4/\text{Al}_2\text{O}_3$ , is, however, observable at lower temperatures, which is again attributed to the influence of ion substitution.

A manuscript about the results is in preparation. Additionally, temperature dependent XRD is scheduled. Here, measurements above and below the transition temperature of bulk  $\text{LiBH}_4$  are planned to observe the behaviour of phase change in the various samples. Preliminary results from differential scanning calorimetry (see Figure A1, appendix A) reveal no DSC signals pointing to a phase change in  $\text{LiBH}_4\text{-LiI}/\text{Al}_2\text{O}_3$ .  $\text{LiBH}_4\text{-LiI}$  shows a slight endothermic signal at  $-19^\circ\text{C}$ . For  $\text{LiBH}_4/\text{Al}_2\text{O}_3$  the signal was split (peaks at  $103$  and  $114^\circ\text{C}$ ) and significantly decreased compared to the expected signal of bulk  $\text{LiBH}_4$ , which was found at  $117^\circ\text{C}$ .

Supplemental information about NMR observations can be found in appendix A. Beside the results on  $T_1$  relaxation rates shown above,  $T_{1\rho}$  relaxation rates are presented in Figure A2.  $^1\text{H}$  SLR $\rho$  measurements revealed again similarities between samples  $\text{LiBH}_4\text{-LiI}/\text{Al}_2\text{O}_3$  and  $\text{LiBH}_4/\text{Al}_2\text{O}_3$ , whereas diffusion behaviour of  $\text{LiBH}_4\text{-LiI}$  deviates from the other two. In addition, the magnetization transients of all measurements are shown in Figure A3, which can be found in the appendix A as well.

### Author contributions

R.Z. synthesized the samples, performed static NMR experiments, analysed and illustrated the data. A manuscript is in preparation. All authors contribute to the discussion of intermediate results.

### 4.2.5. Hybrid Liquid-Solid Electrolytes Based on Metal-Organic Frameworks

The final subsection of the *Results* chapter deals with porous metal-organic frameworks (MOFs). MOFs are generally known for their application in *e.g.* gas storage and catalysis. Their ion conduction properties, especially  $\text{Li}^+$  or  $\text{Na}^+$  conduction, is, however, rarely reported. In the past few years the interest in this niche of ion conductors arose. Pioneering work was published by the group of Long.[56] The recent progress in our group will be presented in the following. MIL-121, a MOF based on Al centres and pyromellitic acid linkers, is modified with lithium and sodium acetate to obtain MIL-121, that has Li and Na ions attached to the structure. Two of four carboxylic groups of the linker build the network, while the other two are available for modification. Further sample treatment includes the incorporation of a soaking electrolyte (SI). Here, a 1 M solution of lithium and sodium perchlorate in propylene carbonate, respectively, was used as SI. The purpose of the SI is to increase the conductivity of the material and enable facile ion movement throughout the pores of the MOF.

Combined characterization of ion dynamics by means of impedance spectroscopy and spin-lattice relaxation NMR revealed promising results in terms of diffusion behaviour of Li and Na ions, respectively. Conductivities in the range of  $0.1 \text{ mS cm}^{-1}$  and activation energies around  $0.3 \text{ eV}$  were determined. Interestingly, the material experiences a change in conductivity at a certain transition temperature in both, the lithiated and the sodiated composite. Analysis of this transition temperature with DSC, Raman spectroscopy and MAS NMR at different temperatures excluded first or second order phase transitions as well as structural changes at the observed transition temperatures. This lead us to a phenomenological explanation of this behaviour. We attribute the change in conductivity to the model of Ngai [84, 85], which deals with the change from correlated to uncorrelated motion at a given temperature.

## Hybrid Na<sup>+</sup> and Li<sup>+</sup> Solid Electrolytes Based on MIL-121 Metal Organic Frameworks

Roman Zettl, Sarah Lunghammer, Athmane Boulaoued, Patrik Johansson, H. Martin R. Wilkening and Ilie Hanzu.

*manuscript in final stage before submission*

### Author contributions

R.Z. synthesized the samples, performed impedance spectroscopy, static and MAS NMR experiments, analysed and illustrated the data. S.H. conducted part of static and MAS NMR experiments. A.B. and P. J. were responsible for Raman spectroscopy. The manuscript was written by R.Z. and I.H., together with H.M.R.W. All authors contributed to the discussion of the results. The manuscript is in the final stage before submission.

# Hybrid Na<sup>+</sup> and Li<sup>+</sup> Solid Electrolytes Based on MIL-121 Metal Organic Framework

R. Zettl,<sup>1</sup> S. Lunghammer,<sup>1</sup> A. Boulaoued,<sup>2,3</sup> P. Johansson,<sup>2,3</sup> H. M. R.  
Wilkening,<sup>1,3,†</sup> I. Hanzu<sup>1,3,\*</sup>

<sup>1</sup>*Institute for Chemistry and Technology of Materials, Graz University of Technology  
(NAWI Graz), Stremayrgasse 9, 8010 Graz, Austria*

<sup>2</sup>*Department of Physics, Chalmers University of Technology, 412 96, Gothenburg,  
Sweden*

<sup>3</sup>*Alistore-ERI European Research Institute, CNRS FR3104, Hub de l'Energie, Rue  
Baudelocque, F-80039 Amiens, France*

\*corresponding author: [hanzu@tugraz.at](mailto:hanzu@tugraz.at)

† see also for correspondence: [wilkening@tugraz.at](mailto:wilkening@tugraz.at)

**Abstract.** We report a new lithium- and sodium-conducting solid electrolyte based on the MIL-121 metal organic framework (MOF) structure. Following MIL-121 synthesis and vacuum activation of the MOF, the free carboxylic units along the 1D pores of MIL-121 were functionalized with Li<sup>+</sup> or Na<sup>+</sup> ions by a relatively simple ion exchange procedure. We investigated the ion transport in these materials by impedance spectroscopy and NMR spin-lattice relaxation techniques on <sup>7</sup>Li and <sup>23</sup>Na nuclei. Depending on the soaking electrolyte used, the materials present promising conductivities in the order of 0.1 mS/cm at 298 K and activation energies in the range of 0.28-0.36 eV. Interestingly, we found different ion transport properties at lower temperatures, characterized by an increase between 0.7 – 1 eV in activation energy, below a transition temperature of 283 K for the sodium ion conductor and 323 K for the lithium conductor. In addition, NMR and Raman spectroscopy were used for structural investigations as a function of

temperature. As any phase transition or structural modification can be excluded in the temperature range investigated, we can probably assign the drop in activation energy at low temperature to a, relatively rare, transition from correlated to uncorrelated ion motion.

## 1. Introduction

Advanced batteries are of high importance in many technological fields. From small portable electronics, to much larger implementations such as electric vehicles and grid-relevant batteries for renewable energy storage, there is a constant need for improvement with respect to technical characteristics and costs.<sup>1</sup> The resurgence of Na-ion batteries research, after it was quasi-abandoned following the successful commercialization of Li-ion batteries, is a clear expression of the current strive for alternative, efficient and cost-effective energy storage solutions.<sup>2-4</sup> For instance, we see significant efforts aimed at replacing the conventional liquid electrolyte from a practical galvanic cell with solid-state ion conductors.<sup>5</sup> Not only solid-state electrolytes are perceived as safer materials, but also they might enable the use of metallic negative electrode such as Li or Na. Such a breakthrough would significantly increase the energy density of the battery.

While they are certainly game-changing materials, finding a successful solid-state ion conductor is a complex and challenging task.<sup>6</sup> Indeed, some key features of a good solid electrolyte for lithium ion batteries include:<sup>7-8</sup> i) high ionic conductivity at ambient and sub-ambient temperature, ii) appreciable  $\text{Li}^+$  transference number, iii) thermal and electrochemical stability, iv) compatibility with electrodes, v) good electrical insulator, vi) mechanical strength, vii) environmentally friendly. Hardly can one material concomitantly meet the high conductivity and the good chemical stability requirements, let alone the other criteria above. In fact, it seems that, more often than not, solid-electrolytes are unstable in contact with the active materials.<sup>9-10</sup> Nevertheless, it was very recently shown that, while the relation between redox activity and electrochemical stability is complex, the electrochemical stability window is probable wider than what is expected from first principle thermodynamic calculations.<sup>11</sup> Thus, the main hurdle

remains the ion transport itself – rarely do we see a solid ion conductor with a conductivity similar to that of liquid counterparts, although there are serious and plausible contenders that meet the ionic conductivity criteria.<sup>12-13</sup>

Metal organic frameworks (MOFs) are a class of inorganic-organic hybrid crystalline materials, also called coordination polymers. They are extended arrays composed of isolated metal atoms, also termed connectors, that are connected by organic ligands, called linkers. MOFs can extend in one, two or three dimensions, many have well-defined pores. MOFs have a wide range of applications including gas storage and separation, molecular recognition, nonlinear optics, heterogeneous catalysis and many others. Importantly, judicious ligand choice allows for the custom design of pore size and geometry – the possibilities are truly enormous and the properties of MOFs can be tuned by this approach. Apart from geometry, physical and chemical properties such as, electrical conductivity, magnetic behaviour, reactivity, Lewis acid-base properties etc. can be also tuned by the choice of metal centers and linker functionality. MOFs are in fact becoming a fertile ground for a broad spectrum of functional materials development, including the nascent field of MOF-based ion conductors.<sup>14-17</sup>

Hitherto, few publications have reported MOFs materials with lithium conducting properties.<sup>18-21</sup> Several approaches are known for the realization a MOF ion conductor. One possibility is to do a full post-synthetic modification. Following the successful synthesis of a known MOF structure, a new lithium-bearing functionality is grafted. For instance, lithium alkoxides were grafted on two different MOF structures resulting in lithium ion conductivity.<sup>18-19</sup> The bulky aliphatic part of the secondary or tertiary alkoxide, shields its negative charge thus weakening the lithium alkoxide interaction. The post modification however may involve tedious synthesis procedures. Another possibility is to immobilize the anions of a lithium salt so that the MOF material becomes a Li<sup>+</sup> single ion conductor. This can be achieved by covalently bonding the anion in the MOF structure<sup>21</sup> or by having a strong electric interaction between the lithium salt anion and the framework.<sup>20, 22</sup> Indeed, in many cases, the electron-unsaturated structure of the MOF metal centers leads to a strong coordination of anions of a lithium salt.<sup>20</sup> Alternately, the anion coordinating structure can be grafted on the organic linker.<sup>23</sup> One characteristic of these conductors is that they require the presence

of a liquid solvent or a small molecule confined within the pores to facilitate the transport of the ionic species. Due to the geometry and the large size of the pores, ion conduction is significantly slower in the absence of a mobile solvent. Thus, these materials are probably better categorized as hybrid solid electrolytes. However, unlike lithium conducting polymers, MOF ion conductors are, from a rheological point of view, true solids. Many contain some small molecules confined within the pore structure.

We hereby report a new metal organic framework (MOF) electrolyte based on the MIL-121 structure.<sup>24</sup> Our present study shows a versatile material that can be easily synthesized as an ion conductor for  $\text{Li}^+$ ,  $\text{Na}^+$  and for other metal cations of interest.<sup>25</sup> The MIL-121 structure is briefly illustrated in Figure 1. The flexible structure consists of aluminum chains that are linked by pyromellitic acid (1,2,4,5-benzenetetra-carboxylic acid) units. Of the 4 carboxylic units of the linker, only 2 are used for building the cell. The others are free and the protons of these carboxylic units can be exchanged with lithium or sodium ions that give the material the new ion conduction functionality. Structural, conductivity and diffusion properties of this new lithium ion conductor are presented and discussed.

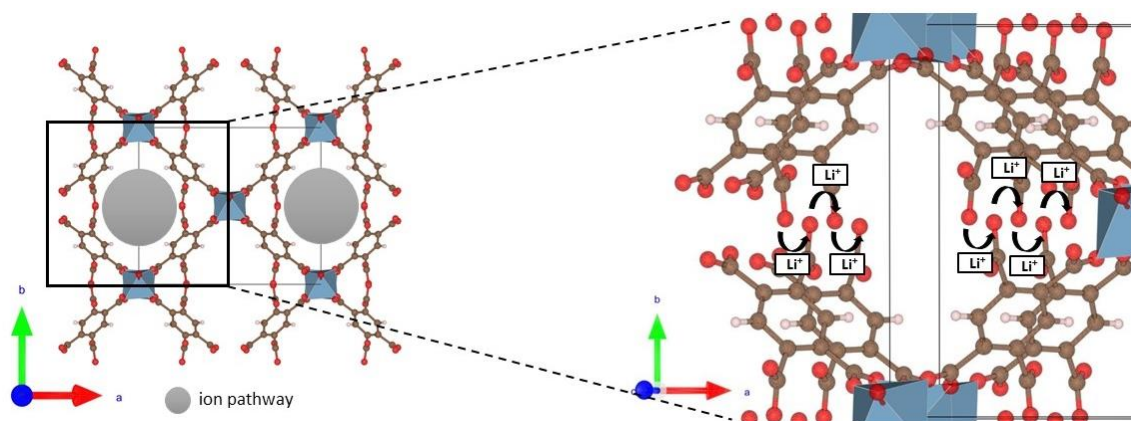


Figure 1. The structure of the MIL-121 MOF. The aluminum centers are coordinated by 1,2,4,5-benzenetetra-carboxylic acid (also known as pyromellitic acid). Only two of the carboxylic units are bonded to the aluminum centers, the others are free and form chains along the walls of 1D pores in the structure through proton bridges. The protons on the free carboxylic units can be exchanged with lithium following a relatively simple ion exchange procedure.

## 2. Experimental

### 2.1. Preparation of MIL-121/Li and MIL-121/Na hybrid electrolytes

The hydrothermal synthesis of MIL-121 was done in a Teflon beaker enclosed in a stainless steel autoclave. After stirring the solution of aluminium nitrate nonahydrate  $[\text{Al}(\text{NO}_3)_3 \cdot 9 \text{H}_2\text{O}]$ , pyromellitic acid ( $\text{H}_4\text{btec} = 1,2,4,5\text{-Benzenetetra-carboxylic acid}$ ) and deionized water (approximately 50 mL) the mixture was heated with a rate of  $4 \text{ }^\circ\text{C}/\text{min}$  and kept at  $210 \text{ }^\circ\text{C}$  for 24 h. After natural cooling, a white crystalline powder was obtained.<sup>24</sup> Separation of the white product from the clear yellow supernatant was done by centrifugation including several washing steps with deionized water. After drying at  $80 \text{ }^\circ\text{C}$  and activation at  $300 \text{ }^\circ\text{C}$  at  $10^{-3}$  mbar under vacuum, MIL-121 was dispersed by stirring in different aqueous solutions of lithium hydroxide (1 M), lithium acetate (1 M) and sodium acetate (1 M) overnight. Via this, so called, post synthetic modification,  $\text{Li}^+$  and  $\text{Na}^+$  ions were introduced to MIL-121 by ion exchange. In a second approach, a 0.1 M solution of LiOH in deionized water was added dropwise while controlling the pH value of the suspension with a pH-meter to keep the pH-value below 10. Before each step of LiOH addition, the suspension was stirred for 5 minutes to distribute LiOH and to stabilize the pH-value. All samples were separated from the liquid through centrifugation and dried at  $80 \text{ }^\circ\text{C}$ . The final products appeared as yellow powders which changed to brown after activation at  $300 \text{ }^\circ\text{C}$  in vacuum at  $10^{-6}$  mbar. The samples were transferred and stored in an Ar filled glovebox with water and oxygen levels below 0.5 ppm.

Finally, the materials were soaked with a liquid electrolyte, further referred to as soaking electrolyte (SE). A 1M solution of  $\text{LiClO}_4$  in PC and 1M  $\text{NaClO}_4$  in PC acted as SE, respectively. For better homogenisation, the two components were thoroughly mixed and kept at  $60 \text{ }^\circ\text{C}$  overnight to evenly distribute the liquid throughout the pores of the solid. All soaking steps were carried out under protective atmosphere. The limit of SE addition was roughly at 50 wt% of SE with respect to the modified MIL-121. Above 50 wt%, the liquid SE got pressed out of the pores during pelletizing the samples for impedance spectroscopy (IS) measurements.

### 2.2. Materials characterization

The samples were characterized by X-ray powder diffraction (XRD) using a Bruker D8-Advance diffractometer equipped with a Lynxeye detector ( $\text{Cu K}_\alpha$  radiation ( $1.5406 \text{ \AA}$ )). We covered a  $2\theta$ -range of diffraction angles from  $10$  to  $100^\circ 2\theta$  with a step size of  $0.02^\circ 2\theta$ . The duration per step was varied from 2 to 4 s. All samples were measured under ambient conditions.

For the conductivity measurements, the samples were pressed into 5 mm pellets with a load of 0.3 ton. The resulting pellets with a thickness between 0.5 and 1.3 mm were plasma coated (Leica,

EM QSG 100) with ion blocking gold layers of 100 nm on both sides. Finally, the Au-sputtered pellets were assembled in coin cells to guarantee protective atmosphere throughout the whole measurement. All steps, including coin-cell encapsulation, were carried out in the glovebox under Ar atmosphere. A Concept 80 system (Novocontrol) with an Alpha-A RF impedance analyser and an active ZGS sample cell was used for the IS measurements. Measurements were done in a temperature range from -90 to 110 °C at frequencies from 10 MHz to 10 mHz. The raw data was fitted with the software ZView by using a constant phase element (CPE) and a resistor connected in parallel. The capacitances  $C$  were obtained with the formula  $C = R^{(1-n)/n} \times Q^{1/n}$ .  $R$  is the resistance in  $\Omega$ , and  $Q$  has the numerical value of the admittance at  $\omega = 1 \text{ rad s}^{-1}$ . The variable  $n$  is dimensionless and it shows the deviation of the CPE from the behaviour of an ideal RC unit, for which  $n = 1$ .

The Raman spectroscopy was performed using a Bruker Multi-RAM FT-Raman spectrometer, equipped with a nitrogen-cooled germanium detector, a Nd-YAG (1064 nm) laser line used at an operating power of 230-400 mW. Every Raman spectrum was derived from 55 min accumulation time (ca. 2000 scans) in the range 0-4000  $\text{cm}^{-1}$  with a resolution of 2  $\text{cm}^{-1}$ . The analysis was focused on the range 200-2000  $\text{cm}^{-1}$ , where localized most of important peaks. The presented Raman spectra were baseline-corrected, to make peaks of interest more apparent. Before carrying out the experiment with the above mentioned settings, a first optimisation step was performed to obtain spectra with a high signal-to-noise ratio by overcoming the sample's huge fluorescence – often overcasting Raman peaks of interest. We have checked first with laser lines in the visible range (namely, 633 nm and 488 nm) and with photobleaching the sample for several hours. This didn't help much in reducing the sample's fluorescence. We have subsequently tested the 1064 nm line in the FT-Raman spectrometer and found it to give the best spectra. The sample's temperature was controlled using a Linkam stage, integrated with the spectrometer, using nitrogen flow as a cooling liquid. The samples' sensitivity to moisture required handling in inert atmosphere. For this purpose, the sample was placed in the Linkam cell inside an Argon filled glovebox, before transferring to the spectrometer. The temperature was stepped by 10C between -20 to 80C, with a ramp of 10C/min, and hold 55 minutes at each step while the Raman spectrum is recording.

$^{23}\text{Na}$  MAS (magic angle spinning) NMR measurements, were carried out for both the soaked and non-soaked samples. The device, a Bruker Avance III 500 spectrometer, was connected to a 11.4 Tesla cryomagnet yielding a resonance frequency of 132.256 MHz for  $^{23}\text{Na}$ . We used Bruker 2.5-mm MAS probes that can be operated a spinning speed of 25 kHz to record the  $^{23}\text{Na}$  MAS NMR spectra with a single pulse excitation experiment.  $^{23}\text{Na}$  NMR spectra and  $T_1$  spin-lattice relaxation

times were recorded at different temperatures. MAS rotors were filled with appropriate tools where the powder is hand-pressed firmly into the rotors. Preparing all NMR samples was strictly carried out under Ar atmosphere. Diffusion data was supplemented with  $^{23}\text{Na}$   $T_1$  spin-lattice relaxation measurements acquired with a static probe to extend the temperature range. Measurements under static conditions were carried out with a Bruker Avance III 300 spectrometer connected to a 7.0 Tesla cryomagnet with a resonance frequency of 79.353 MHz for  $^{23}\text{Na}$  using a Teflon probehead.  $^7\text{Li}$   $T_1$  and  $T_{1\rho}$  measurements under static conditions were performed with a probehead equipped with a ceramic sample chamber and the same spectrometer resulting in a resonance frequency for  $^7\text{Li}$  of 116.590 MHz. Approximately 20 mg of sample was carefully hand-pressed in a Duran NMR tube with separators above and below the sample under Ar atmosphere and fire-sealed. For detailed information about measurement parameters, see table S1 and S2.

Further MAS measurements with Li bearing samples were carried out to gain structural information rather than investigate diffusion behaviour (as obtained by  $T_1$  and  $T_{1\rho}$  relaxation rates).  $^1\text{H}$  and  $^{13}\text{C}$ - $^1\text{H}$  cross polarization (CP) MAS NMR spectra were referenced with benzoic acid as a secondary reference which is originally referenced with tetramethylsilane (TMS) while  $^{27}\text{Al}$  MAS NMR spectra are referenced to  $\gamma\text{-Al}_2\text{O}_3$  as secondary reference. The corresponding resonance frequencies were 500 MHz for  $^1\text{H}$ , 125.721 MHz for  $^{13}\text{C}$  and 130.287 MHz for  $^{27}\text{Al}$ . Sample preparation was done in the same way as explained for  $^{23}\text{Na}$  MAS measurements. For detailed information about measurement parameters, see table S1. For comparison, additional reference samples were prepared. First, a sample of pristine MIL-121 was treated at 400 °C in ambient atmosphere before vacuum activation at 300 °C. Both, heat treatment and activation, were done overnight. Secondly, a sample was kept in  $\text{H}_2\text{O}$  saturated atmosphere in a closed container for 4 days to obtain a water saturated MIL-121 sample.

### **3. Results and Discussion**

#### **3.1. Post synthetic modifications of MIL-121**

Prior to studying ionic conductivities and diffusion properties of our materials, we analysed the influence of different post synthetic modifications of MIL-121 by X-ray powder diffraction (XRD). In Figure 2. Pristine MIL-121 (red) is compared to modified MIL-121 obtained via different approaches.

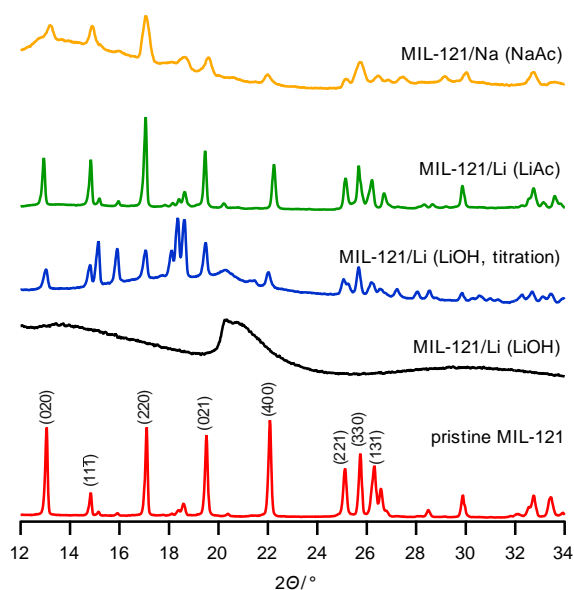


Figure 2. XRD diffraction pattern of lithiated and sodiated MIL-121. To find out the an appropriate procedure for lithiation and sodiation of MIL-121 different approaches were carried out and compared by XRD. The analyzed approaches were modifications with LiOH (black), titration with LiOH (blue), lithiation with LiAc (green) and sodiation with NaAc (yellow). Hkl indices are added to main reflexes of pristine MIL-121 (red) which is shown as reference.

Through lithiation with 1M LiOH (black) we obtained an amorphous material. The reason for the collapse of the structure was likely the high pH of LiOH. A second attempt with LiOH was realized with only 0.1 M LiOH solution (blue) which was added in small amounts while the pH was controlled throughout the experiment in order to keep the pH value below 10. This titration approach led to a XRD pattern much closer to that of pristine MIL-121. We observed that intensities of the reflexes are different, but still crystallinity could be maintained. The main reflexes, they occur at similar positions as in the pristine material. Continuing from that, we chose lithium acetate (LiAc) with a much lower pH-value than LiOH to lithiate MIL-121 (green). Here, the obtained pattern shows that this approach led to a modified MIL-121 with higher crystallinity than the prior approaches using LiOH. Reflexes occur at slightly different positions which can be explained through different strains in the crystal lattice of the material caused by the exchange of  $H^+$  with  $Li^+$  at the COOH-groups in MIL-121. Since lithiation with LiAc was much less complicated, as pH had not be controlled, and led to a much more crystalline material we decided to perform sodiation with sodium acetate (NaAc) on MIL-121 (yellow). Here, crystallinity was decreased compared to lithiation with LiAc. Nevertheless, the main reflexes can be detected at the same positons as in pristine MIL-121.

### 3.2. Li- and Na-ion conductivity in MIL-121 hybrid electrolytes

Conductivity measurements revealed that both  $\text{Li}^+$  and  $\text{Na}^+$  ions are mobile in MIL-121. Figure 3 a) shows the Nyquist plot of both MIL-121/Li and MIL-121/Na soaked with their corresponding electrolytes (SE), *i.e.* 1 M lithium and sodium perchlorate in propylene carbonate. The capacities of both samples from the constant phase element are equal with a value of 17 pF. This gives rise to a bulk conductivity of the material.<sup>26</sup> The constant phase element of both materials used in the equivalent circuit for simulation and fitting of the semicircles is almost behaving like an ideal capacitor as their  $n$ -values are close to 1. The samples differ in their loading of liquid electrolyte. While MIL-121/Na+SE contains 50 wt% of 1M  $\text{NaClO}_4$  in PC, MIL-121/Li+SE contains only 30 wt% of the corresponding  $\text{LiClO}_4$  in PC (MIL-121/Li+SE).

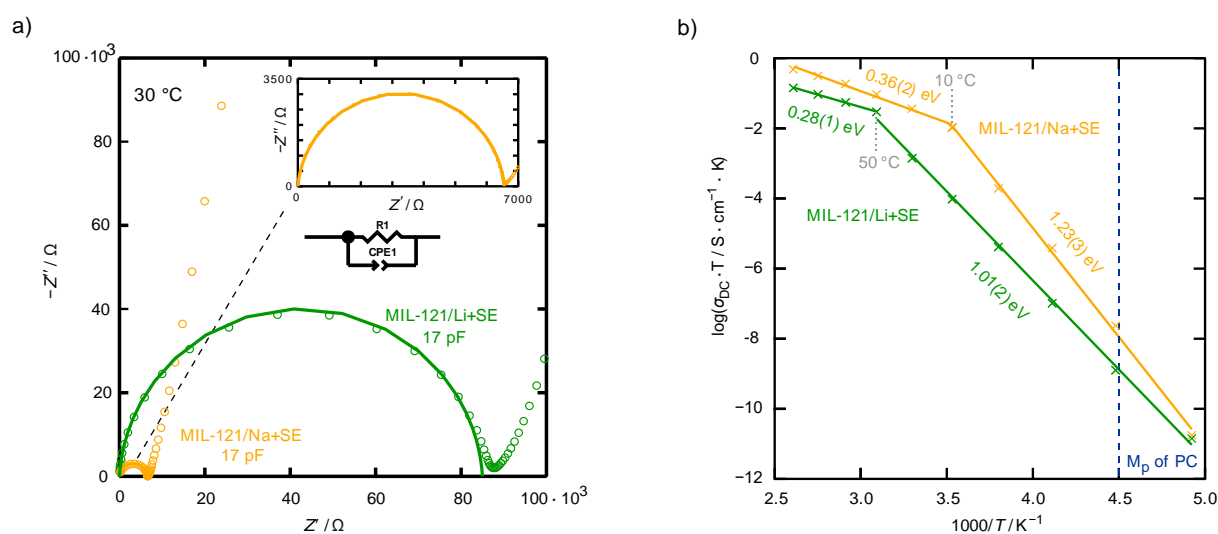


Figure 3. Conductivity measurements of MIL-121/Li+SE and MIL-121/Na+SE: a) Nyquist plot at 30 °C with a larger representation of the Na sample. b) Arrhenius plot with activation energies attached to the corresponding low and high temperature areas of the material. The temperature at the kinks in both samples are shown in grey. Additionally, the melting point of propylene carbonate is marked with a dotted blue line.

The conductivity at room temperature of MIL-121/Na+SE appeared to be higher than in the MIL-121/Li hybrid system. (Figure 3. b) This might be due to the fact that a higher amount of SE was added in MIL-121/Na. The conductivities of the SEs themselves are rather comparable. A 1 M solution of  $\text{NaClO}_4$  in PC has a conductivity of  $6 \text{ mS cm}^{-1}$  and a 1 M solution of  $\text{LiClO}_4$  in PC shows a conductivity as high as  $5 \text{ mS cm}^{-1}$  at 25 °C.<sup>27</sup> At 30 °C MIL-121/Na+SE has an ionic conductivity of  $1.2 \cdot 10^{-4} \text{ S cm}^{-1}$  which is two orders of magnitude higher than its Li equivalent ( $4.6 \cdot 10^{-6} \text{ S cm}^{-1}$ ). Please note that at 30 °C the conductivity of MIL-121/Li+SE is unfortunately in a regime with a higher activation energy than MIL-121/Na+SE. When values are compared at 50 °C the difference is only very little:  $2.88 \cdot 10^{-4} \text{ S cm}^{-1}$  (MIL-121/Na+SE) versus  $9.12 \cdot 10^{-5} \text{ S cm}^{-1}$  (MIL-121/Li+SE). The obtained conductivity values compare well to other different MOF-based

electrolytes that were based on the very different MOF structures.<sup>18-19</sup> To our knowledge, this is the first study showing MIL-121 as a hybrid lithium and sodium electrolyte system. To evaluate the importance of the interaction between the modified MIL-121 and the liquid electrolyte, we measured reference samples where one of the components is missing. First, we see that, by simply modifying MIL-121 with lithium and sodium acetate to introduce Li<sup>+</sup> and Na<sup>+</sup> to the structure does not lead to a conductive MOF. The ions are probably bound too strong to the carboxylic groups and the energy barrier for a jump of an ion in the crystal lattice of MIL-121 might be too high. We shall discuss this in further detail with the NMR data (*vide infra*). We shall only mention now, that when looking at <sup>7</sup>Li NMR lines, the simple dry Li<sup>+</sup> or Na<sup>+</sup> modified MOF we see a very slow ion conductor. On short, in modified MIL-121 without SE, only broad lines are recorded and only a small motional narrowing is seen, even at elevated temperatures. Second, when we tested the material by soaking it in pure PC, we saw that conductivities were extremely poor when ions are missing in the SE. Pure PC seems unable to sufficiently weaken the bonding of the ions and the carboxylic groups in the modified MIL-121 and allow lithium or sodium conduction. These samples showed low conductivities (see Figure S1). Third, samples without lithium or sodium ions at the carboxylic groups but with SE, *i.e.* unmodified MIL-121+SE, showed significantly lower conductivities by at least four orders of magnitude. (see Figure S2) We assume that the ions in the soaking electrolyte tend to bind to the structure of MIL-121. As a consequence, a large fraction of the ions is very likely immobile.

Interestingly, the activation energy in the hybrid electrolyte system increases significantly for both ion species at lower temperatures as shown in Figure 3 b). MIL-121/Na+SE shows an increase in activation energy from 0.36 eV at higher temperatures to 1.23 eV at temperatures below 10 °C. Similarly, the activation energy of MIL-121/Li+SE is significantly lower (0.28 eV) above 50 °C and increases to 0.99 eV at lower temperatures. This kink in the Arrhenius curve occurs when *e.g.* two temperature-activated phenomena contribute to the total diffusion process.<sup>28-29</sup> A similar trend in the Arrhenius plot was found by Souquet *et al.* where polymer composites show a nonlinear behaviour with different activation energies in different temperature regimes.<sup>30</sup> Furthermore, structural phase changes can lead to a different, yet linear behaviour in Arrhenius curves. A structural change or a phase transition can lead to a different diffusion behaviour above and below the transition temperature.<sup>31-33</sup> However, in our case, structural changes or first order phase transitions are largely excluded. Within the temperature range where we observe the kink on the Arrhenius plot, pristine and modified MIL-121 are thermally stable. Moreover, no heat flow, usually associated with a first order phase transition, is detected on lithiated and sodiated samples, see Figure S3 and S4. Furthermore, the melting (-49 °C) and boiling (242 °C) of

propylene carbonate does not occur close the transition temperature we observed in the Arrhenius plot.

### 3.3. Analysis of non-Arrhenius behaviour

As already mentioned, in most cases, first or second order phase transitions or structural changes are responsible for non-Arrhenius behaviour in solid-electrolytes. Therefore, we performed DSC measurements on MIL-121/Li+SE and MIL-121/Na+SE from  $-60\text{ }^{\circ}\text{C}$  to  $100\text{ }^{\circ}\text{C}$  (see Figure S5) to exclude first or second order phase transitions in the samples. The measurements revealed no heat flow and no indication of a sudden heat capacity change that may occur in case of phase transitions of the material in the temperature range where we observed the non-Arrhenius behaviour. The broad endothermic heat flow seen over the entire temperature range is due to the slow evaporation of the PC solvent.

In addition, a temperature dependent Raman spectroscopy investigation was carried out. The temperature dependent Raman spectroscopy, however, was not able to reveal any substantial structural differences (Figure S6). Admittedly, the materials have a high level of fluorescence, but for the Li-based MOFs the background subtraction was not overly complicated and the resulting spectra were of high quality. The recorded spectra did not show significant deviations at different temperatures. Only a few shifts approximately  $1\text{-}2\text{ cm}^{-1}$  are observed as function of temperature. The Na-based MOFs were more difficult to analyze, but they show few if any differences as compared to the Li-based. The negative result of the variable temperature Raman investigation is a strong proof that no structural modifications occur in the material.

Furthermore, we analysed the sodiated sample MIL-121/Na+SE with  $^1\text{H}$  and  $^1\text{H}\text{-}^{13}\text{C}$  CP MAS NMR at two different temperatures. If there is indeed a temperature dependent change in the local structure of the material, MAS NMR is able to detect such changes. Two experiments were carried out at temperatures  $20\text{ }^{\circ}\text{C}$  above and below the observed transition temperature in the Arrhenius curve ( $10\text{ }^{\circ}\text{C}$ ), see Figure S7. The obtained spectra, however, were almost identical. This indicates again that there are no temperature dependent local structure changes in material.

Thus, analysis via DSC,  $^1\text{H}$  and  $^1\text{H}\text{-}^{13}\text{C}$  CP MAS NMR and Raman spectroscopy at different temperatures does not support the phase transition or structural changes as an explanation for the non-Arrhenius behaviour of the samples seen in Figure 3. b). All the above methods were performed at temperatures above and below the transition temperature at which samples

experience a change in their diffusion behaviour and activation energy. Had the material changed when temperature was varied, we should have seen an effect by one of the three experimental techniques described above. As we see no effects, we can disprove the phase transition or structural change mechanism as the cause of the very significant activation energy change seen as a kink on the Arrhenius plots.

The absence of any structural and phase transition, strengthen the hypothesis that surface interactions between the modified MOF and the SE might play a major role in the materials. These interactions could be favoured at the transition temperatures observed, leading to a promoted mobility of ions above certain temperatures in these materials. We speculate that the decreased activation energies at higher temperatures in the materials are due to interface/surface interactions of modified MIL-121 + SE. Such kind of interface or surface interactions were seen in various solid-solid systems. It has been shown, that through different synthesis techniques, an interface of the two solid components is built, creating ion pathways where the mobile charge carriers can move faster than in the individual compounds.<sup>34-39</sup> Together with this hypothesis the coupling model proposed by Ngai and White might be the explanation for the non-Arrhenius behaviour in the hybrid electrolyte system.<sup>40-41</sup> The coupling model holds for a variety of systems with interacting components showing non-Arrhenius behaviour. At elevated temperatures, above the transition temperature, ion diffusion is governed by correlated motion, whereas at lower temperatures uncorrelated motion is responsible for the drastic drop in conductivity and severe rise in activation energy. About 10 years later Ngai could show that his initially phenomenological model is applicable to a variety of different systems.<sup>42</sup> Furthermore a similar phenomenon was found in closo-borates.<sup>43</sup>  $\text{Na}_2(\text{B}_{12}\text{H}_{12})_{0.5}(\text{B}_{10}\text{H}_{10})_{0.5}$  does show significantly higher activation energies at lower temperatures, but not due to structural changes or phase change. The authors refer to Ngai and his coupling model and claim that at a certain crossover temperature diffusion is rather governed by ion-ion interactions while at lower temperatures random particle walks and uncorrelated motion dominates. Briant and Farrington observed a kink in Na- $\beta$ '-alumina ( $\text{Na}_{1.68}\text{Mg}_{0.67}\text{Al}_{10.4}\text{O}_{17.1}$ ) and attributed the observed non-Arrhenius behaviour to an ordered configuration of the mobile ion that might built up at lower temperatures.<sup>44</sup> In the case of our system it may well happen that there is correlated lithium motion along the 1D pore channels. Indeed, free carboxylic groups line these channels on two sides that have their acidic protons exchanged with lithium or sodium cations. It is plausible to consider that above a certain temperature, highly conductive paths open-up along the carboxylic groups units. As for the role of the SE, we can speculate that PC partially solvate the cations on the carboxylic groups, thus lowering the transition temperature. While there are clear

experimental and structural facts supporting the correlated-uncorrelated ion motion transition, the mechanism of ion transport in our MOF is not clear yet and further accurate atomistic investigations are required.

### 3.4. Insights in Li- and Na-ion diffusion by solid-state NMR

As already mentioned, with static  $^7\text{Li}$  NMR we observed very broad lines for MIL-121/Li without SE. For this non-soaked sample, the extent of motional narrowing over a wide temperature range from  $-90$  to  $160$  °C was extremely small as shown in Figure 4. a). At  $-90$  °C the line shapes of MIL-121/Li and MIL-121/Li+SE (Figure 4. b) are almost identical. This is due to the fact that below the melting point of PC ( $-49$  °C) the contribution of the liquid vanishes. This contribution of the liquid, soaking electrolyte can be clearly seen as a sharp line on top of the broad line, which corresponds the solid part of the hybrid electrolyte. With rising temperature, the sharp line remains almost unchanged whereas the broad line at the bottom narrows. A similar behaviour was found in the Na samples, see Figure. S8. Again we observed only little motional narrowing in the non-soaked sample and two clearly distinct detectable components in MIL-121/Na+SE. An obvious difference is the unsymmetrical line shape in the Na samples. Here, the  $^{23}\text{Na}$  central line is perturbed by  $2^{\text{nd}}$  order quadrupole interactions.

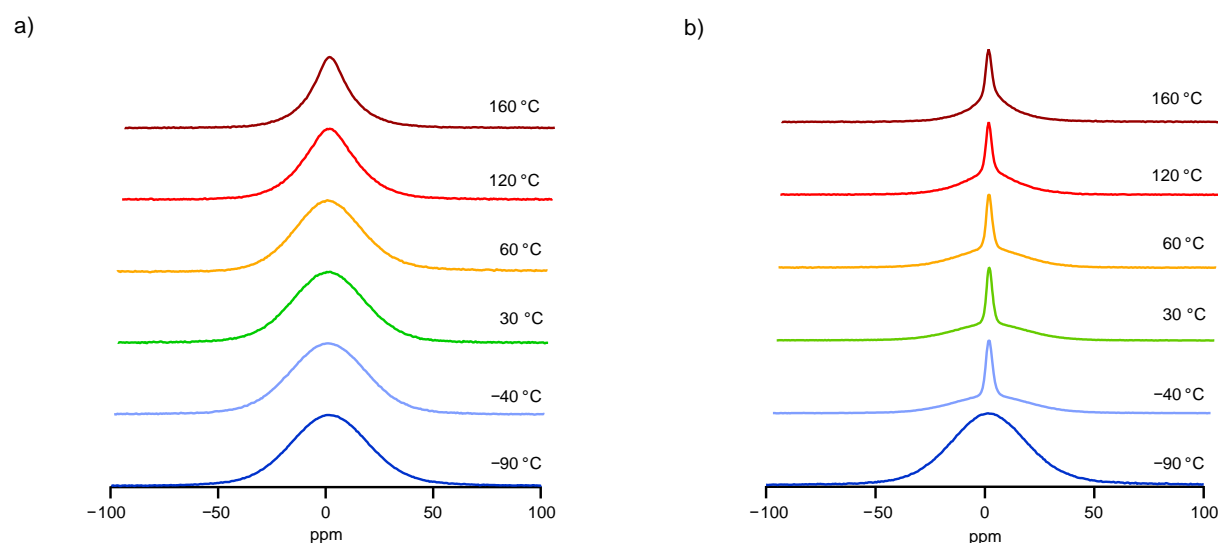


Figure 4.  $^7\text{Li}$  NMR lines of a) MIL-121/Li and b) MIL-121+SE over a temperature range from  $-90$  to  $160$  °C. The observation of the line shapes revealed narrowing of the lines when SE is added, but obviously only above the melting point of PC ( $-49$  °C).

In addition, we had a closer look on  $T_1$  and  $T_{1\rho}$  relaxation rates shown in Figure 5. With  $^{23}\text{Na}$  MAS NMR supplemented with static  $^{23}\text{Na}$  NMR we clearly found a diffusion-induced rate peak at  $260$  K for MIL-121/Na+SE and  $253$  K for MIL-121/Li+SE, respectively. (Figure 5. a) At lower temperatures, the lithiated MIL-121+SE shows lower activation energy than its Na counterpart. This is comparable to impedance spectroscopy where the low temperature activation energy was

smaller for Li than for Na as shown in Figure 3. b). In Figure 5. b) the difference between the lithiated sample, *i.e.* MIL-121/Li, with and without a soaking electrolyte is shown. Both relaxation rates,  $T_1$  and  $T_{1\rho}$ , reveal a diffusion induced behaviour at lower temperatures only for MIL-121/Li+SE. When MIL-121/Li+SE still shows a contribution attributed to mobile charge carriers, MIL-121/Li without SE already reached a regime governed mainly by lattice vibrations. At higher temperatures we see that the addition of SE leads to a decreased activation energy of  $\text{Li}^+$  ions in the sample with SE.  $T_1$  relaxometry revealed activation energies as low as 0.20 eV of MIL-121/Li+SE compared to 0.43 eV without SE. The same trend was observed with  $T_{1\rho}$  relaxometry where activation energies had a value of 0.19 eV (MIL-121/Li+SE) and 0.44 eV (MIL-121/Li), respectively.

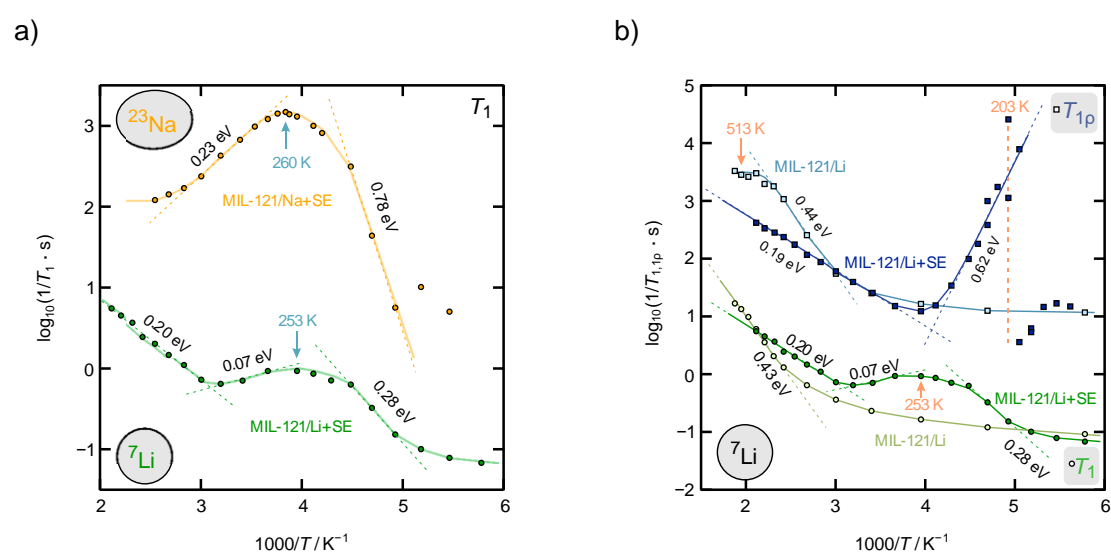


Figure 5. a)  $^7\text{Li}$  and  $^{23}\text{Na}$  NMR under static conditions: The  $T_1$  relaxometry experiment revealed a diffusion induced rate peak at 260 K for MIL-121/Na+SE and 253 K for MIL-121/Li+SE. Part of  $^{23}\text{Na}$  NMR data point were recorded under MAS conditions. b) Comparison of  $^7\text{Li}$   $T_1$  and  $T_{1\rho}$  relaxometry measurements of samples MIL-121/Li with and without SE. For both experiments we observe a diffusion induced behaviour at lower temperature only with SE and a decreased activation energy for the sample with SE compared to the sample without SE.

### 3.5. Structural elucidation of lithiated MIL-121 hybrid electrolyte

Solid-state MAS NMR was used to gain more information about the structure of MIL-121 and how it changes upon PSM and soaking with SE. In Figure 5,  $^1\text{H}$  and  $^1\text{H}$ - $^{13}\text{C}$  CP MAS spectra are shown. The assignments of different H and C atoms to certain signals in the spectra was done following the suggestion by Chen *et al.*<sup>45</sup>  $^1\text{H}$  MAS spectra (Figure 5. a) revealed a chemical shift of the H1 atom which is assigned to the carboxylic group of MIL-121. After lithiation the H1 atom shows a chemical shift of 0.2 ppm which does not change after soaking with SE. We additionally

observe a decreased intensity of the H<sub>1</sub> signal for lithiated and SE sample, which could give rise to lithiated carboxylic groups. This is in line with a study about MIL-121/Na which could also observe a decreased intensity of the H<sub>1</sub> atom upon modification compared to the pristine MIL-121.<sup>46</sup> (Figure S9. a) The relative intensities of the H<sub>1</sub> signal are 0.67 (MIL-121, red), 0.57 (MIL-121/Li, blue) and 0.43 (MIL-121/Li+SE, violet). The H<sub>2</sub> atom experiences a similar shift, but only 0.1 ppm. These chemical shift can be interpreted as deshielding of the acidic protons mediated by the carboxylic groups with which lithium cations interact. As a hard Lewis acid lithium cation is expected to reduce the electron density of the groups to which it interacts. Interestingly, the shoulder occurring at the H<sub>2</sub> atom (grey arrows in Figure 5. a) rises in its relative intensity from the activated MIL-121 (red) to the lithiated form (blue) and reaches its maximum after soaking with SE (violet). In the sample with soaking electrolyte (violet) additional signals at 4.3, 4.0, 3.5 and 0.8 ppm were recorded which are assigned to propylene carbonate in the SE. In contrast to H<sub>1</sub> and H<sub>2</sub>, H<sub>3</sub> does not experience a chemical shift upon lithiation or the addition of SE.

The <sup>1</sup>H-<sup>13</sup>C CP MAS spectra (Figure 5. b) reveal a similar picture in terms of chemical shift as seen by <sup>1</sup>H MAS NMR. After lithiation all C atoms experience a chemical shift towards larger values after lithiation and addition of SE. The CP experiments, however, did not show significant changes upon lithiation, which is expected since upon PSM the basic acetate is supposed to react with the carboxylic H<sub>1</sub> which is shielded by oxygen. Interestingly, we observe a shoulder left-hand side to the signal assigned to C<sub>1</sub> and C<sub>2</sub>. (marked with a grey arrow in Figure 5 b) It could be the case that we were able to see both C atoms separately, which is in contrast to Chen *et al.*, who detected only one combined, but asymmetric, signal for both C atoms.<sup>45-46</sup> In addition, an increase in the relative intensity of the signal assigned to C<sub>4</sub> and C<sub>5</sub> from the activated MIL-121 (red) to the lithiated MIL-121 (blue) was found. A further increase of the relative intensity was additionally observed upon addition of SE (violet). Prior to the final experiments test, runs with different contact times were recorded. In Figure S10. a) you can see that a contact time of 10 ms resulted in the best signal-to-noise ratio.

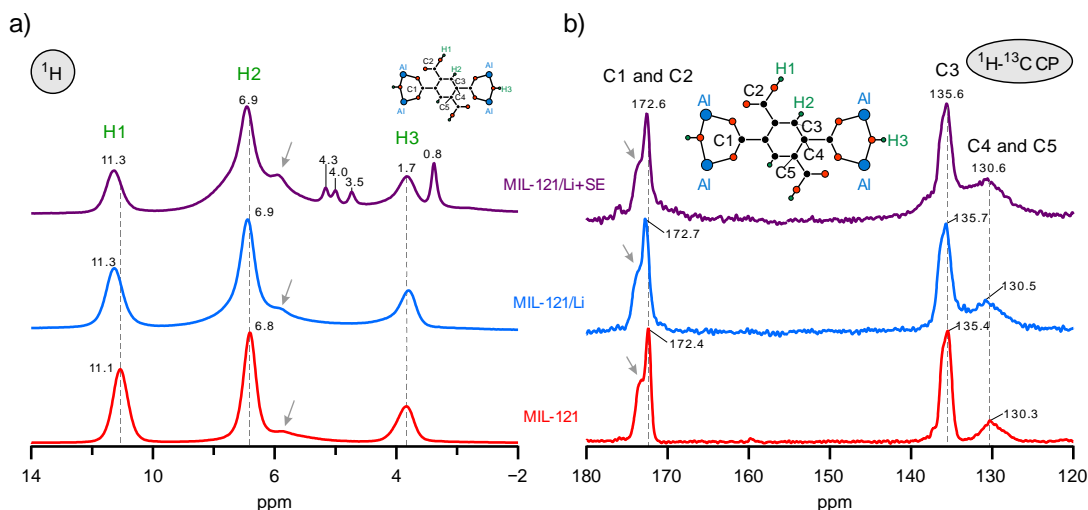


Figure 6. MAS spectra of MIL-121 (red), MIL-121/Li (blue) and MIL-121+SE (violet): a)  $^1\text{H}$  and b)  $^1\text{H}$ - $^{13}\text{C}$  CP. The spectra are normalized and given in arbitrary numbers. The values of the maxima of the lines are attached. A part of the structure is shown to explain which H and C atom is assigned to which line in the NMR spectra. Grey arrows are used to mark certain shoulders in the spectra. For further information see text.

In addition, we further compared our data, for the activated MIL-121 and MIL-121/Li with the mentioned literature.<sup>45-46</sup> In Figure S9 you can find good agreement of our  $^1\text{H}$  and  $^1\text{H}$ - $^{13}\text{C}$  CP MAS spectra with the data from literature. In the spectra of a reference sample of “over-activated” MIL-121 (treatment at 400 °C) we found the H<sub>1</sub> atom almost vanishing whereas an additional signal appears in CP measurements, pointing to the formation of an anhydride.<sup>45</sup> Furthermore, a humid sample was tested to prove that our samples are water free. Indeed, the humid sample and to some extent also the not activated (as prepared) MIL-121 showed traces of water in the  $^1\text{H}$  MAS spectra. For the sake of completeness, we analysed the samples via  $^{27}\text{Al}$  MAS NMR.  $^{27}\text{Al}$  MAS NMR did not show significant changes from one sample to the other, which leads us to the conclusion that the Al atoms are not affected by lithiation or addition of SE. (Figure S10. b).

## 4. Conclusions

A hybrid  $\text{Li}^+$  and  $\text{Na}^+$  electrolyte based on the MIL-121 MOF structure was prepared for the first time by a relatively simple ion exchange procedure followed by soaking with an electrolyte. The solid material showed conductivities in the order of  $10^{-4} \text{ S cm}^{-1}$ . While the material exhibits an Arrhenius behaviour, very different activation energies were measured at low and high temperatures. The activation energy decreases by more than 0.7 eV, with transition temperatures around 50 °C for lithium conducting samples and 10 °C for sodium conducting materials. As a phase transition or a structural change was

excluded experimentally, it is very likely that this material undergoes a change from uncorrelated ion motion at low temperature to correlated ion motion above the transition temperature. This materials shows an interesting interplay of the solid conducting framework and the soaking electrolyte. Only the lithium or sodium exchanged MOFs soaked with electrolyte show high conductivity. No appreciable conductivity is seen for the lithiated or sodiated framework with dry or solvent-filled pores and very poor conductivity is seen for the pristine activated MOF by only soaking with the electrolyte. We found that the structure of the lithiated or sodiated MII-121-based ion conductors is preserved and matched well with literature data. However, much remains to be done towards the understanding of the mechanism of conduction in these MOF-based ion conductors.

## References

1. Armand, M.; Tarascon, J. M., Building better batteries. *Nature* **2008**, *451* (7179), 652-657.
2. Chen, M.; Zhang, Y.; Xing, G.; Tang, Y., Building High Power Density of Sodium-Ion Batteries: Importance of Multidimensional Diffusion Pathways in Cathode Materials. *Frontiers in Chemistry* **2020**, *8* (152).
3. Han, M. H.; Gonzalo, E.; Singh, G.; Rojo, T., A comprehensive review of sodium layered oxides: powerful cathodes for Na-ion batteries. *Energy & Environmental Science* **2015**, *8* (1), 81-102.
4. Vaalma, C.; Buchholz, D.; Weil, M.; Passerini, S., A cost and resource analysis of sodium-ion batteries. *Nature Reviews Materials* **2018**, *3* (4), 18013.
5. Sun, C.; Liu, J.; Gong, Y.; Wilkinson, D. P.; Zhang, J., Recent advances in all-solid-state rechargeable lithium batteries. *Nano Energy* **2017**, *33*, 363-386.
6. Zhang, Z.; Shao, Y.; Lotsch, B.; Hu, Y.-S.; Li, H.; Janek, J.; Nazar, L. F.; Nan, C.-W.; Maier, J.; Armand, M.; Chen, L., New horizons for inorganic solid state ion conductors. *Energy & Environmental Science* **2018**, *11* (8), 1945-1976.
7. Goodenough, J. B.; Kim, Y., Challenges for Rechargeable Li Batteries. *Chemistry of Materials* **2010**, *22* (3), 587-603.
8. Goodenough, J. B.; Park, K. S., The Li-Ion Rechargeable Battery: A Perspective. *Journal of the American Chemical Society* **2013**, *135* (4), 1167-1176.
9. Zhu, Y.; He, X.; Mo, Y., Origin of Outstanding Stability in the Lithium Solid Electrolyte Materials: Insights from Thermodynamic Analyses Based on First-Principles Calculations. *Acs Appl Mater Inter* **2015**, *7* (42), 23685-23693.
10. Richards, W. D.; Miara, L. J.; Wang, Y.; Kim, J. C.; Ceder, G., Interface Stability in Solid-State Batteries. *Chem Mater* **2016**, *28* (1), 266-273.

11. Schwietert, T. K.; Arszewska, V. A.; Wang, C.; Yu, C.; Vasileiadis, A.; de Klerk, N. J. J.; Hageman, J.; Hupfer, T.; Kerkamm, I.; Xu, Y.; van der Maas, E.; Kelder, E. M.; Ganapathy, S.; Wagemaker, M., Clarifying the relationship between redox activity and electrochemical stability in solid electrolytes. *Nature Materials* **2020**, *19* (4), 428-435.
12. Knauth, P., Inorganic solid Li ion conductors: An overview. *Solid State Ionics* **2009**, *180* (14), 911-916.
13. Ohno, S.; Banik, A.; Dewald, G. F.; Kraft, M. A.; Krauskopf, T.; Minafra, N.; Till, P.; Weiss, M.; Zeier, W. G., Materials design of ionic conductors for solid state batteries. *Progress in Energy* **2020**, *2* (2), 022001.
14. Guan, X.; Chen, F.; Fang, Q.; Qiu, S., Design and applications of three dimensional covalent organic frameworks. *Chemical Society Reviews* **2020**, *49* (5), 1357-1384.
15. Quartarone, E.; Mustarelli, P., Review—Emerging Trends in the Design of Electrolytes for Lithium and Post-Lithium Batteries. *Journal of The Electrochemical Society* **2020**, *167* (5), 050508.
16. Zhao, R.; Wu, Y.; Liang, Z.; Gao, L.; Xia, W.; Zhao, Y.; Zou, R., Metal-organic frameworks for solid-state electrolytes. *Energy & Environmental Science* **2020**, *13* (8), 2386-2403.
17. Zhao, R.; Liang, Z.; Zou, R.; Xu, Q., Metal-Organic Frameworks for Batteries. *Joule* **2018**, *2* (11), 2235-2259.
18. Ameloot, R.; Aubrey, M.; Wiers, B. M.; Gomora-Figueroa, A. P.; Patel, S. N.; Balsara, N. P.; Long, J. R., Ionic Conductivity in the Metal-Organic Framework UiO-66 by Dehydration and Insertion of Lithium tert-Butoxide. *Chem-Eur J* **2013**, *19* (18), 5533-5536.
19. Wiers, B. M.; Foo, M. L.; Balsara, N. P.; Long, J. R., A Solid Lithium Electrolyte via Addition of Lithium Isopropoxide to a Metal-Organic Framework with Open Metal Sites. *J Am Chem Soc* **2011**, *133* (37), 14522-14525.
20. Singh, A.; Vedarajan, R.; Matsumi, N., Modified Metal Organic Frameworks (MOFs)/Ionic Liquid Matrices for Efficient Charge Storage. *Journal of The Electrochemical Society* **2017**, *164* (8), H5169-H5174.
21. Park, S. S.; Tulchinsky, Y.; Dincă, M., Single-Ion Li<sup>+</sup>, Na<sup>+</sup>, and Mg<sup>2+</sup> Solid Electrolytes Supported by a Mesoporous Anionic Cu-Azolate Metal-Organic Framework. *J Am Chem Soc* **2017**, *139* (38), 13260-13263.
22. Shen, L.; Wu, H. B.; Liu, F.; Brosmer, J. L.; Shen, G.; Wang, X.; Zink, J. I.; Xiao, Q.; Cai, M.; Wang, G.; Lu, Y.; Dunn, B., Creating Lithium-Ion Electrolytes with Biomimetic Ionic Channels in Metal-Organic Frameworks. *Adv Mater* **2018**, *30* (23), 1707476.
23. Huo, H.; Wu, B.; Zhang, T.; Zheng, X.; Ge, L.; Xu, T.; Guo, X.; Sun, X., Anion-immobilized polymer electrolyte achieved by cationic metal-organic framework filler for dendrite-free solid-state batteries. *Energy Storage Materials* **2019**, *18*, 59-67.
24. Volkringer, C.; Loiseau, T.; Guillou, N.; Ferey, G.; Haouas, M.; Taulelle, F.; Elkaim, E.; Stock, N., High-Throughput Aided Synthesis of the Porous Metal-Organic Framework-Type Aluminum Pyromellitate, MIL-121, with Extra Carboxylic Acid Functionalization. *Inorg Chem* **2010**, *49* (21), 9852-9862.
25. Wang, Z.; Hu, J.; Han, L.; Wang, Z.; Wang, H.; Zhao, Q.; Liu, J.; Pan, F., A MOF-based single-ion Zn<sup>2+</sup> solid electrolyte leading to dendrite-free rechargeable Zn batteries. *Nano Energy* **2019**, *56*, 92-99.

26. Irvine, J. T. S.; Sinclair, D. C.; West, A. R., Electroceramics: Characterization by Impedance Spectroscopy. *Adv. Mater.* 1990, pp 132-138.
27. Cvjeticanin, N. D.; Mentus, S., Conductivity, viscosity and IR spectra of Li, Na and Mg perchlorate solutions in propylene carbonate/water mixed solvents. *Phys Chem Chem Phys* **1999**, *1* (22), 5157-5161.
28. Wu, F.; Tan, G. Q.; Chen, R. J.; Li, L.; Xiang, J.; Zheng, Y. L., Novel Solid-State Li/LiFePO<sub>4</sub> Battery Configuration with a Ternary Nanocomposite Electrolyte for Practical Applications. *Adv Mater* **2011**, *23* (43), 5081-5085.
29. Neouze, M. A.; Le Bideau, J.; Gaveau, P.; Bellayer, S.; Vioux, A., Ionogels, new materials arising from the confinement of ionic liquids within silica-derived networks. *Chem Mater* **2006**, *18* (17), 3931-3936.
30. Souquet, J. L.; Levy, M.; Duclot, M., A Single Microscopic Approach for Ionic Transport in Glassy and Polymer Electrolytes. *Solid State Ionics* **1994**, *70*, 337-345.
31. Matsuo, M.; Nakamori, Y.; Orimo, S.; Maekawa, H.; Takamura, H., Lithium superionic conduction in lithium borohydride accompanied by structural transition. *Appl Phys Lett* **2007**, *91* (22).
32. Gombotz, M.; Lunghammer, S.; Breuer, S.; Hanzu, I.; Preishuber-Pflugl, F.; Wilkening, H. M. R., Spatial confinement - rapid 2D F<sup>-</sup> diffusion in micro- and nanocrystalline RbSn<sub>2</sub>F<sub>5</sub>. *Phys Chem Chem Phys* **2019**, *21* (4), 1872-1883.
33. Yoshio, M.; Mukai, T.; Ohno, H.; Kato, T., One-dimensional ion transport in self-organized columnar ionic liquids. *J Am Chem Soc* **2004**, *126* (4), 994-995.
34. Breuer, S.; Pregartner, V.; Lunghammer, S.; Wilkening, H. M. R., Dispersed Solid Conductors: Fast Interfacial Li-Ion Dynamics in Nanostructured LiF and LiF:γ-Al<sub>2</sub>O<sub>3</sub> Composites. *J Phys Chem C* **2019**, *123* (9), 5222-5230.
35. Blanchard, D.; Nale, A.; Sveinbjornsson, D.; Eggenhuisen, T. M.; Verkuijlen, M. H. W.; Suwarno; Vegge, T.; Kentgens, A. P. M.; de Jongh, P. E., Nanoconfined LiBH<sub>4</sub> as a Fast Lithium Ion Conductor. *Adv Funct Mater* **2015**, *25* (2), 184-192.
36. Lee, Y. S.; Cho, Y. W., Fast Lithium Ion Migration in Room Temperature LiBH<sub>4</sub>. *J Phys Chem C* **2017**, *121* (33), 17773-17779.
37. Choi, Y. S.; Lee, Y. S.; Oh, K. H.; Cho, Y. W., Interface-enhanced Li ion conduction in a LiBH<sub>4</sub>-SiO<sub>2</sub> solid electrolyte. *Phys Chem Chem Phys* **2016**, *18* (32), 22540-22547.
38. Choi, Y. S.; Lee, Y. S.; Choi, D. J.; Chae, K. H.; Oh, K. H.; Cho, Y. W., Enhanced Li Ion Conductivity in LiBH<sub>4</sub>-Al<sub>2</sub>O<sub>3</sub> Mixture via Interface Engineering. *J Phys Chem C* **2017**, *121* (47), 26209-26215.
39. Zettl, R.; de Kort, L.; Gombotz, M.; Wilkening, H. M. R.; de Jongh, P. E.; Ngene, P., Combined Effects of Anion Substitution and Nanoconfinement on the Ionic Conductivity of Li-Based Complex Hydrides. *J Phys Chem C* **2020**, *124* (5), 2806-2816.
40. Ngai, K. L.; White, C. T., Frequency-Dependence of Dielectric Loss in Condensed Matter. *Phys Rev B* **1979**, *20* (6), 2475-2486.
41. Ngai, K. L.; Jonscher, A. K.; White, C. T., Origin of the Universal Dielectric Response in Condensed Matter. *Nature* **1979**, *277* (5693), 185-189.
42. Ngai, K. L.; Rendell, R. W., Basic physics of the coupling model: Direct experimental evidences. *Acs Sym Ser* **1997**, *676*, 45-66.
43. Duchene, L.; Lunghammer, S.; Burankova, T.; Liao, W. C.; Embs, J. P.; Coperet, C.; Wilkening, H. M. R.; Remhof, A.; Hagemann, H.; Battaglia, C., Ionic Conduction Mechanism in the Na-2(B<sub>12</sub>H<sub>12</sub>)(0.5)(B<sub>10</sub>H<sub>10</sub>)(0.5) closo-Borate Solid-State Electrolyte: Interplay of Disorder and Ion-Ion Interactions. *Chem Mater* **2019**, *31* (9), 3449-3460.

44. Briant, J. L.; Farrington, G. C., Ionic-Conductivity in Na<sup>+</sup>, K<sup>+</sup>, and Ag<sup>+</sup> Beta"-Alumina. *J Solid State Chem* **1980**, 33 (3), 385-390.
45. Chen, S. S.; Mukherjee, S.; Lucier, B. E. G.; Guo, Y.; Wong, Y. T. A.; Terskikh, V. V.; Zaworotko, M. J.; Huang, Y. N., Cleaving Carboxyls: Understanding Thermally Triggered Hierarchical Pores in the Metal-Organic Framework MIL-121. *J Am Chem Soc* **2019**, 141 (36), 14257-14271.
46. Chen, S. S.; Lucier, B. E. G.; Luo, W.; Xie, X. K.; Feng, K.; Chan, H.; Terskikh, V. V.; Sun, X. H.; Sham, T. K.; Workentin, M. S.; Huang, Y. N., Loading across the Periodic Table: Introducing 14 Different Metal Ions To Enhance Metal-Organic Framework Performance. *Acs Appl Mater Inter* **2018**, 10 (36), 30296-30305.



## 5 | Summary and Conclusion

In the frame of this thesis, alternative approaches and materials of common lithium-ion batteries (LIB) are presented. The reasons why such next-generation battery systems are vital are, *e.g.*, the flammability of liquid electrolytes used in most commercial cells and the limited abundance of raw materials. The main focus in this work was, *inter alia*, on sodium-ion batteries (SIB) and alternative solid-state electrolytes (SSEs). The working principle of the SIB is directly related to that of the LIB, but raw materials are much more abundant. Electrochemically, the electrode materials were characterized in half cells or in full cell configuration by means of cyclic voltammetry and galvanostatic cycling with potential limitation. After the characterization of the battery parts, a hybrid device with an organic solar cell was assembled. This work showed that the use of a SIB did not lead to a significant decrease in the performance of the whole device compared to the use of a LIB. The integration of organic photovoltaics with alkali-ion batteries revealed a successful proof of concept and promising results. Electrode materials were chosen in order to match with the potential delivered by the solar cell. New electrode materials might be necessary, if solar cells with higher voltages are integrated. Furthermore, there is still room to improve the total efficiency, which will be the focus of future projects.

In the last decades, research in the field of solid-state electrolytes led to remarkable conductivities, with some of them reaching values even comparable to liquid electrolytes. There are, however, still additional issues like (i) instability with Li metal, (ii) poor compatibility with the cathode materials, (iii) low oxidation voltage, (iv) significant resistances at the interface with the electrodes, (v) low mechanical strength and (vi) expensive large-scale production. This catalysed the research towards alternative SSEs. In the frame of this thesis, hydride-based electrolytes were differently synthesized and diffusion behaviour was investigated by means of impedance spectroscopy and nuclear magnetic resonance. The major advantage of hydride electrolytes, like  $\text{LiBH}_4$ , is the stability against Li metal. Due to its low room temperature conductivity, there are well-established methods to increase the conductivity of  $\text{LiBH}_4$  at ambient temperature. A combination of these approaches,

---

*i.e.* (i) nanoconfinement in oxide supports and (ii) anion substitution of  $\text{BH}_4^-$  with halides, turned out to be effective to further boost the room temperature conductivity of  $\text{LiBH}_4$ . Worth noting that the interplay between the electrolyte and the insulator is one of the key factors of the significant conductivity enhancement. It is shown that this approach is also applicable to a variety of different metal hydrides, substituting anion species and oxides.

Alternatively, ionic conductors based on metal organic frameworks were designed, prepared and investigated. After the synthesis, the MOF, *i.e.* MIL-121, was modified in order to conduct Li or Na ions. The MOF was treated in a solution containing Li and Na, respectively and a soaking electrolyte was added. Ion conductors based on MOFs are rarely reported and therefore the results are highly promising. A variety of different MOFs can be synthesized relatively easy by combining metal nodes with organic linkers bearing different functional groups. In that way, the MOF can be designed for the specific needs of ionic conductors. This is to give you an impression, that this field of ion conductors might have a promising future. In general, the field of solid-state electrolytes will continue its intensive research in order to fulfil all the requirements (i)-(iv) to be finally applied in commercial batteries.

# A | Supplemental Material

In the first chapter of the appendix the *Supporting Information* of published papers and unpublished manuscripts included in this thesis are shown. This chapter serves to further validate the results and underline the hypotheses stated in the main articles and manuscripts. At certain paragraphs it is often referred to the *Supporting Information* and its content is directly related to the main articles. Thus, the following chapter helps to get a better understanding and a deeper view into the topics of the published articles and unpublished manuscripts. The Supplemental Material is structured in the same order as the papers and manuscripts appear in this thesis and are listed as follows:

- **A New Solar Cell – Battery Hybrid Energy System: Integrating Organic Photovoltaics with Li-Ion and Na-Ion Technologies** Sebastian F. Hoeffler, [Roman Zettl](#), Daniel Knez, Georg Haberfehlner, Ferdinand Hofer, Thomas Rath, Gregor Trimmel, Martin Wilkening and Ilie Hanzu. *Sustain. Energ. Fuels*, **2020**  
*in peer review*
- **Redox processes in sodium vanadium phosphate cathodes – insights from *operando* magnetometry** Gregor Klinser, [Roman Zettl](#), Martin Wilkening, Heinz Krenn, Ilie Hanzu and Roland Würschum. *Phys. Chem. Chem. Phys.*, **2019**, 21, 20151
- **Combined Effects of Anion Substitution and Nanoconfinement on the Ionic Conductivity of Li-Based Complex Hydrides** [Roman Zettl](#), Laura de Kort, Maria Gombotz, H. Martin R. Wilkening, Petra E. de Jongh and Peter Ngene. *J. Phys. Chem. C*, **2020**, 124, 5, 2806-2816

- 
- **Li-Ion Diffusion in Nanoconfined  $\text{LiBH}_4\text{-LiI}/\text{Al}_2\text{O}_3$ : From 2D Bulk Transport to 3D Long-Range Interfacial Dynamics** Roman Zettl, Maria Gombotz, David Clarkson, Steven G. Greenbaum, Peter Ngene, Petra E. de Jongh and H. Martin R. Wilkening. *ACS Appl. Mater. Interfaces*, **2020**, 12, 38570-38583
  
  - **Towards the origin of Li-Ion Diffusion in Nanoconfined and Anion-substituted Lithium Boron Hydride** Roman Zettl, Peter Ngene, Petra E. de Jongh and H. Martin R. Wilkening.  
*manuscript in preparation*
  
  - **Hybrid  $\text{Na}^+$  and  $\text{Li}^+$  Solid Electrolytes Based on MIL-121 Metal Organic Frameworks** Roman Zettl, Sarah Lunghammer, Athmane Boulaoued, Patrik Johansson, H. Martin R. Wilkening and Ilie Hanzu.  
*manuscript in final stage before submission*

# A New Solar Cell – Battery Hybrid Device: Integrating Organic Photovoltaics with Li-Ion and Na-Ion Technologies

*Sebastian F. Hoefler<sup>a,b</sup>, Roman Zettl<sup>a</sup>, Daniel Knez<sup>c,d</sup>, Georg Haberfehlner<sup>c</sup>,  
Ferdinand Hofer<sup>c</sup>, Thomas Rath<sup>a</sup>, Gregor Trimmel<sup>a,†</sup>, Martin Wilkening<sup>a,e</sup>, and  
Ilie Hanzu<sup>a,e,\*</sup>*

<sup>a</sup> Institute for Chemistry and Technology of Materials Graz University of Technology, Stremayrgasse 9, 8010 Graz, Austria

<sup>b</sup> Infineon Technologies Austria AG, Siemensstraße 2, 9500 Villach, Austria

<sup>c</sup> Graz Centre for Electron Microscopy, Steyrergasse 17, 8010 Graz, Austria

<sup>d</sup> CNR-IOM, TASC Laboratory, Area Science Park, Basovizza, 34149, Trieste, Italy

<sup>e</sup> ALISTORE – European Research Institute, CNRS FR3104, Hub de l’Energie, Rue Baudelocque, 80039 Amiens, France

\* Corresponding author: hanzu@tugraz.at

† See also for correspondence: gregor.trimmel@tugraz.at

## **Additional experimental details**

### ***Chemicals and Materials***

PTB7-Th (medium molecular weight, 100 kDa), O-IDTBR, and PFN-Br were purchased from 1-Material Inc.; ITO-coated glass substrates ( $15 \times 15$  mm,  $15 \Omega \text{ sq}^{-1}$ ) from Lumtec; zinc acetate dihydrate ( $\geq 99.5\%$ ) from Fluka; methanol ( $\geq 99.8\%$ ) from VWR Chemicals; 2-propanol ( $\geq 99.8\%$ ), 2-methoxyethanol (99.8%, anhydrous), ethanolamine ( $\geq 98\%$ ), *ortho*-dichlorobenzene (99%), chlorobenzene (99.9%), and molybdenum(VI) oxide (99.98%, trace metals basis) from Sigma-Aldrich; aluminium (99.999%) and silver (99.99%) from Kurt J. Lesker Company Ltd; copper/nickel foil from Christine Gröpl Elektronenmikroskopie; SIGRACET<sup>®</sup> Gas Diffusion Media, Type GDL 28 BC from Ion Power Inc.; aluminium foil (50  $\mu\text{m}$ ) from Goodfellow Cambridge Limited; copper foil (30  $\mu\text{m}$ ) from Schlenk; glass microfiber separators (Whatman<sup>™</sup> glass microfiber filter GF/B) from GE Healthcare Life Sciences; Selectilyte LP 30 electrolyte (1 M  $\text{LiPF}_6$  in a mixture of ethylene carbonate (EC) and dimethyl carbonate (DMC), 1:1 (w/w)) from BASF; NaFSI electrolyte (1 M sodium bis(fluorosulfonyl)imide (NaFSI) in ethylene carbonate (EC):diethyl carbonate (DEC) (4:6, v/v)) all from Sigma-Aldrich; Viton O-ring from Landefeld; conductive epoxy resin (CW2400, Chemtronics) from RS Components; UHU Plus Sofortfest 2-K Epoxidharzkleber from Conrad Electronic. All chemicals were used as received without further purification.

### **Characterization techniques**

Solar cell stability measurements were performed under continuous illumination with a white light light-emitting diode (LED) and maximum power point tracking in intervals of 30 min. See Figure S9 for the results.

Cycling voltammetry (CV) was performed in half-cells at various sweep rates, namely 0.05 mV/s, 0.1 mV/s, 0.2 mV/s, 0.5 mV/s, 1.0 mV/s, 2.0 mV/s, 5.0 mV/s, 10 mV/s, 20 mV/s, 50 mV/s. Routine galvanostatic cycling with potential limitation was carried out in three electrode half-cells at C/10, C/5, C/2, C, 2C, 5C and again C/10 rates (each 25 cycles). The currents corresponding to these cycling rates were calculated according to the theoretical capacities. The above testing protocols were applied to all of the materials

synthesized while only the potential limits being adjusted to the interval where electrochemical activity is expected. The full-cells were also tested in three electrode cells with the reference electrode used only to monitor the potentials at the positive and at the negative electrode.

### *Non-Fullerene Organic Tandem Solar Cells*

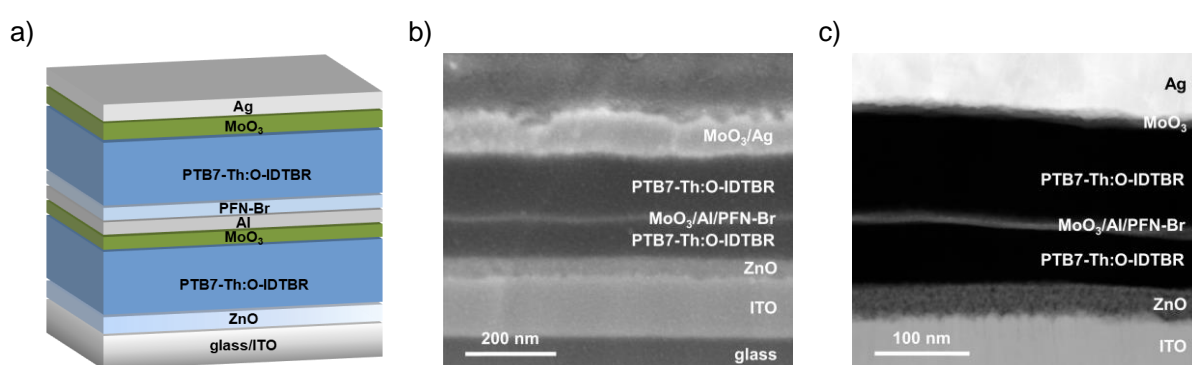


**Figure S1.** a) Schematic representation of a PTB7-Th:O-IDTBR-based organic homo-tandem solar cell in inverted device architecture with a MoO<sub>3</sub>/Al/PFN-Br recombination layer. b) Cross-sectional scanning electron microscope (SEM) image and c) cross-sectional scanning transmission electron microscope (STEM) high-angle annular dark-field (HAADF) image of a focused ion beam (FIB) prepared lamella of the corresponding device.<sup>1</sup>

**Table S1.** Photovoltaic performance parameters of PTB7-Th:O-IDTBR organic homo-tandem solar cells with MoO<sub>3</sub>/Al/PFN-Br intermediate layers and different electrode areas

| Device (Electrode Area)                              | V <sub>oc</sub> [V] | J <sub>sc</sub> [mA cm <sup>-2</sup> ] | FF [%]     | PCE [%]                   |
|--|---------------------|--|------------|---------------------------|
| Single-Junction (8.41 mm <sup>2</sup> ) <sup>a</sup> | 0.99                | 15.9 ± 0.2                             | 63.7 ± 0.8 | 10.01 ± 0.12 (max. 10.19) |
| Tandem (9 mm <sup>2</sup> )                          | 1.92 ± 0.02         | 6.6 ± 0.2                              | 54.2 ± 0.6 | 6.79 ± 0.15 (max. 7.01)   |
| Tandem (79 mm <sup>2</sup> )                         | 1.89 ± 0.03         | 5.5 ± 0.2                              | 50.0 ± 0.7 | 5.19 ± 0.32 (max. 5.56)   |

<sup>a</sup> The performance of single-junction solar cells is shown as reference (with an active electrode area of 8.41 mm<sup>2</sup>).

## Li-Ion and Na-Ion Batteries

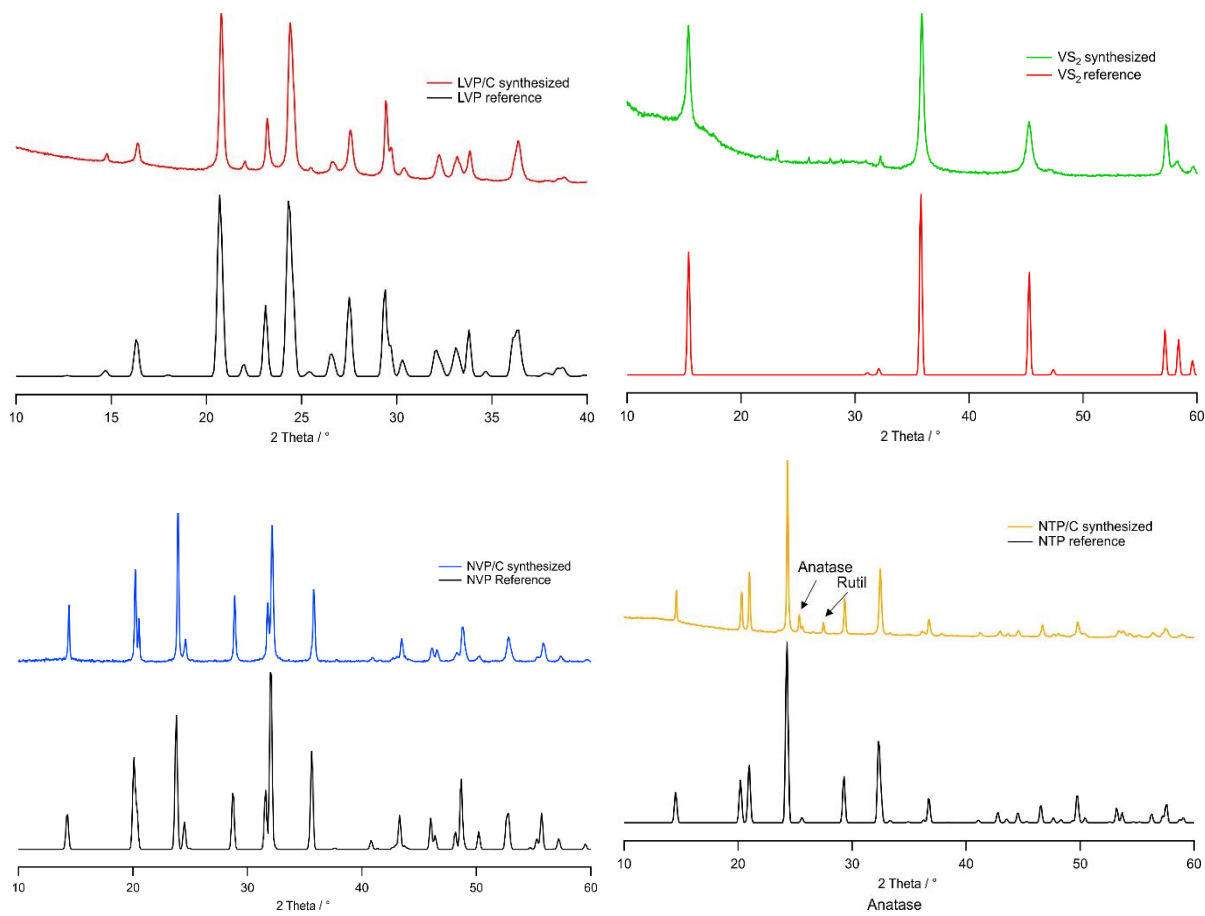


**Figure S2.** X-ray diffraction patterns of a) LVP-C, b) VS<sub>2</sub>, c) NVP-C, and d) NTP-C powder samples and the corresponding reference data taken from literature.<sup>2-5</sup>

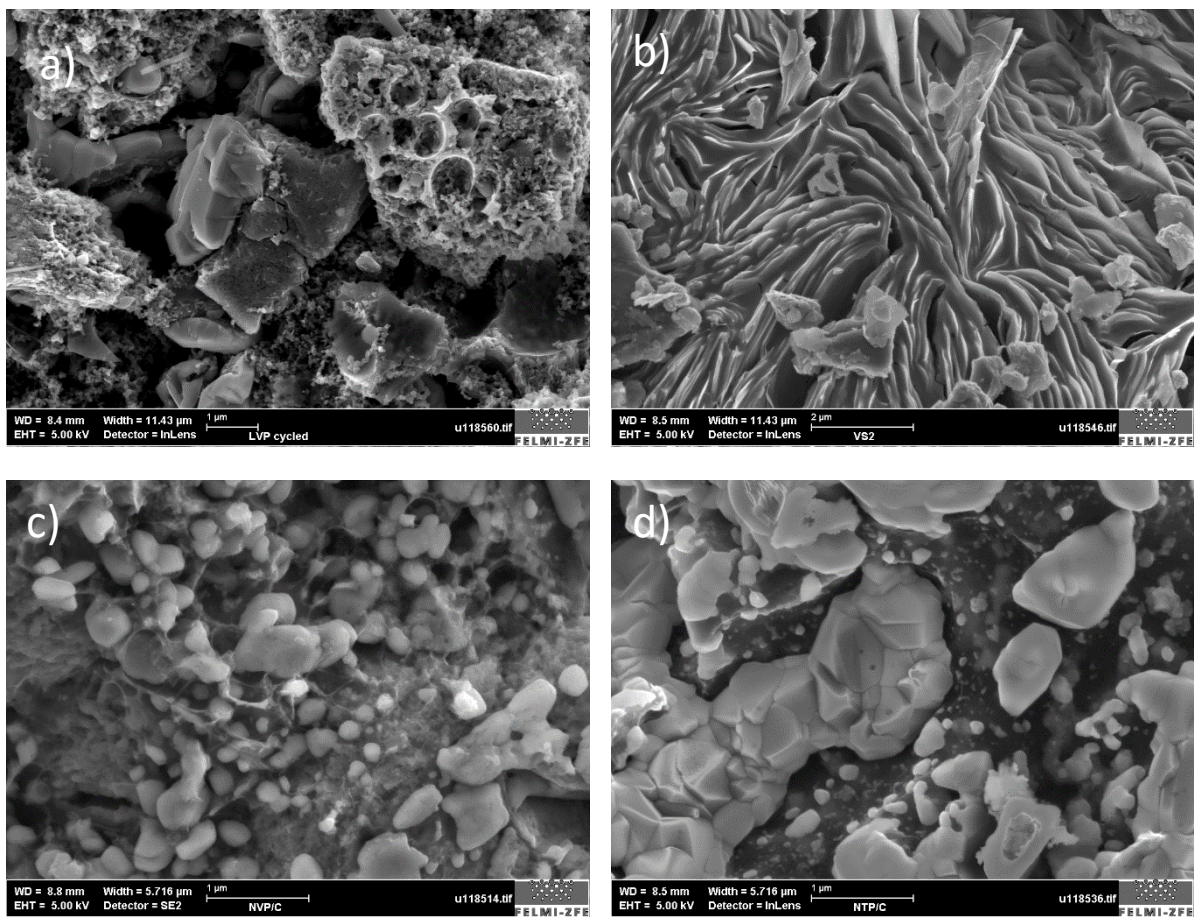


**Figure S3.** SEM images of a) LVP-C, b) VS<sub>2</sub>, c) NVP-C and d) LTP-C powders that were used for the assembly of the hybrid device. The LVP-C micrograph shown here is after 100 cycles between 3.5 and 4.2 V vs. Li<sup>+</sup>/Li.

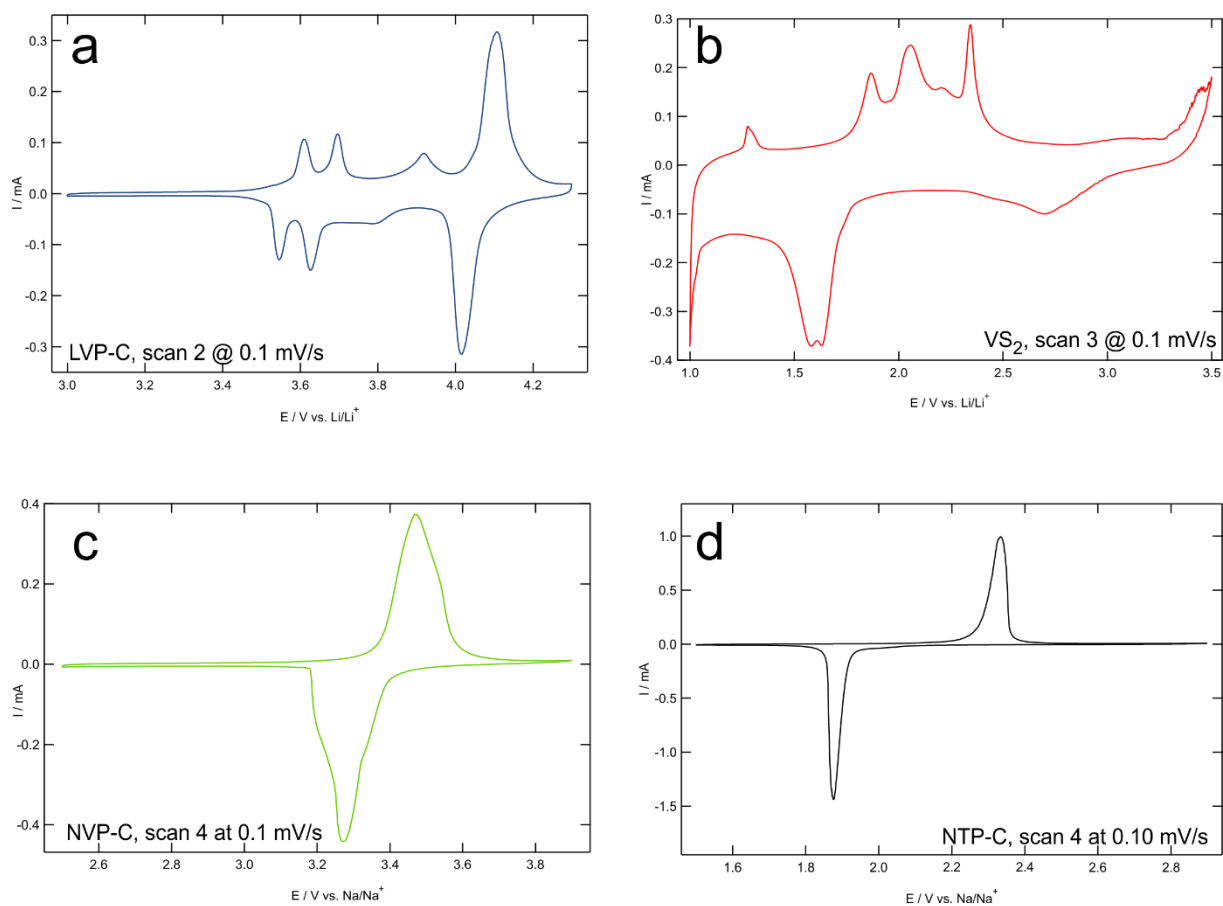


**Figure S4.** Cyclic voltammetry of a) LVP-C, b) VS<sub>2</sub> c)NVP-C, d)NTP-C active materials.

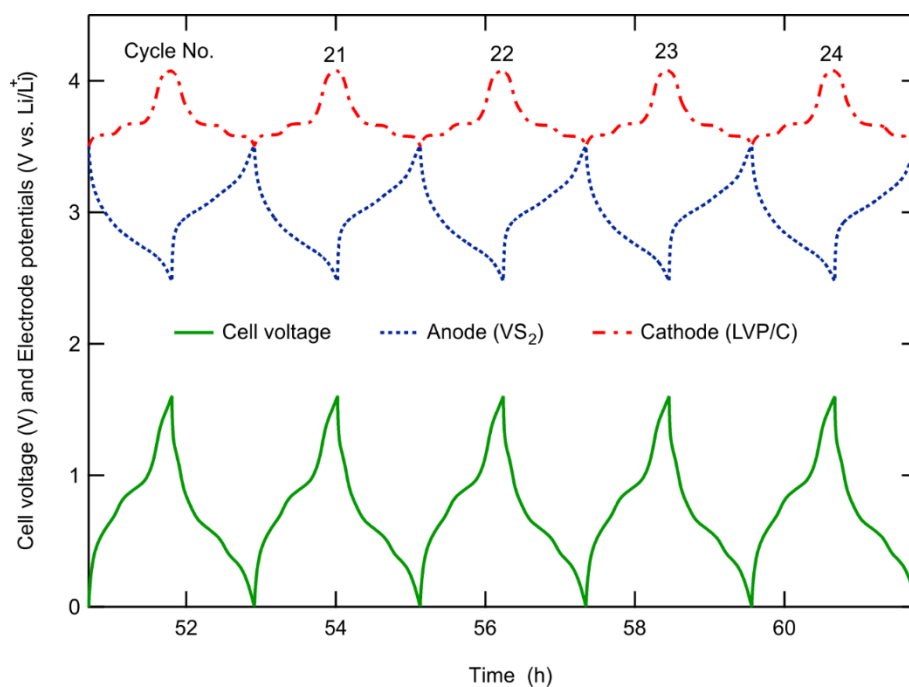


**Figure S5.** Potential and voltage characteristics of the individual electrodes and the full cell respectively for the Cu | VS<sub>2</sub> | LP30 | LVP-C | Al configuration acquired during galvanostatic cycling at approximately 1 C.

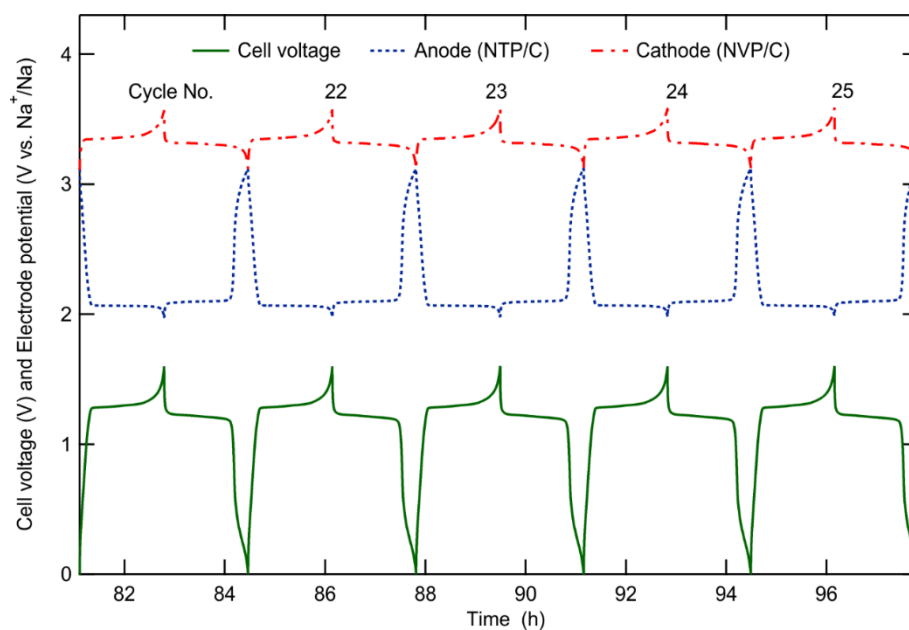


**Figure S6.** Potential and voltage characteristics of the individual electrodes and the full cell respectively for the Cu | NTP-C | NaFSI in EC:DEC 4:6 | NVP-C | Al configuration acquired during galvanostatic cycling at approximately 0.75 C.

## *Materials Selection and Compatibility*

For the organic solar cell sub-system, an adequate selection of electron donor and electron acceptor materials with properly aligned energy levels along with a high energy offset between the  $\text{HOMO}_{\text{donor}}$  and the  $\text{LUMO}_{\text{acceptor}}$  is necessary to obtain high open-circuit voltage ( $V_{\text{OC}}$ ) values. The  $V_{\text{OC}}$  values are still limited by aspects such as recombination losses, and thus maximum  $V_{\text{OC}}$  values of only up to 1.24 V have been reported for organic solar cells.<sup>6</sup> The photovoltage provided by the photovoltaic (PV) system, however, is of considerable importance for the realization of the integrated hybrid energy system since it limits the working potential, *i.e.* it defines the upper charging potential limit of the battery sub-system. Therefore, series-connected organic tandem solar cells were fabricated because of the significant higher  $V_{\text{OC}}$  values, *i.e.* according to Kirchhoff's law the  $V_{\text{OC}}$  of a series-connected tandem solar cell equals the  $V_{\text{OC}}$  of each contributing subcell which is only valid for ideal, fully-transparent intermediate layers enabling loss-free charge recombination.<sup>7</sup> It should be noted that the working potential of the PV system under load corresponds to the voltage at the maximum power point ( $V_{\text{mpp}}$ ) and is considerably smaller than the  $V_{\text{OC}}$  value, which means that even higher photovoltages are required to meet the prerequisites. For the battery sub-system, the working potential needs to be matched to the photovoltage provided by the tandem solar cells and should be operated in a voltage regime matching the  $V_{\text{mpp}}$  of the tandem solar cell. Since an additional overpotential is required to fully charge the battery, the upper potential limit needs to be slightly below the  $V_{\text{mpp}}$ , which is about 1.6 V in the presented photovoltaic device. For this purpose, battery electrode materials with a low cathode potential and a high anode potential are essential to provide a battery charging potential limit of approx. 1.6 V, which is obviously lower compared to the typical charging potential in the range of 3.6 to 4.2 V (for a typical lithium-ion battery).

In order to demonstrate the feasibility of the integration concept of a solar energy conversion and an electrochemical energy storage system within a hybrid photo-rechargeable battery, several challenges such as the materials incompatibility need to be overcome. For the direct integration of the photovoltaic and the battery system, the **electrochemical properties** of both sub-systems need to be matched in order to ensure an effective energy conversion and storage process. From the electrochemical

perspective, the conductivity, impedance and internal resistance of both devices play a key role in determining parameters such as the cycling behaviour, capacity retention, and performance. Further noteworthy aspects are that (i) no constant current flow is provided by the PV system during the charging processes due to the increase in the internal resistance, and (ii) ohmic drops deteriorate the overall device performance during discharging sequences. Moreover, the rate capability is an essential aspect for the cycling performance of the hybrid energy system: Under illumination, the photovoltaic device produces a high current (approx. 3.2 mA) leading to high charging rates of the battery sub-system, while batteries are efficiently charged with relatively low currents (*i.e.* low C-rates)

Effective energy conversion and storage systems not only require a high performance of the individual components but also a good compatibility of the materials and of both sub-systems as well as a high stability.<sup>8,9</sup> Therefore, the **chemical compatibility** of the materials used in the organic solar cell and the alkali metal ion battery, in particular between the liquid electrolyte of the battery and the active layer materials of the organic solar cell, needs to be evaluated prior to the assembling the integrated hybrid energy system. This is important since non-fullerene acceptors typically show a good solubility in common organic solvent which limits the usability of the liquid electrolyte, in particular upon long-term contact. Therefore, the choice of the liquid electrolyte is a critical aspect. In our study, a commercially available Selectilyte LP 30 electrolyte (BASF) was used for the lithium-ion battery. The electrolyte shows a good compatibility with PTB7-Th and O-IDTBR without any dissolution or swelling effects of both compounds upon direct contact, and macroscopically no changes of the silver electrode (*e.g.* corrosion) were observed. Moreover, the electrolyte does not considerably deteriorate the photovoltaic performance of the non-fullerene organic solar cells (Figure S7), implying an adequate material compatibility between the photovoltaic system and the liquid electrolyte of the lithium-ion battery. Additionally, the potential window of the liquid electrolyte needs to be matched to the working potential of the hybrid energy system in order to avoid decomposition of the electrolyte or gas evolution, which might damage the packaging upon gas formation.

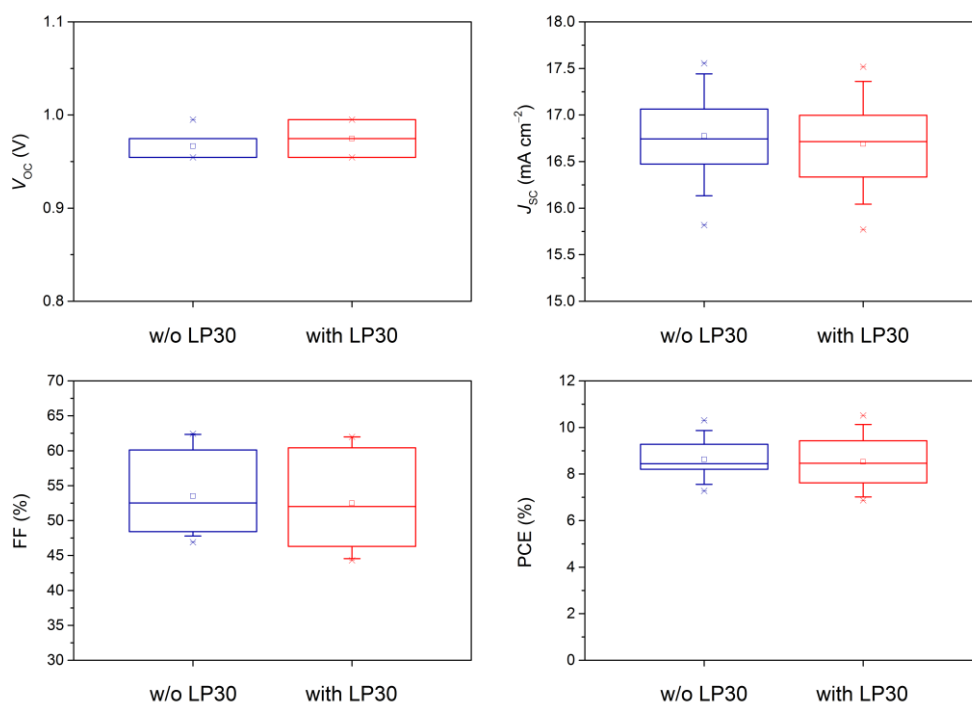


**Figure S7.** Performance analysis of PTB7-Th:O-IDTBR solar cells without (blue) and with (red) LP 30 electrolyte treatment averaged over 22 individual photovoltaic devices presented as box plot diagram for the characteristic photovoltaic parameters ( $V_{oc}$ ,  $J_{sc}$ , FF, PCE). The horizontal lines denote the 25<sup>th</sup>, 50<sup>th</sup>, and 75<sup>th</sup> percentiles. The whiskers are given by the 5<sup>th</sup> and 95<sup>th</sup> percentile values. The highest and the lowest values observed are denoted with a cross, while the mean average values are represented as an empty square. For the compatibility test, Selectilyte LP 30 electrolyte was dropped onto the solar cells (30  $\mu$ L, soaking for 60 s), followed by spin coating (10,000 rpm, 60 s) to remove the electrolyte.  $J$ - $V$  curves were monitored before and after the treatment with the electrolyte in order to assess the chemical compatibility and to determine the influence on the photovoltaic performance.

Beside the chemical and electrochemical compatibility of the individual components, several challenges need to be overcome during the **assembling of the hybrid photo-rechargeable battery** (*e.g.* mechanical damage of photovoltaic device, poor electrical contact, inadequate encapsulation strategy). The solution-based deposition of the battery composite electrode onto the top contact of the PV system using a slurry casting method (drop-coating) did not work out since the solvent (NMP) dissolves the active layer upon direct contact. Furthermore, the adhesion of the battery composite electrode was really poor due to its low surface roughness of the top contact. Therefore, the battery composite electrodes were prepared separately by casting a slurry on surface-treated, relatively rough metal foil current collectors, exhibiting an

improved adhesion capability. However, the direct application of the composite electrode on the top electrode caused a mechanical damage of the thin film PV system (with total thicknesses of hundreds of nanometers), leading to a failure of the device. This is attributable to the piercing of the organic solar cells because of the sharp edges of the current collector originating from cutting the electrodes. In addition, interface phenomena and reactions such as bi-metal corrosion effects need to be considered, *i.e.* corrosion of metals with markedly different electrochemical potentials such as silver (top contact of PV system) and aluminium (cathode current collector of battery), and might cause device failure as well. Therefore, several conductive interlayer materials were evaluated to avoid mechanical damage of the solar cell, to prevent bi-metal corrosion effects, and to provide a good electrical contact between both sub-systems: (i) a carbon tape (typically used for electron microscopic investigations) showed a poor conductivity, (ii) a liquid silver conductive paint (RS Components) exhibited dissolution effects and a poor compatibility, (iii) an adhesive copper/nickel foil (C. Gröpl) resulted in a poor reproducibility with regard to the application of the interlayer because of the adhesive surface, while (iv) a thin carbon-based conductive paper (SIGRACET<sup>®</sup> Gas Diffusion Media, Type GDL 28 BC, Ion Power Inc.) showed a good electrical conductivity, easy applicability and worked out the best for our system. Moreover, the interlayer material provides an additional barrier for the diffusion of the liquid electrolyte or other species from the battery to the PV sub-system, which might otherwise lead to degradation phenomena. The electrical contacts required for measuring the performance of the photoelectrochemical hybrid energy device were provided by adhesive copper/nickel stripes mounted to the electrodes with a conductive two-component epoxy resin (CW2400, Chemtronics) prior to the assembling procedure.

In addition, a proper **encapsulation strategy** is required in order to provide an air- and moisture-tight sealing, to avoid chemical reactions or interactions of the employed materials with the ambient atmosphere, in particular with oxygen and water vapor, and to improve the mechanical stability of the integrated power pack. Furthermore, the assembling and encapsulation should be performed under inert conditions, for example in a glovebox system with low oxygen and moisture levels to prevent any chemical interactions with the ambient atmosphere and to keep the particle contamination at very low levels since it might cause device failure as well. In a first approach, the hybrid

energy system was encapsulated with a UV-curable epoxy resin. Dissolution effects of the absorber materials, originating from the epoxy resin and side products during curing, together with temperature-induced effects upon irradiation with a halogen lamp (75 W, Philips) are expected to lead to the degradation of the organic solar cells. This is why a non-curable, two-component epoxy resin (UHU Plus Sofortfest) was used, and no problems with regard to the encapsulation were observed. Moreover, an encapsulation gadget was developed by our group to properly assemble and encapsulate both sub-systems within an integrated hybrid energy device architecture (Figure S8).

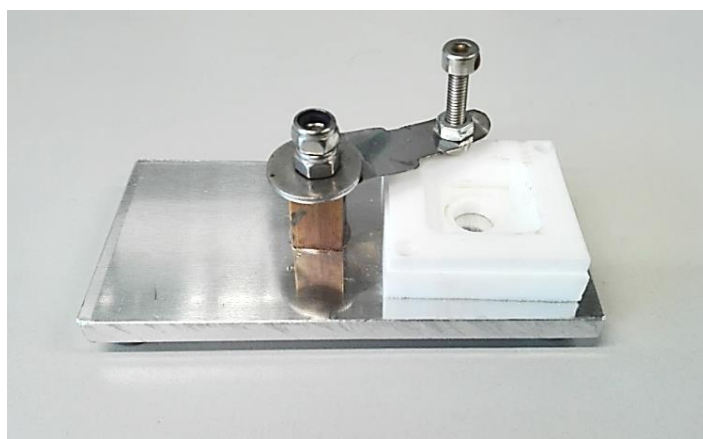


**Figure S8.** Encapsulation gadget

The **electrochemical characterization of the integrated hybrid energy system** was performed using a white light light-emitting diode (LED) to exclude temperature induced changes in the solar cell or the battery part. Measurements of encapsulated non-fullerene organic solar cells showed a promising device performance and stability over the examined time period of 200 h under continuous illumination with the LED (Figure S9). Moreover, the solar cells exhibited a burn-in free behavior, *i.e.* no typical initial exponential loss of the photovoltaic performance was obtained under illumination.<sup>10, 11</sup>

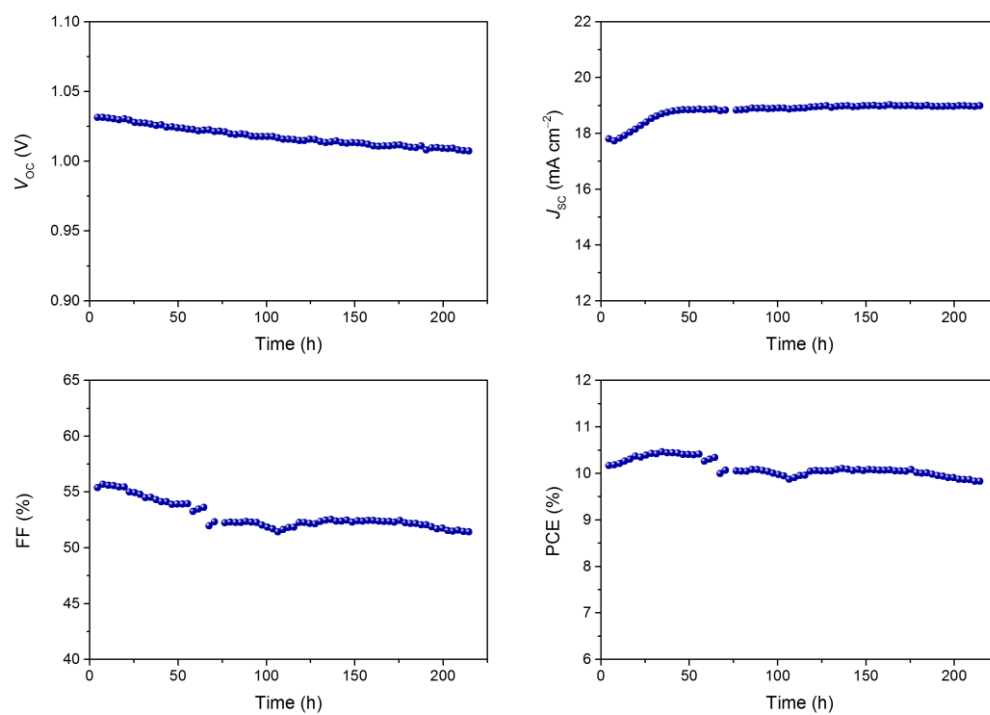


**Figure S9.** Device stability measurement of an encapsulated PTB7-Th:O-IDTBR single-junction solar cell under continuous illumination with white light LEDs and maximum power point tracking in intervals of 30 min.

## *Integrated Solar Cell-Battery Hybrid Energy System*

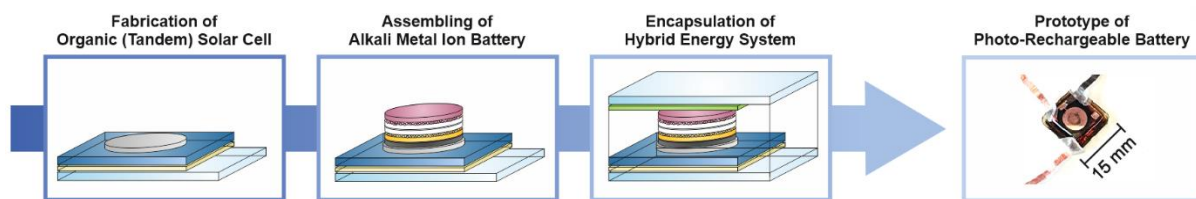


**Figure S10.** Schematic representation of the assembling and encapsulation procedure of the integrated hybrid energy system.

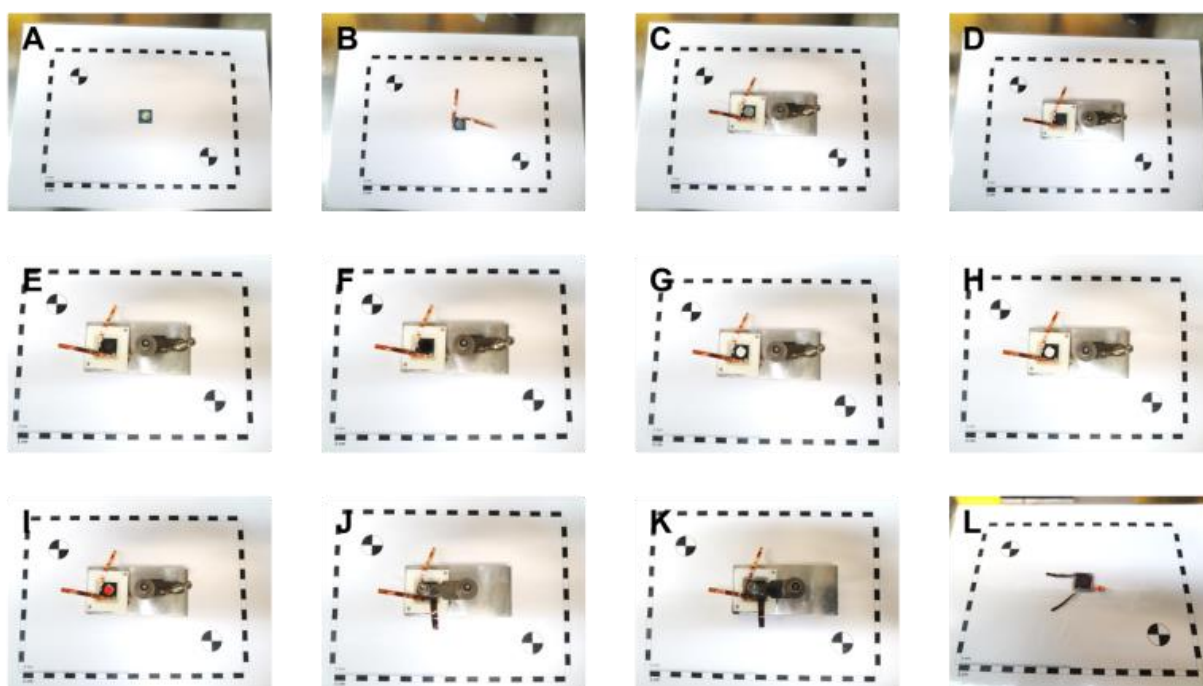


**Figure S11.** Assembling and encapsulation procedure of the integrated photo-rechargeable battery. A – Organic solar cell, B – after installing the Cu external contacts, C – inside the encapsulation gadget, D – after applying the conductive carbon paper interfacial layer, E – after applying the positive electrode (LVP-C for LIB, NVP-C for SIB), F – after applying the O-ring, G – after applying the separator, H – after soaking the separator with electrolyte, I – after applying the negative electrode (VS<sub>2</sub> for LIB, NTP-C for SIB), J – after applying the external Cu contacts on the battery negative electrode, K – after encapsulation in epoxy resin and curing, L – final solar battery hybrid device.

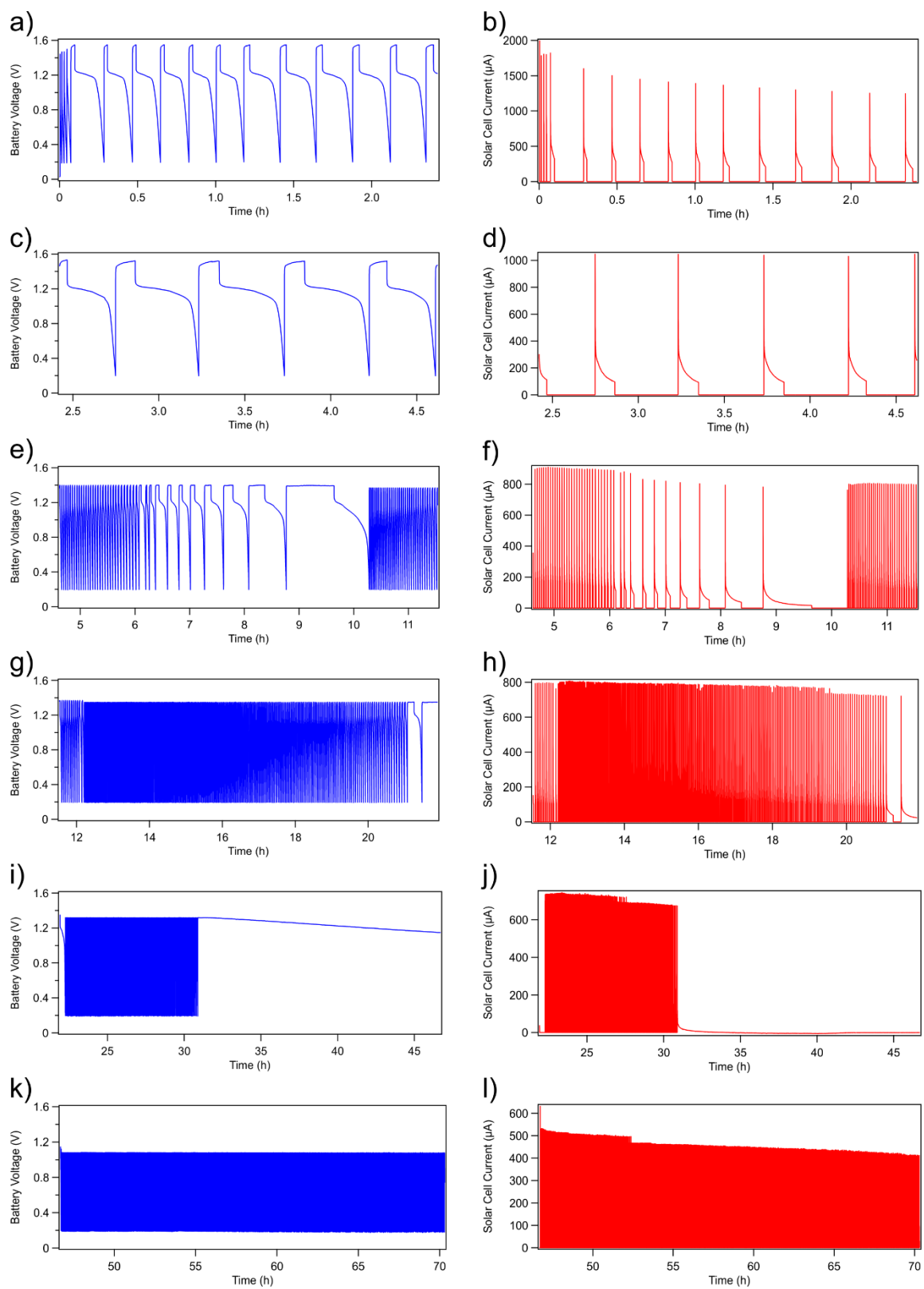


**Figure S12.** Voltage and current profiles as well as their dependence on time for a Na-based hybrid device.

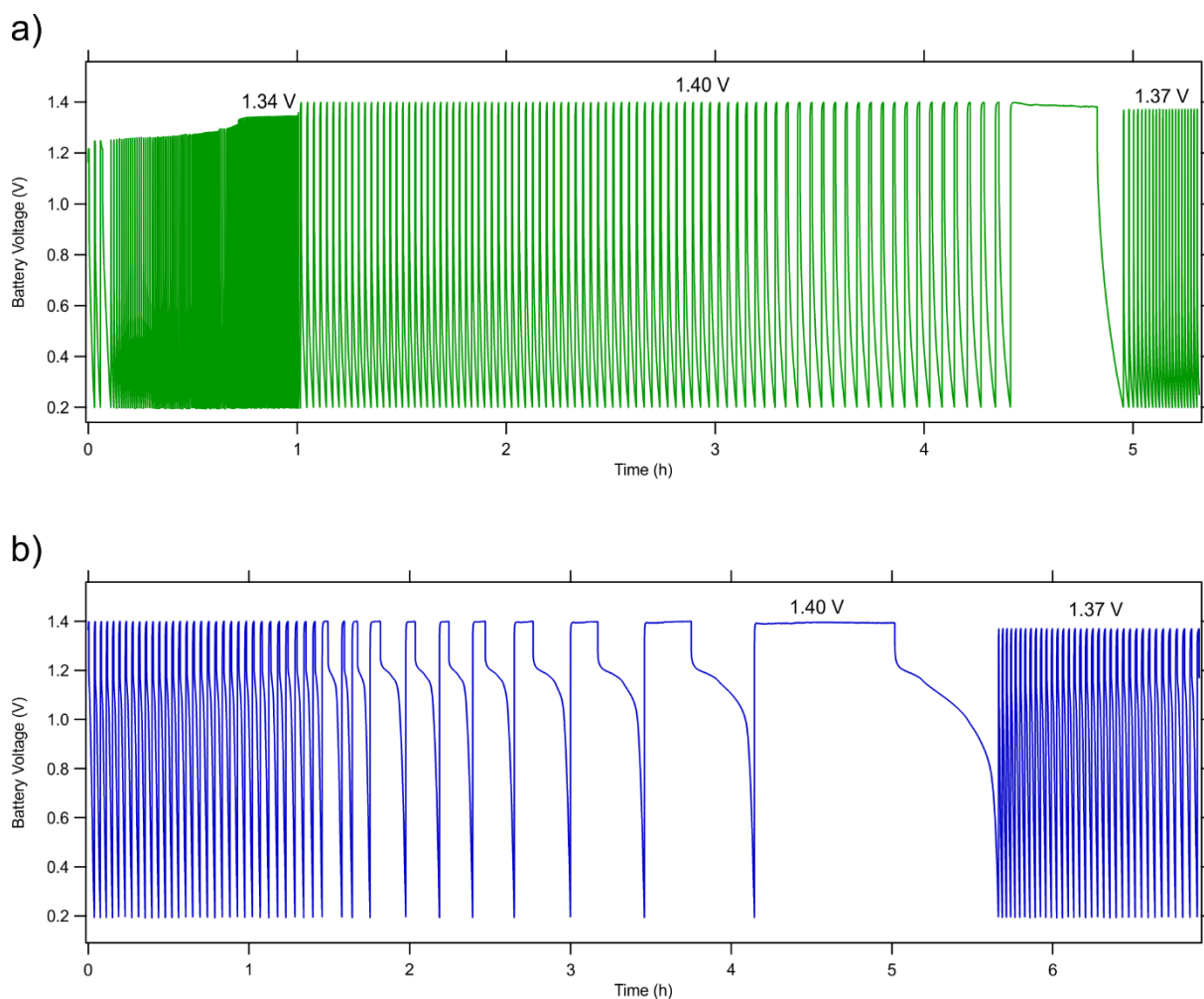


**Figure S13.** Battery voltage with respect to time for a) lithium- and b) sodium-ion based hybrid devices. Degradation of the performance is visible in both cases by the increased time required to reach the cut-off limit of 1.40 V.

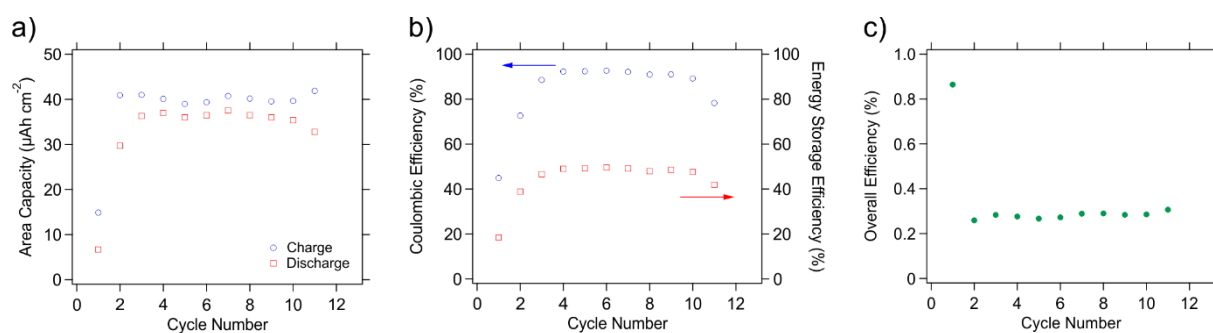


**Figure S14.** Performance of a Li-based hybrid device that was cycled by photocharging for 10 minutes followed by a discharge at a 50  $\mu\text{A}$  constant current. The time limitation circumvents the issues encountered when a voltage limit was set.

## References

1. S. F. Hoefler, G. Haberfehlner, T. Rath, R. Canteri, M. Barozzi, F. Hofer and G. Trimmel, *Advanced Materials Interfaces*, 2019, **6**, 1901053.
2. J. Yoon, S. Muhammad, D. Jang, N. Sivakumar, J. Kim, W.-H. Jang, Y.-S. Lee, Y.-U. Park, K. Kang and W.-S. Yoon, *Journal of Alloys and Compounds*, 2013, **569**, 76-81.
3. G. A. Wiegers, *Physica B+C*, 1980, **99**, 151-165.
4. I. V. Zatonvsky, *Acta crystallographica. Section E, Structure reports online*, 2010, **66**, i12-i12.
5. J. Liu, D. Chang, P. Whitfield, Y. Janssen, X. Yu, Y. Zhou, J. Bai, J. Ko, K.-W. Nam, L. Wu, Y. Zhu, M. Feyngenson, G. Amatucci, A. Van der Ven, X.-Q. Yang and P. Khalifah, *Chemistry of Materials*, 2014, **26**, 3295-3305.
6. A. Tang, W. Song, B. Xiao, J. Guo, J. Min, Z. Ge, J. Zhang, Z. Wei and E. Zhou, *Chemistry of Materials*, 2019, **31**, 3941-3947.
7. T. Ameri, N. Li and C. J. Brabec, *Energy & Environmental Science*, 2013, **6**, 2390.
8. A. Gurung and Q. Qiao, *Joule*, 2018, **2**, 1217-1230.
9. A. E. Ostfeld, A. M. Gaikwad, Y. Khan and A. C. Arias, *Sci Rep*, 2016, **6**, 26122.
10. N. Gasparini, M. Salvador, S. Strohm, T. Heumueller, I. Levchuk, A. Wadsworth, J. H. Bannock, J. C. de Mello, H.-J. Egelhaaf, D. Baran, I. McCulloch and C. J. Brabec, *Advanced Energy Materials*, 2017, **7**, 1700770.
11. H. Cha, J. Wu, A. Wadsworth, J. Nagitta, S. Limbu, S. Pont, Z. Li, J. Searle, M. F. Wyatt, D. Baran, J.-S. Kim, I. McCulloch and J. R. Durrant, *Advanced Materials*, 2017, **29**, 1701156.

*Electronic Supplementary Information for*

## Redox Processes in Sodium Vanadium Phosphate Cathode – Insights from operando Magnetometry

Gregor Klinser<sup>a</sup>, Roman Zettl<sup>b</sup>, Martin Wilkening<sup>b</sup>, Heinz Krenn<sup>c</sup>, Ilie Hanzu<sup>b</sup>, Roland Würschum<sup>a</sup>

<sup>a</sup> Institute of Material Physics, Graz University of Technology, Petersgasse 16, A-8010 Graz, Austria

<sup>b</sup> Institute for Chemistry and Technology of Materials, Christian Doppler Laboratory for Lithium Batteries, Stremayrgasse 9, Graz University of Technology, A-8010 Graz, Austria

<sup>c</sup> Institute of Physics, University of Graz, Universitätsplatz 5, A-8010 Graz, Austria

### Voltage profiles of the NVP cathode at different C-rates (see Fig. 1b)

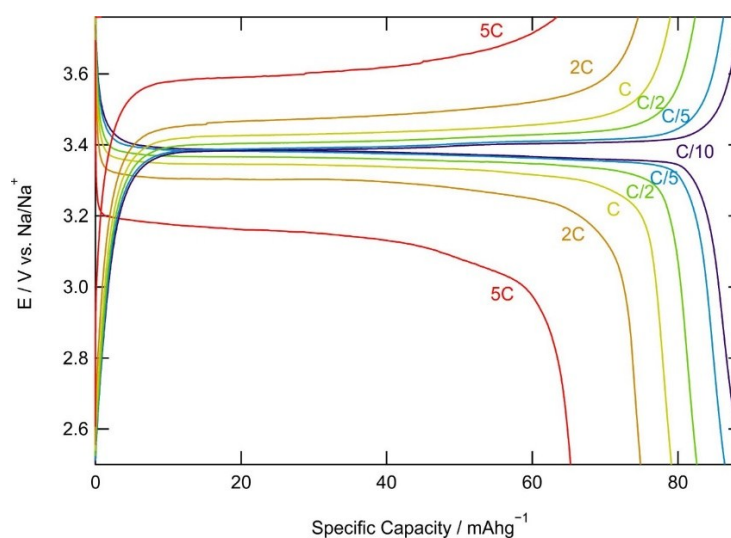


**Figure S1.** Charge and discharge profiles at the C-rates used to characterize the NVP material.

### Elemental analysis with Inductively Coupled Plasma - Mass Spectrometry (ICP-MS)

A Microwave heated pressurized autoclave digestion system - Ultraclave IV, MLS and a ICPMS 7700x from Agilent Technologies were used to determine concentrations of the elements Na, V and P. Sample preparation was done by dissolving the NVP/C sample in 10% HNO<sub>3</sub>. He was used as cell gas and Be (m/z 9) and Ge (m/z 74) were used as internal standards. The results are shown in Table S1 together with the relative *n* values in mol of Na, V and P which were calculated by setting *n* of P to 3 as it is in Na<sub>3</sub>V<sub>2</sub>(PO<sub>4</sub>)<sub>3</sub>. Based on this *n* of Na and

V were calculated. It can be seen that the values fit to the desired stoichiometric NVP within the measurement uncertainties. An additional screening of elements did not show any conspicuous elements present in the sample.

Table S1: Results of ICP-MS as concentrations  $c$  of Na, V and P in g of element per kg sample. From these results the relative amount of substance  $n$  in mol have been calculated by setting  $n$  of P to 3 mol.

|                               | Na     | V       | P      |
|-------------------------------|--------|---------|--------|
| <b><math>c</math> in g/kg</b> | 117(4) | 182(6)  | 162(7) |
| <b><math>n</math> in mol</b>  | 2.9(1) | 2.05(7) | 3.0(1) |

### Cyclic voltammetry

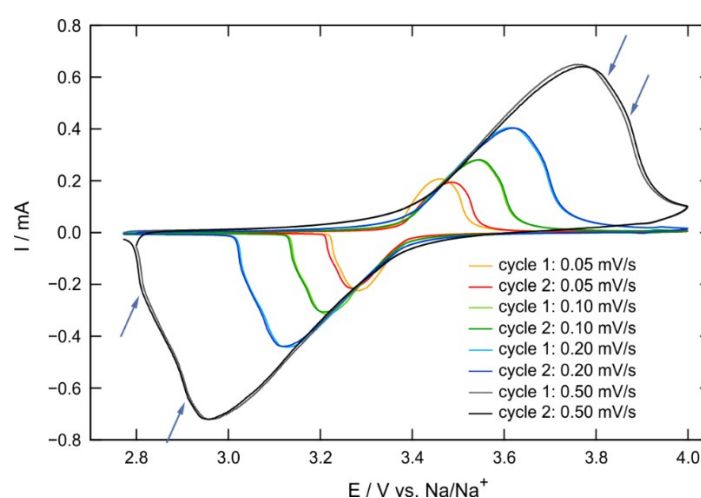


**Figure S2.** Cyclic voltammetry of NVP/C with different cycling rates of 0.05, 0.10, 0.20 and 0.50 mV/s.

### Ex-situ magnetic susceptibility measurement

Ex-situ magnetic susceptibility measurements on  $\text{Na}_2\text{V}_2(\text{PO}_4)_3$  were performed at an applied magnetic field of 5000 Oe in the temperature range between 300 and 8 K.

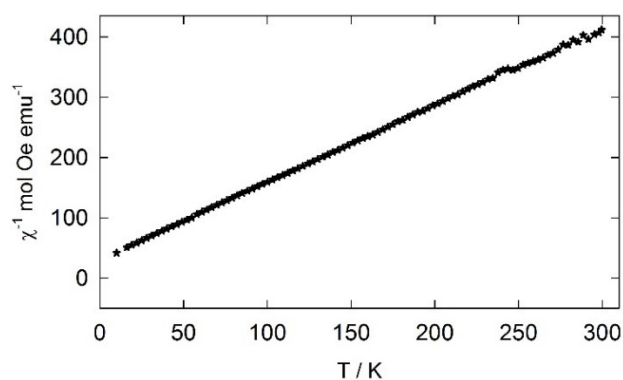


**Figure S3.** Inverse of the magnetic susceptibility  $\chi$  as a function of temperature  $T$  (field cooling measurement).

### X-ray powder diffraction (XRD)

The synthesized NVP carbon composite (NVP/C) material was characterized by X-ray diffractometry using a Bruker D8-Advance X-ray powder diffractometer equipped with a Lynxeye detector in Bragg-Brentano geometry with Cu-K $\alpha$  radiation. The diffraction angle was varied by 0.02° (counting time 2-4 s per step) between 10 and 100°. The pattern obtained from NVP/C after the synthesis is compared to a reference spectra from Inorganic Crystal Structure Database.<sup>1</sup>

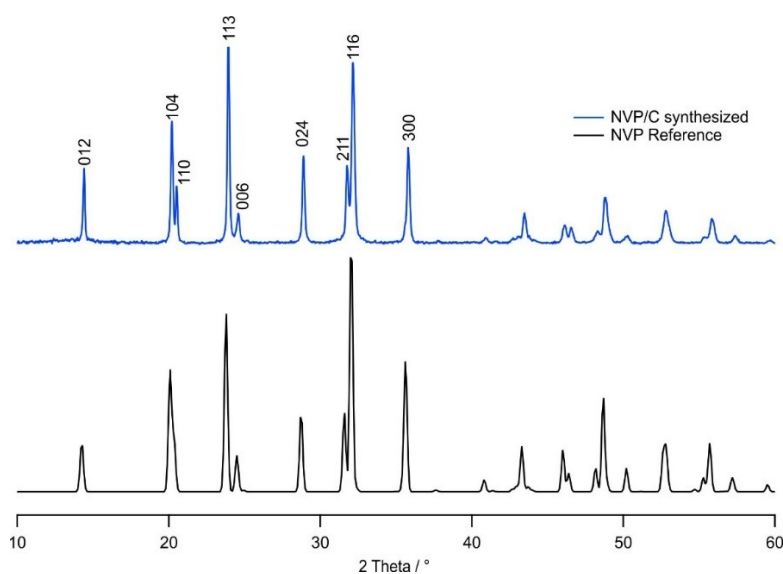


**Figure S4.** XRD pattern of NVP/C (blue) in comparison with a reference taken from the Inorganic Crystal Structure Database (ICSD) (black). No crystalline impurities were identified in the synthesized NVP material.

### References

- (1) Zatovsky, I. V. NASICON-Type Na<sub>3</sub>V<sub>2</sub>(PO<sub>4</sub>)<sub>3</sub>. *Acta Crystallogr. Sect. E Struct. Reports Online* **2010**, 66 (2), 0–5. <https://doi.org/10.1107/S1600536810002801>.

# Supporting Information

## Combined Effects of Anion Substitution and Nanoconfinement on the Ionic Conductivity of Li-based Complex Hydrides

Roman Zettl<sup>†§</sup>, Laura de Kort<sup>§</sup>, Maria Gombotz<sup>†</sup>, H. Martin R. Wilkening<sup>†</sup>, Petra de Jongh<sup>§\*</sup>, Peter Ngene<sup>§\*</sup>

<sup>†</sup> *Institute for Chemistry and Technology of Materials, and Christian Doppler Laboratory for Lithium Batteries, Graz University of Technology (NAWI Graz), Stremayrgasse 9, 8010 Graz, Austria*

<sup>§</sup> *Inorganic Chemistry and Catalysis, Debye Institute for Nanomaterials Science, Utrecht University, Universiteitweg 99, 3584 Utrecht, Netherlands*

\* Corresponding authors: p.ngene@uu.nl, P.E.deJongh@uu.nl

### S1. Calculation for synthesis: exemplarily shown for MCM-41 and 20 mol% of LiI

For the solid solution  $(1-x)\text{LiBH}_4-x\text{LiI}$  the right mass ratio was calculated through the molecular weight of  $\text{LiBH}_4$  (21.78 g/mol) and  $\text{LiI}$  (133.85 g/mol) and the respective mol% of the final product. 10, 20, 30 and 40 mol%  $\text{LiI}$  samples were synthesized via melt infiltration. For 20 mol%  $\text{LiI}$  the respective weight ratios are 61 wt%  $\text{LiI}$  and 39 wt%  $\text{LiBH}_4$ . Prior to melt infiltration, for 1 g total mass of the final solid solution we have to physically mix 0.61 g  $\text{LiI}$  and 0.39 g of  $\text{LiBH}_4$  together

Nanoconfined samples were calculated based on the amount of porous material (0.5 g) and the specific pore volume (MCM-41: 1.11  $\text{cm}^3/\text{g}$ ) determined through nitrogen physisorption. This results in 0.55  $\text{cm}^3$  to be filled. Filling of pores was realized for 130, 150 and 200 %. For 130 % we end up with a final volume of 0.72  $\text{cm}^3$ , which we want to fill with  $\text{LiBH}_4$ . With the specific volume of  $\text{LiBH}_4$  (1.50  $\text{cm}^3/\text{g}$ ) we can know calculate the final mass of  $\text{LiBH}_4$ , which we have to add to fill the pores of 0.5 g MCM-41 by 130 %: 0.48 g  $\text{LiBH}_4$ .

For the combined approach, the volume we have to fill is still 0.72  $\text{cm}^3$  (130 % pore filling). The masses of  $\text{LiI}$  ( $x$ ) and  $\text{LiBH}_4$  ( $y$ ) were calculated according to the equations (1) and (2). (1) is the weight ratio of  $\text{LiI}$  to  $\text{LiBH}_4$  and (2) includes the specific volumes of  $\text{LiI}$  (0.29  $\text{cm}^3/\text{g}$ ) and  $\text{LiBH}_4$  (1.50  $\text{cm}^3/\text{g}$ ). If they are multiplied by the mass, they sum up to the total pore volume of MCM-41, which we want to fill. With these two equations we obtain the amount of  $\text{LiI}$  ( $x = 0.57$  g) and  $\text{LiBH}_4$  ( $y = 0.37$  g), which we physically mix by mortaring before we gently mix it with MCM-41 (0.5 g) and finally put the mixture into stainless steel autoclaves for melt infiltration. The compositions of the samples in wt%. are given in Table S1

$$x/y = 0.61/0.39 \quad (1)$$

$$(x \text{ g} \cdot 0.29 \text{ cm}^3/\text{g}) + (y \text{ g} \cdot 1.50 \text{ cm}^3/\text{g}) = 0.72 \text{ cm}^3 \quad (2)$$

**Table S1. Composition of samples given in wt%**

| sample   | LiBH <sub>4</sub> content (wt%) | LiI or LiNH <sub>2</sub> content (wt%) | Oxide content (wt%) |
|--|---------------------------------|--|---------------------|
| LiBH <sub>4</sub> /MCM-41  | 49.0                            | -                                      | 51.0                |
| LiBH <sub>4</sub> -LiI/MCM-41 co-melt infiltration                         | 25.8                            | 39.6                                   | 34.6                |
| LiBH <sub>4</sub> -LiI/MCM-41 impregnation (H <sub>2</sub> O)              | 25.8                            | 39.6                                   | 34.6                |
| LiBH <sub>4</sub> -LiI/MCM-41 impregnation (EtOH)                          | 25.8                            | 39.6                                   | 34.6                |
| LiBH <sub>4</sub> -LiI/SBA-15 co-melt infiltration                         | 25.3                            | 38.8                                   | 35.9                |
| LiBH <sub>4</sub> -LiI/Al <sub>2</sub> O <sub>3</sub> co-melt infiltration | 17.8                            | 27.4                                   | 54.8                |
| LiBH <sub>4</sub> -LiI   | 39.4                            | 60.6                                   | -                   |
| LiBH <sub>4</sub> -LiNH <sub>2</sub>                                       | 48.8                            | 51.2                                   | -                   |
| LiBH <sub>4</sub> -LiNH <sub>2</sub> /MCM-41                               | 26.6                            | 27.9                                   | 45.5                |

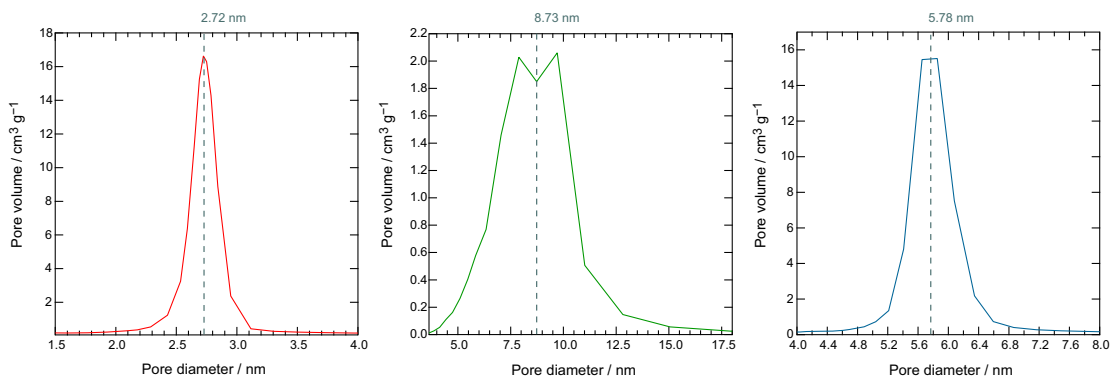
## S2. Nitrogen Physisorption

N<sub>2</sub> physisorption measurements were used to determine the properties (surface area and porosity) of the metal oxide before and after preparation of the nanocomposites. The measurements were carried out at -196 °C in a Micromeritics Tristar 3000. The pore size distribution and pore volumes were determined with the help of a Barrett-Joyner-Halenda analysis on the adsorption branch of the isotherm.

For the LiBH<sub>4</sub>-LiI / Al<sub>2</sub>O<sub>3</sub> and LiBH<sub>4</sub>-LiI / SBA-15 system N<sub>2</sub>-physisorption was repeated with the result of no pore volume or surface left.

**Table S2. Pore size, specific pore volume and BET surface from N<sub>2</sub>-physisorption of MCM-41, SBA-15 and Al<sub>2</sub>O<sub>3</sub>**

|                                    | Pore size (nm) | Specific pore volume (cm <sup>3</sup> g <sup>-1</sup> ) | BET surface area (m <sup>2</sup> g <sup>-1</sup> ) |
|------------------------------------|----------------|---|--|
| <b>MCM-41</b>                      | 2.7            | 1.11  | 1071   |
| <b>SBA-15</b>                      | 5.8            | 1.05  | 800  |
| <b>Al<sub>2</sub>O<sub>3</sub></b> | 8.7            | 0.49  | 186  |

**Figure S1.** Desorption branch of alumina, **Figure S2.** Desorption branch of MCM-41, and **Figure S3.** Desorption branch of SBA-15

### S3. Scanning Electron Microscopy (SEM)

SEM (scanning electron microscopy) pictures (see Figures S4 to S6) were taken with a Thermo Fischer XL30SFEG instrument operating at an acceleration voltage of 5 kV measuring secondary electrons. For larger magnifications a Through-Lens-Detector (TLD) was used. Samples were sputter-coated with 8 nm of Pt before loading into the SEM instrument.

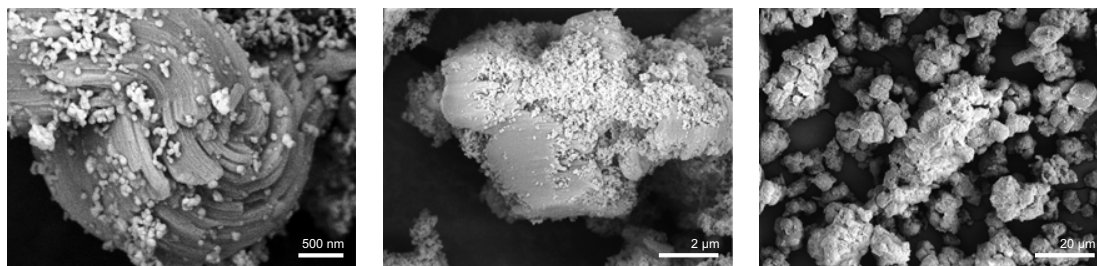


Figure S4. SEM images of MCM-41 at different magnifications.

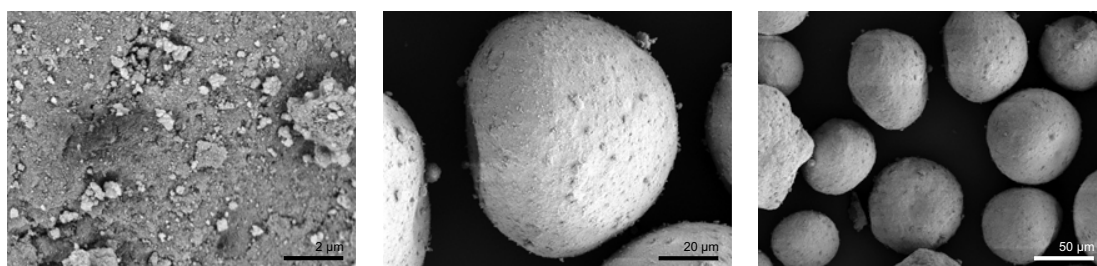


Figure S5. SEM images of Al<sub>2</sub>O<sub>3</sub> at different magnifications.

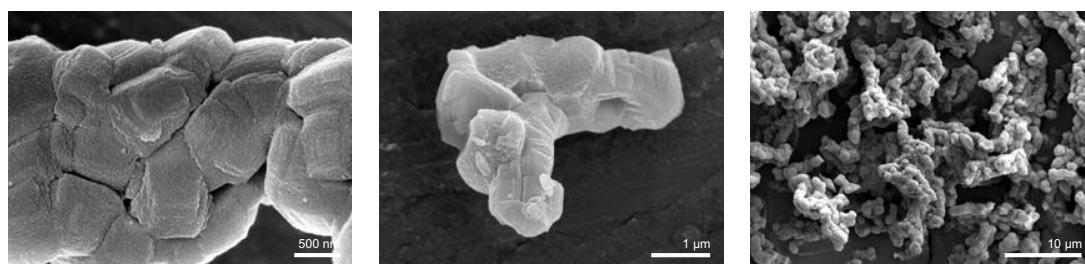
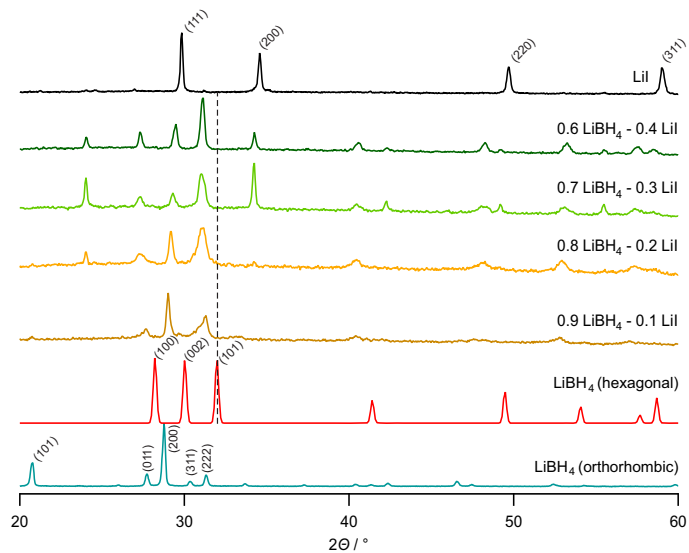


Figure S6. SEM images of SBA-15 at different magnifications.

#### S4. X-ray Diffractometry (XRD)

Figures S7 and S8 show additional XRD patterns including  $(1-x)\text{LiBH}_4-x\text{LiI}$  and  $(1-x)\text{LiBH}_4-x\text{LiI}/\text{MCM-41}$ .



**Figure S7.** XRD powder patterns of the samples indicated  $((1-x)\text{LiBH}_4-x\text{LiI})$  with different mol% of LiI. The patterns of the two different modifications of  $\text{LiBH}_4$  as well as that of LiI are shown for comparison.

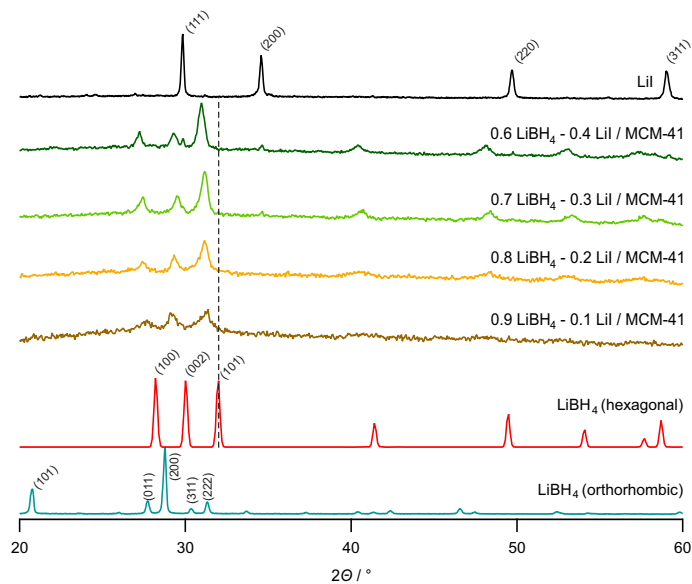


**Figure S8.** XRD powder patterns of the samples indicated  $((1-x)\text{LiBH}_4-x\text{LiI}/\text{MCM-41})$  with different mol% of LiI. The patterns of the two different modifications of  $\text{LiBH}_4$  as well as that of LiI are shown for comparison.

## S5. Diffuse Reflectance Infrared Fourier Transform Spectrometry (DRIFTS)

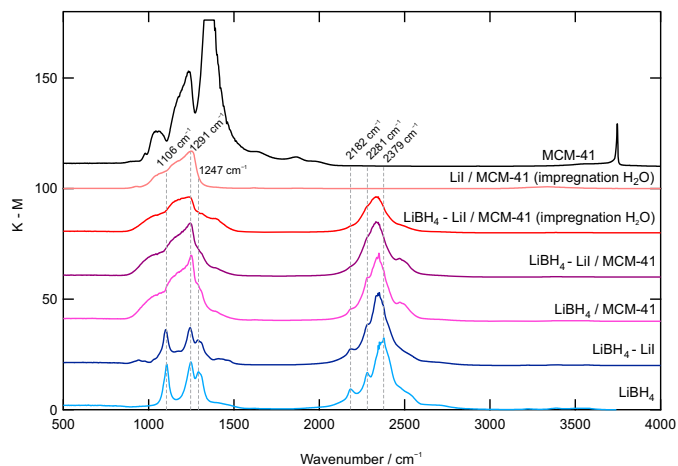


**Figure S9.** DRIFT spectra of samples confined in MCM-41. Spectra of  $\text{LiBH}_4$ , the solid solution of  $\text{LiBH}_4$  with 20mol% of  $\text{LiI}$  and pristine MCM-41 serve as references.

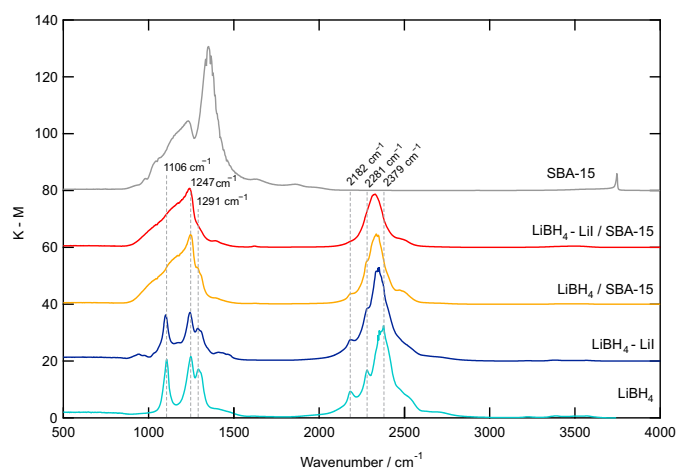


**Figure S10.** DRIFT spectra of the samples with SBA-15; spectra belonging to lithium borohydride and nonconfined  $\text{LiH}_4\text{-LiI}$  serve a references. Main peaks are marked with a dotted grey line; the corresponding wavenumbers are indicated. K-M intensities are in arbitrary units.

## S6. Impedance Spectroscopy

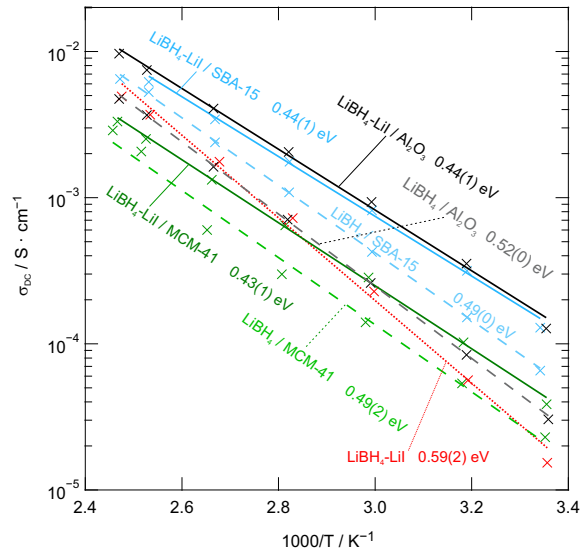


**Figure S11.** Arrhenius plot illustrating the change in conductivity of  $LiBH_4$  and  $LiBH_4-LiI$  using  $SiO_2$  or  $Al_2O_3$  for nanoconfinement. Lines represent linear fits; values denote activation energies  $E_a$ .

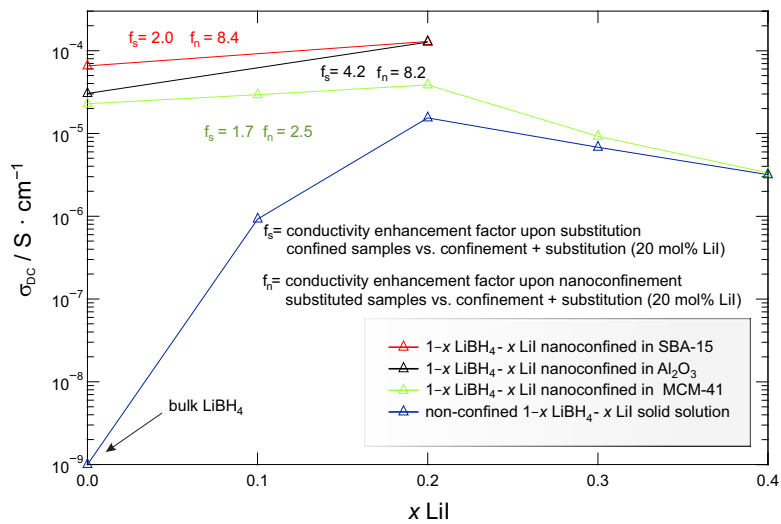


**Figure S12.** Conductivity enhancement factors and change of ionic conductivity upon incorporation of  $LiI$  when  $LiBH_4$  is nanoconfined with either MCM-41, SBA-15 or alumina.

**Table S3. Comparison of conductivities, activation energies and pre-exponential factors of the differently prepared samples within this study**

| mol% of LiI Added <sup>a</sup> | Kind of Confinement | Conductivity <sup>b</sup><br>$\sigma$ / S/cm | $T$ / °C | Activation Energy <sup>c</sup><br>$E_a$ / eV | Pre-Exponential Factor<br>$\log_{10}(A)$ |
|--------------------------------|---------------------|--|----------|--|--|
| 0                              | -                   | $1.00 \times 10^{-9}$ (1 Hz) <sup>d</sup>    | 25.2     | 0.82(5)                                      | 7.4(7)                                   |
| 0                              | MCM-41              | $2.29 \times 10^{-5}$                        | 25.2     | 0.49(2)                                      | 6.0(3)                                   |
| 0                              | MCM-41 <sup>e</sup> | $3.94 \times 10^{-5}$                        | 24.0     | 0.40(1)                                      | 4.9(2)                                   |
| 0                              | SBA-15              | $6.55 \times 10^{-5}$                        | 26.1     | 0.49(0)                                      | 6.5(1)                                   |
| 0                              | alumina             | $3.04 \times 10^{-5}$                        | 24.6     | 0.52(0)                                      | 6.8(1)                                   |
| 10                             | -                   | $9.26 \times 10^{-7}$                        | 24.6     | 0.88(7)                                      | 11(1)                                    |
| 10                             | MCM-41              | $2.94 \times 10^{-5}$                        | 24.6     | 0.49(2)                                      | 6.3(3)                                   |
| 20                             | -                   | $1.54 \times 10^{-5}$                        | 24.8     | 0.59(2)                                      | 7.8(3)                                   |
| 20                             | MCM-41              | $3.86 \times 10^{-5}$                        | 24.9     | 0.43(1)                                      | 5.3(1)                                   |
| 20                             | MCM-41 <sup>f</sup> | $7.27 \times 10^{-5}$                        | 24.0     | 0.44(1)                                      | 5.8(1)                                   |
| 20                             | SBA-15              | $1.29 \times 10^{-4}$                        | 26.1     | 0.44(1)                                      | 6.0(2)                                   |
| 20                             | alumina             | $1.27 \times 10^{-4}$                        | 25.0     | 0.44(1)                                      | 6.1(1)                                   |
| 30                             | -                   | $6.79 \times 10^{-6}$                        | 24.7     | 0.53(1)                                      | 6.2(2)                                   |
| 30                             | MCM-41              | $9.25 \times 10^{-6}$                        | 24.6     | 0.44(0)                                      | 4.9(0)                                   |
| 40                             | -                   | $3.17 \times 10^{-6}$                        | 24.5     | 0.54(1)                                      | 6.0(2)                                   |
| 40                             | MCM-41              | $3.34 \times 10^{-6}$                        | 24.5     | 0.41(1)                                      | 4.0(1)                                   |

<sup>a</sup> (1-x) LiBH<sub>4</sub>-xLiI (x = 0.0, 0.1, 0.2, 0.3, 0.4); x = 0.1 is equivalent to 10 mol% LiI

<sup>b</sup> room temperature value after the second cooling cycle

<sup>c</sup> activation energy calculated from the second cooling curve

<sup>d</sup> value determined at a frequency of 1 Hz, *i.e.*, the last point of the measurement was used to estimate the conductivity as no plateau was observed in the conductivity isotherm.

<sup>e</sup> MCM-41 from a different batch

<sup>f</sup> MCM-41 from a different batch

# Li-Ion Diffusion in Nanoconfined $\text{LiBH}_4\text{-LiI}/\text{Al}_2\text{O}_3$ : From 2D Bulk Transport to 3D Long-Range Interfacial Dynamics

Roman Zettl<sup>1,2\*</sup>, Maria Gombotz<sup>1</sup>, David Clarkson<sup>3</sup>, Steven G. Greenbaum<sup>3</sup>, Peter Ngene<sup>2</sup>,  
Petra E. de Jongh<sup>2</sup>, and H. Martin. R. Wilkening<sup>1,4\*</sup>

<sup>1</sup> Institute for Chemistry and Technology of Materials, and Christian Doppler Laboratory for Lithium Batteries, Graz University of Technology, Stremayrgasse 9, 8010 Graz, Austria

<sup>2</sup> Inorganic Chemistry and Catalysis, Debye Institute for Nanomaterials Science, Utrecht University, Universiteitweg 99, 3584 Utrecht, Netherlands

<sup>3</sup> Department of Physics and Astronomy, Hunter College of the City University of New York, New York, NY 10065, USA

<sup>4</sup> Alistore–ERI European Research Institute, CNRS FR3104, Hub de l’Energie, Rue Baudelocque, F-80039 Amiens, France

\* E-mail: [zettl@tugraz.at](mailto:zettl@tugraz.at) ; [wilkening@tugraz.at](mailto:wilkening@tugraz.at)

## NMR measurement parameters and magnetization transients

**Table S1:** NMR pulse lengths (p1), delay times (D1) and number of scans (ns) used to measure one-pulse spectra and spin-lattice relaxation rates (static)

| Parameter          | MAS              |                  |                      |                                      | static                   |                          |                          |
|--------------------|------------------|------------------|----------------------|--------------------------------------|--------------------------|--------------------------|--------------------------|
|                    | <sup>1</sup> H   | <sup>6</sup> Li  | <sup>11</sup> B      | <sup>27</sup> Al                     | <sup>1</sup> H           | <sup>7</sup> Li          | <sup>11</sup> B          |
| p1 / $\mu\text{s}$ | 1.0 <sup>a</sup> | 3.0 <sup>b</sup> | 1.0-2.0 <sup>b</sup> | 1.5 <sup>b</sup> or 3.0 <sup>c</sup> | 1.05 - 1.89 <sup>c</sup> | 2.30 - 2.66 <sup>c</sup> | 3.00 - 3.43 <sup>c</sup> |
| D1 / s             | 1-5              | 10-120           | 4-8                  | 5                                    | 1                        | 1                        | 0.5                      |
| ns                 | 4                | 32-128           | 4-8                  | 128                                  | 4                        | 4                        | 4                        |

<sup>a</sup> at 50 W power level for the excitation pulse

<sup>b</sup> at 150 W power level for the excitation pulse

<sup>c</sup> at 200 W power level for the excitation pulse

Figure S1 shows the magnetization transients of the spin-lattice relaxation measurements in both the rotating and laboratory frame of reference.

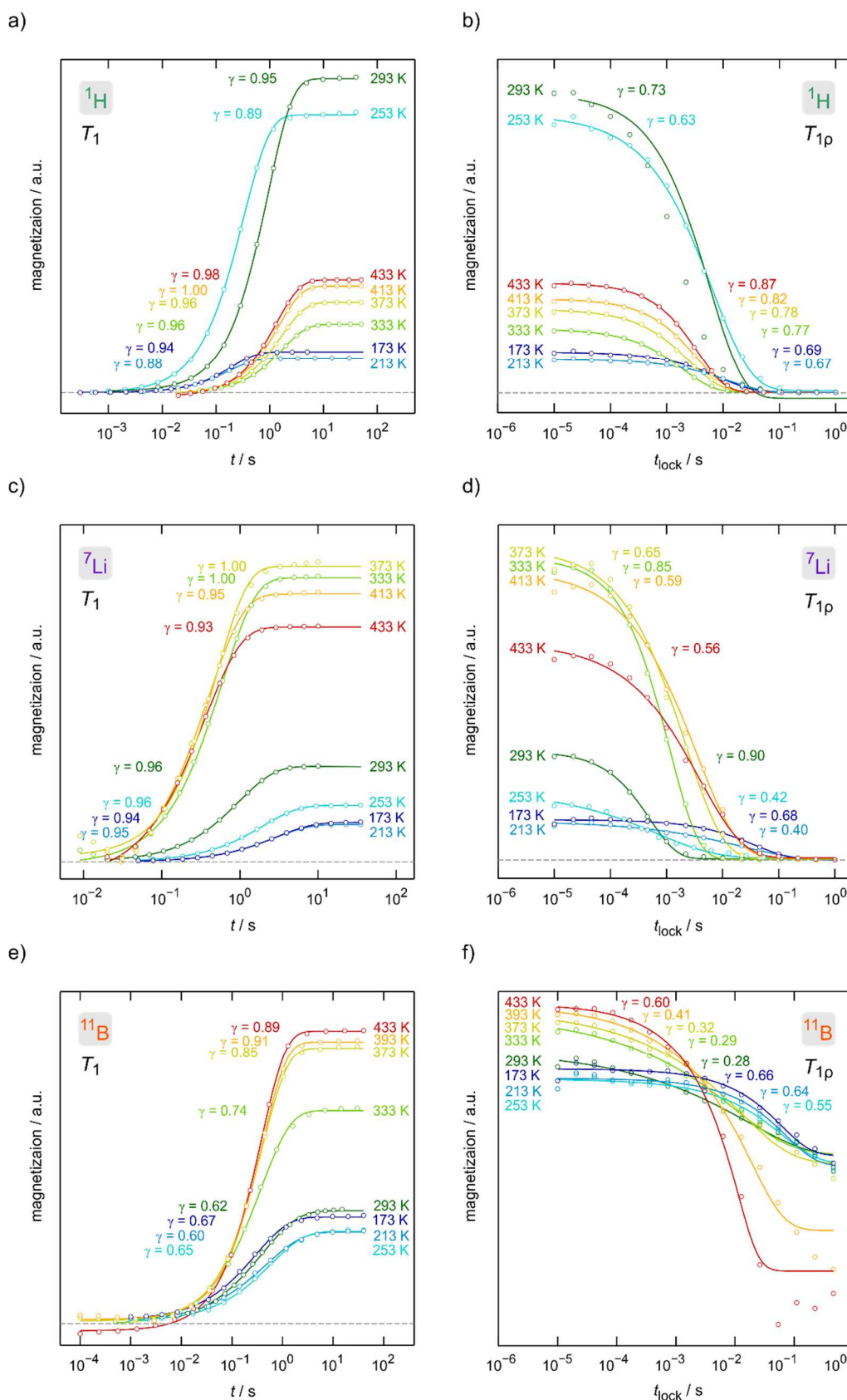


**Figure S1.** Magnetization transients of static NMR measurements: a)  $T_1$  of  $^1\text{H}$  NMR, b)  $T_{1\rho}$  of  $^1\text{H}$  NMR, c)  $T_1$  of  $^7\text{Li}$  NMR, d)  $T_{1\rho}$  of  $^7\text{Li}$  NMR, e)  $T_1$  of  $^{11}\text{B}$  NMR and f)  $T_{1\rho}$  of  $^{11}\text{B}$  NMR. The corresponding  $\gamma$ -values are included as well.

The PFG-DOSY experiments work on the principle of encoding the longitudinal position of spins in their phase by means of applying a magnetic field gradient and measuring the dephasing that occurs due to diffusion when a gradient of opposite polarity is applied. These large pulsed gradients produce eddy currents within the electronics of the probe, which can interfere with measurements, creating artefacts in the spectra and attenuating the signal, which in further consequence, artificially increases the measured diffusion coefficients  $D_{\text{PFG}}$ . A number of techniques exist to mitigate the effects of eddy currents on measurements to the point of insignificance. Here, we utilized a longitudinal eddy current delay (LECD) in which the diffusion-attenuated echo is stored on the longitudinal axis after refocusing with a  $\pi/2$ -pulse, waiting for an eddy current delay time allowing eddy currents to naturally fade. Afterwards, the stored echo is observed using a second  $\pi/2$ -pulse. This pulse sequence eliminates eddy current effects but comes at the cost that the sample relaxes according to  $T_1$  during the eddy current delay time, creating an attenuation curve in which peaks decay to a nonzero intensity rather than decaying to zero as in PFG sequences without this delay. This makes the LECD technique only favorable for samples in which an eddy current delay much less than  $T_1$  allows all eddy currents to dissipate. For our apparatus, a 5 ms delay time is sufficient, which is approximately 1% of the  $T_1$  time of the sample, but it still makes a major contribution to the uncertainty in our measurement

PFG NMR data were evaluated with the help of the Stejskal-Tanner equation for stimulated echo pulse sequences with square pulses:  $M(g) = M_0 \exp(-(\gamma \delta g)^2 D (\Delta - \delta/3))$  where  $M$  is the echo attenuation. The experimental variables are denoted as the strength of the gradient  $g$ , the length of the gradient  $\delta$  and the diffusion delay  $\Delta$ . The pre-exponential factor  $M_0$  follows the condition  $g \times \delta = 0$ . With these parameters and  $\gamma$ , being the magnetogyric ratio of the  $^7\text{Li}$  spins, the diffusion coefficient  $D$  can be estimated.

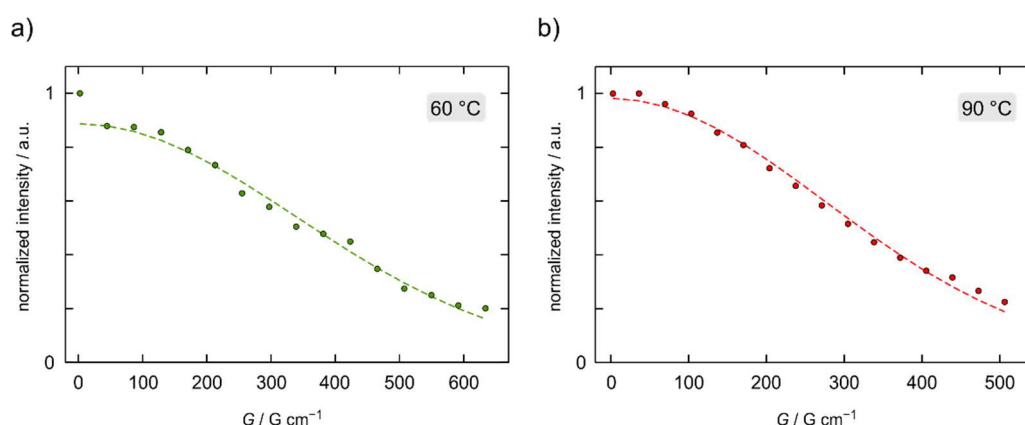


**Figure S2.** a) and b) PFG decay curves to probe  $^7\text{Li}$  diffusion coefficients at  $60^\circ\text{C}$  (a) and  $90^\circ\text{C}$  (b). Intensities are given in arbitrary units.

Figure S3 shows  $T_2$  magnetization transients recorded at the temperatures indicated. In Figure S3 the PFG NMR decay curves are shown which we recorded at 60 °C and 90 °C, respectively.

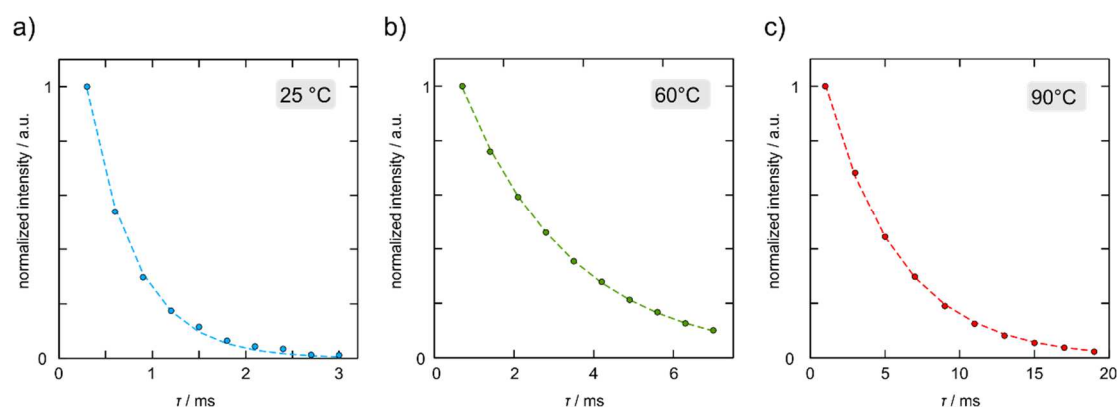


**Figure S3.** a), b) and c) magnetization transients from which the transverse relaxation times  $T_2$  at 25 °C (a), 60 °C (b) and 90 °C (c) were extracted. Intensities, in arbitrary units, are normalized to the highest intensity.

## Supporting Information

### Towards the origin of Li-Ion Diffusion in Nanoconfined and Anion-substituted Lithium Boron Hydride

Roman Zettl, Peter Ngene, Petra E. de Jongh and H. Martin R. Wilkening.  
*manuscript in preparation*

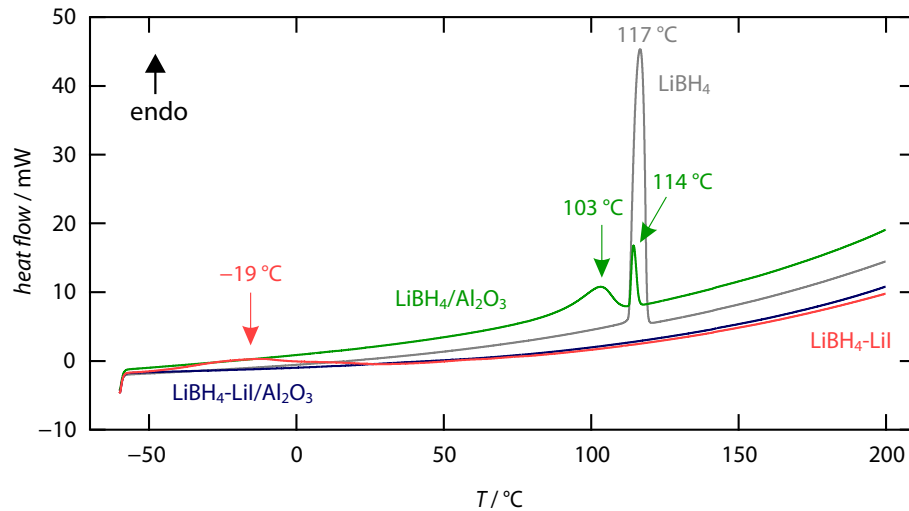


**Figure A1.** Dynamic scanning calorimetry results of  $\text{LiBH}_4\text{-LiI}/\text{Al}_2\text{O}_3$  (blue),  $\text{LiBH}_4/\text{Al}_2\text{O}_3$  (green),  $\text{LiBH}_4\text{-LiI}$  (red) and  $\text{LiBH}_4$  (grey).

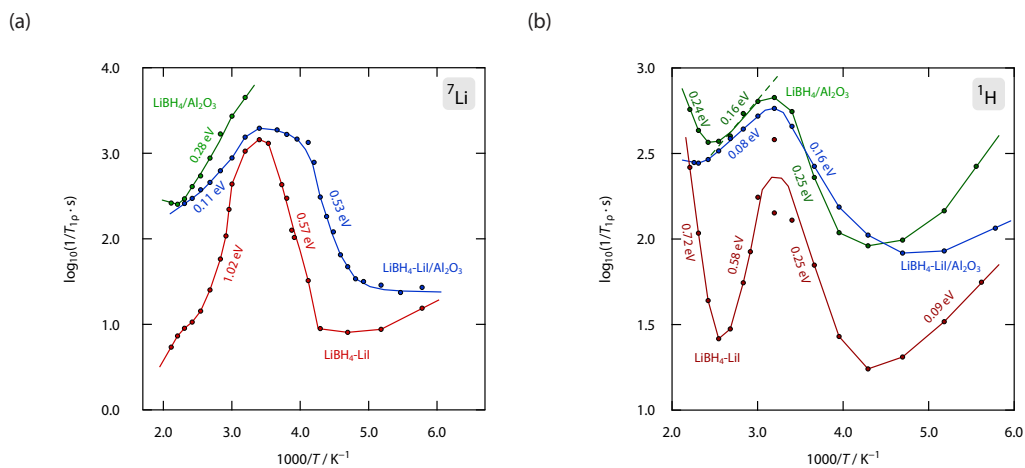


**Figure A2.** Arrhenius representation of  $T_{1\rho}$  spin-lattice relaxation rates of  $\text{LiBH}_4\text{-LiI}/\text{Al}_2\text{O}_3$  (blue),  $\text{LiBH}_4/\text{Al}_2\text{O}_3$  (green) and  $\text{LiBH}_4\text{-LiI}$  (red) of nuclei a)  $^7\text{Li}$  and b)  $^1\text{H}$

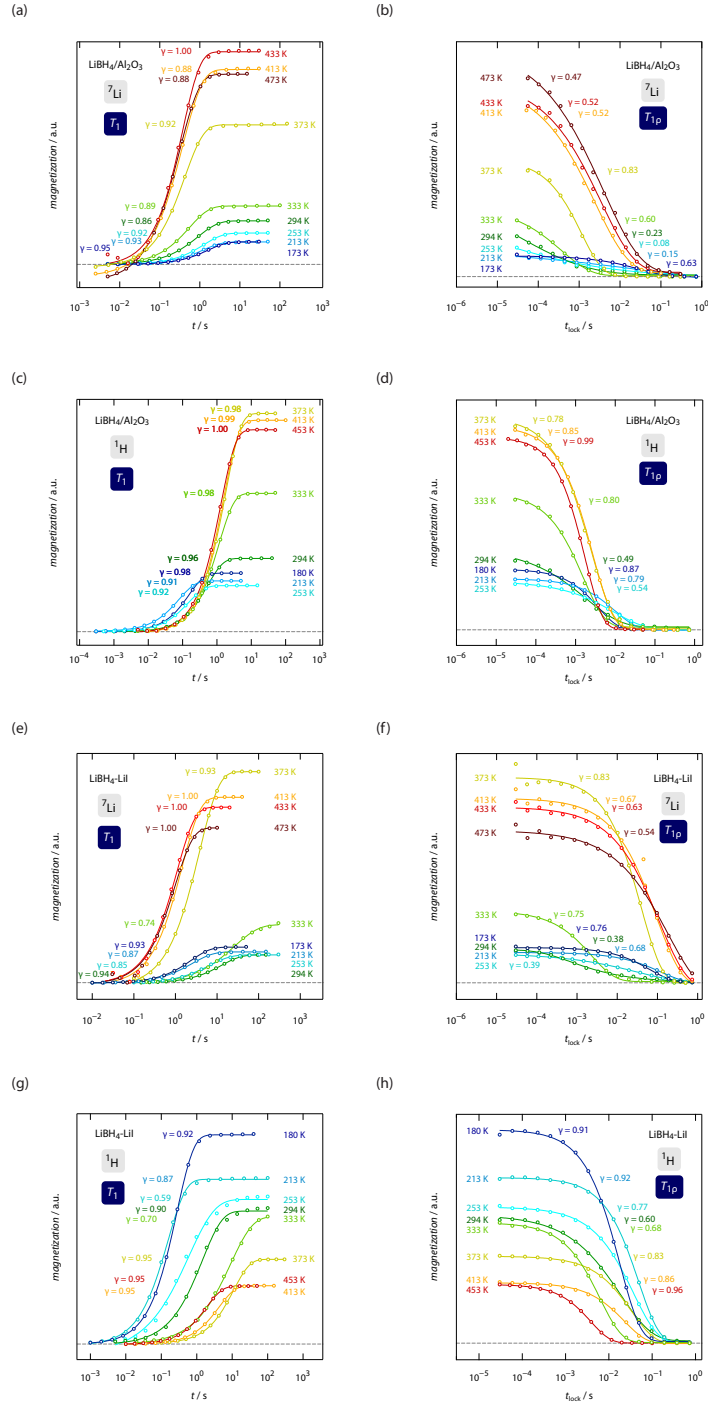


**Figure A3.** Selected transients of  $T_1$  and  $T_{1\rho}$  spin-lattice relaxation measurements with  $\gamma$  from the stretched exponential fit attached to the transients. a)  ${}^7\text{Li}$   $T_1$  relaxation of  $\text{LiBH}_4/\text{Al}_2\text{O}_3$  b)  ${}^7\text{Li}$   $T_{1\rho}$  relaxation of  $\text{LiBH}_4/\text{Al}_2\text{O}_3$  c)  ${}^1\text{H}$   $T_1$  relaxation of  $\text{LiBH}_4/\text{Al}_2\text{O}_3$  d)  ${}^1\text{H}$   $T_{1\rho}$  relaxation of  $\text{LiBH}_4/\text{Al}_2\text{O}_3$  e)  ${}^7\text{Li}$   $T_1$  relaxation of  $\text{LiBH}_4\text{-LiI}$  f)  ${}^7\text{Li}$   $T_{1\rho}$  relaxation of  $\text{LiBH}_4\text{-LiI}$  g)  ${}^1\text{H}$   $T_1$  relaxation of  $\text{LiBH}_4\text{-LiI}$  h)  ${}^1\text{H}$   $T_{1\rho}$  relaxation of  $\text{LiBH}_4\text{-LiI}$ .

# Hybrid Na<sup>+</sup> and Li<sup>+</sup> Solid Electrolytes Based on MIL-121 Metal Organic Framework

– Electronic Supplementary Information –

Roman Zettl<sup>1</sup>, Sarah Lunghammer<sup>1</sup>, Athmane Boulaoued<sup>2,3</sup>, Patrik Johansson<sup>2,3</sup>, H. Martin R. Wilkening<sup>1,3,†</sup>, Ilie Hanzu<sup>1,3,\*</sup>

<sup>1</sup> Institute for Chemistry and Technology of Materials, Graz University of Technology (NAWI Graz), Stremayrgasse 9, 8010 Graz, Austria

<sup>2</sup> Department of Physics, Chalmers University of Technology, 412 96, Gothenburg, Sweden

<sup>3</sup> Alistore–ERI European Research Institute, CNRS FR3104, Hub de l’Energie, Rue Baudelocque, F-80039 Amiens, France

\* Corresponding author: [hanzu@tugraz.at](mailto:hanzu@tugraz.at)

† See also for correspondence: [wilkening@tugraz.at](mailto:wilkening@tugraz.at)

## S1. Impedance Spectroscopy

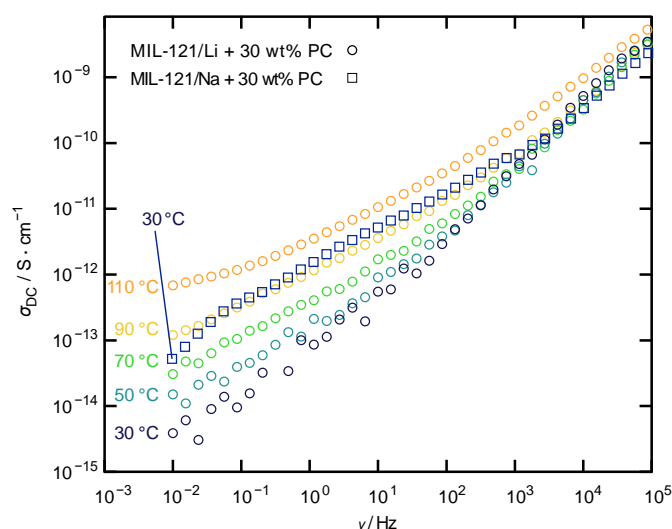


**Figure S1.** Conductivity isotherms of lithiated and sodiated MIL-121 soaked with PC lacking LiClO<sub>4</sub> or NaClO<sub>4</sub>. MIL-121/Li +PC is measured at different temperatures and shown in circles whereas MIL-121/Na +PC was only measured at 30 °C which is shown in squares.

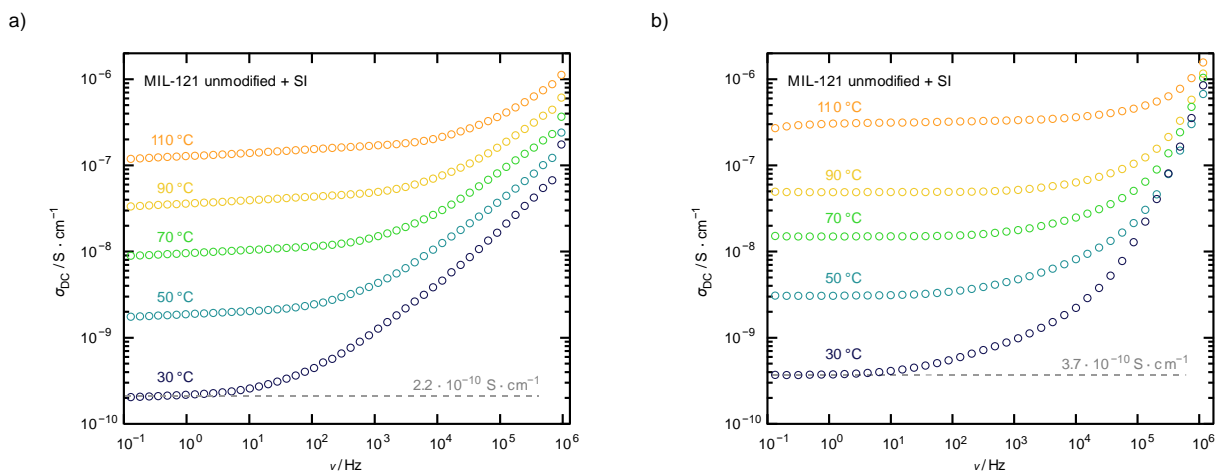


**Figure S2.** Conductivity isotherms of unmodified MIL-121 soaked with a) 1M LiClO<sub>4</sub> and b) 1M NaClO<sub>4</sub> in PC.

## S2. Thermogravimetric analysis (TGA) and Differential scanning calorimetry (DSC)

TGA measurements were carried out with a STA (simultaneous thermal analysis)-device from Netzsch (STA 449 C) coupled with a mass spectrometer QMS 403 C (Netzsch). This analysis method connects two methods, DSC and TGA. Samples were measured with a rate of 1 °C/min in helium atmosphere. The temperature range was from room temperature to 550 °C.

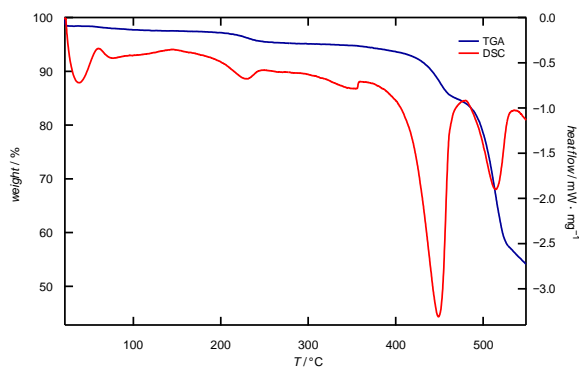


**Figure S3.** TGA of pristine MIL-121

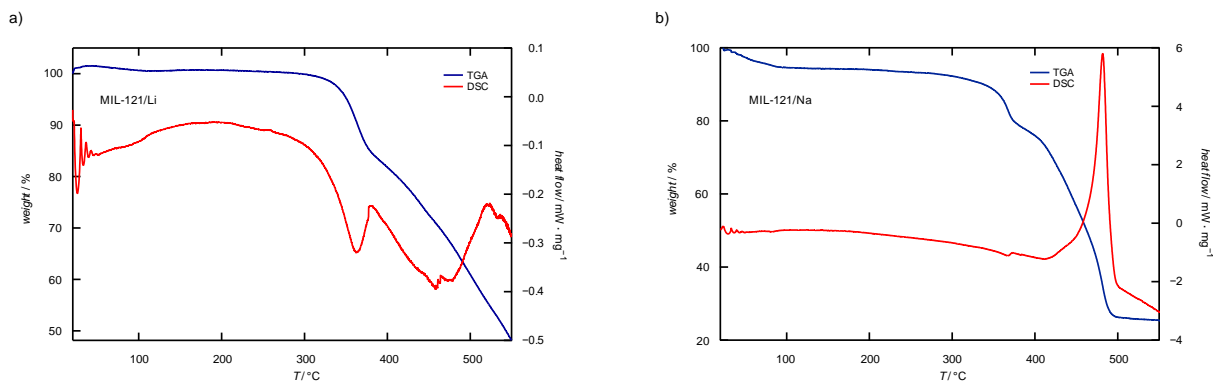


**Figure S4.** TGA of a) lithiated and b) sodiated MIL-121

With a second device, a Perkin Elmer DSC 8500, additional DSC measurements were performed on samples MIL-121/Li+SE and MIL-121/Na+SE in nitrogen atmosphere. The measurement was carried out at temperatures ranging from  $-60\text{ }^{\circ}\text{C}$  to  $100\text{ }^{\circ}\text{C}$  with a rate of  $5\text{ }^{\circ}\text{C}/\text{min}$ . In Figure S5 the second heating cycle (step 7) of both samples MIL-121/Li+SE and MIL-121/Na+SE is shown. The temperature program was as follows:

- 1) Temperature set to  $30\text{ }^{\circ}\text{C}$
- 2) Cool from  $30\text{ }^{\circ}\text{C}$  to  $-60\text{ }^{\circ}\text{C}$
- 3) Hold for 3 min at  $-60\text{ }^{\circ}\text{C}$
- 4) Heat from  $-60\text{ }^{\circ}\text{C}$  to  $100\text{ }^{\circ}\text{C}$  at  $5\text{ }^{\circ}\text{C}/\text{min}$
- 5) Cool from  $100\text{ }^{\circ}\text{C}$  to  $-60\text{ }^{\circ}\text{C}$  at  $5\text{ }^{\circ}\text{C}/\text{min}$
- 6) Hold for 3 min at  $-100\text{ }^{\circ}\text{C}$
- 7) **Heat from  $-60\text{ }^{\circ}\text{C}$  to  $100\text{ }^{\circ}\text{C}$  at  $5\text{ }^{\circ}\text{C}/\text{min}$**

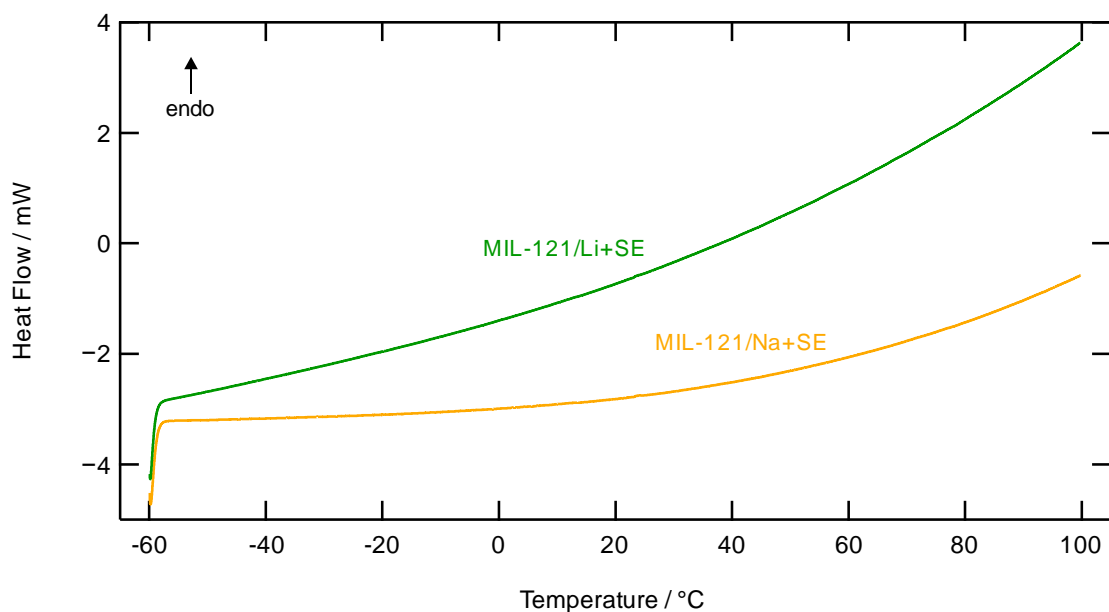


**Figure S5.** DSC of a) lithiated and b) sodiated MIL-121 with supporting electrolyte

### S3. Raman spectroscopy at variable temperatures

FT-Raman measurements were performed with a 1064 nm laser line, a power of 230 to 400 mW and a resolution of  $2\text{ cm}^{-1}$ . The accumulation time was *ca.* 55 min and a point were recorded in the range of 200 to 2000  $\text{cm}^{-1}$  at temperatures from  $-20$  to  $80\text{ }^{\circ}\text{C}$ . The applied temperature does include the transition temperature from the lower to the higher activation energy of the sample. The temperature was controlled using a Linkam cell with a flow of liquid nitrogen. Samples were treated inside a glovebox and the measurement was performed with an air tight sample cell. Shown spectra are baseline corrected.

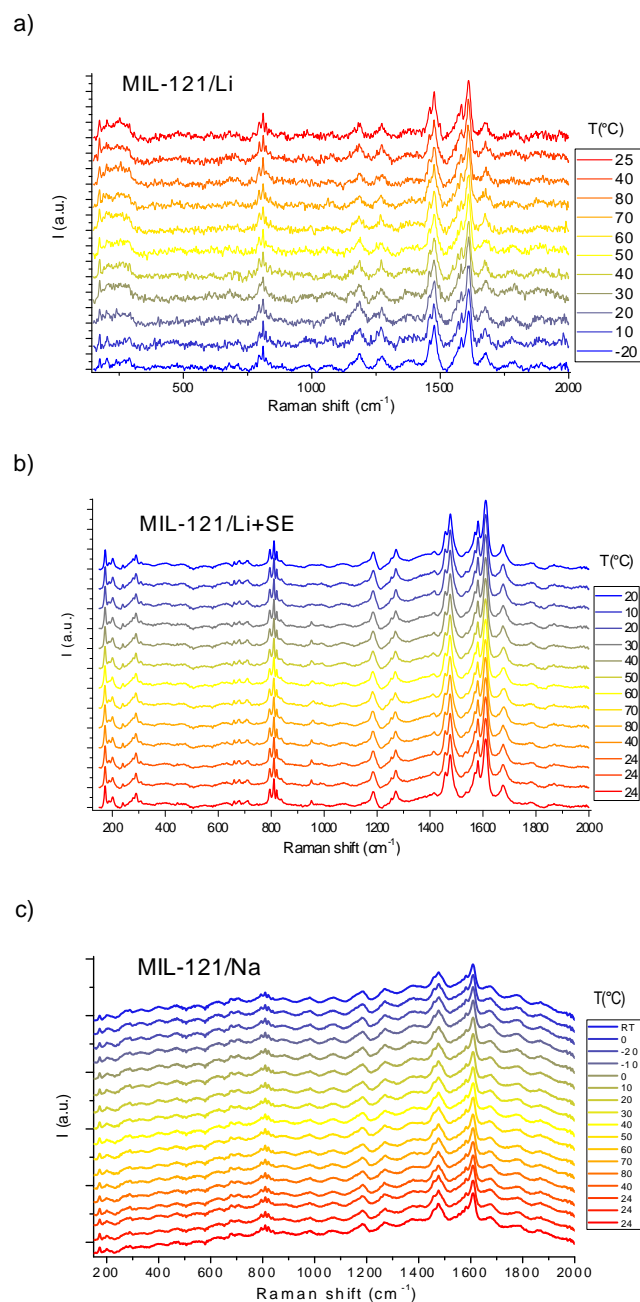


**Figure S6.** Raman spectra at different temperatures of a) MIL-121/Li, b) MIL-121/Li+SE and c) MIL-121/Na. None of the samples shows significant changes of the most pronounced peaks in the spectra.

## S4. Nuclear Magnetic Resonance (NMR)

### S4.1. NMR measurement parameter

In table S1 and S2 you can find the parameters used in the MAS and static NMR experiments, respectively. Different settings were used for different nuclei. *E.g.* in CP MAS NMR experiments the number of scans was increased, because of its weak signal.

**Table S1:** Parameters from MAS NMR measurements of  $^1\text{H}$ ,  $^1\text{H}$ - $^{13}\text{C}$  cross polarization (CP) and  $^{27}\text{Al}$ .  $p_1$  denotes the pulse length in  $\mu\text{s}$ ,  $D_1$  is the delay time before pulses in s and  $ns$  stands for number of scans.

|                     | $^1\text{H}$     | CP <sup>a</sup>  | $^{27}\text{Al}$  | $^{23}\text{Na}$         |                          |
|---------------------|------------------|------------------|-------------------|--------------------------|--------------------------|
|                     |                  |                  |                   | lines                    | $T_1$                    |
| $p_1 / \mu\text{s}$ | 1.0 <sup>b</sup> | 2.5 <sup>c</sup> | 0.71 <sup>d</sup> | 3.35 – 4.15 <sup>d</sup> | 3.35 – 4.15 <sup>d</sup> |
| $D_1 / \text{s}$    | 1                | 3                | 1                 | 0.5                      | -                        |
| $ns$                | 8                | 4096             | 512               | 256                      | 32                       |

<sup>a</sup> contact time of 10 ms

<sup>b</sup> at 50 W power level for excitation pulse

<sup>c</sup> at 20 W decoupling power level and 70 W power level during contact

<sup>d</sup> at 200 W power level for excitation pulse

**Table S2:** Parameters from static NMR measurements of  $^7\text{Li}$  and  $^{23}\text{Na}$ .  $p_1$  denotes the pulse length in  $\mu\text{s}$ ,  $D_1$  is the delay time before pulses in s and  $ns$  stands for number of scans.

|                       | $^7\text{Li}$ |             |                       | $^{23}\text{Na}$ |             |
|-----------------------|---------------|-------------|-----------------------|------------------|-------------|
|                       | lines         | $T_1$       | $T_{1p}$              | lines            | $T_1$       |
| $p_1^a / \mu\text{s}$ | 2.40 – 2.55   | 2.35 – 2.55 | 2.25 – 2.55           | 2.00 – 2.65      | 2.00 – 2.65 |
| $D_1 / \text{s}$      | 10 - 30       | 1           | 0.3 – 44 <sup>b</sup> | 5                | 1 - 3       |
| $ns$                  | 64 - 126      | 4           | 4 - 8                 | 512              | 8 - 32      |

<sup>a</sup> at 200 W power level for excitation pulse

<sup>b</sup>  $D_1$  in the  $T_{1p}$  experiments is set to  $5 \times T_1$  ( $T_1$  was obtained from  $T_1$  relaxation measurements)

## S4.2. MAS NMR spectra comparison at different temperatures

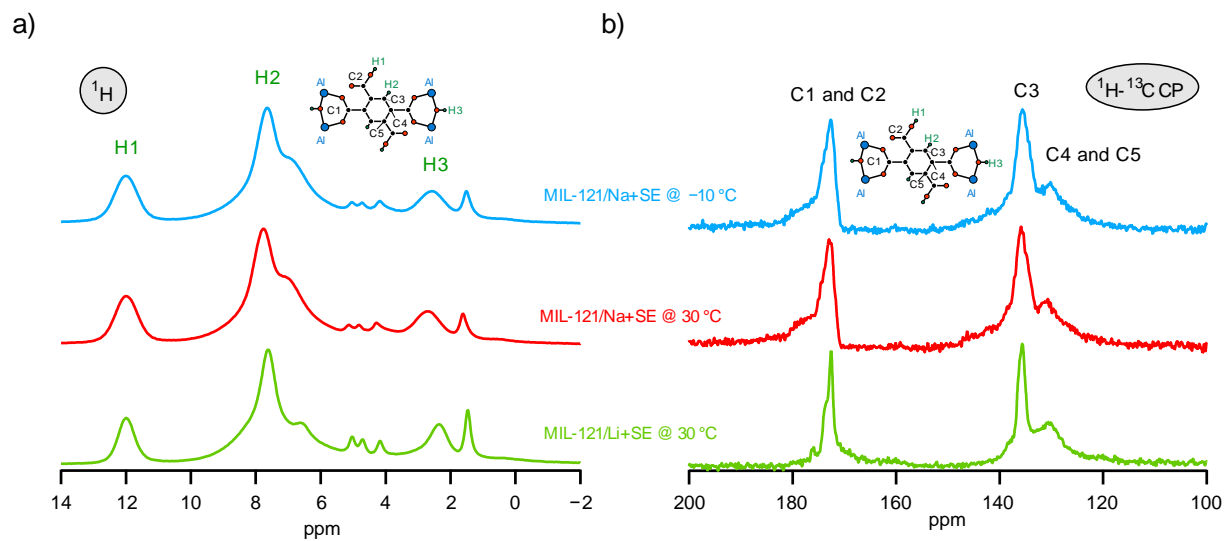


**Figure S7.** MAS spectra of MIL-121/Li+SE at  $30\text{ }^\circ\text{C}$  (green), MIL-121/Na+SE at  $30\text{ }^\circ\text{C}$  (red) and MIL-121/Na+SE at  $-10\text{ }^\circ\text{C}$  (blue). a) shows  $^1\text{H}$  and b) shows  $^1\text{H}$ - $^{13}\text{C}$  CP spectra. The spectra are normalized and given in arbitrary numbers. A part of the structure is shown to explain which H and C atom is assigned to which line in the NMR spectra.

## S4.3. $^{23}\text{Na}$ MAS NMR lines

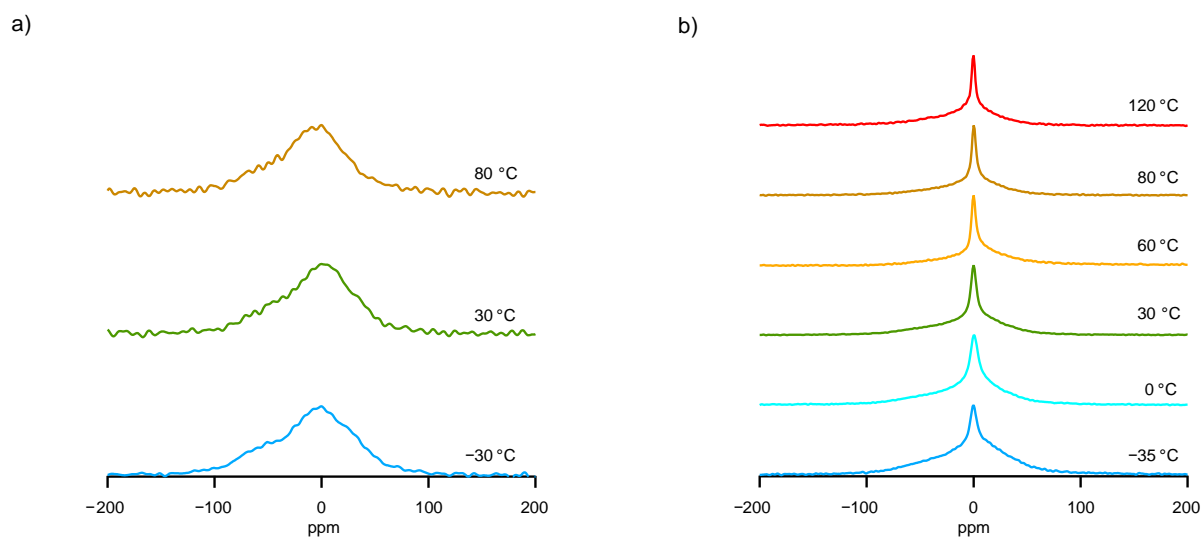


**Figure S8.**  $^{23}\text{Na}$  MAS NMR lines at different temperatures of samples a) MIL-121/Na and b) MIL-121/Na+SE

## S4.4. MAS NMR spectra

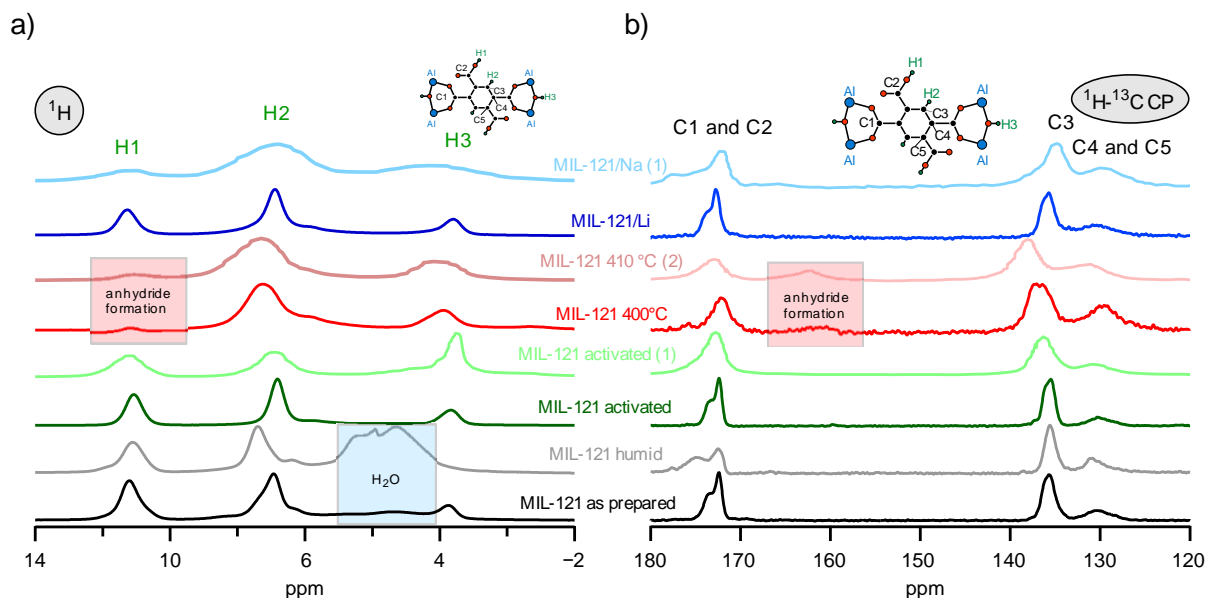


**Figure S9.** MAS spectra of MIL-121 as prepared (black), MIL-121 humid (grey), MIL-121 activated (dark green), MIL-121 activated of reference (1)<sup>1</sup>, MIL-121 activated at 400 °C (red), MIL-121 activated at 410 °C of reference (2)<sup>2</sup>, MIL-121/Li and MIL-121/Na of reference (1)<sup>1</sup>. a) shows <sup>1</sup>H and b) shows <sup>1</sup>H-<sup>13</sup>C CP spectra. The spectra are normalized and given in arbitrary numbers. A part of the structure is shown to explain which H and C atom is assigned to which line in the NMR spectra.

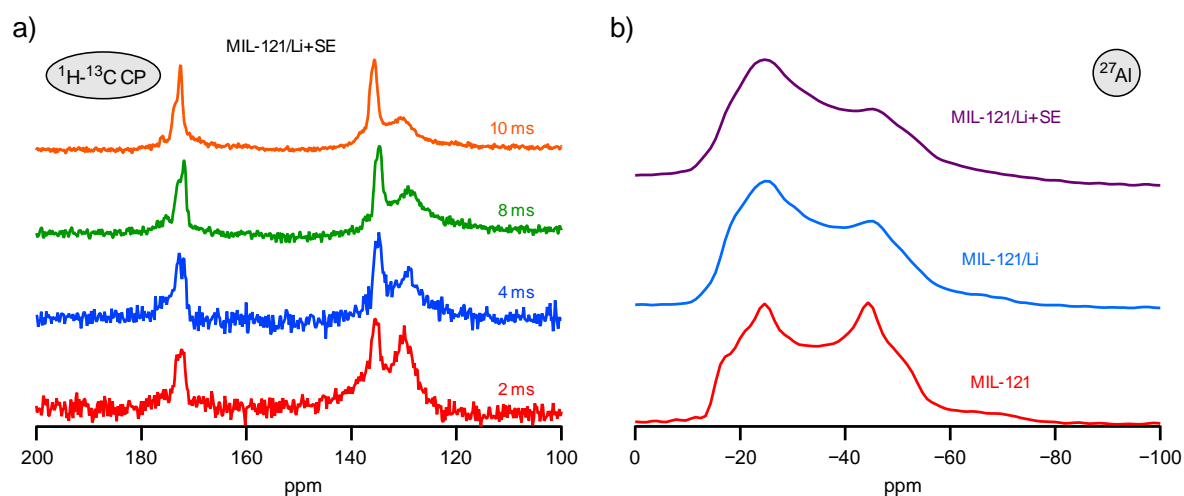


**Figure S10.** a) <sup>1</sup>H-<sup>13</sup>C CP MAS spectra of MIL-121/Li+SE with different contact times of 2 ms (red), 4 ms (blue), 8 ms (green) and 10 ms (orange) and b) <sup>27</sup>Al MAS NMR spectra of MIL-121 (red), MIL-121/Li (blue) and MIL-121/Li+SE (violet) and

## S5.References

1. Chen, S. S.; Lucier, B. E. G.; Luo, W.; Xie, X. K.; Feng, K.; Chan, H.; Terskikh, V. V.; Sun, X. H.; Sham, T. K.; Workentin, M. S.; Huang, Y. N., Loading across the Periodic Table: Introducing 14 Different Metal Ions To Enhance Metal-Organic Framework Performance. *Acs Appl Mater Inter* **2018**, *10* (36), 30296-30305.
2. Chen, S. S.; Mukherjee, S.; Lucier, B. E. G.; Guo, Y.; Wong, Y. T. A.; Terskikh, V. V.; Zaworotko, M. J.; Huang, Y. N., Cleaving Carboxyls: Understanding Thermally Triggered Hierarchical Pores in the Metal-Organic Framework MIL-121. *J Am Chem Soc* **2019**, *141* (36), 14257-14271.



# B | Experimental

In this chapter the different synthesis routes of electrodes and electrolytes are presented. In addition, further sample treatment, cell assembly and sample preparation, which was necessary previous to measurements is described. The standard procedures included the preparation of materials, their characterization with various techniques and the analysis of the data with the help of different software tools. The procedures ought to give an overview of the laboratory work and data analysis done and to list the equipment used in the frame of this thesis. Detailed descriptions of synthesis of materials and analysis methods, however, are given in main manuscripts (see chapter 4) and the supporting information (see appendix A) of the articles.

## B.1. Standard Laboratory Procedures

### B.1.1. Electrode Preparation

**Synthesis of Electrode Materials.** The synthesis of electrode materials was carried out via three different routes. First, the materials, *i.e.* lithium vanadium phosphate (LVP), lithium titanium phosphate (LTP), sodium vanadium phosphate (NVP) and sodium titanium phosphate (NTP), were synthesized via a *sol-gel route*. Citric acid enabled gelation of the respective aqueous mixtures of educts after sufficient solvent evaporation. Further drying steps, grinding and finally sintering under protective atmosphere resulted in carbon coated, well conductive electrode materials. Sintering under ambient atmosphere was realized with NTP samples to obtain an electronically poorly conductive material. The conductivity of the sample was insufficient for battery cycling. Therefore, this NTP sample was treated with glucose and sintered afterwards under protective atmosphere resulting in an, again, well conductive electrode material. Secondly,  $\text{VS}_2$  was obtained after a *hydrothermal synthesis*. An aqueous solution of the reagents resulted in a black precipitate. Thirdly, a solid-state synthesis of LVP was carried out. With high energy ball milling

(*Fritsch, Pulverisette 7, premium line*) the educts are grounded in zirconium oxide beakers and milling balls. The ball mill was additionally used to mix samples with conductive carbon. This was done to increase conductivity of samples, which were not carbon coated upon synthesis.

**Casting of Electrodes.** The slurry was composed of the active material (80 wt%), conductive carbon (Super C65, 20 wt%) and binder (Kynar 761, 20 wt%) as well as a sufficient amount of solvent (N-Methyl-2-pyrrolidone, NMP), which was usually three times the total mass of all solids. The mixture was homogenized in appropriate beakers in a planetary mill (*Fritsch, Pulverisette 7, classic line*) with zirconium oxide balls for 1 h. After each 15 min of milling at 400 rpm a break of 5 min was set. The viscous mixture was *doctor bladed* onto a copper current collector in case of anode materials and onto an aluminium current collector in case of cathode materials. Aluminium was etched with 5 wt% KOH solution at 40 °C previous to casting. The casting was carried out with a velocity of 5 mm s<sup>-1</sup> and a casting gap of 150 µm. The casted current collector foil was dried at 60 °C over night. The final preparation steps included (i) punching of electrode discs with a diameter of 10 mm, (ii) weighing of the discs to determine the mass of active material and (iii) high vacuum drying prior to storage inside a glovebox (*MBraun 150B-G*) with oxygen and water contents usually below 1 ppm.

### B.1.2. Electrolyte Preparation

**Complex Metal Hydrides based Electrolytes.** The complex metal hydride based electrolytes were synthesized by means of *melt-infiltration*. In this process the melted complex metal hydrides, mainly LiBH<sub>4</sub>, infiltrated a porous support *e.g.* silica or alumina. This was realized inside stainless-steel high-pressure autoclaves (*Parr*) under 50 bar hydrogen pressure and about 15 °C above the melting point of the complex metal hydrides. Samples were kept at this temperature for 30 min. After natural cooling, the products were referred to as nanoconfined solid-state electrolytes. In addition, the complex metal hydrides were mixed with anion substituting species like LiI prior to melt-infiltration. Under elevated temperatures this mixture formed a solid solution inside the pores of the supports resulting in nanoconfined anion-substituted solid-state electrolytes.

As an alternative route *solution impregnation* of the supports with LiI was carried out. LiI was dissolved in deionized water or ethanol and added to the support via

a septum. The mixture, inside a round-bottom flask, was connected to a Schlenk line during the whole procedure. The liquid was evaporated that only solid LiI remained inside the pores. Here, the complex metal hydride was only added in a second step, which was again melt-infiltration. All samples were handled inside a glovebox (*MBraunLabmaster*) with H<sub>2</sub>O and O<sub>2</sub> levels typically below 1 ppm.

**Metal Organic Framework based Electrolytes.** MIL-121 was synthesized via a *hydrothermal route* at 220 °C for 24 h in an aqueous environment. The general procedure of MOF based solid-state electrolytes included *post-synthetic modifications (PSMs)* and the addition of a *soaking electrolyte*. PSMs had the purpose of introducing mobile ions to the structure of the MOFs. This was done via acid-base reactions. MIL-121 has acidic groups and with lithium and sodium bases the ions were introduced to the structure. To further enhance the ionic conductivity of the the materials, so-called soaking electrolytes were added to the modified MOFs. Soaking electrolytes are common liquid electrolytes, which are supposed to infiltrate the MOF channels and weaken the bonding of the ions to the structure. Suitable soaking electrolytes were *e.g.* sodium or lithium perchlorate in propylene carbonate. One requirement for the liquid electrolytes was little volatility in order to remain inside the pores when samples were vacuumed during sputtering. Sputtering of gold electrodes was necessary for impedance spectroscopy measurements. (see B.2.2)

## B.2. Measuring Procedures

### B.2.1. Electrochemical Characterization

The electrode materials were characterized electrochemically by means of cyclic voltammetry (CV) and galvanostatic cycling with potential limitation (GCPL). Prior to the electrochemical characterization, electrodes were assembled in *Swagelok-type* or *Pouch cells* inside an Ar-filled glovebox to guarantee no air contamination throughout the measurements. A three-electrode configuration, with a working electrode, a counter electrode and a reference electrode (Li or Na metal), was the usual cell configuration. The cells were connected to a *multichannel MPG-2 and VMP-3 potentiostat from Biologic Science Instruments*. The potentiostat was controlled through the software *EC-LAB VIO-34*. The materials were analysed either in half-cells, where the counter electrode was Li or Na metal or in full-cell configuration, with the counter electrode being the anode and the working electrode being the

cathode. A *Whatman GF/B separator* was placed in between the working and the counter electrode to prevent short circuit. Pouch cells (*Dai Nippon Printing Co., Ltd.*) were assembled and sealed in an Ar-filled glovebox as well. Na or Li metal was used as counter and reference electrode and a separator (*Freudenberg FS 2190*) was placed between each electrode. Typically, LP30<sup>8</sup> for Li cells and 1 M NaFSI in EC:DEC<sup>9</sup> for Na cells were the corresponding electrolytes used in both cell types.

CV was typically performed with scan rates of 0.05, 0.1, 0.2, 0.5, 1.0, 2.0, 5.0, 10, 20 and 50 mV/s in a suitable potential range, depending on the electrode material. Current rates for GCPL measurements were calculated through the corresponding theoretical capacity of the respective electrode. The applied constant currents were in the range of 15  $\mu$ A to 1.5 mA, which corresponds to C-rates between C/10 and 5 C. Typical C-rates of the experiments were C/10, C/5, C/2, 1 C, 2 C and 5 C. When the cell is cycled at a rate of 1 C, the corresponding current will discharge the battery in 1 h. The software EC-LAB provides a calculation tool to obtain anodic and cathodic capacities and coulombic efficiencies.

### B.2.2. Impedance Spectroscopy

Impedance Spectroscopy (IS) measurements were carried out on a *Novocontrol Concept 80 broadband dielectric spectrometer* in the usual frequency range of 10 mHz to 10 MHz. An active sample cell was placed in a cryostat, where N<sub>2</sub> gas is constantly flowing. An *Alpha-AN broadband analyzer* enabled frequencies ranging from 10<sup>-4</sup> Hz to 10<sup>7</sup> Hz. High frequency measurements up to 3 GHz were possible with an *Agilent high frequency analyzer* together with a suitable measurement cell. A *QUATRO cryosystem* controlled the temperature as set prior to the measurement usually between -100 to 120 °C. With the setup, where liquid nitrogen was evaporated and transferred through a gas jet to the cryostat, temperatures from -160 to 400 °C were feasible.[93] The software *WinDETA* was used to set the measurement parameters like temperature and frequency ranges. By entering the geometry of the sample pellet, the software provided results for a large number of parameters, directly or indirectly determined by impedance spectroscopy. These parameters included real part and imaginary part of impedance, conductivity, permittivity, admittance, capacitance, modulus and many more. Prior to the measurement, sample preparation was required. Powder samples were pelletized and sputtered with 100 nm gold lay-

<sup>8</sup>1 M lithium hexafluorophosphate in ethylene carbonate:dimethyl carbonate = 1:1 (v:v)

<sup>9</sup>sodium bis(fluorosulfonyl)imide in ethylene carbonate:diethyl carbonate = 4:6 (v:v)

ers which acted as blocking electrodes for Li and Na ions. Normally samples were pressed with a load of 0.3 tons with a 5 mm die. The thickness of the pellets ranged from 0.5 to 1.5 mm. Special air-tight sample holders or coin cells were used to measure air-sensitive samples.

### B.2.3. Nuclear Magnetic Resonance

**500 MHz spectrometer.** In our laboratories a *Bruker Avance III 500 spectrometer* was mainly used to record high-resolution line spectra of solid-state samples. For this purpose, zirconium oxide NMR rotors (2.5 mm in diameter), provided by Bruker, were filled with powder samples. This was done by applying appropriate tools and step-wise filling. Between each filling step the samples were hand-pressed in order to guarantee a dense packed rotor, which is a requirement for successful rotation. The standard rotation frequency is 25 kHz. In a usual experiment, the measurement temperature was set to 30 °C, but heating and cooling was possible for special purposes. The spectrometer was connected to a 11.7 Tesla cryomagnet which corresponds to different resonance frequencies for different nuclei:

- $^1\text{H}$ : 500.000 MHz
- $^2\text{H}$ : 76.753 MHz
- $^6\text{Li}$ : 73.578 MHz
- $^7\text{Li}$ : 194.317 MHz
- $^{11}\text{B}$ : 160.419 MHz
- $^{13}\text{C}$ : 125.721 MHz
- $^{23}\text{Na}$ : 132.256 MHz
- $^{27}\text{Al}$ : 130.287 MHz

The nuclei are exemplarily listed as they were observed in frame of this thesis. Spectra were usually recorded with a simple single-pulse excitation sequence. The applied pulse length, delay time and number of scans is dependent on the nucleus. Less sensitive nuclei like *e.g.*  $^6\text{Li}$  or  $^{27}\text{Al}$  require much longer measurement times than sensitive nuclei like  $^1\text{H}$ . A crucial parameter is the natural abundance of the measured isotope. Finally, the free induction decays of the measurements were Fourier transformed to obtain the NMR spectra. The spectra are phase corrected with the help of the software *TopSpin* provided by Bruker, that is also used to control the measurements.

Cross polarization (CP) is a useful method to produce spectra of higher resolution of rare or less sensitive nuclei like  $^{13}\text{C}$ . Here, the magnetization of nuclei with strong signals like  $^1\text{H}$  is transferred to  $^{13}\text{C}$ . This enhances the magnetization of  $^{13}\text{C}$ . The enhancement of the signal is proportional to the ratio of the gyromagnetic constants

of the two nuclei ( $\gamma^{\text{H}}/\gamma^{\text{C}}$ ). Additionally, the fast  $T_1$  relaxation time of  $^1\text{H}$  decreases the recycle delay of the measurement and, in further consequence, the duration of the whole experiment. In a CP experiment two contact pulses are applied at the same time. The first pulse, that transfers the polarization, is referred to as spinlock pulse (applied on  $^1\text{H}$  spins). The second pulse (applied on  $^{13}\text{C}$  spins) has to be optimized in order that both nutation frequencies match, which is done by varying the radio frequency power level. If this condition is fulfilled the second contact pulse develops a magnetization. This condition is named after Hartmann and Hahn (*Hartmann-Hahn condition*), who first introduced the method of cross polarization.[117] The contact time is a crucial parameter and depends on the parameters given above; the strength of  $^1\text{H}$ - $^{13}\text{C}$  coupling and relaxation rates. Prior to the two simultaneously applied pulses, a  $90^\circ$  excitation pulse is applied to the  $^1\text{H}$  spins.[117–120]

**300 MHz spectrometer.** A *Bruker Avance III 300 spectrometer* was mainly used to gain information about diffusion related parameters of solid-state ion conductors. Here, a 7.0 Tesla cryomagnet was used to obtain resonance frequencies of certain nuclei:

- $^1\text{H}$ : 300.000 MHz
- $^{11}\text{B}$ : 96.251 MHz
- $^7\text{Li}$ : 116.590 MHz
- $^{23}\text{Na}$ : 79.353 MHz

Sample preparation involved filling a Duran NMR tube and fire sealing under protective atmosphere. The applied ceramic probe head resisted temperatures up to  $300^\circ\text{C}$ . The usual temperature program ranged from  $-100^\circ\text{C}$  to  $200^\circ\text{C}$  in steps of  $20^\circ\text{C}$ . Around a diffusion induced rate peak the number of measurement points was usually increased to every 5 or  $10^\circ\text{C}$ . Cooling and heating was realized with a stream of nitrogen, that is connected to a dewar vessel filled with liquid nitrogen during cooling. The temperature was measured with a *type T thermocouple* and controlled with an *Eurotherm controller*. The measurement of *e.g.*  $^{23}\text{Na}$  required Quartz NMR tubes, since Duran tubes contain sodium, which would interfere the measurement. The same applies to the ceramic probe head, which was replaced by a Teflon probe head when sodium-containing samples were measured.

In the frame of this thesis the 300 MHz spectrometer was used to perform three experiments under static conditions. If a measurement is realized under static conditions it means non-rotating or non-MAS conditions. First, NMR spectra were recorded similar to the basic measurement described above for the 500 MHz spectrometer. A simple one pulse sequence is used to record the spectra. The analysis

of the line shapes at different temperatures gives information about mobility of the nucleus of investigation. A narrowing of the line width with increasing temperature indicates faster diffusion. The line width of the line shape is proportional to the spin-spin relaxation time  $T_2$ , which quantifies the magnetization in y-direction ( $M_y$ ). In contrast to spin-lattice relaxation, where longitudinal magnetization is observed, the determination of  $T_2$  deals with transverse magnetization.[102]

Secondly, a saturation recovery pulse sequence (satrec) was used when  $T_1$  spin-lattice relaxation (SLR) rates ( $1/T_1$ ) were determined. Originally, a longitudinal magnetization is present in z-direction ( $M_z$ ). The *satrec* sequence includes a number of  $\pi/2$  pulses (*approx.* 10) in the order of micro seconds, that destroy  $M_z$ . After this pulse sequence the system is given a certain time  $t_d$  to recover until a single pulse is used to detect the recovery of  $M_z$ . The area under the free induction decay (FID) is used to obtain typical  $M_z$  vs.  $t_d$  curves. Usually  $T_1$  is determined with the help of stretched exponential fits, as  $M_z(t_d)$  is proportional to  $1 - e^{-(\frac{t_d}{T_1})^\gamma}$ . For this purpose the measurement is repeated for *e.g.* 16 times with different  $t_d$ . In SLR measurements extremely fast motional processes with high jump rates  $\tau^{-1}$  in the order of  $10^7$  to  $10^{10} \text{ s}^{-1}$  are detected.[70, 102, 109]

Thirdly,  $T_{1\rho}$  spin-lattice relaxation rates ( $1/T_{1\rho}$ ) were determined under static conditions. Here, slower processes ( $\tau^{-1} = 10^4$  to  $10^6 \text{ s}^{-1}$ ) can be observed by applying the so-called spin-lock technique. While the SLR experiments are carried out in a laboratory frame of reference, in  $\text{SLR}_\rho$  experiments a rotating frame of reference is applied. At the beginning of the pulse sequence a  $\pi/2$  pulse forces the magnetization into the  $x$ - $y$  plane. During a spin-locking period  $t_{lock}$ , a magnetic field  $B_1$  is applied that is responsible for "locking" the magnetization in the  $x$ - $y$  plane. Furthermore, the magnetization ( $M_\rho$ ) relaxes during  $t_{lock}$ , which lasts between  $10 \mu\text{s}$  and 1 s. At the end of  $t_{lock}$  and  $B_1$  the FID serves again to quantify the magnetization; in this case  $M_\rho$ . A number of scans with different locking periods are repeated. After each scan longitudinal magnetization is required to be zero, which is guaranteed by a pre-scan delay that is set to 5 times  $T_1$ . Determination of  $T_{1\rho}$  is again realized with the help of stretched exponential fits:  $M_\rho(t_{lock}) \propto e^{-(\frac{t_{lock}}{T_{1\rho}})^\varphi}$ . As mentioned slower processes can be observed with the spin-lock technique in the rotating frame of reference as the locking frequencies are in the kHz range. In this work a locking frequency of 20 kHz was applied in all  $\text{SLR}_\rho$  experiments.[70, 102, 109]

## B.3. Data Analysis

As already mentioned in section B.2 some software, which controls the measurements also contributes to some extent to the data analysis, *e.g.* EC-Lab provides anodic and cathodic capacities or WinDETA various parameters like conductivity or permittivity. The following software was used additionally to finalize the data analysis and to present the data. To visualize crystallographic structures of materials the software *VESTA* was used. Structures of materials are extremely useful to describe hypotheses like predicted ion pathways or diffusion mechanisms in the materials. The software *ZView* served as a complementary tool for the analysis of impedance spectroscopy data. *ZView* uses equivalent circuits to fit the data points from IS measurements. If there is only one contribution to the total ionic conductivity, *e.g.* from grain boundaries, the equivalent circuit consists of a resistor and a constant phase element connected in parallel. With the fitting parameters the capacitance of the electrolyte can be determined and incomplete semicircles can be fitted by simulating a larger frequency range. For a more detailed description see the publication *Combined Effects of Anion Substitution and Nanoconfinement on the Ionic Conductivity of Li-Based Complex Hydrides* (4.2.2). Furthermore, data was processed and plotted with the software IGOR Pro. Corel Draw was finally used to post-process the figures by adding *e.g.* features for guiding the eye and additional annotations as well as to export the figures as high quality images.

# C | List of Publications

## C.1. Journal Articles

### **A New Solar Cell – Battery Hybrid Energy System: Integrating Organic Photovoltaics with Li-Ion and Na-Ion Technologies**

Sebastian F. Hoefler, [Roman Zettl](#), Daniel Knez, Georg Haberfehlner, Ferdinand Hofer, Thomas Rath, Gregor Trimmel, Martin Wilkening and Ilie Hanzu. *Sustain. Energ. Fuels*, **2020**  
*in peer review*

### **Redox processes in sodium vanadium phosphate cathodes – insights from *operando* magnetometry**

Gregor Klinser, [Roman Zettl](#), Martin Wilkening, Heinz Krenn, Ilie Hanzu and Roland Würschum. *Phys. Chem. Chem. Phys.*, **2019**, 21, 20151  
DOI: 10.1039/c9cp04045e

### **Combined Effects of Anion Substitution and Nanoconfinement on the Ionic Conductivity of Li-Based Complex Hydrides**

[Roman Zettl](#), Laura de Kort, Maria Gombotz, H. Martin R. Wilkening, Petra E. de Jongh and Peter Ngene. *J. Phys. Chem. C*, **2020**, 124, 5, 2806-2816  
DOI: 10.1021/acs.jpcc.9b10607

**Li-Ion Diffusion in Nanoconfined  $\text{LiBH}_4\text{-LiI}/\text{Al}_2\text{O}_3$ : From 2D Bulk Transport to 3D Long-Range Interfacial Dynamics**

Roman Zettl, Maria Gombotz, David Clakson, Steven G. Greenbaum, Peter Ngene, Petra E. de Jongh and H. Martin R. Wilkening. *ACS Appl. Mater. Interfaces*, **2020**, 12, 38570-38583

DOI: 10.1021/acsami.0c10361

## C.2. Oral Presentations

**Lithium-Ion Conductors Based on Porous MIL-121 Metal Organic Frameworks**

Roman Zettl, H. Martin R. Wilkening, Ilie Hanzu. *International Functional Nanomaterials and Nanodevice Conference (Nanomat2017)*, **2017/09/26**, Budapest (Hungary)

**A Hybrid Electrolyte System Based on MIL-121 Metal Organic Frameworks**

Roman Zettl, Sarah Lunghammer, Ilie Hanzu, H. Martin R. Wilkening. *DocDays 2019*, **2019/04/25**, Graz (Austria)

**A Hybrid Electrolyte System Based on MIL-121 Metal Organic Frameworks**

Roman Zettl, Sarah Lunghammer, Ilie Hanzu, H. Martin R. Wilkening. *European Congress and Exhibition on Advanced Materials and Processes (EUROMAT2019)*, **2019/09/05**, Stockholm (Sweden)

## C.3. Poster Presentations

**Towards a Solar-Cell Battery Hybrid System**

Roman Zettl, Sebastian F. Höfler, Thomas Rath, Gregor Trimmel, H. Martin R. Wilkening, Ilie Hanzu. *Americas International Meeting on Electrochemistry and Solid State Science (AiMES2018)*, **2018/10/02**, Cancun (Mexico)

**Towards Ceramic Solid-State Batteries – A Case Study on  $\text{LiBH}_4$  Solid Electrolyte**

Roman Zettl, Martin Philipp, Marlena Volck, Volker Hennige, H. Martin R. Wilkening, Ilie Hanzu. *D-A-CH Keramiktagung 2019*, **2019/05/06**, Leoben (Austria)



## D | Bibliography

- [1] M. Finsterbusch, T. Danner, C. L. Tsai, S. Uhlenbruck, A. Latz, O. Guillon, *ACS Appl. Mater. Interfaces* **2018**, *10*, 22329–22339.
- [2] S. Yu, A. Mertens, H. Tempel, R. Schierholz, H. Kungl, R. A. Eichel, *ACS Appl. Mater. Interfaces* **2018**, *10*, 22264–22277.
- [3] Y. Kato, S. Hori, T. Saito, K. Suzuki, M. Hirayama, A. Mitsui, M. Yonemura, H. Iba, R. Kanno, *Nat. Energy* **2016**, *1*, 1–7.
- [4] J. J. Berzelius, *J. Chem. Phys.* **1818**, *21*, 44–48.
- [5] M. Winter, B. Barnett, K. Xu, *Chem. Rev.* **2018**, *118*, 11433–11456.
- [6] J.-K. Park, *Principles and Applications of Lithium Secondary Batteries*, Wiley-VCH Germany, **2012**.
- [7] B. Scrosati, *J. Solid. State. Electr.* **2011**, *15*, 1623–1630.
- [8] A. Volta, *Philos. Trans.* **1800**, *2*, 430.
- [9] S. K. Lower, *Electrochemistry - Chemical reactions at an electrode, galvanic and electrolytic cells*, **2004**, pp. 3–37.
- [10] C. Daniel, J. O. Besenhard, *Handbook of Battery Materials*, **2011**, pp. 21–27, 66.
- [11] P. Ruetschi, *J. Power Sources* **1977**, *2*, 3–24.
- [12] G. Plante, *C.R. Acad. Sci.* **1860**, *50*, 640.
- [13] G.-L. Leclanché, *Compt. Rend.* **1866**, *83*, 54.
- [14] J. B. Phipps, T. G. Hayes, P. M. Skarstad, D. F. Untereker, *Solid State Ion.* **1986**, *18*, 1073–1077.
- [15] The Royal Swedish Academy of Sciences, The Nobel Prize in Chemistry 2019, **2019**.
- [16] M. S. Whittingham, *Science* **1976**, *192*, 1126–1127.

- 
- [17] K. Mizushima, P. Jones, P. Wiseman, J. Goodenough, *Solid State Ion.* **1981**, 3-4, 171–174.
- [18] R. Yazami, P. Touzain, *J. Power Sources* **1983**, 9, 365–371.
- [19] A. Yoshino, K. Sanechika, T. Nakajima, USP4,668,595, **1985**.
- [20] A. Yoshino, *Angew. Chem. Int. Ed* **2012**, 51, 5798–5800.
- [21] D. Mazouzi, B. Hammouti, *J. Mat. Environ. Sci.* **2019**, 10, 1194–1199.
- [22] C. Vaalma, D. Buchholz, M. Weil, S. Passerini, *Nat. Rev. Mater.* **2018**, 3, 18013.
- [23] V. Palomares, P. Serras, I. Villaluenga, K. B. Hueso, J. Carretero-González, T. Rojo, *Energy Environ. Sci.* **2012**, 5, 5884–5901.
- [24] J. W. Choi, D. Aurbach, *Nat. Rev. Mater.* **2016**, 1, 16013.
- [25] M. Winter, J. O. Besenhard, M. E. Spahr, P. Novak, *Adv. Mater.* **1998**, 10, 725–763.
- [26] M. S. Balogun, W. Qiu, Y. Luo, H. Meng, W. Mai, A. Onasanya, T. K. Olaniyi, Y. Tong, *Nano Res.* **2016**, 9, 2823–2851.
- [27] W. J. Zhang, *J. Power Sources* **2011**, 196, 13–24.
- [28] H. B. Wu, J. S. Chen, H. H. Hng, X. W. Lou, *Nanoscale* **2012**, 4, 2526–2542.
- [29] K. M. Colbow, J. R. Dahn, R. R. Haering, *J. Power Sources* **1989**, 26, 397–402.
- [30] M. Wilkening, W. Iwaniak, J. Heine, V. Epp, A. Kleinert, M. Behrens, G. Nusspl, W. Bensch, P. Heitjans, *Phys. Chem. Chem. Phys.* **2007**, 9, 6199–6202.
- [31] M. D. Bhatt, J. Y. Lee, *Int. J. Hydrogen Energ.* **2019**, 44, 10852–10905.
- [32] N. Nitta, G. Yushin, *Part. Part. Syst. Char.* **2014**, 31, 317–336.
- [33] H. Jia, X. Li, J. Song, X. Zhang, L. Luo, Y. He, B. Li, Y. Cai, S. Hu, X. Xiao, C. Wang, K. M. Rosso, R. Yi, R. Patel, J. G. Zhang, *Nat. Commun.* **2020**, 11, 1474.
- [34] H. Pan, S. Zhang, J. Chen, M. Gao, Y. Liu, T. Zhu, Y. Jiang, *Mol. Syst. Des. Eng.* **2018**, 3, 748–803.
- [35] R. Chen, M. Knapp, M. Yavuz, R. Heinzmann, D. Wang, S. Ren, V. Trouillet, S. Lebedkin, S. Doyle, H. Hahn, H. Ehrenberg, S. Indris, *J. Phys. Chem. C* **2014**, 118, 12608–12616.

- [36] J. Ma, P. Hu, G. Cui, L. Chen, *Chem. Mater.* **2016**, *28*, 3578–3606.
- [37] J. W. Fergus, *J. Power Sources* **2010**, *195*, 939–954.
- [38] X. Rui, Q. Yan, M. Skyllas-Kazacos, T. M. Lim, *J. Power Sources* **2014**, *258*, 19–38.
- [39] W. Li, E. M. Erickson, A. Manthiram, *Nat. Energy* **2020**, *5*, 26–34.
- [40] L. Hu, S. S. Zhang, Z. Zhang, *Electrolytes for lithium and lithium-ion batteries*, Springer, **2015**, pp. 5–200.
- [41] K. Xu, *Chem. Rev.* **2004**, *104*, 4303–4417.
- [42] G. H. Wrodnigg, J. O. Besenhard, M. Winter, *J. Electrochem. Soc.* **1999**, *146*, 470–472.
- [43] K. Abe, Y. Ushigoe, H. Yoshitake, M. Yoshio, *J. Power Sources* **2006**, *153*, 328–335.
- [44] C. Sun, J. Liu, Y. Gong, D. P. Wilkinson, J. Zhang, *Nano Energy* **2017**, *33*, 363–386.
- [45] A. Manthiram, X. Yu, S. Wang, *Nat. Rev. Mater.* **2017**, *2*, 16103.
- [46] L. Fan, S. Wei, S. Li, Q. Li, Y. Lu, *Adv. Energy Mater.* **2018**, *8*, 1702657.
- [47] M. Uitz, V. Epp, P. Bottke, M. Wilkening, *J. Electroceram.* **2017**, *38*, 142–156.
- [48] J. Evans, C. A. Vincent, P. G. Bruce, *Polymer* **1987**, *28*, 2324–2328.
- [49] L. Xu, S. Tang, Y. Cheng, K. Wang, J. Liang, C. Liu, Y. C. Cao, F. Wei, L. Mai, *Joule* **2018**, *2*, 1991–2015.
- [50] V. Thangadurai, H. Kaack, W. J. Weppner, *J. Am. Ceram. Soc.* **2003**, *86*, 437–440.
- [51] R. Murugan, V. Thangadurai, W. Weppner, *Angew. Chem. Int. Ed.* **2007**, *46*, 7778–7781.
- [52] J. B. Goodenough, H. Y.-P. Hong, J. A. Kafalas, *Mater. Res. Bull.* **1976**, *11*, 203–220.
- [53] I. Hanghofer, M. Brinek, S. L. Eisbacher, B. Bitschnau, M. Volck, V. Hennige, I. Hanzu, D. Rettenwander, H. M. Wilkening, *Phys. Chem. Chem. Phys.* **2019**, *21*, 8489–8507.
- [54] R. Chen, W. Qu, X. Guo, L. Li, F. Wu, *Mater. Horiz.* **2016**, *3*, 487–516.
- [55] H. C. J. Zhou, S. Kitagawa, *Chem. Soc. Rev.* **2014**, *43*, 5415–5418.

- 
- [56] B. M. Wiers, M. L. Foo, N. P. Balsara, J. R. Long, *J. Am. Chem. Soc.* **2011**, *133*, 14522–14525.
- [57] R. Ameloot, M. Aubrey, B. M. Wiers, A. P. Gõmora-Figueroa, S. N. Patel, N. P. Balsara, J. R. Long, *Chem. Eur. J.* **2013**, *19*, 5533–5536.
- [58] S. S. Park, Y. Tulchinsky, M. Dincă, *J. Am. Chem. Soc.* **2017**, *139*, 13260–13263.
- [59] A. Petronico, T. P. Money Penny, B. G. Nicolau, J. S. Moore, R. G. Nuzzo, A. A. Gewirth, *J. Am. Chem. Soc.* **2018**, *140*, 7504–7509.
- [60] Z. Wang, R. Tan, H. Wang, L. Yang, J. Hu, H. Chen, F. Pan, *Adv. Mater.* **2018**, *30*, 1704436.
- [61] A. Cisak, L. Werblan, *High-energy non-aqueous batteries*, **1993**, pp. 197–201.
- [62] J. Heinze, *Angew. Chem.* **1984**, *96*, 832–840.
- [63] D. A. C. Brownson, C. E. Banks, *The Handbook of Graphene Electrochemistry*, **2014**, pp. 35–44.
- [64] G. A. Mabbott, *J. Chem. Educ.* **1983**, *60*, 697–702.
- [65] P. T. Kissinger, W. R. Heineman, *J. Chem. Educ.* **1983**, *60*, 702–706.
- [66] T. Kim, W. Choi, H.-C. Shin, J.-Y. Choi, J. M. Kim, M.-S. Park, W.-S. Yoon, *J. Electrochem. Sci. Technol.* **2020**, *11*, 14–25.
- [67] P. J. Gellings, H. Bouwmeester, *The CRC Handbook of Solid State Electrochemistry*, CRC Press, **1997**.
- [68] E. Lifshin, *X-ray Characterization of Materials*, Wiley-VCH, **1999**.
- [69] V. K. Pecharsky, P. Y. Zavalij, *Fundamentals of Powder Diffraction and Structural Characterization of Materials*, Springer, **2003**.
- [70] P. Heitjans, J. Kräger, *Diffusion in Condensed Matter*, Springer, **2005**.
- [71] A. Fick, *Ann. Phys.* **1855**, *170*, 59.
- [72] M. Helmut, *Diffusion in Solids*, Springer, **2007**.
- [73] A. Paul, T. Laurila, V. Vuorinen, S. V. Divinski, *Thermodynamics, Diffusion and the Kirkendall Effect in Solids*, Springer, **2014**.
- [74] S. Breuer, PhD thesis, **2018**.
- [75] R. J. D. Tilley, *Defects in Solids*, Wiley, **2008**.
- [76] B. Gadermaier, B. Stanje, A. Wilkening, I. Hanzu, P. Heitjans, H. M. R. Wilkening, *J. Phys. Chem. C* **2019**, *123*, 10153–10162.

- [77] A. R. West, *Solid state chemistry and its applications*, Wiley, **2014**.
- [78] E. C. Subbarao, *Solid Electrolytes and Their Applications*, Plenum Press, **1980**.
- [79] R. J. D. Tilley, *Understanding Solids*, Wiley, **2004**.
- [80] K. L. Ngai, *Phys. Rev. B* **1993**, *48*, 13481.
- [81] C. León, M. L. Lucía, J. Santamaría, M. A. París, J. Sanz, A. Varez, *Phys. Rev. B* **1996**, *54*, 184–189.
- [82] I. Svare, F. Borsa, D. R. Torgeson, S. W. Martin, *Phys. Rev. B* **1993**, *48*, 9336.
- [83] K. Funke, I. Riess, *Z. Phys. Chem. Neue Folge* **1984**, 217–232.
- [84] K. L. Ngai, C. T. White, *Phys. Rev. B* **1979**, *20*, 2475–2486.
- [85] K. L. Ngai, A. K. Jonscher, C. T. White, *Nature* **1979**, *277*, 185–189.
- [86] K. Funke, *Prog. Solid St. Chem.* **1993**, *22*, 111–195.
- [87] K. Funke, *Z. Phys. Chem. Neue Folge* **1987**, *154*, 251–295.
- [88] K. L. Ngai, R. W. Rendell, *ACS Sym. Ser.* **1997**, *676*, 45–66.
- [89] V. F. Lvovich, *Impedance Spectroscopy, Applications to Electrochemical and Dielectric Phenomena*, **2012**, pp. 1–49.
- [90] J.-P. Diard, B. Le Gorrec, C. Montella, *Handbook of Electrochemical Impedance Spectroscopy*, **2017**.
- [91] E. Barsoukov, J. R. Macdonald, *Impedance Spectroscopy - Theory, Experiment and Applications*, Wiley, **2005**.
- [92] R. Zettl, I. Hanzu, *Lithium Ion Conductors based on MIL-121 Metal Organic Frameworks*, **2017**, p. 16.
- [93] F. Preishuber-Pflügl, PhD thesis, **2016**, p. 102.
- [94] D. L. Sidebottom, *Rev. Mod. Phys.* **2009**, *81*, 999–1014.
- [95] B. J. T. S. Irvine, D. C. Sinclair, A. R. West, *Adv. Mater.* **1990**, *2*, 132–138.
- [96] A. K. Jonscher, *Nature* **1977**, *267*, 673–679.
- [97] D. L. Sidebottom, *Phys. Rev. Lett.* **1999**, *83*, 983–986.
- [98] F. Preishuber-Pflügl, V. Epp, S. Nakhal, M. Lerch, M. Wilkening, *Phys. Status Solidi C* **2015**, *12*, 10–14.
- [99] F. Preishuber-Pflügl, M. Wilkening, *Dalton Trans.* **2016**, *45*, 8675–8687.

- 
- [100] C. Cramer, K. Funke, T. Saatkamp, D. Wilmer, M. D. Ingram, *Z. Naturforsch.* **1995**, *50a*, 613–623.
- [101] M. Wilkening, PhD thesis, **2005**, pp. 3–9.
- [102] V. Epp, M. Wilkening, *Handbook of Solid State Batteries*, (Eds.: N. J. Dudney, W. C. West, J. Nanda), World Scientific, **2015**, pp. 133–190.
- [103] A. Abragam, *The Principles of Nuclear Magnetism*, Oxford University Press, **1961**.
- [104] J. Keeler, *Understanding NMR Spectroscopy*, Wiley, **2002**.
- [105] C. Vinod Chandran, P. Heitjans, *Solid-State NMR Studies of Lithium Ion Dynamics Across Materials Classes, Vol. 89*, 1st ed., Elsevier Ltd., **2016**, pp. 1–102.
- [106] N. Bloembergen, E. M. Purcell, R. V. Pound, *Phys. Rev.* **1948**, *73*, 679–712.
- [107] A. Kuhn, S. Narayanan, L. Spencer, G. Goward, V. Thangadurai, M. Wilkening, *Phys. Rev. B* **2011**, *83*, 1–11.
- [108] E. O. Stejskal, J. E. Tanner, *J. Chem. Phys.* **1965**, *42*, 288–292.
- [109] R. Zettl, M. Gombotz, D. Clarkson, S. G. Greenbaum, P. Ngene, P. E. de Jongh, H. M. R. Wilkening, *ACS Appl. Mater. Interfaces* **2020**, *12*, 38570–38583.
- [110] E. R. Andrew, *Phil. Trans. R. Soc. Lond. A* **1981**, *299*, 505–520.
- [111] M. J. Duer, *Solid-state NMR Spectroscopy - Principles and Applications*, Blackwell Science, **2002**, pp. 73–85.
- [112] G. Klinser, R. Zettl, M. Wilkening, H. Krenn, I. Hanzu, R. Würschum, *Phys. Chem. Chem. Phys.* **2019**, *21*, 20151–20155.
- [113] J.-P. Soulie, G. Renaudin, R. Cerny, K. Yvon, *J. Alloys Compd.* **2002**, *346*, 200–205.
- [114] C. Volkringer, T. Loiseau, N. Guillou, G. Férey, M. Haouas, F. Taulelle, E. Elkaim, N. Stock, *Inorg. Chem.* **2010**, *49*, 9852–9862.
- [115] S. Chen, S. Mukherjee, B. E. Lucier, Y. Guo, Y. T. A. Wong, V. V. Terskikh, M. J. Zaworotko, Y. Huang, *J. Am. Chem. Soc.* **2019**, *141*, 14257–14271.
- [116] R. Zettl, L. De Kort, M. Gombotz, H. M. R. Wilkening, P. E. De Jongh, P. Ngene, *J. Phys. Chem. C* **2020**, *124*, 2806–2816.
- [117] S. R. Hartmann, E. L. Hahn, *Phys. Rev.* **1962**, *128*, 2042–2053.

- [118] A. M. Pyle, D. W. Christianson, S. P. Colowick, N. O. Kaplan, *Methods in Enzymology*, Elsevier, **2019**, pp. 281–304.
- [119] B. H. Meier, *Chem. Phys. Lett.* **1992**, *188*, 201–207.
- [120] E. O. Stejskal, J. Schaefer, J. S. Waugh, *J. Magnet. Reson.* **1977**, *28*, 105–112.